



**EXPERIMENTS, MODELLING AND ANALYSIS OF  
FRETTING FATIGUE FOR INCONEL 718 AND TI-6AL-4V  
UNDER TIME-VARYING CONTACT NORMAL LOAD  
AT ROOM AND HIGH TEMPERATURE**

**GABRIEL MAGALHÃES JUVENAL ALMEIDA**

**TESE DE DOUTORADO EM ENGENHARIA MECÂNICA  
DEPARTAMENTO DE ENGENHARIA MECÂNICA**

**FACULDADE DE TECNOLOGIA**

**UNIVERSIDADE DE BRASÍLIA**

**UNIVERSIDADE DE BRASÍLIA  
FACULDADE DE TECNOLOGIA  
DEPARTAMENTO DE ENGENHARIA MECÂNICA**

**EXPERIMENTS, MODELLING AND ANALYSIS OF  
FRETTING FATIGUE FOR INCONEL 718 AND TI-6AL-4V  
UNDER TIME-VARYING CONTACT NORMAL LOAD  
AT ROOM AND HIGH TEMPERATURE**

**GABRIEL MAGALHÃES JUVENAL ALMEIDA**

Orientador: JOSÉ ALEXANDER ARAÚJO, D.PHIL. - UNIVERSIDADE DE BRASÍLIA

Coorientadora: SYLVIE POMMIER, PH.D. - UNIVERSITÉ PARIS-SACLAY

**TESE DE DOUTORADO EM ENGENHARIA MECÂNICA**

**PUBLICAÇÃO PCMEC.TD - XXX/2022  
BRASÍLIA-DF, 16 DE SETEMBRO DE 2022.**

**UNIVERSIDADE DE BRASÍLIA  
FACULDADE DE TECNOLOGIA  
DEPARTAMENTO DE ENGENHARIA MECÂNICA**

**EXPERIMENTS, MODELLING AND ANALYSIS OF  
FRETTING FATIGUE FOR INCONEL 718 AND TI-6AL-4V  
UNDER TIME-VARYING CONTACT NORMAL LOAD  
AT ROOM AND HIGH TEMPERATURE**

**GABRIEL MAGALHÃES JUVENAL ALMEIDA**

TESE DE DOUTORADO ACADÊMICO SUBMETIDA AO DEPARTAMENTO DE ENGENHARIA MECÂNICA DA FACULDADE DE TECNOLOGIA DA UNIVERSIDADE DE BRASÍLIA, COMO PARTE DOS REQUISITOS NECESSÁRIOS PARA A OBTENÇÃO DO GRAU DE DOUTOR EM ENGENHARIA MECÂNICA.

**APROVADA POR:**

José Alexander Araújo, D.Phil. - Universidade de Brasília  
(Orientador)

Sylvie Pommier, Ph.D. - Université Paris-Saclay  
(Coorientadora)

Marie-Christine Baietto, Ph.D. - Institut National des Sciences Appliquées de Lyon  
(Examinadora externa)

David Nowell, D.Phil. - Imperial College London  
(Examinador externo)

Fábio Comes de Castro, Ph.D. - Universidade de Brasília  
(Examinador interno)

**BRASÍLIA, 16 DE SETEMBRO DE 2022.**

## **FICHA CATALOGRÁFICA**

GABRIEL MAGALHÃES JUVENAL ALMEIDA

**Experiments, modelling and analysis of fretting fatigue for Inconel 718 and Ti-6Al-4V under time-varying contact normal load at room and high temperature**

**2022xv, 181p., 201x297 mm**

(ENM/FT/UnB, Doutor, Engenharia Mecânica, 2022)

Tese de Doutorado - Universidade de Brasília

Faculdade de Tecnologia - Departamento de Engenharia Mecânica

## **REFERÊNCIA BIBLIOGRÁFICA**

GABRIEL MAGALHÃES JUVENAL ALMEIDA (2022) Experiments, modelling and analysis of fretting fatigue for Inconel 718 and Ti-6Al-4V under time-varying contact normal load at room and high temperature. Tese de Doutorado em Engenharia Mecânica, Publicação xxx/2022, Departamento de Engenharia Mecânica, Universidade de Brasília, Brasília, DF, 181p.

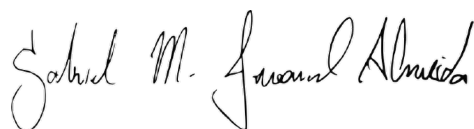
## **CESSÃO DE DIREITOS**

AUTOR: Gabriel Magalhães Juvenal Almeida

TÍTULO: Experiments, modelling and analysis of fretting fatigue for Inconel 718 and Ti-6Al-4V under time-varying contact normal load at room and high temperature.

GRAU: Doutor ANO: 2022

É concedida à Universidade de Brasília permissão para reproduzir cópias desta tese de Doutorado e para emprestar ou vender tais cópias somente para propósitos acadêmicos e científicos. O autor se reserva a outros direitos de publicação e nenhuma parte desta tese de Doutorado pode ser reproduzida sem a autorização por escrito do autor.



---

Gabriel Magalhães Juvenal Almeida

# Experiments, modelling and analysis of fretting fatigue for Inconel 718 and Ti-6Al-4V under time-varying contact normal load at room and high temperature

**Doctoral thesis of the University of Paris-Saclay and the University of Brasilia**

École doctorale n° 579, Sciences Mécaniques et Énergétiques, Matériaux et Géosciences (SMEMaG)  
Spécialité de doctorat: Mécanique

Programa de Pós-Graduação em Ciências Mecânicas (PCMEC)

Thesis prepared in the GFFM and the LMT research units, under the supervision of José Araújo, Ph.D. (UnB) and Sylvie Pommier, Ph.D. (UPS), and co-supervision of the Guillaume Chassaing, Ph.D. (Safran Group) as industrial partner.

**Thesis defended at University of Paris-Saclay on September 16, 2022, by**

**Gabriel Magalhães Juvenal Almeida**

## Doctoral jury

<b>Marie-Christine Baietto</b> Ph.D., Institut National des Sciences Appliquées de Lyon	Présidente
<b>David Nowell</b> Ph.D., Imperial College London	Rapporteur & Examineur
<b>Noël Brunetière</b> Ph.D., Institut Pprime	Rapporteur & Examineur
<b>Fábio Castro</b> Ph.D., University of Brasilia	Examineur
<b>José Alexander Araújo</b> Ph.D., University of Brasilia	Thesis director
<b>Sylvie Pommier</b> Ph.D., Université Paris-Saclay	Thesis director

**Title:** Experiments, modelling and analysis of fretting fatigue for Inconel 718 and Ti-6Al-4V under time-varying contact normal load at room and high temperature.

**Key words:** Fretting Fatigue; Cyclic contact normal load; High temperature; Wear; Inconel 718; Ti-6Al-4V.

**Abstract:** This work has been developed within the scope of a joint PhD agreement between the University of Paris-Saclay (UPS) and the University of Brasilia (UnB). The scientific context of the thesis has been chosen to try to provide data and solutions for problems in the aeronautical sector, as Safran Aircraft Engines has been an important industrial partner for this and other thesis in both universities. In this setting, one of the motivations to study the effect of a variable contact normal loading in the fretting fatigue problem comes, not only from the fact that there are few reliable experimental data and analyses in these conditions, but also that, in practical applications, such as the one existing between the blade root and the disk interface of an aircraft turbine, such contact load is also time-varying. Within this context, to be more precise, the present thesis has three main goals. The first one is to design and construct a new fretting fatigue apparatus capable of performing different types of tests, where the loads and their respective actuators involved in the experiments can be independently controlled. The test rig will be designed so that fretting fatigue experiments can also be carried out at high temperatures. The second goal is to evaluate the effect of cyclic normal load in fretting fatigue strength for the titanium alloy Ti-6Al-4V at room temperature and for the Inconel 718 alloy at room and elevated temperature. These materials were specially chosen due to the great interest of the aeronautical industry. The third and final aim is to assess fretting life by means of a finite element model which considers wear effects and a multiaxial fatigue parameter.

A new four actuators fretting fatigue apparatus was entirely designed to tackle the problem of imposing cyclic contact normal load. The cyclic normal load is now applied by two MTS servo-hydraulic actuators, which were installed perpendicularly to the fretting specimen. Further, the tangential and fatigue loads are applied by independent servo-hydraulic actuators. Due to these upgrades, the new fretting fatigue rig of the

University of Brasilia can independently control all the loads involved in the fretting tests (bulk, normal and tangential loads). All these loads can not only vary with time in-phase or out-of-phase, but their waveforms can also be applied synchronously or asynchronously. Moreover, two ceramic igniters were placed next to the contact parts to conduct tests at elevated temperatures. The heating system is capable to reaches to reach temperatures up to 750°C and maintaining it stable within a range of  $\pm 10^\circ\text{C}$ .

In order to evaluate the influence of the cyclic normal load on the fretting fatigue strength, tests under the partial-slip condition with a constant and cyclic contact normal load were conducted at room temperature for the Ti-6Al-4V alloy and at room and 540°C for the Inconel 718 alloy. The experimental results indicate that cyclic normal load has a beneficial effect on fretting life for the specific conditions of tests here conducted. This behaviour was observed for the Ti-6Al-4V and Inconel 718 alloys at both tested temperatures. Besides that, an experimental campaign to assess the influence of time-varying normal load on the friction coefficient was also carried out. Based on this experimental evaluation, the presence of cyclic normal loads does not seem to influence the coefficient of friction under partial slip conditions. However, comparing the friction coefficient results of the Inconel 718 alloy at room and elevated temperature, a significant reduction was observed for both contact normal loading situations with the increase of the temperature.

In addition, a finite element model (considering and neglecting wear effects) was used in conjunction with the Smith-Watson-Topper critical plane parameter and a non-local stress averaging approach to estimate fretting life. Concerning the life estimate approaches considered in this study, for the constant and cyclic normal load cases, both implemented methodologies, whether accounting or neglecting wear, provided satisfactory results, with the one disregarding wear being slightly more accurate.

**Titre:** Expériences, modélisation et analyse de la fatigue par fretting pour Inconel 718 et Ti-6Al-4V sous charge normale de contact variable dans le temps à température ambiante et élevée.

**Mots clés:** Fatigue par fretting; Force normale de contact cyclique; Élevée Température; Usure; Inconel 718; Ti-6Al-4V.

**Résumé:** Ce travail a été développé dans le cadre d'une convention de cotutelle entre l'Université Paris-Saclay (UPS) et l'Université de Brasília (UnB). Le contexte scientifique de la thèse a été choisi pour tenter de fournir des données et des solutions aux problèmes du secteur aéronautique, sachant que Safran Aircraft Engines a été un partenaire industriel important pour cette thèse et d'autres dans les deux universités. Dans ce cadre, l'une des motivations pour étudier l'effet d'un chargement normal de contact variable dans le problème de fretting fatigue devient important, non seulement du fait qu'il existe peu de données expérimentales et d'analyses fiables dans ces conditions, mais aussi que, dans les applications pratiques, comme celle existant entre le pied d'aube et l'interface disque d'une turbine d'aéronef, cette charge de contact est également variable dans le temps. Dans ce contexte, pour être plus précis, la présente thèse a trois objectifs principaux. Le premier consiste à concevoir et construire un nouvel appareil de fretting fatigue capable d'effectuer différents types d'essais, où les charges et leurs actionneurs respectifs impliqués dans les expériences peuvent être contrôlés indépendamment. Le banc d'essai sera conçu de manière à ce que les expériences de fretting fatigue puissent également être réalisées à des températures élevées. Le deuxième objectif est d'évaluer l'effet de la charge normale cyclique sur la résistance à la fatigue par frottement pour l'alliage de titane Ti-6Al-4V à la température ambiante et pour l'alliage Inconel 718 à la température ambiante et à une température élevée. Ces matériaux ont été spécialement choisis en raison du grand intérêt qu'ils présentent dans l'industrie aéronautique. Le troisième et dernier objectif est d'évaluer la durée de vie due au fretting au moyen d'un modèle d'éléments finis prenant en compte les effets d'usure et un paramètre de fatigue multiaxiale. Le nouvel appareil de fatigue par frottement à quatre actionneurs a été entièrement conçu pour résoudre le problème de l'imposition d'une charge normale de contact cyclique. La charge normale cyclique est maintenant appliquée par deux actionneurs servo-hydrauliques MTS qui ont été installés perpendiculairement à l'éprouvette de fretting. De plus, les charges tangentielles et de fatigue sont appliquées par des actionneurs servo-hydrauliques indépendants. Grâce à ces mises à niveau, le nouveau banc de fatigue de fretting de l'Université de Brasília peut contrôler in-

dépendamment toutes les charges dans les tests de fretting (charges en vrac, normales et tangentielles). Toutes ces charges peuvent non seulement varier dans le temps en phase ou en déphasage, mais leurs formes d'onde peuvent également être appliquées de manière synchrone ou asynchrone. De plus, deux allumeurs en céramique ont été placés à côté des pièces de contact pour effectuer des tests à des températures élevées. Le système de chauffage est capable d'atteindre des températures allant jusqu'à 750° et de les maintenir dans une plage stable de  $\pm 10^\circ$ . Afin d'évaluer l'influence de la charge normale cyclique sur la résistance à la fatigue par fretting, des essais en condition de glissement partiel avec une charge normale de contact constante et cyclique ont été réalisés à la température ambiante pour l'alliage Ti-6Al-4V et à température ambiante et à 540 °C pour l'alliage Inconel 718. Les résultats expérimentaux indiquent que la charge normale cyclique a un effet bénéfique sur la durée de vie au frottement pour les conditions spécifiques des tests effectués dans ce travail. Ce comportement a été observé pour les alliages Ti-6Al-4V et Inconel 718 aux deux températures testées. Par ailleurs, une campagne expérimentale pour évaluer l'influence de la charge normale variant dans le temps sur le coefficient de frottement a également été menée. Sur la base de cette évaluation expérimentale, la présence de charges normales cycliques ne semble pas influencer le coefficient de frottement dans des conditions de glissement partiel. Cependant, en comparant les résultats du coefficient de frottement de l'alliage Inconel 718 à la température ambiante et élevée, une réduction significative a été observée pour les deux situations de chargement normal de contact avec l'augmentation de la température. De plus, un modèle d'éléments finis, tenant compte et négligeant les effets d'usure, a été utilisé en conjonction avec le paramètre du plan critique de Smith-Watson-Topper et une approche de moyenne des contraintes non locales pour estimer la durée de vie au frottement. Concernant les approches d'estimation de durée de vie considérées dans cette étude, pour les cas de charges normales constantes et cycliques, les deux méthodologies mises en œuvre, qu'elles tiennent compte ou négligent l'usure, ont fourni des résultats satisfaisants, toutefois celle qui ne tient pas compte de l'usure étant légèrement plus précise.

**Título:** Experimentos, modelagem e análise de fadiga por fretting para as ligas Inconel 718 e Ti-6Al-4V sob carga normal de contato variável em temperaturas ambiente e elevada.

**Palavras Chaves:** Fadiga por fretting; Carga de contato normal cíclica; Temperatura elevada; Desgaste; Inconel 718; Ti-6Al-4V.

**Resumo:** Este trabalho foi desenvolvido no âmbito de um acordo internacional de doutorado conjunto entre a Universidade de Paris–Saclay (UPS) e a Universidade de Brasília (UnB). O contexto científico da tese foi escolhido para tentar fornecer dados e soluções para problemas no setor aeronáutico, pois a Safran Aircraft Engines tem sido um importante parceiro industrial para esta e outras teses em ambas as universidades. Neste cenário, uma das motivações para estudar o efeito de uma carga de contato normal variável no problema de fadiga por fretting vem, não só devido ao fato de que existem poucos dados experimentais e análises confiáveis nestas condições, mas também que, em aplicações práticas, como a interface de contato entre a raiz das pás e o disco em uma turbina aeronáutica, essa carga de contato normal também é variável no tempo. Dentro deste contexto, para ser mais preciso, a presente tese tem três objetivos principais. A primeira é projetar e construir um novo aparato de fadiga por fretting capaz de realizar diferentes tipos de testes, onde as cargas e seus respectivos atuadores envolvidos nos experimentos possam ser controlados de forma independente. O equipamento de teste será projetado de forma que experimentos de fadiga por fretting também possam ser realizados em altas temperaturas. O segundo objetivo é avaliar o efeito da carga normal cíclica na resistência à fadiga por fretting da liga de titânio Ti-6Al-4V à temperatura ambiente e da liga de níquel Inconel 718 à temperatura ambiente e elevada. Esses materiais foram especialmente escolhidos devido ao grande interesse da indústria aeronáutica. O terceiro e último objetivo é avaliar a vida de fretting por meio de um modelo de elementos finitos que considera efeitos do desgaste e um parâmetro de fadiga multiaxial.

Um novo aparato de fadiga por fretting com quatro atuadores hidráulicos foi inteiramente projetado para solucionar o desafio de como aplicar cargas normal de contato cíclicas. Tal carga agora é aplicada através de dois atuadores servo-hidráulicos MTS posicionados perpendicularmente ao corpo de prova. Além disso, as cargas tangenciais e de fadiga também são aplicadas por atuadores servo-hidráulicos independentes. Devido a essas atualizações, a nova bancada experimental de fadiga por fretting da Universidade de Brasília pode

controlar de forma independente todas as cargas envolvidas nos testes de fretting (cargas de fadiga, normais e tangenciais). Todas as referidas cargas podem não apenas variar com o tempo em fase ou fora de fase, mas suas formas de onda também podem ser aplicadas de forma síncrona ou assíncrona. Além disso, dois ignitores cerâmicos foram colocados próximos às partes de contato para realizar testes em temperaturas elevadas. O sistema de aquecimento é capaz de atingir temperaturas de até 750°C e mante-la estável dentro de uma faixa de erro de  $\pm 10^\circ\text{C}$ .

A fim de avaliar a influência da carga normal cíclica na resistência à fadiga por fretting, foram realizados ensaios sob a condição de deslizamento parcial com carga normal constante e cíclica à temperatura ambiente para a liga Ti-6Al-4V e à temperatura ambiente e à 540°C para a liga Inconel 718. Os resultados experimentais indicaram que a carga normal cíclica tem um efeito benéfico na vida de fretting (considerando as condições de teste aqui testadas). Este comportamento foi observado para as ligas Ti-6Al-4V e Inconel 718 em ambas as temperaturas testadas. Além disso, também foi realizada uma campanha experimental para avaliar a influência da carga normal variável no coeficiente de atrito. Com base nesta avaliação experimental, a presença de cargas normais cíclicas não parece influenciar o coeficiente de atrito em condições de deslizamento parcial. No entanto, comparando os resultados do coeficiente de atrito da liga Inconel 718 em temperatura ambiente e elevada, observou-se uma redução significativa para ambas as condições de carga normal de contato.

Além disso, um modelo de elementos finitos (considerando e desprezando os efeitos de desgaste) foi usado em conjunto com o parâmetro de plano crítico de Smith-Watson-Topper e uma abordagem de tensão não-local para estimar a vida de fadiga por fretting. Em relação às abordagens de estimativa de vida consideradas neste estudo, para os casos de carga normal constante e cíclica, ambas as metodologias numéricas implementadas, seja ela incluindo ou desprezando o desgaste, forneceram resultados satisfatórios, sendo o que desconsidera o desgaste forneceu estimativas de vida mais precisas.



# Acknowledgments

First of all, I would like to especially thank my advisor, Professor José Alexander Araújo, who I consider an inspiring person and an example of a researcher. During my academic journey, master's and doctorate's, I have had the pleasure and the great opportunity to work closely with him. During these years, he has always been very thoughtful to me and provided numerous advices of great importance. In this trajectory, there were also difficult moments where I always got good advice, understanding, and help from him. Please, accept my deepest gratitude. I would also like to thank my advisor from UPS, Professor Sylvie Pommier, for all help, suggestions, and attention during this doctorate. I also thank you for your support during the time that I have been in France. It was an extraordinary experience that significantly changed my life and brought me great professional maturity.

I am also deeply grateful to Safran Group for the opportunity and trust given me in order to conduct this work and for funding all this research. To Jean Meriaux, Claudio Montebello, and especially to Guillaume Chassaing, my sincere thanks.

Also, I could not fail to thank the professor, and longtime friend, Raphael Cardoso, who has always been very supportive. To the professors, Fábio Castro, Thiago Doca, and Luís Veloso, also find here in this thesis my thanks.

Agradeço também aos amigos, técnicos e colaboradores da UnB: Remy, Cainã, Caixeta, Lucas Carneiro, João Quintiliano, Miguel, Ivan, Adriano, Rafael, Wesley, Sra Raimunda e Sr Reginaldo. Aos meus amigos, os quais sempre me proporcionaram importantes conversas, momentos prazerosos e boas risadas, jamais poderia esquecer de aqui menciona-los: Sergio Gabriel, Jamilly, João Miguel, Andre Pes, João Américo e família, Rubens, Wanessa, Pedro Cappelleso, Raul, Tâmara, Victor, Djalma, Caio Felipe, Guilherme Fachineto, Andre Rezende, Caio Wichrowski e família, Arthur Barcelos, Gabriel José, Victor Ximenes, Luciano... obrigado a todos!

E por último, e mais importante, agradeço aos meus pais, Jucimar e Mariana, e aos meus irmãos Bruno e Ana Carolina. Ao longo de toda a minha vida, sempre obtive o apoio incondicional de todos vocês. Sozinho, jamais chegaria até aqui. Muito obrigado!

*"A question that sometimes drives me  
hazy: am I or are the others crazy?"  
– Albert Einstein*

*"Seek freedom, and it will lie stretched  
out before your eyes. If the endless  
dream guides your restless spirit, seize  
it! Raise your flag, and stand tall!"  
– Gol D. Roger*

*"Power is not determined by your size,  
but the size of your heart and dreams!"  
– Monkey D. Luffy*

*"And those who were seen dancing were  
thought to be insane by those who could  
not hear the music."  
– Friedrich Nietzsche*

# Preface

This thesis is result of the international cooperation carried out by the author, the University of Brasilia (UnB) in Brazil, the University of Paris-Saclay (UPS) in France, and Safran Group as industrial partner also located in France.

This work was conducted under the supervision of D.Phil. José Alexander Araújo (UnB), Ph.D. Sylvie Pommier (UPS), and Ph.D. Guillaume Chassaing (Safran). Some of the main results here described have been published in the following papers:

- Almeida, G. M. J., Cardoso, R. A., Garcia, M. A., Chassaing, G., Pommier, S., & Araújo, J. A. (2022). Four actuators fretting fatigue rig and tests with cyclic normal load for Ti-6Al-4V. *Theoretical and Applied Fracture Mechanics*, 119, 103292.
- Almeida, G. M. J., Cardoso, R. A., Chassaing, G., Pommier, S., & Araújo, J. A. (2022) Fretting fatigue with cyclic normal load for Inconel 718 at room and elevated temperatures. Abstract submitted to the ISFFM 10.

# List of symbols

$P$	Contact normal load
$P = const.$	Constant contact normal load
$P(t)$	Time varying contact normal load
$P_m$	Mean contact normal load
$P_a$	Alternated contact normal load
$p(x)$	Pressure distribution
$p_0$	Peak pressure
$Q$	Tangential force
$Q_a$	Alternated tangential force
$q(x, y), q(x)$	Shear stress distribution
$q_1(x), q_2(x)$	First and second shear stress perturbation
$B(t)$	Fatigue bulk load
$a$	Semi-width of the contact
$c, c'$	Half-size of the stick zone, half-size of the stick zone under reverse sliding condition
$x$	Coordinate
$y$	Coordinate
$z$	Complex coordinate
$e$	Offset of the stick zone
$V$	Total wear volume
$S$	Total relative slip distance
$K$	Wear coefficient
$H$	Material hardness

$dh$	Increment of material remove depth
$ds$	Increment of relative slip
$E_d$	Dissipated energy in one fretting cycle
$R_B$	Bulk load ratio
$R_Q$	Tangential load ratio
$R_P$	Normal load ratio
$L$	Critical distance
$E, E_{eq}$	Young modulus, Young modulus equivalent
$R, R_{eq}$	Pad radius, Pad radius equivalent
$D_{f,n}$	Sum up the fatigue damage by using Miner's rule
$N_{f,i}$	Estimated total life
$SWT$	Smith-Watson-Topper multiaxial fatigue parameter
$SWT_{Ti6-4,RT}$	SWT for the Ti-6Al-4V at room temperature
$SWT_{IN718,RT}$	SWT for the Inconel 718 at room temperature
$SWT_{IN718,HT}$	SWT or the Inconel 718 at high temperature
$cf$	Coefficient of friction
$ff$	Fretting fatigue
$in$	Inconel 718
$ti$	Ti-6Al-4V
$rt$	Room temperature (20°C)
$ht$	High temperature (540°C)
$pc$	Constant normal load or pressure constant
$pv$	Cyclic normal load or pressure variable
$\nu$	Poisson's ratio

$\Phi$	Potential function
$\phi$	Phase angle
$\theta$	Measurement of fretting crack initiation direction
$\bar{\theta}$	Average of fretting crack initiation direction
$\kappa$	Local coefficient of wear
$\alpha$	Coefficient of energy wear
$\mu$	Coulomb's coefficient of friction
$\mu_m$	Mean coefficient of friction (measured from experiments, Methodology 1)
$\mu_s$	Estimated friction coefficient of the slip zone (Methodology 1)
$\bar{\mu}_s^*$	Average friction coefficient of the slip zone for constant normal load (Methodology 1)
$\mu_{\max}$	Maximum friction coefficient (measured from experiments, Methodology 2)
$\bar{\mu}_{\max}$	Average of maximum friction coefficient (Methodology 2)
$\bar{\mu}_{\max}^*$	Average of maximum friction coefficient for constant normal load (Methodology 2)
$\mu_{M1,M2}$	Average of maximum friction coefficient (Methodology 1 and 2)
$\underline{\underline{\sigma}}(t)$	Cauchy stress tensor
$\sigma_{xx}$	xx component of the stress tensor
$\sigma_{yy}$	yy component of the stress tensor
$\sigma_{xy}$	xy component of the stress tensor
$\sigma_{zz}$	zz component of the stress tensor
$\sigma_{n,\max}$	Maximum normal stress
$\sigma_{eff}$	Effective stress
$\sigma_B$	Bulk stress
$\tau$	Shear tensor
$\tau_a$	Shear stress amplitude
$\Delta K_{th}$	Threshold stress intensity factor range

$\Delta\sigma_{-1}$	Uniaxial fatigue limit range
$\Delta N$	Jump factor
$\delta_a$	Prescribed tangential displacement amplitude
UnB	University of Brasilia
UPS	Universite Paris-Saclay
HFC	High cycle fatigue
LFC	Low cycle fatigue
SAE	Safran Aircraft Engines
TCD	Theory of Critical Distances
X-FEM	Extended Finite Element Method
FEM	Finite Element Method
MSSR	Modified Shear Stress Range
MRH	Maximum Rectangular Hull Method
PM	Point Method
SEM	Scanning Electron Microscopy
EDX	Energy dispersive X-ray spectroscopy

# Contents

List of Figures	xiii
List of Tables	xxii
<b>1 Introduction</b>	<b>1</b>
1.1 Motivation . . . . .	1
1.2 Industrial context . . . . .	7
1.3 Main objectives . . . . .	9
1.4 Review of the state of the art . . . . .	10
1.5 Summary . . . . .	25
<b>2 Literature review</b>	<b>29</b>
2.1 Basic contacts mechanics . . . . .	29
2.1.1 Introduction . . . . .	29
2.1.2 Contact between cylinders . . . . .	32
2.1.3 Influence of the fatigue bulk stress on the tractions . . . . .	39
2.2 Multiaxial Fatigue . . . . .	40
2.2.1 Introduction . . . . .	40
2.2.2 Decomposition of the Cauchy stress tensor and shear stress amplitude definition	41
2.2.3 Smith-Watson-Topper criterion . . . . .	43
2.2.4 Fatemi-Socie parameter . . . . .	44
2.2.5 Modified Wöhler Curve Method . . . . .	44
2.3 Methodologies to incorporate stress-gradient in fatigue problems . . . . .	45



2.3.1	Critical distance approach . . . . .	45
2.3.2	Asymptotic and short crack arrest methods . . . . .	46
2.4	Wear evaluation on fretting fatigue . . . . .	49
2.5	Summary . . . . .	51
<b>3</b>	<b>Design of the the four actuators and high temperature UnB Fretting Fatigue rig</b>	<b>53</b>
3.1	Review of high-temperature fretting fatigue rigs . . . . .	53
3.2	Previous fretting fatigue rig of the University of Brasilia . . . . .	55
3.3	New four actuators high-temperature fretting fatigue rig . . . . .	61
3.3.1	Normal load application system . . . . .	62
3.3.2	Heating system . . . . .	63
3.3.3	Cooling system . . . . .	66
3.3.4	Alignment procedure between the contacting parts . . . . .	67
3.3.5	Temperature calibration . . . . .	69
3.4	Summary . . . . .	75
<b>4</b>	<b>Experimental methodology and results</b>	<b>79</b>
4.1	Materials and specimens . . . . .	79
4.1.1	Ti-6Al-4V . . . . .	79
4.1.2	Inconel 718 . . . . .	82
4.1.3	Fretting specimen and pad design . . . . .	83
4.2	Tests nomenclature . . . . .	86
4.3	Determination of coefficient of friction in partial slip condition . . . . .	87
4.3.1	Methodology . . . . .	88
4.3.2	Results . . . . .	92
4.3.3	Summary and final remarks on the friction tests . . . . .	95
4.4	Fretting fatigue tests at room and elevated temperature . . . . .	96

4.4.1	Methodology . . . . .	97
4.4.2	Results - Ti-6Al-4V at room temperature . . . . .	97
4.4.3	Results - Inconel 718 at room temperature . . . . .	100
4.4.4	Results - Inconel 718 at elevated temperature . . . . .	105
4.4.5	Scanning Electron Microscope analysis on Inconel 718 . . . . .	108
4.4.6	Summary and final remarks on on the fretting fatigue tests . . . . .	114
<b>5</b>	<b>Life estimation and numeric modelling</b>	<b>117</b>
5.1	Multiaxial fatigue life evaluation . . . . .	117
5.2	Damage accumulation methodology and surface geometry update . . . . .	120
5.3	Numerical model . . . . .	123
5.4	Results . . . . .	124
5.5	Summary . . . . .	137
<b>6</b>	<b>Conclusions and perspectives</b>	<b>141</b>
6.1	Overview . . . . .	141
6.2	Concluding remarks . . . . .	141
6.3	Suggestions for future work . . . . .	144
	<b>Bibliography</b>	<b>145</b>
	<b>Appendix</b>	<b>162</b>



# List of Figures

1.1	Illustration of fretting fatigue case under the partial slip condition. . . . .	2
1.2	Engine parts typically threatened by fretting (adapted from the Aeroengine Safety Institute of Thermal Turbomachinery and Machine - Dynamics Graz University Technology). Available on < <a href="https://aeroenginesafety.tugraz.at">https://aeroenginesafety.tugraz.at</a> >. . . . .	3
1.3	In-flight relative displacement at the contact interface. Modified from Mary (2009). . . . .	4
1.4	Most common types of blade disc connections in aero engines: (a) dovetail and (b) fir tree (Montebello, 2015). . . . .	5
1.5	Engine failure of the Boeing 747-436 aircraft G-BNLD (ATSB, 2002). . . . .	5
1.6	Engine failure of the McDonnell Douglas MD-88. Available on < <a href="https://en.wikipedia.org/wiki/Delta_Air_Lines_Flight_1288">https://en.wikipedia.org/wiki/Delta_Air_Lines_Flight_1288</a> >. . . . .	6
1.7	Photo of what remained of the fan of the rear engine of a DC-10 that crashed in Sioux City in 1989. Available on < <a href="https://en.wikipedia.org/wiki/United_Airlines_Flight_232">https://en.wikipedia.org/wiki/United_Airlines_Flight_232</a> >. . . . .	6
2.1	Contact classification: (a) Incomplete and non-conformal, (b) Incomplete and conformal, and (c) Complete. . . . .	30
2.2	Normal contact between two elastically similar bodies. . . . .	31
2.3	Illustration of the (a) partial slip regime, and (b) gross slip condition. . . . .	32
2.4	Illustration of a half-plane under normal $p(x)$ and shear $q(x)$ distributions. . . . .	32
2.5	Normalized contact tractions under partial slip condition. $Q/\mu P = 0.6$ . $ x/a  \leq 0.6325$	36
2.6	Tangential load in a full fretting cycle. . . . .	37
2.7	Shear traction distribution in a fretting cycle as described in Fig. 2.6. $Q_{\max}/(\mu p_0) = 0.6$ . . . . .	38

2.8	Shear traction with (blue dashed line) and without (solid red line) fatigue bulk load.	40
2.9	Stress vector decomposition considering the material plane $\Delta$ .	42
2.10	Illustration of MRH Method assessed in the material plane $\Delta$ .	43
2.11	Schematic representation of the Theory of Critical Distances: (a) Point Method, (b) Line Method, and (c) Area Method.	47
2.12	Crack growth curves in the modified K-T diagram.	49
3.1	Schematics and photos of high-temperature fretting fatigue machines with a single actuator used by (a) <a href="#">Kwon et al. (2011)</a> , (b) <a href="#">Sahan (2002)</a> , and (c) <a href="#">Murthy et al. (2003)</a> .	55
3.2	Schematics and photos of high-temperature fretting fatigue rigs with a dedicated contact normal load actuator used by (a) <a href="#">Fleury (2015)</a> , and by (b) <a href="#">Abbasi and Majzoobi (2018a)</a> .	56
3.3	Schematics and photos of high-temperature fretting fatigue machines which operates at high-frequency used in works (a) <a href="#">Zhai et al. (2020)</a> , (b) <a href="#">Lavella et al. (2013)</a> , and (c) <a href="#">Matlik et al. (2006)</a> .	57
3.4	Previous version of the UnB's Fretting Fatigue Machine.	58
3.5	Schematic view and component list of the previous UnB's Fretting Fatigue Machine.	59
3.6	Enerpac hydraulic system.	60
3.7	Photo with details of the pad's carrier in the previous version of the UnB fretting fatigue rig.	60
3.8	Schemes of pressure fields and alignment marks on the pressure paper of two cases: (a) misaligned and (b) aligned.	60
3.9	Photo of the new fretting apparatus (without the contact normal load actuators).	61

3.10 Drawings of the UnB's fretting apparatus: (a) Side cut view; (b) Transverse cut view; (c) Isometric view. Numbering caption: 1 - MTS servo hydraulic actuators; 2 - apparatus main plate; 3 - actuator bracket; 4 - stiffness bars; 5 - linear bearings; 6 - pad holder; 7 - igniter; 8 - ceramic casing; 9 - igniter support; 10 - pre-loading screws; 11 - bracket plates; 12 - pad. . . . .	63
3.11 MTS Hydraulic actuator model 242.03. . . . .	63
3.12 Cut view of the fretting apparatus detailing the igniters and its supports, and ceramic enclosure: (a) view without specimen and (b) view with the fretting specimen. . . .	65
3.13 Photo with details of the the heating system during an exploratory test. . . . .	65
3.14 Ceramic enclosure parts. . . . .	66
3.15 Lynx Technology Temperature Controller in operation. . . . .	66
3.16 Cooling system of the fretting rig: (a) Photo and (b) Isometric and cut view of the pad holder. . . . .	67
3.17 CAD drawing and photos of the pad holder and the cylindrical pad. a) Blue arrows indicate the lateral screws used to align the fretting pads, and b) red arrows indicate the top screws used for blocking any pad slip within the slot. . . . .	68
3.18 Schematic of the alignment between the cylindrical pad and the fretting specimen and photo of the contacting marks on the sensitive pressure paper for the a) aligned and b) misaligned cases. . . . .	69
3.19 Fretting dummy specimen and contact pad with drilled holes where temperatures were measured. The faded blue rectangle illustrates the local where the contact would occur in a fretting test. . . . .	70
3.20 a) K-type thermocouple, b) contact pad with hole to place the control thermocouple, and c) experimental setup of the temperature tests. . . . .	71
3.21 Heating system tested in a real fretting testing conditions. . . . .	71
3.22 a) experimental setup of the temperature test, and b) running temperature test. . .	72

3.23	Complete view of the temperature test. . . . .	72
3.24	Temperature over time measured at different positions on the dummy specimen (along of the 15mm region). . . . .	73
3.25	Photo of the XH7132 Vertical Machine Center. . . . .	73
3.26	Correlation between the temperature measured at the control point by the control thermocouple ( $T_c$ ) and the average temperature measured on the dummy fretting specimen. . . . .	75
3.27	New Fretting Fatigue Machine of the University of Brasilia (UnB). . . . .	77
3.28	Schematic view and component list of the new Fretting Fatigue Machine of the University of Brasilia (UnB). . . . .	78
4.1	a) Thermo-mechanical treatment applied to the Ti-6Al-4V (Modified from (Belle- cave, 2015)). b) Nodules $\alpha_P$ and $\alpha_S/\beta$ lamellar colonies c) Lamellar colony in detail (Castany, 2007). . . . .	81
4.2	Microstrucure of the Inconel 718 alloy (Nascimento, 2022). . . . .	82
4.3	Photo and dimensions of the fretting specimen. . . . .	84
4.4	Photo and dimensions of the contacting pad. . . . .	85
4.5	Photo of the Olympus LEXT OLS4100 confocal laser microscope. . . . .	85
4.6	Mapped surface of an inconel pad. . . . .	86
4.7	Friction Methodology 1: determination of the mean coefficient of friction ( $\mu_m$ ) with (a) constant contact normal load, and (b) cyclic contact normal load. . . . .	89
4.8	Plot of the normal and tangential force ratio against time and determination of the mean friction coefficient ( $\mu_m$ ) for the cf-in-rt-pc-01 test conducted according to the Friction Methodology 1. Normalized with respect to $\bar{\mu}_s^*$ . . . . .	90
4.9	Friction Methodology 2: determination of the maximum coefficient of friction ( $\mu_{max}$ ) with (a) constant contact normal load, and (b) cyclic contact normal load. . . . .	91

4.10 Plot of the normal and tangential force ratio against number of cycles, and determination of the maximum friction coefficient ( $\mu_{\max}$ ) for the cf-in-rt-pc-04 test conducted according to the Friction Methodology 2. Normalized with respect to  $\bar{\mu}_{\max}^*$ . . . . . 92

4.11 Photos of the fretting hysteresis loops recorded by the rig controller/software for the (a) partial slip regime and (b) gross slip regime observed during a friction test conducted according to the Friction Methodology 2. . . . . 93

4.12 Schematic of loading history for (a) Testing Set 1 (constant contact normal load), (b) Testing Set 2 (cyclic contact normal load), and (c) experimental fretting fatigue configuration. . . . . 98

4.13 (a) Fracture surface of ff-ti-rt-pc-01 specimen, and (b) measurement of the crack initiation angle. . . . . 100

4.14 Fretting fatigue contact scar and fracture surface of a test with Ti-6Al-4V at RT and constant contact normal load (ff-ti-rt-pc-04). . . . . 101

4.15 Fretting fatigue contact scar and fracture surface of a test for Inconel 718 at RT with constant contact normal load ff-in-rt-pc-01). . . . . 103

4.16 Fretting fatigue contact scar and fracture surface of a test for Inconel 718 at RT with cyclic contact normal load test (ff-in-rt-pv-04). . . . . 104

4.17 Fretting fatigue contact scar and fracture surface of a test for Inconel 718 at 540°C with constant contact normal load (ff-in-ht-pc-03). . . . . 106

4.18 Fretting fatigue contact scar and fracture surface of a test for Inconel 718 at 540°C with cyclic contact normal load (ff-in-ht-pv-02). . . . . 107

4.19 Photo of the JEOL JSM-7100F scanning electron microscope. . . . . 108

4.20 SEM observations of the test specimen ff-in-rt-pc-03: (a) Fretting contact mark, (b) Zoom view of the slipping zone, and (c) zoom view of the stick zone. . . . . 109



4.21	SEM observations of the test specimen ff-in-rt-pc-03: (a) Fracture surface, (b) Inclined view, and (c) zoom view of a carbide inclusion. . . . .	110
4.22	SEM observations of the test specimen in-rt-pv-04: (a) Fretting contact mark, (b) zoom view pf the slipping zone, and (c) zoom view of the stick zone. . . . .	111
4.23	SEM observations of the test specimen ff-in-rt-pv-04: (a) Fretting scar and fracture surface, (b) crack propagation region, (c) zoom view of the crack propagation region, (d) fast fracture region, and (e) further amplification of the final fracture region showing the dimples. . . . .	112
4.24	SEM and confocal laser observations of the test specimen ff-in-ht-pv-03: (a) Specimen fracture surface, (b) detail of the contact surface, (c) inclined photo with view of the crack initiation site and (d) and (e) arrested cracks at the opposite contact region. . . . .	113
4.25	Illustration of the locals where the SEM/EDX analyses were carried out. . . . .	114
5.1	Stresses non-proportionality of the loading conditions of the Testing Sets 1 ( $P = const.$ ) and 2 ( $Pt(t)$ ) for the Ti-6Al-4V at the point where the multiaxial criterion is evaluated ( $x/a = -1, y = L/2$ ) over a complete fretting fatigue cycle. . . . .	118
5.2	Normalized stresses inward the contact for loading conditions with cyclic contact normal load for the Ti-6Al-4V at the point where the multiaxial criterion is evaluated ( $x/a = -1, y = L/2$ ) when $P(t) = P_{max}$ . . . . .	118
5.3	Uniaxial fatigue data for the Ti-6Al-4V expressed in terms of the $SWT$ parameter and curve fitting ( <a href="#">Cardoso, 2019</a> ). . . . .	119
5.4	Uniaxial fatigue data for the Inconel 718 expressed in terms of the $SWT$ parameter and curve fitting (room temperature). . . . .	120
5.5	Uniaxial fatigue data for the Inconel 718 expressed in terms of the $SWT$ parameter and curve fitting (elevated temperature). . . . .	121

5.6	Illustration of the methodology used in order to transfer the cumulative damage from a previous fretting cycle simulation to the next (adapted from <a href="#">Cardoso (2019)</a> ).	123
5.7	TCD applied to fretting problems when wear effects are a) neglected and b) included (adapted from <a href="#">Cardoso (2019)</a> ).	124
5.8	FE-based model for wear analysis using the remeshing technique.	125
5.9	Finite element model used to simulate fretting fatigue.	126
5.10	Comparison between the analytical and numerical solutions for the normal and shear tractions (test with constant contact normal load).	126
5.11	Specimen final worn superficial profiles predicted by the FE simulations for the loading case with constant contact normal load (dashed line), and cyclic contact normal load (solid line). a) Ti-6Al-4V at RT; b) Inconel 718 at RT; c) Inconel 718 at HT.	128
5.12	Illustration of changes in the contact, stick and slip zones showing the resulting fretting scar for (a) constant contact normal load and (b) cyclic contact normal load.	129
5.13	Tractions for Ti-6Al-4V tests at room temperature: (a) with constant contact normal load and neglecting wear, (b) with constant contact normal load and considering wear, (c) with cyclic contact normal load and neglecting wear, and (d) with cyclic contact normal load and considering wear. All tractions were normalized considering the peak pressure, $p_0$ , for the case with constant contact normal load and neglecting wear.	130
5.14	Tractions for Inconel 718 tests at room temperature: (a) with constant contact normal load and neglecting wear, (b) with constant contact normal load and considering wear, (c) with cyclic contact normal load and neglecting wear, and (d) with cyclic contact normal load and considering wear. All tractions were normalized considering the peak pressure, $p_0$ , for the case with constant contact normal load and neglecting wear.	131

5.15 Traction for Inconel 718 tests at elevated temperature: (a) with constant contact normal load and neglecting wear, (b) with constant contact normal load and considering wear, (c) with cyclic contact normal load and neglecting wear, and (d) with cyclic contact normal load and considering wear. All tractions were normalized considering the peak pressure,  $p_0$ , for the case with constant contact normal load and neglecting wear. . . . . 132

5.16 Attempts to determine wear depth of the specimen ff-ti-pc-04 under different magnifications: (a) 108x, (b) 432x, and (c) 1080x. . . . . 134

5.17 Comparison of accumulated fatigue damage along contact at  $L/2$  depth for the cases with constant and cyclic contact normal loads. a) Ti-6Al-4V at RT; b) Inconel 718 at RT; c) Inconel 718 at HT. . . . . 139

# List of Tables

1.1	Summary of literature review of fretting and fretting fatigue tests conducted at elevated temperatures. . . . .	18
2.1	Shear components at different zones in a fretting cycle. . . . .	38
3.1	Average temperatures measured from three temperature calibration tests. . . . .	74
3.2	Forces, displacements, and temperature ranges of the New UnB's four actuators high temperature fretting fatigue rig. . . . .	76
4.1	Main elements and chemical composition of the Ti-6Al-4V alloy (ASTM B861-19, 2019). . . . .	80
4.2	Basic mechanical and material properties of the Ti-6Al-4V alloy at room temperature (20°C). . . . .	81
4.3	Main elements and chemical composition of the Inconel 718 alloy (ASTM B637-16, 2016). . . . .	83
4.4	Basic mechanical and material properties of the Inconel 718 alloy at room temperature (20°C) and elevated temperature (540°C). . . . .	83
4.5	Roughness measurements of the Ti-6Al-4V and Inconel 718 specimens and pads. . .	86
4.6	Loading parameters and results for the coefficient of friction tests performed with constant and cyclic contact normal load for the Ti-6Al-4V at room temperature (20°C). Results are normalized with respect to the average friction coefficient of the slip zone for the constant contact normal load condition, $\bar{\mu}_s^*$ . . . . .	94

4.7	Loading parameters and normalized results for the coefficient of friction tests performed with constant and cyclic contact normal load for the Inconel 718 at room temperature (20°C). Tests conducted according to the Friction Methodology 1. Results are normalized with respect to the average friction coefficient of the slip zone for the constant contact normal load condition, $\bar{\mu}_s^*$ . . . . .	94
4.8	Loading parameters and normalized results for the coefficient of friction tests performed with constant and cyclic contact normal load for the Inconel 718 at room temperature (20°C). Tests conducted according to the Friction Methodology 2. Results normalized with respect to the average friction coefficient for the constant contact normal load condition, $\bar{\mu}_{\max}^*$ . . . . .	95
4.9	Loading parameters and results for the coefficient of friction tests performed with constant and cyclic contact normal load for the Inconel 718 alloy at elevated temperature (540°C). Tests conducted according to the Friction Methodology 1. Results are normalized with respect to the average friction coefficient of the slip zone for the static contact normal load condition at room temperature, $\bar{\mu}_s^*$ of Table 4.7. . . . .	95
4.10	Loadings parameters and life results of the fretting fatigue tests with constant and cyclic contact normal load at room temperature for the Ti-6Al-4V. Contact normal load ratio $R_p = 0.6$ . . . . .	99
4.11	Measurements of fretting crack initiation angles for the fretting fatigue tests with Ti-6Al-4V parts at room temperature. . . . .	101
4.12	Loading parameters and life results of the fretting fatigue tests with constant and cyclic contact normal load at room temperature for the Inconel 718 alloy. Contact normal load ratio $R_p = 0.6$ . . . . .	102
4.13	Measurements of fretting crack initiation angles for the fretting fatigue tests with Inconel 718 parts at room temperature. . . . .	104

4.14	Loading parameters and life results of the fretting fatigue tests with constant and cyclic contact normal load at elevated temperature (540°C) for the Inconel 718 alloy. Contact normal load ratio $R_p = 0.8$ . . . . .	105
4.15	Measurements of fretting crack initiation angles for the fretting fatigue tests with Inconel 718 parts at elevated temperature (540°C). . . . .	107
4.16	Mass percentage of Oxygen estimated by SEM/EDX analyses on different locals of two selected Inconel 718 specimens. . . . .	114
4.17	Average life results of the Fretting Fatigue experimental campaign and life comparison.	115
4.18	Average fretting crack initiation directions of the Fretting Fatigue experimental campaign. . . . .	115
5.1	Wear volume comparison between the constant and cyclic contact normal load cases. All volumes expressed in $10^{-4}\text{mm}^3$ . . . . .	127
5.2	Experimental and estimated lives for the Inconel 718 alloy and Ti-6Al-4V alloys. RT = 20°C and HT = 540°C. All lives are expressed in cycles. . . . .	136
5.3	Percentile error of experimental and estimated fretting lives. . . . .	136

# Chapter 1

## Introduction

*This chapter introduces the fretting phenomenon and some of its impacts in the industry, mainly regarding about the aeronautical one. After defining the main objectives of this thesis, a literature review is presented on the subject, in which the high temperature and variable contact normal load topics are highlighted.*

### 1.1 . Motivation

*Fretting* is a complex tribological phenomenon characterized by a mild surface wear, where oscillatory forces provoke a small relative movement at corresponding points of the contact interface in mechanical couplings. The *fretting fatigue* term refers to the cumulative damage process described by the initiation and propagation of cracks in the presence of fretting (Hills and Nowell, 1994; Araújo, 2000; Liskiewicz and Dini, 2022). Figure 1.1 shows an scheme of a contact configuration subjected to fretting fatigue. In this figure one can observe at the contact between a cylindrical pad and a tensile specimen (half-plane). Also, the tractions (normal and shear distributions) formed due to a normal load,  $P$ , and an oscillating tangential load,  $Q(t)$ , at the same time that the specimen experiences an oscillating fatigue bulk stress,  $\sigma_b(t)$  are shown in this figure. One can also observe the different zones formed at the contact (stick and slip zones) when the partial slip regime is respected and fretting crack formed at the edge of the contact,  $-a$ .

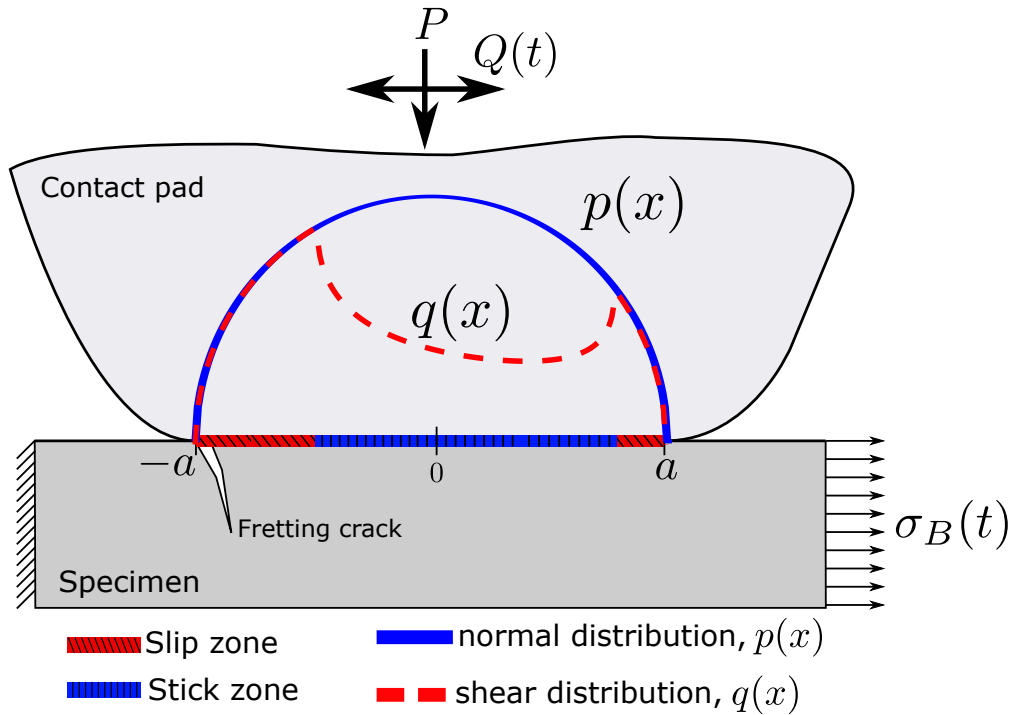


Figure 1.1: Illustration of fretting fatigue case under the partial slip condition.

It is well known that the durability of mechanical assemblies subjected to time varying loads, such as dovetail joints (Rajasekaran and Nowell, 2006), bolted joints (Juoksukan-gas et al., 2016), overhead conductors (Zhou et al., 1996) among others, are significantly affected by fretting conditions. In the last two to three decades a special attention has been drawn to the study of the fretting fatigue problem in turbofan aeroengines. These engines contain different interfaces which may experience small relative movement leading to fretting (Figure 1.2), e.g. spline couplings between shafts and the compressor and turbine blade/disc connections being the most usually reported (Ruiz and Nowell, 2000; Limmer et al., 2001; Mugadu et al., 2002; Rajasekaran and Nowell, 2006; Araújo and Nowell, 2009). Due to the complexity of such a phenomenon and the increasing need to reduce weight and fuel consumption of the aeroengine, while keeping safety at the highest levels, massive investments have been carried out by private and governmental funds to avoid premature failures and develop more robust design techniques. In this setting, one of the largest research initiatives that is worthy of notice was the National Turbine



Engine High Cycle Fatigue (HCF) Science and Technology (S&T) Program, funded by the Air Force, the Navy, and NASA, which started in 1994. The refereed program aimed to reduce the level of conservatism involved in the design of such structures and also to diminish the economic impacts that high cycle fatigue have caused on engine safety, reliability and readiness, which was estimated to be over some hundred million dollars per year (Garrison, 2000).

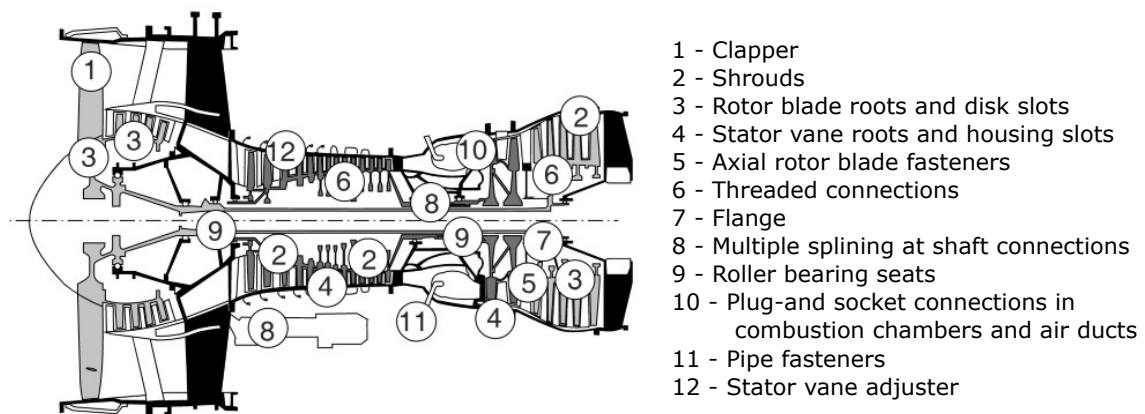


Figure 1.2: Engine parts typically threatened by fretting (adapted from the Aeroengine Safety Institute of Thermal Turbomachinery and Machine - Dynamics Graz University Technology). Available on <<https://aeroenginesafety.tugraz.at>>.

It is quite well known in the aeronautical sector that the design and maintenance against fatigue of the connection between blade and disc is critical for safety, and this explains why most of the available research work on fretting for couplings within aeroengines has been focused on these connections. Concerning the geometrical configuration of such connections, the most common are either a dovetail or a fir-tree configuration, which ensure the radial retention of the blade but at the same time transmitting tangential forces to the disk. In addition, they allow the easy installation and removal of the blades, which represents an important requirement since in case of failure only the damaged blade is replaced with positive consequences in terms of maintenance cost and reliability. These connection regions experience two sources of fretting damage, which

are directly associated with the loading characteristics generated by the different stages of the flight (take-off, cruise, landing), as shown in Figure 1.3. The first is correlated to variations in the rotational speed, which occur during take-off and landing. As the disc spins up the hoop stress will increase causing an expansion of the disc and its fixing slots. Under the action of the centrifugal force the blade will then move slightly upwards giving rise to a relative motion between the contacting surfaces.

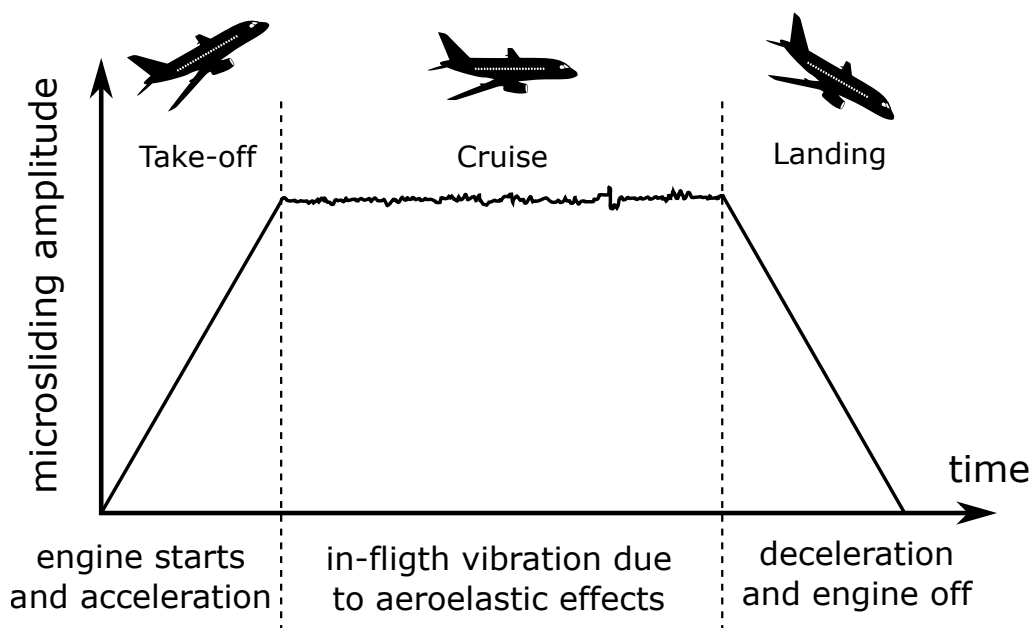


Figure 1.3: In-flight relative displacement at the contact interface. Modified from [Mary \(2009\)](#).

The second source of fretting damage in this coupling comes from high frequency vibrational loads caused by aerodynamic forces during cruise time. The interaction between air and blade induces bending moments at the root of the fixing leading to small relative displacements at the contact interface. An illustration of the most common type of blade disc connections in aero engines is shown in Figure 1.4.

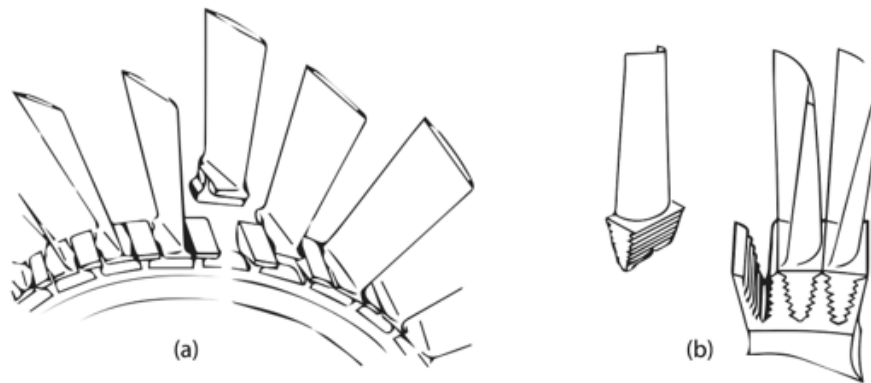


Figure 1.4: Most common types of blade disc connections in aero engines: (a) dovetail and (b) fir tree (Montebello, 2015).



Figure 1.5: Engine failure of the Boeing 747-436 aircraft G-BNLD (ATSB, 2002).

Under such loading conditions, cracks can initiate and propagate either in the blade root or in the disc. The failure of a blade root with consequent detachment of the part can be absorbed entirely by the external structure of the engine, as it was the case for the accident shown in Fig. 1.5 (ATSB, 2002). Therefore, this is a “less dangerous” failure mode of the assembly. On the contrary, the disc failure will inevitably have a much more impact for the safety of the flight since its mass coupled with the high rotational speed gives it enough energy to destroy the casing. For instance, on July 6, 1996, a McDonnell Douglas MD-88 was on takeoff roll when it experienced an uncontained, catastrophic turbine engine failure that caused debris from the front compressor hub

of the left engine to penetrate the fuselage (Fig. 1.6). This accident, which caused the death of two passengers, was associated with the fracture of the engine's front compressor fan hub. A much worse scenario occurred in 1989 at Sioux City, Iowa, after the catastrophic failure of a DC-10 tail-mounted engine due to crack propagation in the engine's fan disk (Figure 1.7). The loss of many flight controls unfortunately led to the death of 112 of the 296 passengers and crew on board.

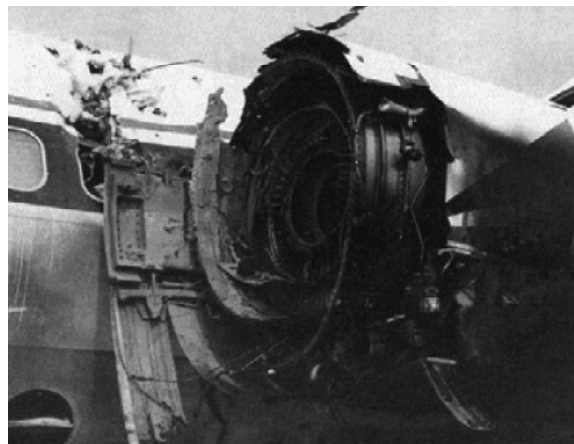


Figure 1.6: Engine failure of the McDonnell Douglas MD-88. Available on <[https://en.wikipedia.org/wiki/Delta\\_Air\\_Lines\\_Flight\\_1288](https://en.wikipedia.org/wiki/Delta_Air_Lines_Flight_1288)>.

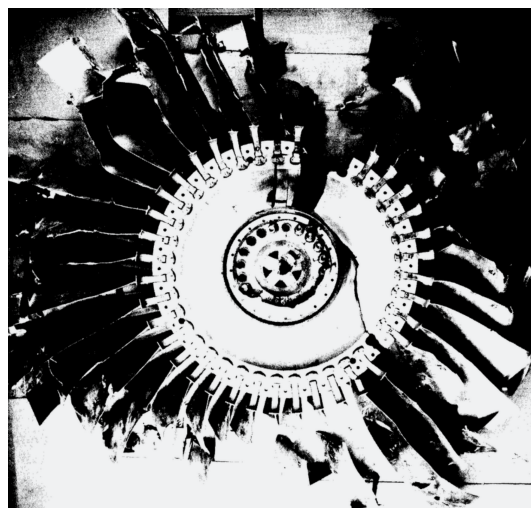


Figure 1.7: Photo of what remained of the fan of the rear engine of a DC-10 that crashed in Sioux City in 1989. Available on <[https://en.wikipedia.org/wiki/United\\_Airlines\\_Flight\\_232](https://en.wikipedia.org/wiki/United_Airlines_Flight_232)>.

## 1.2 . Industrial context

This thesis has been developed within the context of a medium/long term research initiative funded by Safran Aircraft Engines, which is part of the French group SAFRAN. In 2014, Safran has initiated this important research campaign denominated COGNAC project (Competition between the Gradient effect and the scale effect in Notch fatigue And Contact fatigue), whose main aim was to improve the understanding of fretting-fatigue with a direct impact on the design of blade/disc connections either at the fan stage (room temperature) or at the low-pressure compressor (LPC) and high-pressure compressor (HPC) interfaces (high temperature). Within a historic perspective of the COGNAC research program this is the fourth joint PhD thesis conducted in partnership between Université Paris-Saclay (UPS - ENS-Cachan) and the University of Brasília (UnB). The first thesis of the series was carried out by [Bellecave \(2015\)](#). These work investigated the effect of the stress gradient on Ti-6Al-4V fan disc material. 22 fretting fatigue tests at room temperature were conducted using a single actuator hydraulic rig and considering a cylinder on plane contact configuration. Pads and specimens were machined from an actual turbine disk and delivered at the UnB laboratories for testing by Safran. Inspired by previous works by [Bramhall \(1973\)](#), [Nowell \(1988\)](#) and [Araújo \(2000\)](#) pads were machined with radius of 70 mm and 20 mm to generate different stress gradients, but keeping the surface stress state the same for all tests with both pad sizes. This could be achieved by using a same/constant peak pressure for all range of tests. From the modeling point of view, the thesis aimed to model the short crack growth regime under fretting fatigue loading conditions by considering a criterion based on linear elastic fracture mechanics quantities, which also accounted for the first non-singular terms of the asymptotic expansion, namely the T-stresses. The Modes I and II Stress Intensity Factors and the T-stresses were computed by the finite element method under plane strain hypothesis. Such a model proved capable of correctly estimating short crack arrest and to find the threshold fretting conditions separating failure from infinite

life (defined by tests which reached one million cycles). An optimization technique was also implemented to the numerical model so that it could also estimate crack path. The second thesis of the joint agreement between UPS and UnB series was conducted by [Ferry \(2017\)](#). The aim of her work was to carry out an experimental campaign to further investigate size effects on fretting fatigue. Tests were carried out on a two vertical-actuators fretting-fatigue rig at UnB. The study of the size effect was divided into two parts. First, the influence of the volume of material stressed under the contact region on fretting fatigue life was investigated. In order to do so, the specimens were manufactured with two different thickness and the loading history designed so that to maintain not only the same variation of a chosen multiaxial fatigue parameter with the distance from the surface, but also the damaged area within the slip zones constant. The other size parameter investigated was the damaged area within the slip zones. This was conducted by reducing the superficial area within the slip zones, while maintaining all other experimental parameters constant, i.e. the bulk fatigue load and the tangential load per unit length. It was found that none of these two parameters (volume of material stressed or amount of damaged area within the slip zones) seems to have a significant influence on the fretting fatigue resistance for the Ti-6Al-4V alloy investigated. These two experimental campaigns were designed and analyzed by applying a multiaxial fatigue criterion in conjunction with the Theory of the Critical Distances (TCD). Ferry also applied another non-local approach based on equivalent velocity fields within a specific area around the contact to estimate lives. Such an approach provided good life estimates. Further, the influence of the bulk stress for the description of the fretting crack initiation and propagation phases was studied. It was concluded that 75% of the crack initiation stage for these tests conducted with Ti-6Al-4V was mainly dominated by the contact stresses.

A essentially numerical based approach for the fretting problem was adopted by [Cardoso \(2019\)](#) in the third thesis of this series. Aiming to reduce the high computational costs involved when assessing the fatigue life for actual industrial couplings, such as the

dovetail and fir tree blade disc connections, an enrichment approach was proposed in this work. The proposed method took advantage of the fact that the mechanical fields around the contact edges in cylindrical contact configurations under fretting conditions are similar to the ones close to the crack tip in linear elastic fracture mechanics problems. This similarity encouraged Cardoso to enrich finite element fretting simulations by means of the X-FEM framework, which allowed one to work with coarser meshes while keeping a good accuracy. Cardoso also investigated the influence of considering wear effects in the prediction of fretting fatigue lives. In this setting, fretting fatigue FE simulations were conducted considering the geometry updated due to the material removal and results were compared to both, available experimental data and FE simulations where wear effects were neglected (a simplified strategy usually adopted when evaluating fretting fatigue problems). Conventional multiaxial fatigue criteria in association with the Theory of Critical Distances were then used in order to predict life. Results showed that, for the data assessed (Ti-6Al-4V alloy under partial slip conditions), the use of a wear based approach within the life methodology slightly increased the accuracy of predictions. However, the computational cost was substantially higher when compared to standard approaches, where wear is neglected.

### **1.3 . Main objectives**

The present study/thesis has three main goals. The first one is to design and construct a new four actuators fretting fatigue apparatus. It will be capable of performing tests at high or room temperature. Further, it can independently control all the loads involved in the fretting tests (bulk, normal and tangential loads). Therefore, these can not only vary with time in-phase or out-of-phase but also their wave-forms can be applied in a synchronous or asynchronous way. The second aim is to evaluate the effect of cyclic contact normal load in fretting fatigue strength for the titanium alloy Ti-6Al-4V at room temperature and for the Inconel 718 alloy at room and elevated temperature. At last, but not least a finite element model including wear effects and a multiaxial fatigue parameter

is used to assess fretting life under these more challenging conditions, which involve not only the presence of a cyclic contact normal load but also temperatures as high as 540°C. The motivation to introduce a variable contact normal loading comes from the fact that, in actual loading conditions, the normal contact load between the blade root and disk interface of an aircraft turbine is time varying, following the profile of the centrifugal force during the airplane take-off, flying, and landing (as already shown in Fig. 1.3). Further, as will be shown in the next section of this chapter (review of the state of the art) there is an extremely limited amount of research work on fretting considering the presence of varying contact normal load, despite its clear existence in real engineering applications. Thus, further efforts to understand more complex loading conditions within the fretting context are necessary. The high temperature effect in tests with Inconel 718 has been introduced to simulate conditions close to the ones existing in the coupling of the low-pressure compressor (LPC) and high-pressure compressor (HPC). All tests will be conducted using a simple Hertzian cylinder against plane contact configuration. Here it is worth mentioning there is no doubt that experimental evaluation of full or even small scale configurations of the blade-disk connection could provide more realistic information to Safran, which is crucial for the design process and later maintenance of this complex structure, however, these tests are much more costly and lengthy. On the other hand, the new experimental apparatus and tests with two different materials (Ti-6Al-4V and Inconel 718) proposed in this work will allow the Safran engineering team to gain a more fundamental understanding of the fretting fatigue process but with the inclusion of a number of complicating factors which have not been considered in previous studies in the literature.

#### **1.4 . Review of the state of the art**

In 1911, [Eden et al.](#) made one of the first observations of fretting fatigue. These authors observed the initiation of cracks in the contact interface between the specimen and the testing machine grips. Over the years, with the development of high-speed



testing machines, this effect became more frequent. Consequently, the interest among the scientific community and industry grew to understand this phenomenon. In order to discover the possible causes of this damage mechanism, Tomlinson (1927) conducted an extensive experimental study about hard steel surfaces subjected to a relative motion under contact pressure. The work by Tomlinson has been considered one of the first systematic research on fretting. He recognized that superficial damage could be provoked by small relative movements that he termed *slip*. Warlow-Davies (1941) performed tests with two types of steel (medium carbon steel and chromium-nickel molybdenum alloy steel) and found that the loss of resistance to fatigue under severe fretting conditions for these materials were 13% and 18%, respectively. Later studies conducted by McDowell (1952) showed that the joint action of fretting and fatigue can cause much more damage than plain fatigue. Such fatigue strength reduction factors were found to be between 2 and 5.

One of the first scientific investigation of the effect of temperature on fretting was conducted in the 50's decade by Uhlig et al. (1953). These authors investigated mild steel (SAE 1018) between  $-125^{\circ}\text{C}$  to  $150^{\circ}\text{C}$ . Surprisingly, the authors found that the maximum wear damage occurred at the lower temperature investigated. Some years later, Swikert and Johnson (1968) also conducted experimental investigations of fretting wear at elevated temperatures. The tests were conducted on wires of Ti-6Al-4V and Inconel 600 at room and at  $260^{\circ}\text{C}$ . The results also indicated reduction in friction and wear damage at high temperatures.

Hamdy and Waterhouse (1979a) performed one the first fretting fatigue tests at high temperature on Inconel 718 alloy. The results showed that at  $540^{\circ}\text{C}$  the fretting fatigue life was doubled compared with room temperature. The better life performance was attributed to the formation of a protective layer of glaze oxide noticed at high temperatures. In the same year, those authors also evaluated the fretting strength of the Ti-6Al-4V alloy (Hamdy and Waterhouse, 1979b). However, the fretting strength was observed to decrease as the temperature was raised for this titanium alloy. Later,

using a new high temperature fretting rig [Hamdy et al. \(1981\)](#) evaluated the friction coefficient and wear damage on Inconel 718 and Ti-6Al-4V under fretting conditions from room temperature to 600°C for the titanium alloy and to 540°C for the nickel alloy ([Hamdy and Waterhouse, 1981](#)). For the Inconel 718 alloy, the increasing temperature has resulted in a reduction of friction coefficient and higher levels of material removal. Also, for this material, at 540°C the friction coefficient was four times lower than at room temperature due to the lubricant effect of the glaze oxide. However, for the titanium alloy, the friction coefficient and wear rates remained high even under high temperatures, once it was not observed the formation of glaze oxide at this temperature, which may explain the high friction coefficient at elevated temperatures. These results are consistent and explain the differences in fretting strengths found in their previous works ([Hamdy and Waterhouse, 1979a,b](#)).

Almost three decades after the first investigation of fretting at high temperature, [Bill \(1982\)](#) made a review work about many factors that can influence fretting wear, including the temperature effect. For this author, the temperature affects the fretting process increasing the oxidation or corrosion rate and changing the mechanical properties of the materials. Furthermore, according to this author, a correlation may exist between fretting wear resistance and the ability of a metal to form a protective oxide film at elevated temperatures. Another review work by ([Waterhouse, 1984](#)) also affirmed that the wear rate under fretting conditions is reduced at high temperatures due to the development of an oxide layer.

Continuing the investigation of the temperature influence on the fretting fatigue damage, [Hamdy and Waterhouse \(1982\)](#) performed a series of experiments in two different loading conditions to compare the fatigue strengths in plain fatigue and in fretting fatigue from 20°C to 600°C on the titanium alloy IMI 829. The experimental results have shown the same behaviour for both loading conditions. In plain fatigue, the fatigue strength decreases with temperature. On the contrary, in fretting fatigue, for the same bulk fatigue stress level, the fretting resistance increases as the temperature raises, and

at 600°C the fatigue strength for the fretting fatigue was even higher than for the plain fatigue tests. For this titanium alloy, an oxide layer is observed from 400°C and is well developed at 600°C. A completely different tribological behaviour was revealed by the Ti-6Al-4V alloy, where no oxide layer was developed on the contacting surfaces ([Hamdy and Waterhouse, 1979b](#)).

As the fretting phenomenon is also present in steam turbines, [Mutoh et al. \(1989\)](#) focused their efforts on analyzing three steel alloys commonly used in this application: 12Cr-Mo-W-V, Cr-Mo-V, and 11Cr-Mo-V-Nb. These authors carried out fretting fatigue and plain fatigue tests at room temperature and at 500°C. The specimens were fabricated in 12Cr-Mo-W-V and Cr-Mo-V, and the contact pads were made of 11Cr-Mo-V-Nb. For these materials, the plain fatigue strength decreases with the temperature. Fretting fatigue is shown to add a huge (almost 1/3) reduction of the fatigue strength by comparison with plain fatigue at both temperatures. Based on the elastic-plastic fracture mechanics analysis, the prediction of the fretting fatigue lives agreed well with the experimental observations. In a further work, [Mutoh et al. \(1992\)](#) using a shot-peened 12Cr-Mo-W-V steel alloy, noticed that the fretting fatigue strength was substantially improved (by a factor of 1.8) at room temperature and at 500°C due to the compressive residual stress added on the specimen surface by the shot-peening process.

Continuing the investigation of the shot-peening process under fretting fatigue conditions at elevated temperatures, a series of experiments were conducted evaluating the Ti-6Al-4V. The fretting resistance of shot-peened Ti-6Al-4V specimens were determined at room temperature by [Mall et al. \(2002\)](#), and at 260°C by [Lee et al. \(2003\)](#). On the other hand, ([Sahan, 2002](#); [Jin et al., 2005](#)) evaluated the fretting strength of unpeened Ti-6Al-4V specimens at room temperature and at 260°C. Comparing those results, it was observed that shot-peening process increased the fretting fatigue life of the Ti-6Al-4V alloy only at room temperature. In contrast, the fretting resistance of shot-peened specimens was similar to unpeened ones at high temperature. Measuring the level of residual stress before and after the tests, [Lee et al. \(2003\)](#) noticed that

the residual compressive stress was relaxed during the fretting fatigue tests, and even more relaxation was observed under high temperature, explaining the life reduction of the shot-peened specimens at 260°C. [Lee and Mall \(2004\)](#) further evaluated the residual stress relaxation behaviour by performing additional fretting fatigue tests on Ti-6Al-4V shot-peened specimens at high temperature, but now at 100°C. To isolate the role of temperature on stress relaxation, a set of experiments only exposing the specimens at 100°C was carried out. The results have shown that stress relaxation can be obtained due to exposition at high temperatures and by mechanical loads. Further, as these processes seem to be independent of each other, the total stress relaxation can be estimated by a linear superposition of the effects caused by each one.

Also investigating methods to improve fretting fatigue life, the influence of using some lubricants, coatings, and shot-peening process in Ti-17 specimens against Ti-8-1-1 pads at 315°C was evaluated by [Gean and Farris \(2006\)](#). The experimental results have shown that only the shot-peening treatment was effective in increasing the fretting fatigue life. [Zhang and Liu \(2009\)](#) carried out tests on a shot-peened Ti-8-1-1 alloy at 350°C and at 500°C, noticed that at 350°C, the fretting fatigue resistance was increased due to strong reduction in crack growth rate associated with the presence of the residual stress induced by the shot-peening process. However, a lower fretting fatigue resistance was observed when tested at 500°C. This behaviour may be explained by the further stress relaxation induced by temperature ([Lee and Mall, 2004](#)).

[Attia \(2000\)](#) studying the fretting fatigue behaviour of two nickel alloys (Inconel 600 and Incoloy 800) carried out tests at room temperature and at 265°C in a steam (water vapor) environment. For these tests, the Inconel 600 and Incoloy 800 were tested against carbon steel and stainless steel, respectively. The results have shown that in the presence of fretting, the fatigue strengths were significantly reduced at both temperatures for both nickel alloys.

For the aircraft industry, fretting plays an important role, and it is considered a very important and complicating factor in modeling an approach against the HFC problem

(Cowles, 1996). In this setting, trying to reproduce the contact between two common materials used in aircraft engines, Hansson et al. (2000) conducted plain fatigue tests on an  $\gamma$ -based TiAl alloy at 675°C. Also, fretting fatigue tests were carried out using the same titanium alloy as the fretting specimen and the Inconel 718 as the contacting pad material. The life of the fretting fatigue tests was 26% smaller than the one of the plain fatigue tests.

Murthy et al. (2003) developed a fretting machine capable of performing tests up to 600°C heated by ceramic igniters, in which several fretting-fatigue experiments were conducted (Murthy and Farris, 2003; Murthy et al., 2006; Gean and Farris, 2006). Murthy and Farris (2003) simulating engine type-loading present in dovetail joints, performed fretting fatigue tests on Single Crystal Nickel (SCN) specimens, and Inconel 100 cylindrical pads at 600°C to analyze the crystal orientation of the fracture planes. Some time later, Murthy et al. (2006) also using SCN specimens and Inconel 100 pads, focused their attention on the fatigue life instead of crystal orientation planes. Applying many life prediction criteria (e.g., Socie, Findley, Chu-Conle-Bonnen, and others), the predicted lives were compared with the experimental ones, and their results have shown that conventional life prediction criteria could be used to assess the fretting fatigue problem at high temperatures. Among the different parameters aforementioned, the best lives predictions were provided by the Findley parameter.

Kwon et al. (2010) studying the fatigue life of the Inconel 600 alloy, performed plain and fretting fatigue tests at room temperature and at 320°C and observed that for the plain case, the fatigue lives were almost the same for both investigated temperatures. In the same way, the fretting fatigue lives did not change significantly for both temperatures. However, a significant reduction in the fatigue life (about 70% at  $10^7$  cycles) was observed in the presence of fretting fatigue. Attia (2000) also report the fatigue life reduction effect in the presence of fretting on this same nickel alloy at different temperatures. Later, using the same pad geometry, load ratio, and testing temperatures of their previous work (Kwon et al., 2010), Kwon et al. (2011) performed fretting fatigue and

plain fatigue tests on the Inconel 690. For this alloy, fretting also leads to a reduction in the fatigue strength for both temperatures. However, due to the formation of glaze oxide, the fretting fatigue life at high temperatures was bigger than one at room temperature. As the changes of friction coefficient and wear properties induced by temperature appears to play a crucial role on high temperature fretting fatigue, a new wear law based on the energy wear coefficient was developed, and the results of some fretting wear tests on stainless steel showed good agreement with this approach (Rybiak et al., 2010).

Fleury (2015) conducted a series of fretting fatigue tests at 680°C using flat specimens of a polycrystalline Ni-based alloy (RR100) and two sets of cylindrical pads, one made of RR100 and the other of a single-crystal alloy (CMSX-4). Besides evaluating the influence of the crystallographic orientation of single-crystal pads, Fleury also observed an increase in fretting fatigue life when tests with identical loading conditions were conducted at lower frequencies due to the longer cycle time that favors the oxide formation. More recently, Zhai et al. (2020) built an ultrasonic fretting fatigue rig and carried out tests in a very high cycle fatigue regime on a nickel-based alloy (Niomic 80A).

Using a new fretting apparatus capable to perform fretting fatigue tests with variable contact loadings, Abbasi and Majzoubi (2018a) conducted an investigation on Al7075-T6 alloy studying the effect of out-of-phase loadings at room temperature, and latter evaluating the influence of high temperatures under cyclic normal contacting loads in this same alloy (Abbasi and Majzoubi, 2018d). These authors reported a considerable reduction in fretting fatigue life at high temperature, being even worst when also associated with cyclic contact normal load condition. However, the results of their work (Abbasi and Majzoubi, 2018a) were severely criticized by Ciavarella (2018).

Almost 70 years after the first studies on fretting fatigue at high temperatures, this topic remains very challenging. By now, the works have shown that fretting fatigue associated with elevated temperatures can lead to different results depending on the material, surface treatment, temperature level, and others. Therefore, it is still important to continue the investigation on this subject. Table 1.1 summarizes the fretting

experiments conducted at high-temperature assessed in this review.

Table 1.1: Summary of literature review of fretting and fretting fatigue tests conducted at elevated temperatures.

Author	Year	University/Company	Material	Temperature [°C]
Uhlig et al.	1953	Massachusetts Institute of Technology	SAE 1018	-125 to 150
Swikert and Johnson	1968	NASA	Ti-6Al-4V and Inconel 600	20 and 260
Hurricks	1972	Swansen Tribology Centre	EN3B mild steel	20 to 200
Stott et al.	1973	University of Manchester	Nimonic 75, Nimonic C263, Nimonic 108 and Incoloy 901	150 to 800
Hurricks	1974		EN3B mild steel	20 to 500
Bill	1974	NASA Lewis Research Center and U. S. Army Air Mobility R&D Laboratory	99.9% pure Nickel and four types of Ni-Cr-Al alloys	23, 540, 650 and 816
Hamdy and Waterhouse	1979	University of Nottingham	Ti-6Al-4V	20, 200, 400 and 600
Hamdy and Waterhouse	1979	University of Nottingham	Inconel 718	20, 280, 540 and 700
Kayaba and Iwabuchi	1981	Tohoku University	0.45% C steel (S45C) and Stainless steel (SUS304)	S45C: 20 to 500; SUS304: 20 to 650



Hamdy et al.	1981	University of Nottingham	Ti-6Al-4V and Inconel 718	Ti64: 20, 200, 400, 600; IN 718: 20, 280, 540
Hamdy and Waterhouse	1982	University of Nottingham	IMI 829	20, 400, 500 and 600
Waterhouse and Iwabuchi	1985	University of Nottingham	IMI 550, IMI 679, IMI 685 and IMI 829	20, 400, 500 and 600
Bill	1985	NASA Lewis Research Center	Ti-6Al-4V	150 and 300
Mutoh et al.	1989	Nagaoka University of Technology and Toshiba Corporation	12Cr-Mo-W-V, Cr-Mo-V against 11Cr-Mo-V-Nb	20 and 500
Mutoh et al.	1992	Nagaoka University of Technology and Toshiba Corporation	12Cr-Mo-W-V	20 and 500
Attia	2000	Ontario Power Technologies	Inconel 600 and Incoloy 800	20 and 265
Hansson et al.	2000	Nagaoka University of Technology and Volvo Aero Corporation	TiAl against Inconel 718	20 and 675
Sahan	2002	Air Force Institute of Technology	Ti-6Al-4V	20 and 260
Ramalho and Celis	2002	University of Coimbra and University of Louven	TiN-coated steel against corundum balls	23 to 500

Murthy et al.	2003	Purdue University and Toyama University	Single Nickel Crystal against Inconel 100	In-600
Murthy and Farris	2003	Purdue University	Single Nickel Crystal against Inconel 100	In-600
Lee et al.	2003	Air Force Institute of Technology	Ti-6Al-4V	20 and 260
Lee and Mall	2004	Air Force Institute of Technology	Ti-6Al-4V	100
Jin et al.	2005	Mercer University and Air Force Institute of Technology	Ti-6Al-4V	20 and 260
Matlik et al.	2006	Rolls Royce Corporation, Purdue University, United Technologies Corporation, NASA, Sverdrup Technology	Single Crystal Nickel	20, 540 and 650
Murthy et al.	2006	Purdue University	Single Nickel Crystal against Inconel 100	In-600
Gean and Farris	2006	Purdue University	Ti-17 against Ti-8-1-1	20 and 315

Hager et al.	2006	Universal Technology Corporation and Air Force Institute of Technology	Ti-6Al-4V	20 and 450
Ownby	2008	Air Force Institute of Technology	Inconel 100	20 and 600
Mary et al.	2008	Ecole Centrale Lyon and Snecma	Ti17 against Ti6242 coated	20, 250, 350 and 450
Hager et al.	2009	Universal Technology Corporation, Air Force Institute of Technology and The Pennsylvania State University	Ti-6Al-4V	20 to 450
Zhang and Liu	2009	Northwestern Polytechnical University	Ti-8-1-1	350 and 500
Kwon et al.	2010	Yeungnam University	Inconel 600	20 and 320
Rybiak et al.	2010	Laboratoire de Tribologie et Dynamique des Systèmes, Technical University of Lodz and Snecma	M152 steel against A-286 steel	23 to 400

<a href="#">Kwon et al.</a>	2011	Yeungnam University, Korea Aerospace Research Institute and Korea Textile Machinery Institute	Inconel 690	20 and 320
<a href="#">Korashy et al.</a>	2015	McGill University, National Research Council Canada and Pratt and Whitney Canada Corp.	cobalt-based Haynes 25 superalloy against cobalt-based Haynes 188 superalloy	20, 350 and 550
<a href="#">Mi et al.</a>	2015	Tribology Research Institute and Shanghai Nuclear Engineering Research and Design Institute	Inconel 690 against 405 stainless steel	20, 90, 200 and 285
<a href="#">Abbasi and Majzoobi</a>	2018	Faculty of Engineering and Bu-Ali Sina University	Al7075-T6 against stainless steel	20, 100 and 200 410

---

As described in this review, fretting fatigue has been investigated over the century. However, the majority of the studies available on the literature were carried out under a constant contact normal load condition. Even when several engineering applications, such as dovetail connections, experience cyclic contact normal load at the contact interface, only a minimal number of works have evaluated fretting under this contact normal load condition. One possible reason for this is the greater complexity of the experimental rig required to perform this kind of test compared to constant pressure ones. In the following, one can find a literature review focused in the fretting evaluations associated with variable contact normal load conditions.

[Huq and Celis \(2002\)](#) focused on the determination of the number of cycles required to form a threshold crack of  $20\mu\text{m}$  in alumina versus a WC-Co ball-on-flat contact. For that, fretting tests with an oscillating normal force were carried out and interrupted at a different number of cycles. Two fretting tests under a constant contact normal load condition were also performed. As main result, a curve of maximum contact force versus number of fretting cycles was determined. The results also indicate that under cyclic contact normal loads, fretting cracks seem to have a shorter initiation life when compared to the one under constant contact normal load. The fretting rig uses an electromagnetic actuator to vary contact normal load, and its design was presented in work ([Huq et al., 2000](#)).

A series of master thesis evaluating the effects of cyclic contact normal load conditions on the Ti-6Al-4V alloy and the Modified Shear Stress Range (MSSR) parameter were conducted at Air Force Institute of Technology (AFIT). In the first one, [Jutte \(2004\)](#) investigated the effects of a cyclic contact load on the HCF regime. The experimental campaign results also suggested that variable contact loading has a damaging effect. However, the MSSR parameter was inaccurate in estimating fretting fatigue life for variable contact loads conditions. Later, [Lee \(2004\)](#) investigated the fretting fatigue behavior under constant and cyclic contact loads using shot-peened specimens and unpeened ones. No significant correlation between contact load type and fretting fatigue

mechanisms was observed, and the shot-peening process proved effective in improving fretting fatigue life for both contact load conditions. Moreover, according to Lee, the MSSR parameter accurately predicted fretting fatigue life, crack initiation location, and orientation despite the contact normal load condition, contradicting the numerical life of the previous work of this series.

Continuing the work series of the AFIT, [Almajali \(2006\)](#) investigate the effect of phase difference ( $0^\circ$ ,  $45^\circ$ , and  $90^\circ$ ) between fatigue bulk and contact normal load. In Almajali's experimental campaign, the axial stress range and the phase angle were varied, while frequency and other loads were kept the same. The fretting fatigue resistance for the in-phase condition was almost the same as for the constant one. On the other hand, the out-of-phase condition increased the fretting life up to 30% in the LCF regime and up to 150% in the HCF one. [Al-Noaimi \(2008\)](#) also evaluates the effect of the phase angle difference between the fatigue bulk and the contact normal loads. However, unlike ([Almajali, 2006](#)), some of his tests were conducted under combinations between fretting and plain fatigue. Al-Noaimi reported that as the ratio of plain fatigue to fretting fatigue increases, the fretting fatigue life increases despite the contact normal load condition.

The effect of a different phase angle ( $0^\circ$ ,  $90^\circ$ , and  $180^\circ$ ) between axial and tangential load on fretting fatigue behaviour was evaluated, but now considering the aluminum alloy Al2024-T3 ([Hojjati-Talemi et al., 2014](#)). Moreover, the cyclic contact normal load effect on the fretting crack initiation lifetime was investigated. In this case, the cylinder-to-plane contact geometry was used, and the stress ratios for the axial, tangential, and contact load were equal to 0.1. The axial and tangential stress ratios for the test with constant contact normal load were equal to 0.1 and -1, respectively. By comparing these results, Hojjati-Talemi et al. reported that cyclic contact normal load condition has a detrimental effect on the fretting fatigue crack initiation lifetime.

More recently, another series of works assessing the effects of cyclic contact normal load conditions was conducted on the aeronautical aluminium alloy Al7075-T6. Abbasi and Majzoubi conducted these works at the Bu-Ali Sina University (Iran). These authors

evaluated the contact load frequency (Majzoobi and Abbasi, 2018), phase difference between axial and contact loads (Abbasi and Majzoobi, 2018b), peak pressure (Abbasi and Majzoobi, 2017), shot-peening (Majzoobi and Abbasi, 2017), and temperature (Abbasi and Majzoobi, 2018c). In general lines, Abbasi and Majzoobi's results indicate that fretting under cyclic contact normal load conditions reduces fretting resistance. However, when different phase angle was considered, an increase in fretting life was reported. The life improvement was up to 57% and 101%, for phase differences of 90° and 180°, respectively. The Majzoobi and Abbasi's test apparatus is not able to apply and control tangential forces. Such a component is generated due to a reaction of the system's stiffness. Thus, the level of tangential force varies accordingly with oscillating the contact load in-phase with the axial load. However, some of Abbasi and Majzoobi's results have been questioned. Ciavarella (2018) was shocked that gross slip (observed on the Abbasi and Majzoobi tests) has occurred under proportional loading. He then concludes that contact mechanics looks unable to explain this basic point that its basics may not be applicable to the case where the frequencies of the contact and the other loads are different.

## 1.5 . Summary

In the previous section it was carried out an extensive review of the state of the art about fretting fatigue tests and modelling specially at high temperature conditions involving high performance aeronautical alloys used in aeroengines. From this review it was possible to conclude that the great majority of data available concerns tests carried out with constant contact normal load considering either a cylinder against flat contact or bridge type (flat-on-flat) geometries. Further, these tests have been usually conducted at room temperature. Only a few works were carried out considering variable contact normal load. However, none of them was able to isolate such a load since the experimental devices used in these works had some of the fatigue and contact loads coupled to each other. Furthermore, some of these results were severely criticized by for

presenting mechanical inconsistencies.

In this setting, this thesis has tried to shadow more light in these aspects which have received less attention in the literature, i.e. to develop a fretting fatigue apparatus that is capable to carry out fretting fatigue tests under time-varying contact normal load and at high temperature. Also, the work will seek to validate the application of some life estimation methodologies based on these much more challenging contact configurations. In order to do so, this thesis has been organized as follows:

The second chapter presents an essential literature review covering the fundamental concepts necessary to understand this thesis subject. In such a chapter, the basics of the contact mechanics of the two-dimensional case are presented, as well as the contact formulation between two elastically similar bodies. Some fundamental concepts about multiaxial fatigue, such as the decomposition of the Cauchy tensor, the definition of shear stress amplitude, the Smith-Watson-Topper critical plane parameter, and the Theory of Critical Distances, a non-local stress averaging methodology, are also quickly introduced. The chapter ends by presenting some crucial aspects of wear and how this effect has recently been taken into account in fretting simulations.

The third chapter of this thesis is dedicated to discussing fretting fatigue rigs capable of performing tests under elevated temperatures. For this, a brief literature review of fretting fatigue rigs capable of carrying out such a complex test is presented. Particularly, the previous version of the Fretting fatigue rig of the University of Brasilia (UnB) is presented. On this previous rig, it was not possible to carry out fretting tests at elevated temperatures nor under time-varying normal contact loads. To overcome such limitations, one of the main objectives of this thesis was to upgrade the UnB's fretting fatigue so that it becomes capable of performing fretting fatigue tests with cyclic contact normal load and at high temperatures. In this way, the upgrades done by the author to the UnB's fretting rig are highly detailed, are they: *i)* The conception and design of the new fretting apparatus; *ii)* The new normal contact load application system; *iii)* The heat and cooling systems; and *iv)* The methodology developed and validated to



indirectly measured the temperature at the fretting contact.

The experimental campaign carried out in this work is fully reported in Chapter 4. Some aspects of the materials assessed here (Ti-6Al-4V and Inconel 718) and different aspects of the geometry of the experimental parts are also described. However, this chapter describes the methodologies and the results obtained from the new fretting fatigue tests conducted in this thesis. New experiments determining the coefficient of friction under fretting conditions for both alloys under study are presented. For the titanium alloy, tests under constant and cyclic contact normal load at room temperature were performed, and for the nickel one, these tests were also carried out at 540°C. Once the friction coefficient is an important property for the fretting case, these tests aimed to evaluate the influence of temperature and the normal contact load condition on this coefficient. Moreover, and most important, fretting fatigue tests were carried out varying the temperature and the normal load condition (constant or cyclic) to evaluate the influence of the contact normal load type on the fretting fatigue lives for both materials under study.

Different aspects of the life estimation and numerical modelling used in this work are detailed in Chapter 5. In this thesis fretting fatigue life was estimated by two different methodologies: one that neglects wear effects and another that takes into account wear damage. The numerical analysis carried out in this work was done employing a 2D finite element model. The details of the numerical model as well as the way that wear was computed and included into the simulations are also described in this chapter. The life estimates provided by both methodologies for all test conditions considered in this thesis are presented and compared with the experimental lives. Finally, the last chapter of this thesis draws the main conclusions of this work and presents some suggestions for future work.



# Chapter 2

## Literature review

*The fundamental concepts to understand the scope of this thesis are presented in this chapter. Here, the reader will find basic notions of contact mechanics, multiaxial fatigue, and wear applied in the fretting context.*

### 2.1 . Basic contacts mechanics

#### 2.1.1 . Introduction

In many confirmed cases of fretting fatigue, the contact occurs between components of high geometric complexity of industrial components. In such cases, analytical solutions are not available for complex geometries and numerical methods are used. Usually, finite element methods are used, and when FEM becomes too expensive for very complex problems, semi-analytical methods can also be applied ([Gallego and Nelias, 2007](#); [Gallego et al., 2010](#); [Done et al., 2017](#)). For this reason, most authors use simple and well-defined geometries so that it may also be possible to the application of analytical approaches. Other factors also influence the choice of these geometries, such as greater ease in the manufacturing process and lower cost of the parts.

Contacting parts for fretting-fatigue tests are usually based on the simplest possible test geometries, for which analytical solution are available. Figure 2.1 illustrates some types of analytically well-defined contacts. A contact can be defined as *incomplete* if the contact size depends on the applied contact normal load,  $P$ , as shown in Figures 2.1(a), and 2.1(b), and *complete* if the contact size is not influenced by the contact normal load, Fig. 2.1(c). The contact represented in Figure 2.1(a) is also classified as *non-*

*conformal* since the size of the half-contact width,  $a$ , is much smaller than the cylinder radius for a small contact normal load. For this particular case, the normal pressure at the contact edges is zero. On the other hand, the case represented in Fig. 2.1(b) is defined as *conformal* since the contact size can assume considerable values compared to the cylinder radius. In this case, the ends of the contacts also have null values for normal pressure. Figure 2.1(c) illustrates the case where the contact ends present a singularity since the pad is assumed to have sharp edges and hence a local curvature radius that tends to zero and creates a stress and strain singularity at the contact front.

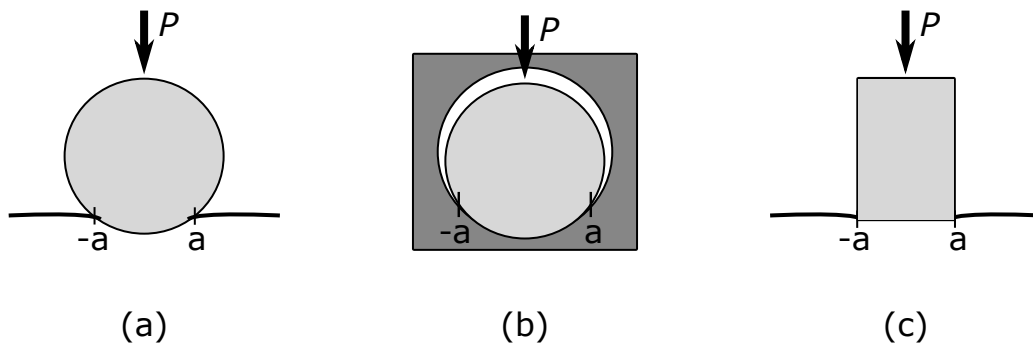


Figure 2.1: Contact classification: (a) Incomplete and non-conformal, (b) Incomplete and conformal, and (c) Complete.

If the contact geometry is symmetrical with respect to the contact plane and the two contacting objects are made of the same material, as illustrated in Figure 2.2, then, when a normal force is applied, the displacement field is also symmetrical with respect to the contact plane. In this way, no tangential movement is introduced to the contact plane and, therefore, no relative movement between the bodies in contact and a fortiori no friction. Considering now the presence of the tangential force,  $Q$ , large enough to cause a slip between the bodies, generates a shear stress distribution,  $q(x, y)$ , which is related with the friction coefficient,  $\mu$ , and the contact pressure distribution,  $p(x, y)$ , as indicated by the following equation:

$$|q(x, y)| = \mu p(x, y) \quad (2.1)$$

The shear stress induces a normal displacement of the contacting surfaces. However, as the bodies are elastically similar and the shear stress acts in opposite directions on the surfaces of the two bodies, the corresponding surface points experience an equal displacement in the normal direction resulting in no changes in the contact pressure distribution  $p(x, y)$ .

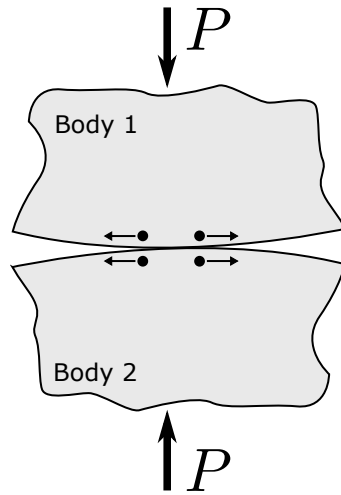


Figure 2.2: Normal contact between two elastically similar bodies.

Regarding the fretting sliding regimes, [Hannel et al. \(2001\)](#) classified it as follows:

- Partial slip regime: when the partial slip condition ( $Q < \mu P$ ) is fulfilled during the whole test duration. In a such case, two different zones are formed in the contact area. The first one is so-called the stick zone (where full adhesion between the contacting surfaces takes place), and the second one is named slip zone (where relative tangential motion are observed on the contacting surfaces), as illustrated in Fig. 2.3(a).
- Gross slip regime: when gross slip condition is observed regardless of the friction evolution. In this case, full sliding is observed across the entire contact surface, as shown in Fig. 2.3(b).
- Mixed slip regime: usually observed when the gross slip regime evolves to the partial slip one due to the friction evolution of the contact surfaces.

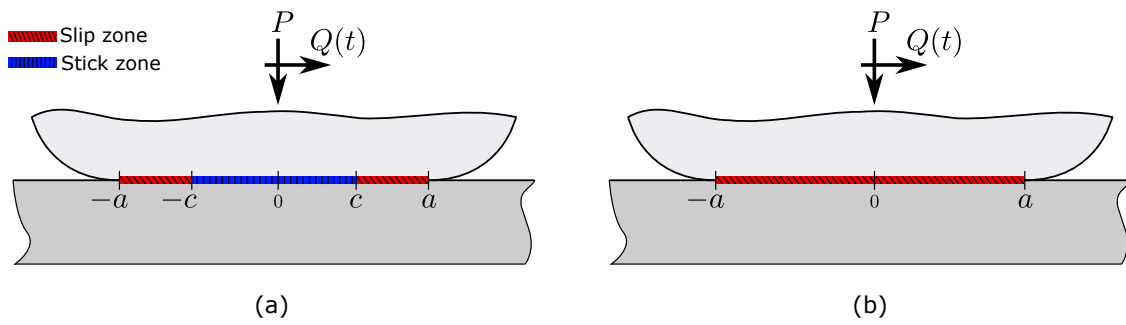


Figure 2.3: Illustration of the (a) partial slip regime, and (b) gross slip condition.

### 2.1.2 . Contact between cylinders

In the present work, only a concise solution of the contact case between elastically similar cylinders will be presented. A complete and detailed description of the contact configurations under study and further ones can be found in [Hills and Nowell \(1994\)](#).

In order to tackle the fretting case, it is fundamental to comprehend and determine the stress field beneath the contact and the relative surface displacements. One way to do this is by using the formulation of Muskhelishvili potential ([Muskhelishvili, 1953](#); [Gladwell, 1980](#); [Hills et al., 1993](#)).

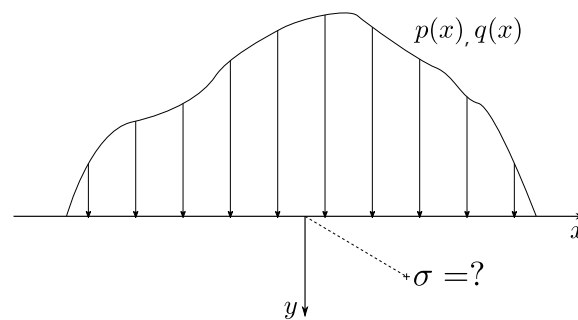


Figure 2.4: Illustration of a half-plane under normal  $p(x)$  and shear  $q(x)$  distributions.

The potential function,  $\Phi(z)$ , depends on the complex coordinate  $z = x + iy$ . Taking into account the geometry and coordinate system shown in Fig. 2.4, the potential  $\Phi(z)$  can be found by performing the contour integral in the contact:

$$\Phi(z) = \frac{1}{2\pi i} \int_{\text{contact}} \frac{p(s) - iq(s)}{s - z} ds \quad (2.2)$$

where  $p(s)$  and  $q(s)$  are arbitrary contact pressure and shear stress distributions, respectively. For contacts in gross slip condition, the previous equation can be rewritten using Eq. 2.1, resulting in:

$$\Phi(z) = \frac{1 - i\mu}{2\pi i} \int_{\text{contact}} \frac{p(s)}{s - z} ds \quad (2.3)$$

Once the potential function is determined, the stress components ( $\sigma_{xx}$ ,  $\sigma_{yy}$ , and  $\tau_{xy}$ ) can be calculated as follows:

$$\sigma_{xx} + \sigma_{yy} = 2[\Phi(z) + \bar{\Phi}(\bar{z})] \quad (2.4)$$

and

$$-\sigma_{xx} + \sigma_{yy} + 2\tau_{xy} = 2[(\bar{z} - z)\Phi'(z) - \bar{\Phi}(z) - \Phi(z)] \quad (2.5)$$

Summing Eqs. 2.4 and 2.5 the following expression can be found:

$$A = \sigma_{yy} + i\tau_{xy} = [(\bar{z} - z)\Phi'(z) - \bar{\Phi}(z) + \bar{\Phi}(\bar{z})] \quad (2.6)$$

Finally, by means of Eq. 2.6 and assuming the plane-strain condition, it is possible to calculate the stress components as:

$$\sigma_{xx} = 4Re[\Phi(z)] - Re(A) \quad (2.7)$$

$$\sigma_{yy} = Re(A) \quad (2.8)$$

$$\tau_{xy} = Im(A) \quad (2.9)$$

$$\sigma_{zz} = \nu(\sigma_{xx} + \sigma_{yy}) \quad (2.10)$$

At this point, still necessary to solve the potential function  $\Phi(z)$  and its variants  $\bar{\Phi}(z)$ ,  $\bar{\Phi}(\bar{z})$ , and  $\Phi'(z)$ . The Hertz solution for cylinders (Hertz, 1882) predicts an elliptical contact distribution  $p(x)$  in the contact defined as:

$$p(x) = -p_0 \sqrt{1 - \left(\frac{x}{a}\right)^2} \quad (2.11)$$

$$p_0 = \frac{2P}{\pi a} \quad (2.12)$$

$$a = \sqrt{\frac{4PR_{eq}}{\pi E_{eq}}} \quad (2.13)$$

$$R_{eq} = \left(\frac{1}{R_1} + \frac{1}{R_2}\right)^{-1} \quad (2.14)$$

$$E_{eq} = \left(\frac{1 - \nu_1^2}{E_1} + \frac{1 - \nu_2^2}{E_2}\right)^{-1} \quad (2.15)$$

where  $p_0$  is the peak pressure and  $a$  is the semi-width of the contact. Besides that,  $R_{eq}$  and  $E_{eq}$  are the equivalent components of the radii cylinders and Young's Modulus, respectively. Substituting the contact pressure distribution  $p(x)$  defined by Eq. 2.11 into Eq. 2.3 results in:

$$\Phi(z) = \frac{-(1 - i\mu) p_0}{2\pi i} \frac{1}{a} \int_{-a}^a \frac{\sqrt{a^2 - x^2}}{x - z} dx \quad (2.16)$$

The solution of Eq. 2.16 is presented by Eq. 2.17, and now from Eq. 2.17 it is possible to define the potential function variants:

$$\Phi(z) = -\frac{p_0}{2a} (i + \mu) \left( z - \operatorname{sgn}(\operatorname{Re}(z)) \sqrt{z^2 - a^2} \right) \quad (2.17)$$



$$\Phi'(z) = -\frac{p_0}{2a}(i + \mu) \left( 1 - \operatorname{sgn}(\operatorname{Re}(z)) \frac{z}{\sqrt{z^2 - a^2}} \right) \quad (2.18)$$

$$\bar{\Phi}(z) = -\frac{p_0}{2a}(-i + \mu) \left( z - \operatorname{sgn}(\operatorname{Re}(z))\sqrt{z^2 - a^2} \right) \quad (2.19)$$

$$\bar{\Phi}(\bar{z}) = -\frac{p_0}{2a}(-i + \mu) \left( \bar{z} - \operatorname{sgn}(\operatorname{Re}(\bar{z}))\sqrt{\bar{z}^2 - a^2} \right) \quad (2.20)$$

Finally, the stress state beneath the contact can be determined by substituting the potential functions and its variants (Eqs. 2.17 to 2.20) into the stress components (Eqs. 2.7 to 2.9).

As the fretting problem is decoupled, it is convenient to isolate the real and the imaginary part on Eq. 2.17 by multiplying the  $(i + f)$  parenthesis. In this way, the imaginary part generates the normal stress state,  $\sigma^n(x, y)$ , and the real one, which contains the friction factor,  $f$ , the tangential stress state,  $\sigma^t(x, y)$ . Similarly, the normal and tangential parts can be separated from all potential function variants. Thus, it is also possible to define the stress states separately as indicated below:

$$\sigma^n(x, y) = \begin{bmatrix} \sigma_{xx}^n & \tau_{xy}^n & 0 \\ \tau_{xy}^n & \sigma_{yy}^n & 0 \\ 0 & 0 & \sigma_{zz}^n \end{bmatrix} \quad (2.21)$$

$$\sigma^t(x, y) = \begin{bmatrix} \sigma_{xx}^t & \tau_{xy}^t & 0 \\ \tau_{xy}^t & \sigma_{yy}^t & 0 \\ 0 & 0 & \sigma_{zz}^t \end{bmatrix} \quad (2.22)$$

If the condition ruled by Eq. 2 is not violated, two distinct zones will be formed at the contact: an adhesion zone  $|x| < c$  and a slip zone  $(c \leq |x| \leq a)$ , as indicated in Fig. 2.2. The shear stress distribution,  $q(x)$ , is usually modeled as a perturbation of the total slip solution (Cattaneo, 1938; Mindlin, 1949). Therefore, the shear distribution  $q(x)$  can

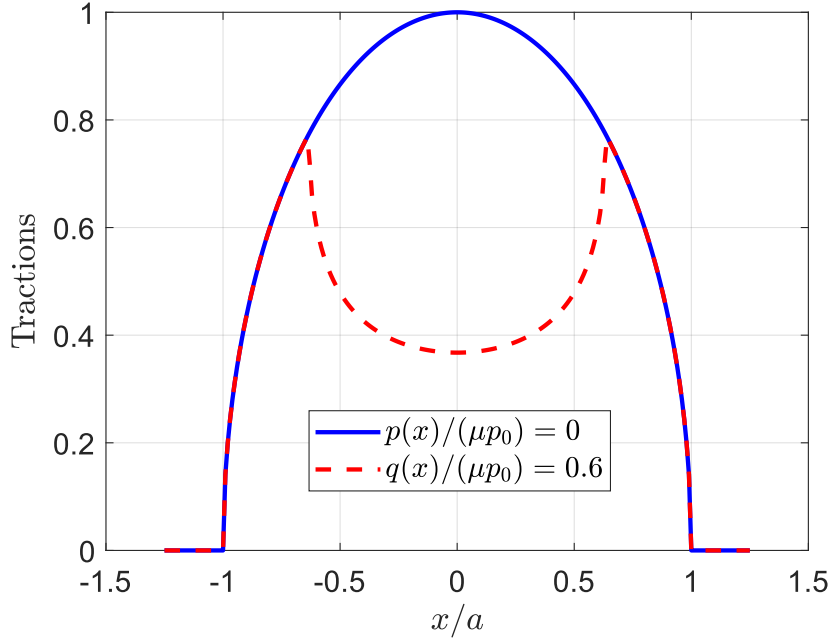


Figure 2.5: Normalized contact tractions under partial slip condition.  $Q/\mu P = 0.6$ .  $|x/a| \leq 0.6325$

be defined as

$$q(x) = \mu p_0 \sqrt{1 - \left(\frac{x}{a}\right)^2} - q_1(x) \quad (2.23)$$

where the shear distribution perturbation  $q_1(x)$  is

$$q_1(x) = \mu p_0 \frac{c}{a} \sqrt{1 - \left(\frac{x}{a}\right)^2} \quad (2.24)$$

Notice that  $q_1(x) = 0$  in the slip zones. Moreover, solving the tangential equilibrium condition, the half-size of the stick zone,  $c$ , is defined as

$$c = a \sqrt{1 - \left(\frac{Q_{\max}}{\mu P}\right)} \quad (2.25)$$

Figure 2.5 shows the contact tractions for a fretting problem under partial slip condition. In this figure, it is possible to notice that a portion of the distribution  $q(x)$  is discounted by the perturbation  $q_1(x)$  in the adhesion region.

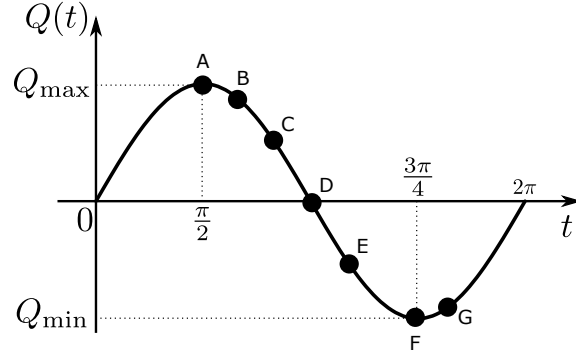


Figure 2.6: Tangential load in a full fretting cycle.

Up to the present moment, the contact problem was evaluated considering the time instant when the tangential load reaches its maximum ( $Q(t) = Q_{\max}$ ). However, as illustrated in Fig. 2.6, this component varies during the fretting cycle. The time required to complete a full fretting cycle was discretized by means of a sinusoidal function varying its argument from 0 to  $2\pi$ , as shown in the same figure.

As the fretting fatigue cycle begins, the tangential load,  $Q(t)$ , initiates a phase of loading up to point A, at which point the tangential load is maximum. From point A to point B, the unloading process begins. Point B represents a time instant immediately after  $Q(t) = Q_{\max}$ . At this instant, when changing from the loading to the unloading phase, adhesion is observed in the entire contact. Such a phenomenon is also observed when the tangential load changes from unloading to loading phase (point G to point F).

Continuing the unloading phase, from point B to point C, reverse slip zones are formed at the ends of the contacts once the contact pressure distribution is not sufficient to keep the partial slip condition. In these new zones ( $c' < x \leq a$ ), here called the reverse slip zones, the shear stress changes from X to Y due to the direction change of the relative motion. In this way, a second perturbation of the shear stress ( $q_2(x)$ ) takes place defined as:

$$q_2(x) = 2\mu p_0 \frac{c'}{a} \sqrt{1 - \left(\frac{x}{c'}\right)^2} \quad (2.26)$$

where the half-size of the stick zone under reverse sliding condition,  $c'$ , is

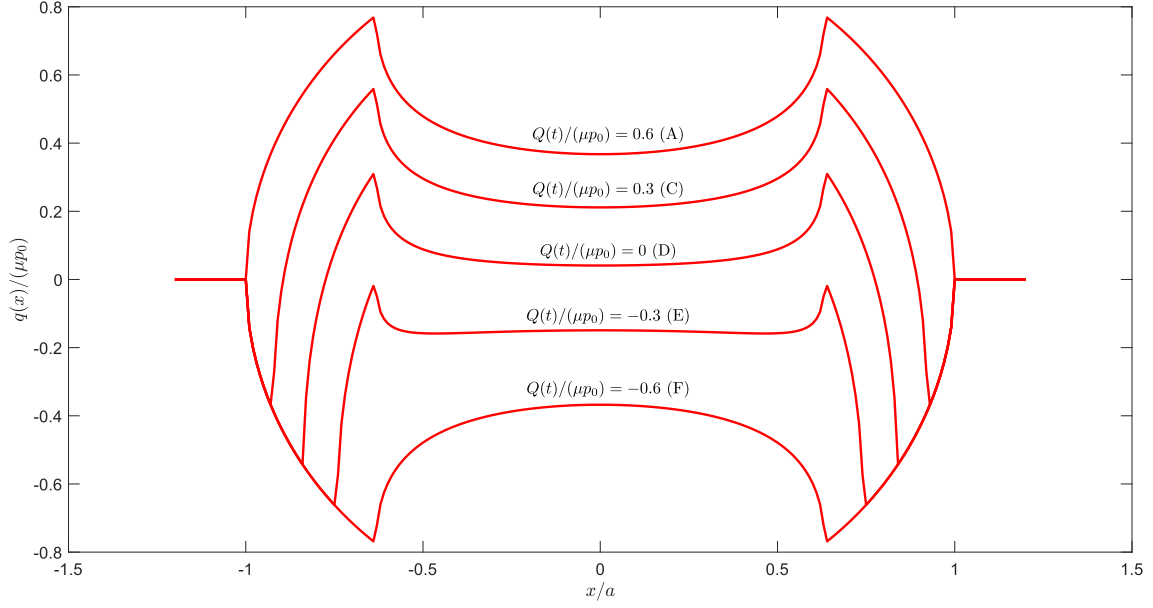


Figure 2.7: Shear traction distribution in a fretting cycle as described in Fig. 2.6.  $Q_{\max}/(\mu p_0) = 0.6$ .

$$c' = a \sqrt{1 - \left| \frac{Q_{\max} - Q(t)}{2\mu P} \right|} \quad (2.27)$$

Table 2.1 summarizes the values assumed by the normalized shear distribution in each contact application zone during a complete fretting cycle.

Table 2.1: Shear components at different zones in a fretting cycle.

$q(x)/\mu p_0$	Application zone
$-\sqrt{1 - (x/a)^2}$	$c' <  x  \leq a$
$-\sqrt{1 - (x/a)^2} + 2\frac{c'}{a}\sqrt{1 - (x/c')^2}$	$c <  x  \leq c'$
$-\sqrt{1 - (x/a)^2} + 2\frac{c'}{a}\sqrt{1 - (x/c')^2} - \frac{c}{a}\sqrt{1 - (x/c)^2}$	$ x  \leq c$

Figure 2.7 shows the the shear traction distributions at different time instants of a fretting cycle, related to points A, C, D, E, and F of Fig. 2.6.

It is important to notice, that the shear stresses depend on the loading history. In this way, it is necessary to perform a superposition of effects to calculate the stress components resulting in each loading phase. There are four distinct loading phases in

a complete fretting cycle: maximum, minimum, loading, and unloading. Finally, the stress-state can be calculated for each phase, as indicated below:

Maximum load:

$$\frac{\sigma_{ij}^n(x, y)}{p_0} = \left[ \frac{\sigma_{ij}^n\left(\frac{x}{a}, \frac{y}{a}\right)}{p_0} \right] + \mu \left[ \frac{\sigma_{ij}^t\left(\frac{x}{a}, \frac{y}{a}\right)}{\mu p_0} \right] - \mu \frac{c}{a} \left[ \frac{\sigma_{ij}^t\left(\frac{x}{c}, \frac{y}{c}\right)}{\mu p_0} \right] \quad (2.28)$$

Minimum load:

$$\frac{\sigma_{ij}^n(x, y)}{p_0} = \left[ \frac{\sigma_{ij}^n\left(\frac{x}{a}, \frac{y}{a}\right)}{p_0} \right] - \mu \left[ \frac{\sigma_{ij}^t\left(\frac{x}{a}, \frac{y}{a}\right)}{\mu p_0} \right] + \mu \frac{c}{a} \left[ \frac{\sigma_{ij}^t\left(\frac{x}{c}, \frac{y}{c}\right)}{\mu p_0} \right] \quad (2.29)$$

Loading:

$$\frac{\sigma_{ij}^n(x, y)}{p_0} = \left[ \frac{\sigma_{ij}^n\left(\frac{x}{a}, \frac{y}{a}\right)}{p_0} \right] + \mu \left[ \frac{\sigma_{ij}^t\left(\frac{x}{a}, \frac{y}{a}\right)}{\mu p_0} \right] + \mu \frac{c}{a} \left[ \frac{\sigma_{ij}^t\left(\frac{x}{c}, \frac{y}{c}\right)}{\mu p_0} \right] - 2\mu \frac{c'}{a} \left[ \frac{\sigma_{ij}^t\left(\frac{x}{c'}, \frac{y}{c'}\right)}{\mu p_0} \right] \quad (2.30)$$

Unloading:

$$\frac{\sigma_{ij}^n(x, y)}{p_0} = \left[ \frac{\sigma_{ij}^n\left(\frac{x}{a}, \frac{y}{a}\right)}{p_0} \right] - \mu \left[ \frac{\sigma_{ij}^t\left(\frac{x}{a}, \frac{y}{a}\right)}{\mu p_0} \right] - \mu \frac{c}{a} \left[ \frac{\sigma_{ij}^t\left(\frac{x}{c}, \frac{y}{c}\right)}{\mu p_0} \right] + 2\mu \frac{c'}{a} \left[ \frac{\sigma_{ij}^t\left(\frac{x}{c'}, \frac{y}{c'}\right)}{\mu p_0} \right] \quad (2.31)$$

### 2.1.3 . Influence of the fatigue bulk stress on the tractions

When fretting acts in conjunction with fatigue bulk loading, fretting fatigue occurs. The presence of the bulk load modifies the shear traction due to an offset in the slip and stick zones. In this way, Eqs. 2.24 and 2.26 can be respectively rewritten as:

$$q_1(x) = \mu p_0 \frac{c}{a} \sqrt{1 - \left[ \frac{(x - e)}{c} \right]^2} \quad (2.32)$$

and

$$q_2(x) = 2\mu p_0 \frac{c'}{a} \sqrt{1 - \left[ \frac{(x - e')}{c'} \right]^2} \quad (2.33)$$

where the normalized displacements  $e/a$  and  $e'/a$  are respectively calculated as

$$\frac{e}{a} = \frac{\sigma_{B,\max}}{4\mu p_0} \quad (2.34)$$

and

$$\frac{e'}{a} = \frac{\sigma_{B,\max} - \sigma_B(t)}{8\mu p_0} \quad (2.35)$$

Figure 2.8 illustrates two cases of shear traction distributions, and one can easily observe the shift effect on the slip and stick zones caused by the fatigue bulk loading.

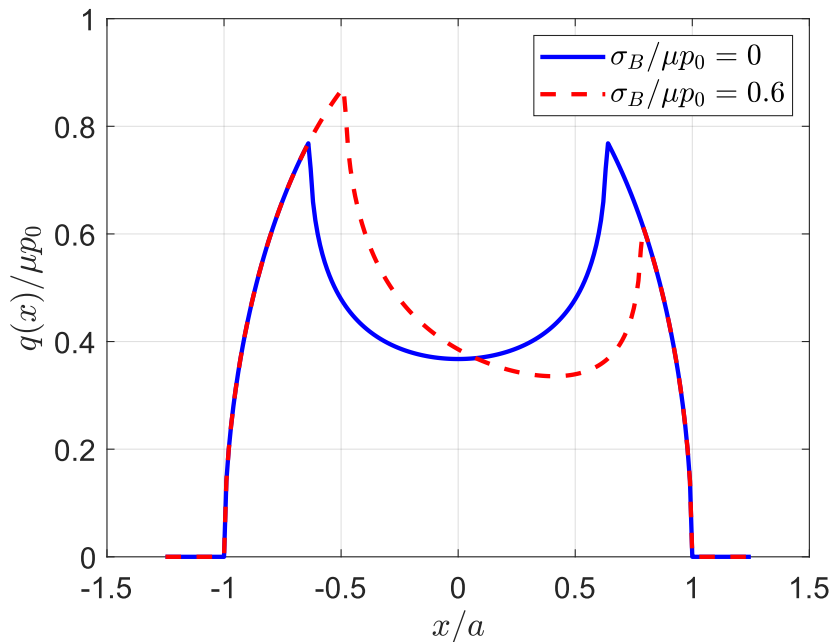


Figure 2.8: Shear traction with (blue dashed line) and without (solid red line) fatigue bulk load.

## 2.2 . Multiaxial Fatigue

### 2.2.1 . Introduction

In real mechanical applications, it is usual that components experience multiaxial loads. However, it have being tried by the use of multiaxial criteria to design such components using experimental data obtained with uniaxial fatigue experiments, since

tests of this kind are simple and less costly to be conducted in laboratory. Gough and Pollard (1935) and Nishihara et al. (1945) conducted a series of experimental results from which, in the future, the first multiaxial criteria would emerge. Sines (1955) proposed a method based on the stress tensor invariants, where by calculating an equivalent stress, it is possible to predict the fatigue life by using  $S \times N$  curves. Later, other multiaxial fatigue criteria based on the stress tensor invariant were proposed by Crossland (1956), Deperrois (1991), Li et al. (2000), Mamiya and Araújo (2002). Critical plane criteria have also become popular for predicting the location and crack initiation, besides the fatigue strength. This type of criterion considers that fatigue cracks are born in material planes where the stress state is the most severe. Among other authors, critical plane models were proposed by Brown and Miller (1973), McDiarmid (1974), Socie (1987), Fatemi and Socie (1988), and Susmel and Lazzarin (2002).

### 2.2.2 . Decomposition of the Cauchy stress tensor and shear stress amplitude definition

Assuming the  $\Delta$  arbitrary material plane where is normal is determined by the unitary vector  $\underline{n}$ , and the directions  $\underline{e}_1$  and  $\underline{e}_2$  are also unitary and orthogonal with respect to each other (Figure 2.9), the stress component normal to this plane at the time instant  $t$ ,  $\sigma_n(t)$ , can be calculated as:

$$\sigma_n(t) = \underline{n} \cdot \underline{\underline{\sigma}}(t)\underline{n} \quad (2.36)$$

where  $\underline{\underline{\sigma}}(t)$  represents the Cauchy stress tensor. The shear stresses can be written as:

$$\tau_1(t) = \underline{e}_1 \cdot \underline{\underline{\sigma}}(t)\underline{n} \quad (2.37)$$

and

$$\tau_2(t) = \underline{e}_2 \cdot \underline{\underline{\sigma}}(t)\underline{n} \quad (2.38)$$

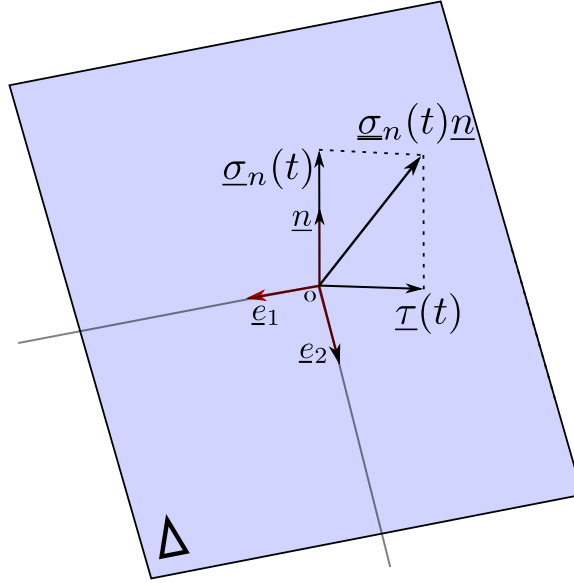


Figure 2.9: Stress vector decomposition considering the material plane  $\Delta$ .

In this study, the maximum normal stress component,  $\sigma_{n,\max}$  is easily determined as the maximum value of  $\sigma_n(t)$ . However, determining the shear stress amplitude,  $\tau_a$ , is more complicated task once the  $\tau(t)$  component draws a loading history path while varies in time. There are several ways to define the shear stress amplitude,  $\tau_a$ , for instance, by means of the Chord Method (Grubisic and Simbürger, 1976), Minimum Circumscribed Method (VAN and Griveau, 1989), Frobenius Minimum Norm Method (Zouain et al., 2006), Maximum Rectangular Hull - MRH Method (Araújo et al., 2011), Moment of Inertia Method (Meggiolaro and de Castro, 2015). In this work, the shear stress amplitude was defined using the method proposed by the MRH Method. Such a method defines the shear stress amplitude as the semi-diagonal of the largest rectangle that can be circumscribed in the time history of the shear tensor, as shown in Fig. 2.10. The halves of the sides of the rectangle that enclose the loading history ( $\Psi$ ) can be written as:

$$a_i(\lambda) = \frac{1}{2} \left[ \max_t \tau_i(\lambda, t) - \min_t(\lambda, t) \right] \quad i = 1, 2 \quad (2.39)$$

where  $\lambda$  is the rotation angle. For each  $\lambda$ -oriented rectangle, the shear stress ampli-



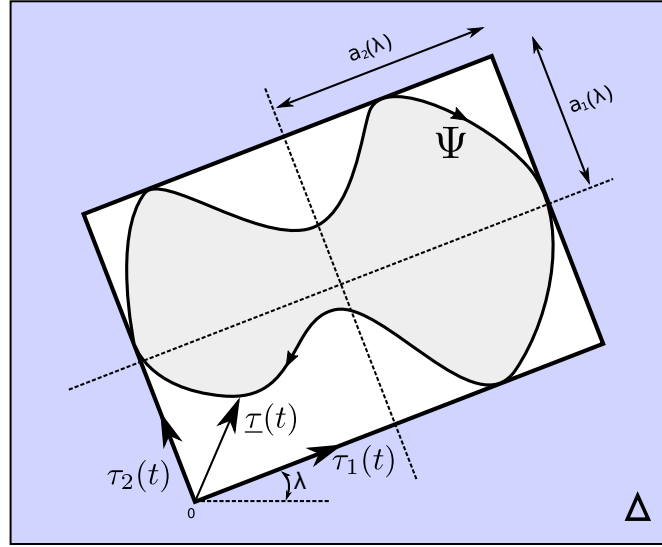


Figure 2.10: Illustration of MRH Method assessed in the material plane  $\Delta$ .

tude is calculated as follows:

$$\tau_a(\lambda) = \sqrt{a_1^2(\lambda) + a_2^2(\lambda)} \quad (2.40)$$

Then, the highest value in Eq.2.40 among all material plane investigated is defined as the shear stress amplitude according to the MRH Method:

$$\tau_{a,MRH} = \max[\tau_a(\lambda)] \quad (2.41)$$

### 2.2.3 . Smith-Watson-Topper criterion

In this work, fatigue damage assessments were carried out by considering the Smith, Watson, and Topper (*SWT*) critical plane-based parameter. This parameter was originally developed to consider the effect of mean fatigue stress in uniaxial cases (Smith et al., 1970). Later, proposed by Socie (1987), the *SWT* parameter can also be used in multiaxial fatigue cases when it is combined with a critical plane approach. In this criterion, the plane in which the *SWT* fatigue parameter is maximum is also defined as the critical plane. The *SWT* parameter can be described as:

$$SWT = \sigma_{n,\max} \varepsilon_{n,a} \quad (2.42)$$

where  $\sigma_{n,\max}$  and  $\varepsilon_{n,a}$  are the maximum normal stress and the normal strain amplitude, respectively. In this setting, the critical plane is defined as the one which maximizes Equation 2.42.

In this work the SWT criterion will be used to estimate fretting fatigue life once the materials under study in this thesis (Ti-6Al-4V and Inconel 718) indicates to have the crack initiation mechanism mode-I dominant. For instance, [Ferry \(2017\)](#) performed fretting fatigue tests considering the same titanium alloy and observed crack initiation mode-I dominant. Besides in this work only the SWT parameter will be used to assess life, other classical critical plane criteria will be described for the reader on the following subsections.

#### 2.2.4 . Fatemi-Socie parameter

[Fatemi and Socie \(1988\)](#), based on the model by [Brown and Miller \(1973\)](#), developed the Fatemi-Socie (FS) parameter to predict multiaxial fatigue cases with in-phase and out-of-phase loads. This fatigue parameter gives great importance to the shear effects on the crack initiation process. Considering the high-cycle fatigue case (HCF), the FS parameter can be written as:

$$FS = \tau_a \left( 1 + \kappa \frac{\sigma_{n,\max}}{\sigma_y} \right) \quad (2.43)$$

where  $\tau_a$  is the shear stress amplitude,  $\kappa$  is a material constant, and  $\sigma_y$  is the yield point of the material. For this parameter, the critical plane is usually defined as the plane with the highest FS index. The material constant  $\kappa$  measures the importance of the effect of normal stress on the Fatemi-Socie criterion.

#### 2.2.5 . Modified Wöhler Curve Method

[Susmel and Lazzarin \(2002\)](#) presented a method to estimate the high cycle fatigue

limit for cases with multiaxial loads. The so-called Modified Curve Wöhler Method (MWCM) parameter can be written as:

$$MWCM = \tau_a + k \frac{\sigma_{n,\max}}{\tau_a} \quad (2.44)$$

where  $\tau_a$  is the amplitude of the shear stress,  $\sigma_{n,\max}$  corresponds to the maximum value of the normal stress, and  $k$  is a material constant. Usually, for this parameter, the critical plane can be determined in two different ways. The first one defines the critical plane as the one with the highest MWCM parameter value. The second one defines the critical plane as the one that experiences the highest value of shear stress amplitude. However, if there is more than one plane with the same value of  $\tau_a$ , the plane among them which presents the highest value of normal stress is defined as the critical one.

## 2.3 . Methodologies to incorporate stress-gradient in fatigue problems

### 2.3.1 . Critical distance approach

It is possible by means of the Theory of Critical Distance (TCD) to estimate accurately the fatigue damage in notched components. [Giannakopoulos et al. \(2000\)](#) noticed similarities between the stresses fields of notched components and the ones observed in the fretting fatigue case, then, the TCD started to be applied in the fretting fatigue case. Since the stress field is not constant in the vicinity of a notch neither beneath of contact interface in the fretting case, the main idea of using TCD is to evaluate, in a more appropriate way, an effective stress ( $\sigma_{eff}$ ) that represents the fatigue damage process of a specific volume around the stress raiser, in other words, the TCD is a nonlocal stress-based criteria. In the TCD volume method, the first step of the analysis is the calculation of an average stress tensor defined by

$$\sigma_{eff} = \frac{1}{V} \int_V \bar{\sigma} dV \quad (2.45)$$

where  $\bar{\sigma}$  represents the stress tensor within a process zone with volume  $V$  of a

process zone. This particular volume is generally related with a characteristic length,  $L$ , commonly referred to as the critical distance (Taylor, 1999):

$$L = \frac{1}{\pi} \left( \frac{\Delta K_{th}}{\Delta \sigma} \right)^2 \quad (2.46)$$

where  $\Delta K_{th}$  and  $\Delta \sigma$  are the threshold stress intensity factor range and the uniaxial fatigue limit range, respectively, both obtained under the same fatigue loading ratio. Moreover, considering the 2D case, it is possible to calculate the effective stress from different methods, namely the Point, the Line, and the Area Methods, as shown in Figure 2.11. However, it is important to notice that the value of the critical distance  $L$  relays on the choice of the average method (point, line, or area) and on the fatigue parameter that has being used, once fatigue damage is estimated differently by different fatigue parameters (Castro et al., 2009). In this work, a simplified version of the TCD by means of the Point Method (PM) is considered in the analyses. In other words, in this work the average stress is determined as follows:

$$\sigma_{eff} = \bar{\sigma}(L/2) \quad (2.47)$$

In this case, fatigue assessments are carried out considering a point  $L/2$  distant from the stress raiser, see Fig. 2.11(a). For fretting problems, the stress raiser is commonly regarded as the contact edge (hot-spot). Besides in this work only the TCD by means of the point method will be used to assess life, other methodologies to incorporate stress gradient in the fretting problem will be described for the reader in the following subsection.

### 2.3.2 . Asymptotic and short crack arrest methods

A main phase of evaluating fretting fatigue is to predict crack initiation conditions. Recently, the critical plane approach is a common one to find a criterion for crack initiation. However, there are other ways to predict crack initiation under fretting fatigue conditions, such as by means of methods based on fracture mechanics. Here, two of them

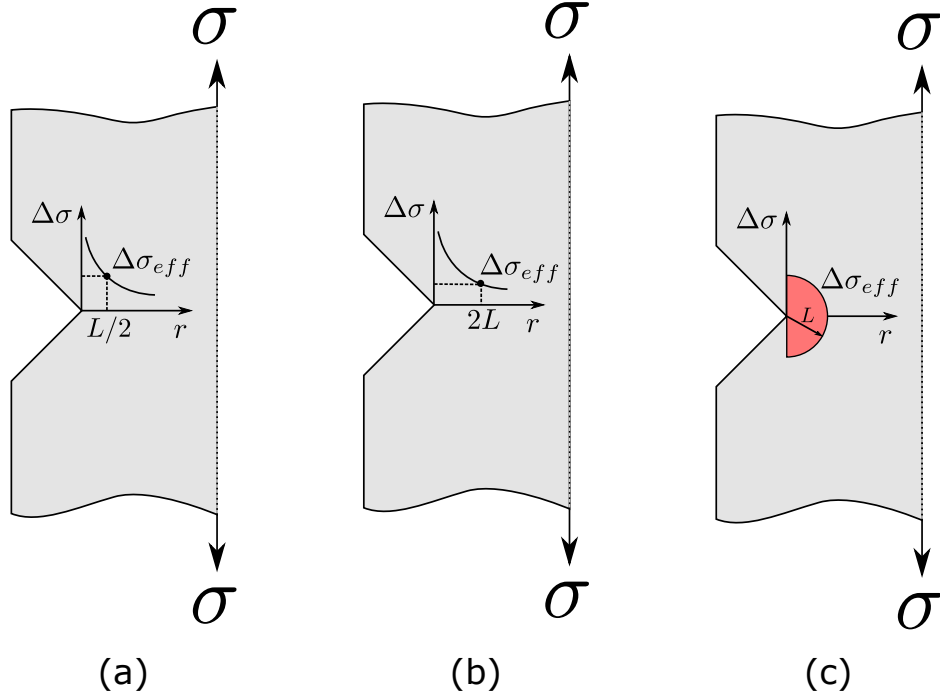


Figure 2.11: Schematic representation of the Theory of Critical Distances: (a) Point Method, (b) Line Method, and (c) Area Method.

will be quickly described, the so-called asymptotic and short crack arrest methods. In the former, the stresses distributions are calculated by means of an asymptotic analysis. For instance, assuming the cylinder-on-flat geometry case (incomplete contact) at the edge of the contact, the normal distribution falls to zero and  $p(x) \propto \sqrt{r}$ . Further, considering the peak pressure  $p_0$  (Eq. 2.12) and the contact semi-size  $a$  (Eq. 2.13), the pressure distribution  $p(x)$  (Eq. 2.11) can be assessed at the point  $x = -a$  by substituting  $r = x + a$ . In this way, the pressure distribution can now be written in a spatial form as follows:

$$p(r) = p_0 \sqrt{\frac{2}{a}} \sqrt{r} = K_N \sqrt{r} \quad (2.48)$$

where  $K_N$  is a constant which relays on the contact geometry and load. In this way, all stresses can be determined from the contact edge as consequence of the  $K_N$  constant and the distance  $r$ . The one can observe a strong correspondence between this approach and the use of the stress intensity factor, which characterize the stresses from the crack tip.

Further, including now a tangential force to the problem, the shear distribution  $q(x)$  (Eq. 2.23 applied into the slip-zones) can now be written in its asymptotic form as:

$$q(r) = \mu p_0 \sqrt{\frac{a}{2}} \frac{1}{\sqrt{r}} = K_T \frac{1}{\sqrt{r}} \quad (2.49)$$

where the  $K_T$  constant quantifies the severity of the tangential load. Thus, by means of this asymptotic approach, a life prediction approach can be formed based on the idea of the fretting fatigue tests may be conducted in laboratory with the same  $K_N$  and  $K_T$  as the real components.

Moreover, the so-called short crack arrest method [Araújo and Nowell \(1999\)](#) relays on the assumption that the stresses are so severe in the fretting fatigue case that a crack will always nucleate at the hot-spot (usually defined at the trailing edge of the contact). However, as fast stress gradient is observed in the fretting fatigue problem, the main question is: Will the stresses at the crack tip be strong enough to surpass the crack threshold limit propagating the fretting crack up to the component total failure? This is the main idea behind the short crack arrest method. Keeping the hypothesis that a crack will always nucleate, the three possible conditions of crack propagation are illustrated in Figure 2.12. In such a figure, the solid black line represents the modified  $K$ - $T$  diagram. Any crack plotted above this threshold means that it is a propagating one. In contrast, if a crack is plotted below the threshold, it is an arrested one. The curves A, B, and C represent a continually propagating crack, the boundary condition between propagating and arrested, and one that is initially propagating but will arrest, respectively. In this way, the application of the short crack arrest method consist in determining the stress intensity factor range  $\Delta K$  for the crack length  $l_0$ , also known as El-Haddad crack length. If  $\Delta K(l_0) > \Delta K_0$ , the crack will propagate, where  $\Delta K_0$  is the long crack threshold. On the other hand, if  $\Delta K(l_0) < \Delta K_0$ , the crack will arrest.

More details about these methodologies and further information covering the fretting fatigue topic can be found in the work ([Araújo et al., 2022](#)).

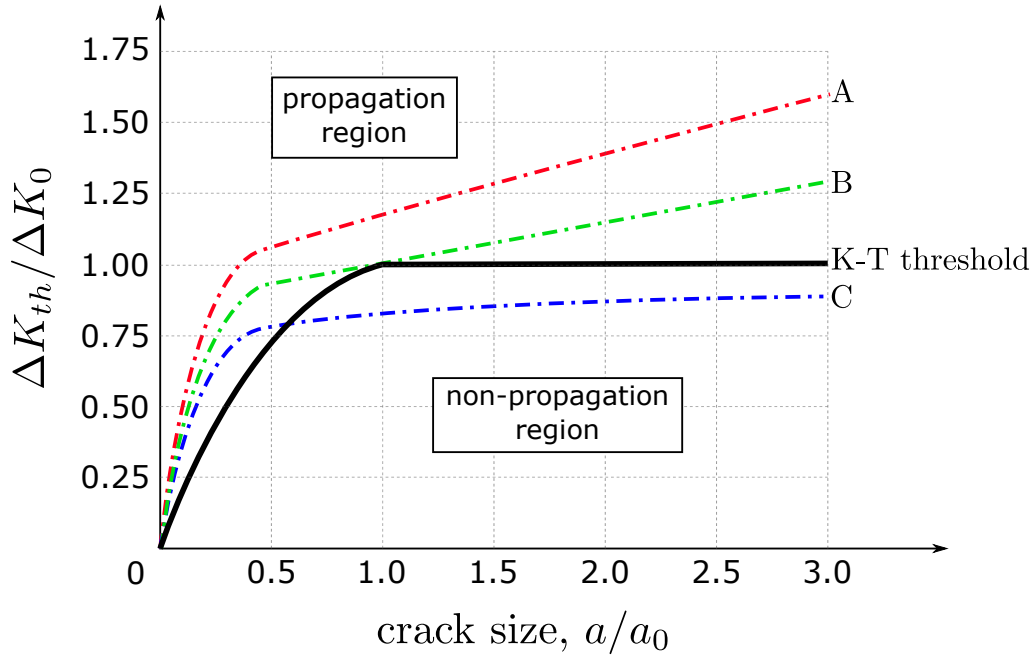


Figure 2.12: Crack growth curves in the modified K-T diagram.

#### 2.4 . Wear evaluation on fretting fatigue

Considering the fretting problem, the sliding regime is usually divided into three categories: (i) partial slip regime, when the contacting forces (normal and tangential) do not violate the Coulomb's law ( $Q < \mu P$ ), where  $P$  and  $Q$  are respectively the normal and tangential forces, and  $\mu$  is the friction coefficient. If this condition is respected and assuming an Hertzian contact, two distinct zones are formed on the fretting scar due to the parabolic shape of the contacting pressure, the so-called stick and slip zones. In this regime, small slip amplitudes are observed; (ii) gross slip regime, when the frictional force becomes equal to the tangential force ( $Q = \mu P$ ), complete motion is experienced among the contacting surfaces. In this way, as total slipping is observed along all fretting contact, the fretting scar is composed only by the slip zone; (iii) mixed slip regime, an intermediate regime among the partial and gross slip regimes, which one presents characteristics of both regimes. Besides wear is an effect intrinsic to the fretting problem and it is directly associated to surface damage and crack nucleation, most of fretting models do not include wear effects in its formulation.

In an attempt to develop a more robust fretting model, authors have been taking into account the wear effect in their simulations (McColl et al., 2004; Ding et al., 2004; Madge et al., 2007b,a; Garcin et al., 2015; Cardoso et al., 2019; Pinto et al., 2020). The material removal in the simulations is commonly governed by a local formulation of the Archad's equation (McColl et al., 2004; Ding et al., 2004) or the dissipated friction energy (Fouvry et al., 2003; Doca and Pires, 2017). The global formulation of Archard's approach can be expressed as:

$$\frac{V}{S} = K \frac{P}{H} \quad (2.50)$$

where  $V$ ,  $S$ ,  $K$ ,  $P$ , and  $H$  are the total wear volume, the total relative slip distance, the wear coefficient, the normal contact load and the material hardness, respectively. Considering an infinitesimal area, Equation 2.50 can be written as:

$$dh = \kappa p ds \quad (2.51)$$

where  $p$  is contact pressure,  $\kappa$  is the local coefficient of wear, and  $dh$  and  $ds$  are, respectively, the increment of material remove depth and relative slip.

In contrast, the friction energy wear approach relates the total wear volume to the accumulated friction energy, which one was dissipated on the contact interface. The global formulation of this approach can be expressed as:

$$V = \alpha \sum E_d \quad (2.52)$$

where  $\alpha$  and  $E_d$  are the coefficient of energy wear and the dissipated energy in one cycle of fretting. Thus, the total friction energy accumulated is referred to the sum of the dissipated energy in each fretting cycle. Once more, considering an infinitesimal area, Equation 2.52 can be calculated as:

$$dh = \alpha q ds \quad (2.53)$$



where  $q$  is the shear traction.

## 2.5 . Summary

In this chapter, some aspects of two-dimensional contact mechanics are presented. The formulation of plane strain contact problems for normal contact between two elastically similar bodies is given. Further, different aspects of multiaxial fatigue and an approach to evaluate wear on fretting fatigue were presented. In this work, the definition of shear stress amplitude is given by the Maximum Rectangular Hull (MRH) Method ([Araújo et al., 2011](#)). Among other alternatives, this one was chosen due to the fact that the method is extremely fast to calculate, does not need to solve a non-trivial max-min problem as the MCC method does, its implementation does not require complex algorithms, and presents additional capabilities such as the clear distinguishing between proportional and non-proportional loading histories.

Further, among many multiaxial fatigue parameters available in the literature and different methodologies to incorporate stress-gradient effects into the fatigue problem, here, only the  $SWT$  criterion associated with the TCD method was chosen to estimate fretting fatigue life according to the following reasons. In a previous study, [Cardoso et al. \(2019\)](#) evaluated the use of the different multiaxial fatigue criteria in order to estimate fretting lives considering contact parts of the Ti-6Al-4V titanium alloy. They concluded that the non-local  $SWT$  criterion provided the most accurate results. Also, the fractography of the fractured surfaces of the fretting fatigue specimens (further presented in Chapter 4) indicates that the crack initiation was mode I dominated for the two materials under study (Ti-6Al-4V and Inconel 718). In this way, the  $SWT$  parameter is an appropriate choice for estimating fretting fatigue life, considering that the materials and test conditions resulted in fretting cracks initiating in material planes dominated by the maximum amplitude of normal stress.



# Chapter 3

## Design of the the four actuators and high temperature UnB Fretting Fatigue rig

*In this chapter, after reviewing fretting rigs capable of performing tests under high temperatures, the fretting fatigue rig of the University of Brasilia (UnB) is presented. In the first moment, the previous version of the UnB's fretting rig and its main advantages and drawbacks is described to the reader. After that, the design of the so-called new UnB's Four Actuators fretting Fatigue Rig is presented, as well as all upgrades that have been implemented in the heating, cooling, and contact normal load application systems. In addition, the experimental methodologies used to align the contacting parts and control the test temperature are described.*

### **3.1 . Review of high-temperature fretting fatigue rigs**

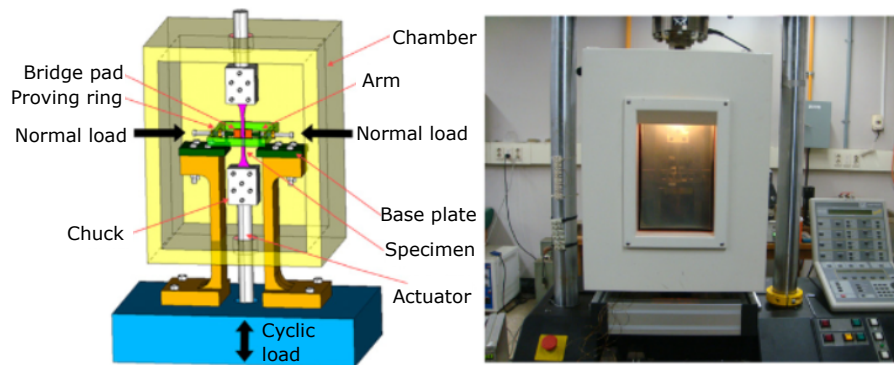
To conduct fretting tests it is required for any machine to be able to apply and monitor contact normal and the tangential loads (Matlik et al., 2006). Further, to perform a fretting fatigue test, an additional actuator is required to apply and control the fatigue load on the specimen. Testing assemblies in fretting fatigue require precisely imposing, controlling, and monitoring partial slip between the contacting parts. For such an application, there are no standard test rigs and to build it, there is a need for a stiff frame and high precision actuators and sensors to precisely control loads and

displacements. Moreover, tests under elevated temperatures implies more difficulties and resources invested in these experimental rigs. Because of this, it is very limited the number of fretting fatigue rigs capable of working at high temperatures around the world.

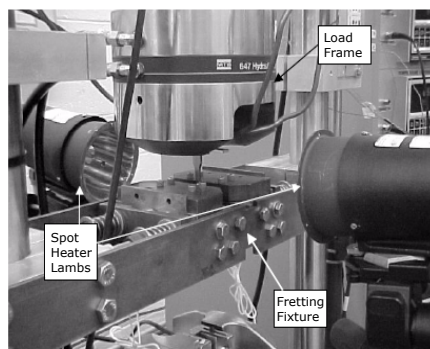
One of the most common fretting fatigue rig setups is with a single actuator applying the bulk load and any static mechanical system to clamp the pads against the specimen, such as static hydraulic actuators or loading screws, as seen in Fig. 3.1. In this case, the oscillatory tangential load,  $Q(t)$ , is coupled with the fatigue bulk load,  $B(t)$ . Upgrading this sort of experimental rig with a heating system, some fretting fatigue studies were conducted under high temperature using bridge pads ([Hamdy and Waterhouse, 1979b](#); [Mutoh et al., 1989](#); [Attia, 2000](#); [Zhang and Liu, 2009](#); [Hansson et al., 2000](#); [Kwon et al., 2010, 2011](#)), cylindrical pads ([Sahan, 2002](#); [Murthy et al., 2003](#)), and spherical pads ([Matlik et al., 2006](#)).

Besides the fatigue load actuator, some fretting fatigue machines have other actuators for independently applying the tangential or contact normal loads. In the works by [Fleury \(2015\)](#), and [Abbasi and Majzoubi \(2018a\)](#), the fretting fatigue rigs have an exclusive actuator for applying the contact normal load. Besides, these rigs have a furnace to heat the specimens. The main advantage of using a dedicated contact normal load actuator is to conduct tests with time varying contact normal loads,  $P(t)$ . However, the tangential load is coupled with the fatigue bulk one in the refereed fretting rigs. Photos and schematics of such test benches can be seen in Fig. 3.2.

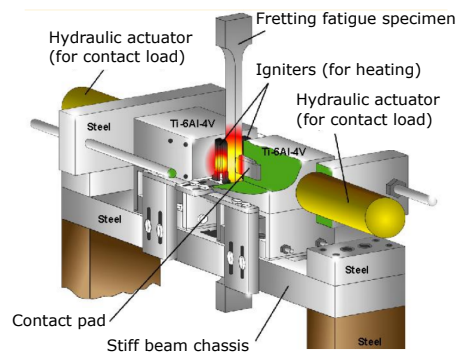
One disadvantage of using hydraulic actuators is the the relatively low testing frequencies. Then, to perform tests in the high or very high cycle fatigue regime, a single test can last for too much time, e.g., 10 million cycles at 10 Hz last about 12 days. To overcome this problem, some authors using other types of actuators, such as piezoelectric ones, developed high-frequency fretting fatigue rigs, some of them also equipped with heating systems. [Matlik et al. \(2006\)](#) upgraded the high-frequency fretting fatigue machine equipped with a piezoelectric actuator ([Matlik and Farris, 2003](#)) to work at



(a)



(b)



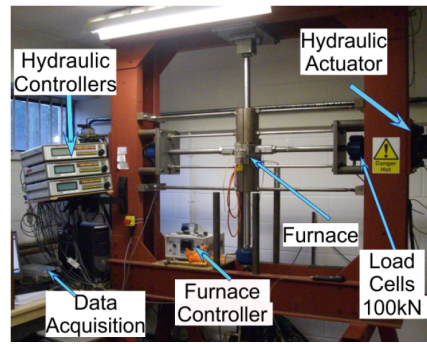
(c)

Figure 3.1: Schematics and photos of high-temperature fretting fatigue machines with a single actuator used by (a) [Kwon et al. \(2011\)](#), (b) [Sahan \(2002\)](#), and (c) [Murthy et al. \(2003\)](#).

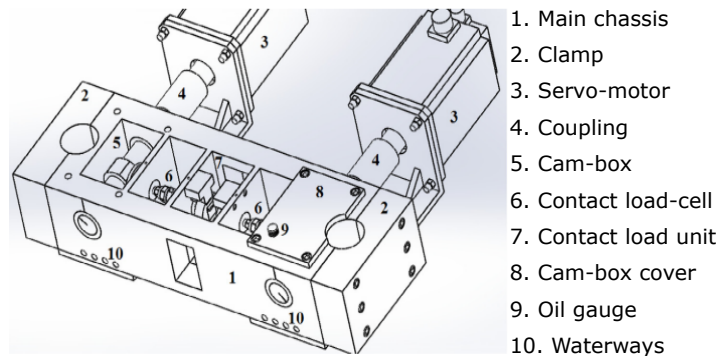
elevated temperatures and at even higher frequencies (up to 650°C and 600Hz). They conducted a series of experiments on Single Nickel Crystal (SNC). [Lavella et al. \(2013\)](#) built a high-precision, high-frequency fretting apparatus capable of working up to 1000°C by heat induction. [Zhai et al. \(2020\)](#) worked on an ultrasonic fretting fatigue test machine also heated by an electric induction furnace and evaluated the Nimonic 80A alloy at 600°C. Photos and schematics of high-frequency, high-temperature fretting rigs can be seen in Fig 3.3.

### 3.2 . Previous fretting fatigue rig of the University of Brasilia

Any fretting fatigue machine must be capable of applying normal, tangential, and fatigue bulk loads. Usually, these rigs have the tangential load coupled with the bulk



(a)



(b)

Figure 3.2: Schematics and photos of high-temperature fretting fatigue rigs with a dedicated contact normal load actuator used by (a) Fleury (2015), and by (b) Abbasi and Majzoubi (2018a).

fatigue one (Mutoh et al., 1989; Attia, 2000; Murthy et al., 2003; Ownby, 2008). In this kind of machine setup, the contact pads are placed in flexible beams that provoke tangential loads as a reaction to the fatigue bulk load application.

Since 2015 the fretting fatigue team of the University of Brasilia (UnB) had been working with a two independent vertical hydraulic actuators test rig. It was capable of applying independent time varying tangential and bulk fatigue loads, which could be in phase or out-of-phase, synchronous or asynchronous, while the normal contact load was applied by a static actuator (shown in Fig. 3.4). The actuator responsible for applying the tangential load, denominated the fretting actuator, had a limit of 100 kN of force, and the other, responsible for the fatigue load (thus called fatigue actuator), had a capacity of 250 kN. Although the fretting actuator had the capacity to apply tangential forces of relatively high magnitude, its load cell and the control software were specially

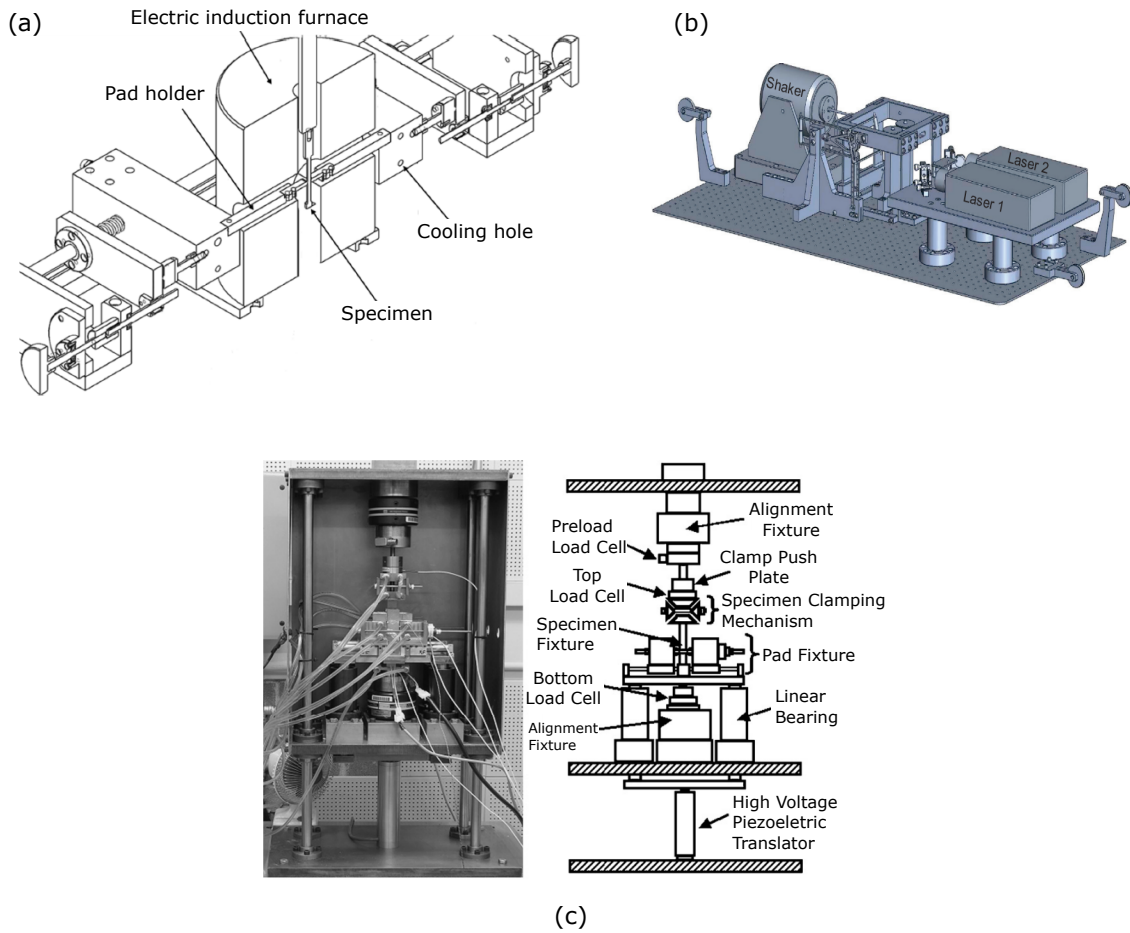


Figure 3.3: Schematics and photos of high-temperature fretting fatigue machines which operates at high-frequency used in works (a) [Zhai et al. \(2020\)](#), (b) [Lavella et al. \(2013\)](#), and (c) [Matlik et al. \(2006\)](#).

calibrated to work at a maximum of 10 kN to better control the tangential force even at lower levels. The monitoring and data acquisition systems were composed of two LVDT sensors, three load cells, and a robust MTS FlexTest 40 controller. A schematic view of the previous UnB'S Fretting Fatigue Machine with a detailed list of its components is shown in Fig. 3.5.

As previously mentioned, the normal contact load was applied by the manual Enerpac hydraulic system as shown in Fig. 3.6. This setup was composed of a manual hydraulic pump model P-39 (maximum capacity of 700 bars), a coupler ACBS-202, an accumulator ACL202 (maximum capacity of 350 bars), and a single acting hydraulic actuator RC-51 (maximum capacity of 700 bars; 640 mm<sup>2</sup> of effective piston area), all components



Figure 3.4: Previous version of the UnB's Fretting Fatigue Machine.

made by Enerpac. This Enerpac setup could apply a maximum normal contact load of 22.4 kN, limited by the pressure of the accumulator. The pressure was measured by means of a manometer placed on the coupler, and the force was converted using a simple relationship between the effective area of the hydraulic cylinder and the pressure measured.

The pad's carrier in this version of the UnB rig (Figure 3.7), was connected to the fretting actuator. A bearing was used as holder. It was also possible to work with



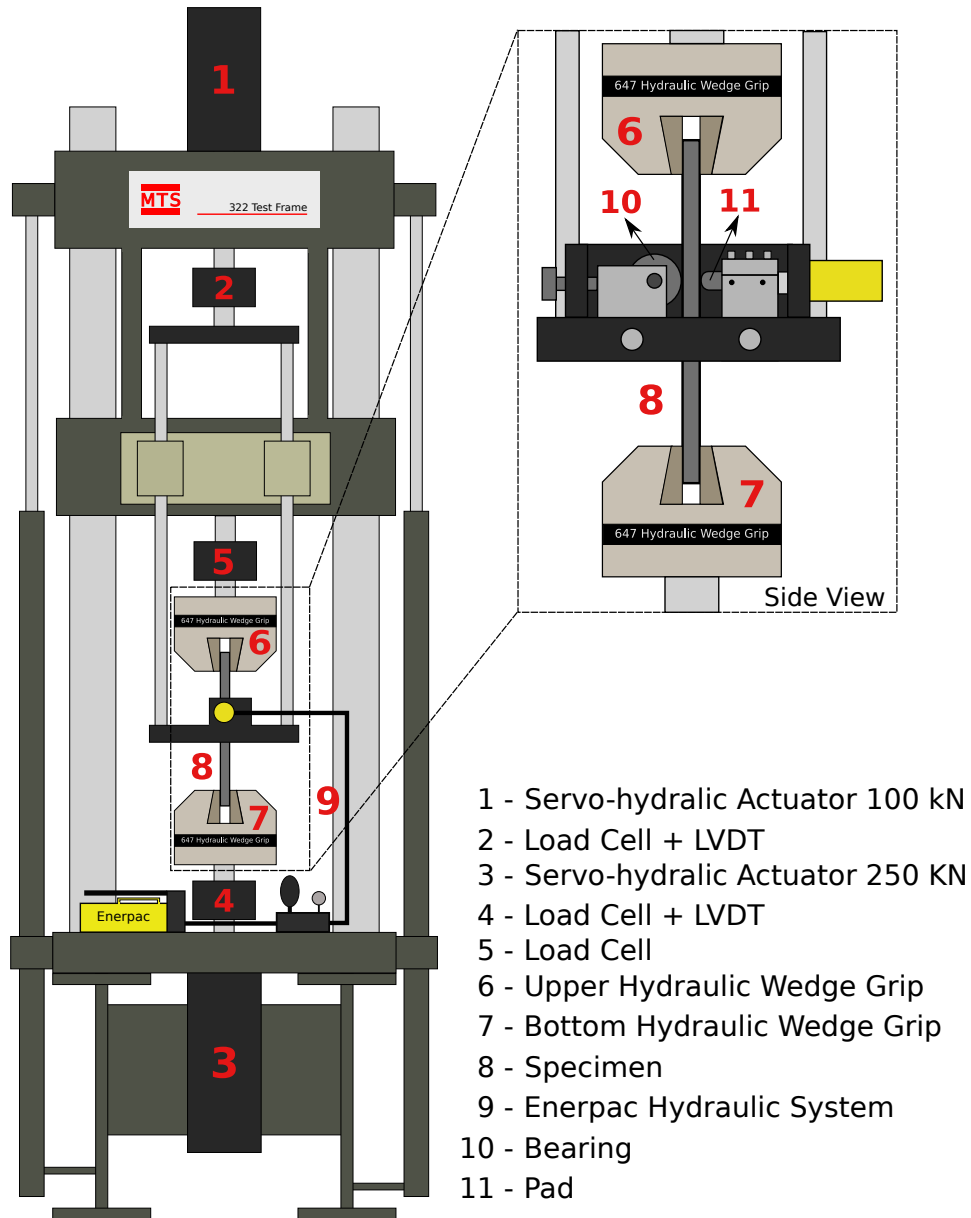


Figure 3.5: Schematic view and component list of the previous UnB's Fretting Fatigue Machine.

the pad-pad configuration instead of the pad-bearing configuration. To guarantee the alignment between the pad and specimen we used the side screws, and also a pressure sensitive film paper to verify the pressure field along the contact, as shown in Figure 3.8.

Many works have been conducted using this fretting fatigue machine (Ferry, 2017; Almeida, 2017; Gaillieue, 2018). Ferry (2017) studying the Ti-6Al-4V alloy, carried out a series of experiments focusing her analysis on the size effect in the fretting fatigue

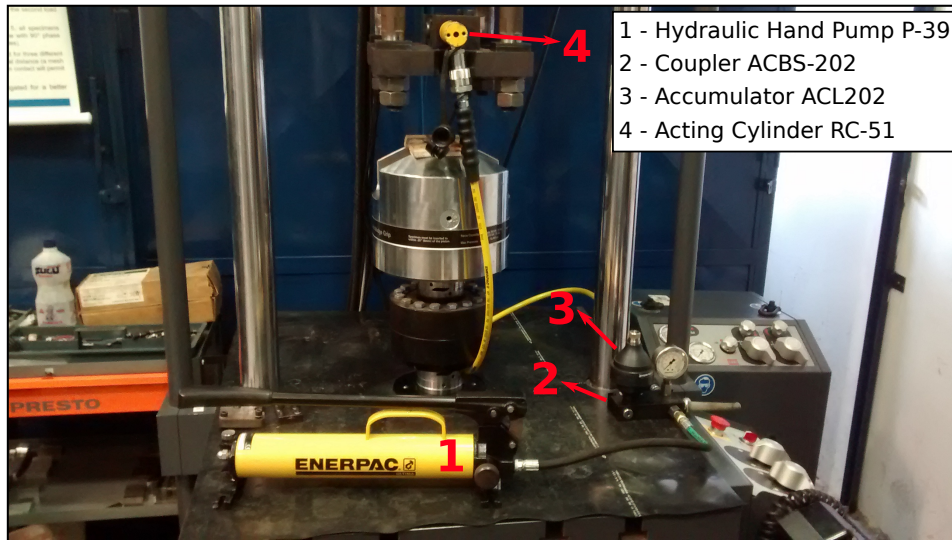


Figure 3.6: Enerpac hydraulic system.

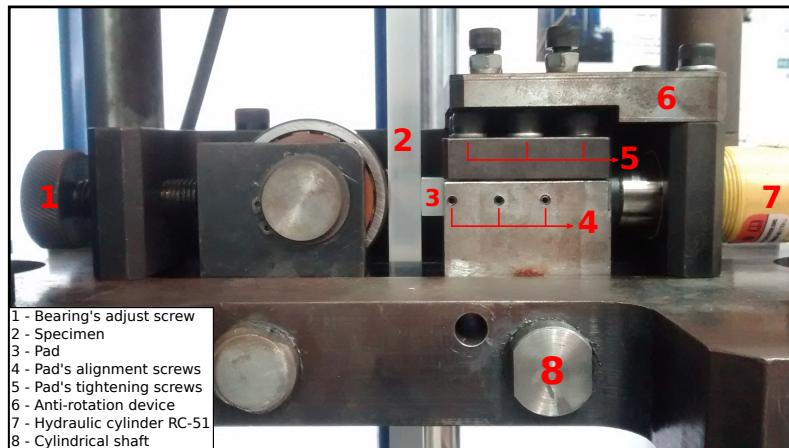


Figure 3.7: Photo with details of the pad's carrier in the previous version of the UnB fretting fatigue rig.

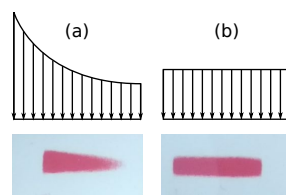


Figure 3.8: Schemes of pressure fields and alignment marks on the pressure paper of two cases: (a) misaligned and (b) aligned.

case. Almeida (2017) conducted an experimental campaign on the Al 7050-T7451 alloy where the influence of the tangential and mean bulk loads, as well as the pad radius, were assessed in order to check their influence on the crack initiation direction. Moreover,

Gaillieue (2018) investigated the effect of phase angle difference between the fretting and bulk fatigue loads on Al 7050-T7451 and ASTM 743 CA6NM alloys.

### 3.3 . New four actuators high-temperature fretting fatigue rig

One of the objectives of the present work is to modify the latest version of UnB's testing machine (presented in Section 3.2) so that it can perform tests with variable loads and under high temperatures. To overcome the limitations of the previous UnB's fretting rig, a completely new fretting apparatus was designed by the author. In Figure 3.9 one can see the new fretting apparatus assembled (without the hydraulic actuators).

Such a fretting device was specifically designed so that new normal load (capable of applying dynamic loads), heating, and cooling systems could be attached to it. These new systems (normal load application, heating, and cooling) were also developed in the scope of this thesis. Such upgrades implemented on the UnB's fretting fatigue rig are individually detailed in the following subsections. Moreover, the procedure to align the contact parts (pads and fretting specimen) and the methodology developed to measure the temperature at the contact will be described in the following subsections.

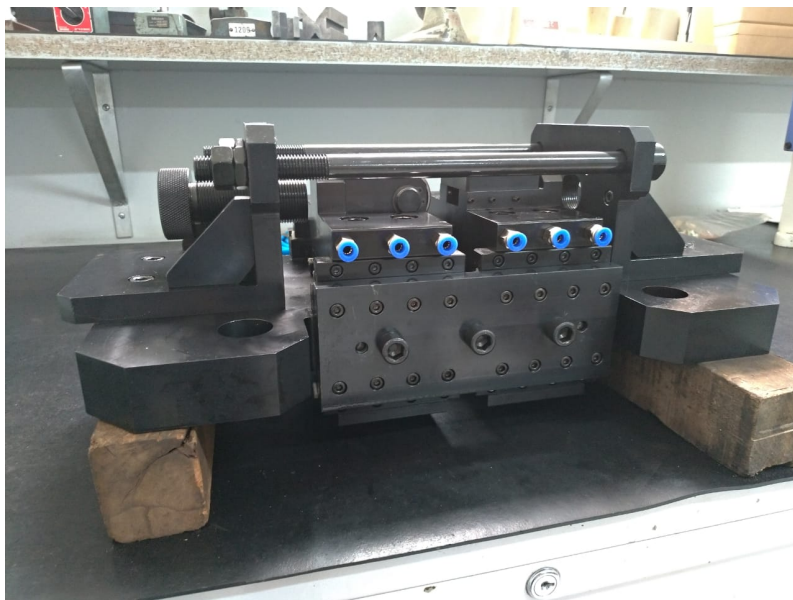


Figure 3.9: Photo of the new fretting apparatus (without the contact normal load actuators).

### 3.3.1 . Normal load application system

Under operating loading conditions the interface between disc and blade root experience a time varying contact normal load. Despite this being a boundary condition quite well known, there are few data or simulation work considering fretting fatigue where the contact normal load was varied. It is clearly a subject poorly evaluated ([Mohrbacher et al., 1995](#); [Majzoobi and Abbasi, 2017](#); [Abbasi and Majzoobi, 2017](#); [Gowda et al., 2014](#); [Mall et al., 2004](#); [Huq and Celis, 2002](#); [Fajdiga and Sraml, 2009](#)), and even less when combined with high temperature ([Abbasi and Majzoobi, 2018a](#)).

To tackle such a problem (capability to impose cyclic contact normal load) a new system for applying the contact normal load was developed. Figure 3.10 shows the 3D CAD model of the new fretting apparatus with the hydraulic actuators (1) responsible for applying the normal contact load. In this new normal load application system, the contact pads (12) are attached to the pad holders (6). Such holders travel guided on linear bearings (5), and they are connected through two pairs of pre-loading screws (10) to the support plates (11). The normal load application system was designed this way so that the pad holders could travel horizontally but not experience clearance in the vertical direction when the tangential fretting load was applied. In addition, as the set formed by the parts (6, 10 and 11) travel horizontally, oblong holes were purposely drilled on the main plate (2) in order to allow such movement.

The servo-hydraulic actuators (1) are placed perpendicularly to the fretting specimen and fixed on the main plate (2) by the brackets (3). The brackets (3) are connected by a pair of cylindrical bars (4) in order to increase the stiffness of the apparatus. The servo-hydraulic actuators chosen for equip this system are two MTS model 242.03. They are specially designed for high-velocity applications and can apply either cyclic forces up to 15 kN or cyclic displacements with 1 micron precision and up to 50 mm (measured or controlled by means of a LVDT), Fig. 3.11. With this new system, it is now possible to carry out experiments with static and cyclic normal contact loads, in or out-of-phase with the fatigue bulk and the tangential loads. Furthermore, all loads or displacements

applied or monitored during the test are controlled by a MTS FlexTest 60 controller.

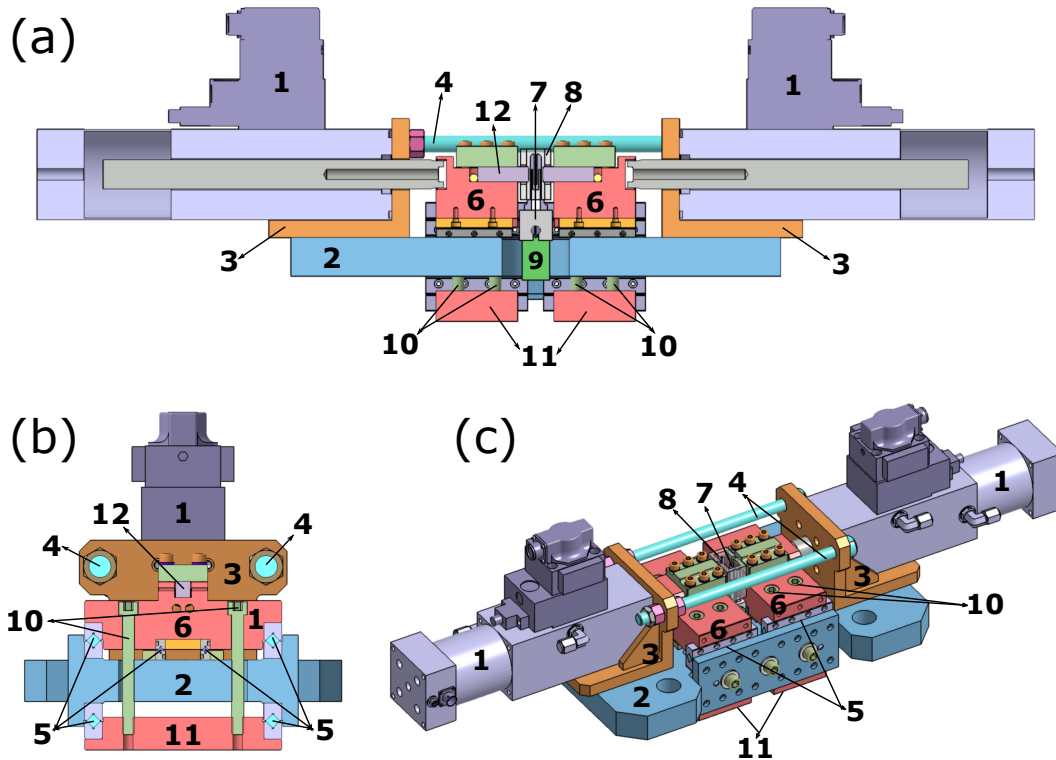


Figure 3.10: Drawings of the UnB's fretting apparatus: (a) Side cut view; (b) Transverse cut view; (c) Isometric view. Numbering caption: 1 - MTS servo hydraulic actuators; 2 - apparatus main plate; 3 - actuator bracket; 4 - stiffness bars; 5 - linear bearings; 6 - pad holder; 7 - igniter; 8 - ceramic casing; 9 - igniter support; 10 - pre-loading screws; 11 - bracket plates; 12 - pad.

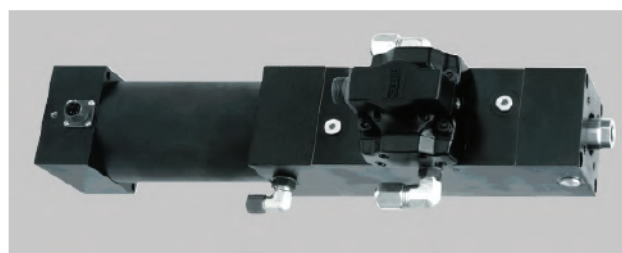


Figure 3.11: MTS Hydraulic actuator model 242.03.

### 3.3.2 . Heating system

Several solutions were considered to carry out the heating of the contact parts. For instance, by using a furnace system, heating cartridges, induction heating system, or heat by electrical resistors. The furnace system has the main advantage of heating the

internal region more homogeneous and controlled way. Besides, the heat loss is very low. However, as the space on the fretting apparatus is very restricted, such an application was not feasible. The use of heating cartridges has the main advantage of being compact. However, such a solution was also discarded as it excessively disturbs the heat flow induced by friction in the contact, as reported by [Chassaing \(2015\)](#). The induction heating system would also face great difficulties in accommodating its induction coils due to the lack of space in the apparatus and the geometric complexity of the fretting apparatus parts. Furthermore, the cost of the induction heating system is elevated, and it is applicable only for limited materials.

In this way, the solution by electrical resistors was adopted to heat the parts in contact. Two ceramic igniters were placed on the laterals of the contacting parts to heat them in a more homogeneous way. This heating solution presents the advantages of not excessively perturbing the heat flow induced by friction work. Besides, it is compact, easy to control, and it is not expensive in case of replacement. Others authors also adopted this kind of solution and were successful in heating the system up to 650°C ([Murthy et al., 2003](#); [Matlik et al., 2006](#); [Ownby, 2008](#)).

The heating system is composed by two Norton 271W ceramic igniters, a dedicated temperature controller, a thermocouple K-type (-270°C to 1260°C), and a pair of ceramic enclosure parts. Figure 3.12 shows in details how the ceramic igniters were attached on the new fretting apparatus. Preliminary tests were carried out to adapt this heating solution in the new fretting apparatus. In a first attempt to heat the contact parts, the two ceramic igniters were placed closest to the Ti-6Al-4V specimen without any enclosure, as shown in Fig. 3.13. As the main result, the highest measured temperature in the contact region was 660°C after almost 30 minutes of heating. To avoid heat loss and improve the performance of the heating system, a ceramic enclosure was designed specifically for this heating system, as depicted in detail in Fig. 3.14. With the ceramic enclosure attached on the heating system, it was possible to reach temperatures up to 750°C in the contact region in a shorter heating time.

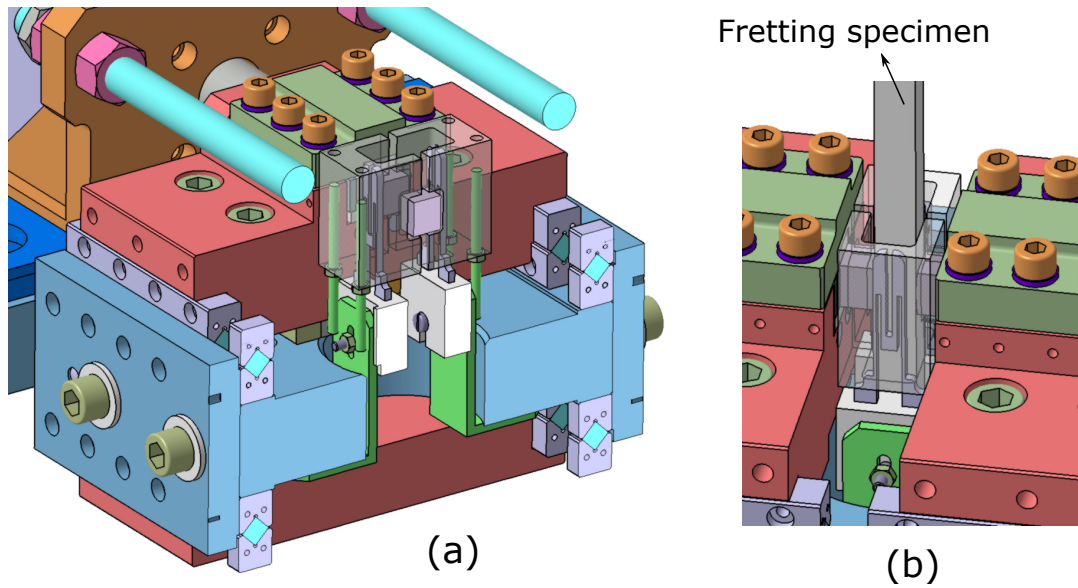


Figure 3.12: Cut view of the fretting apparatus detailing the igniters and its supports, and ceramic enclosure: (a) view without specimen and (b) view with the fretting specimen.

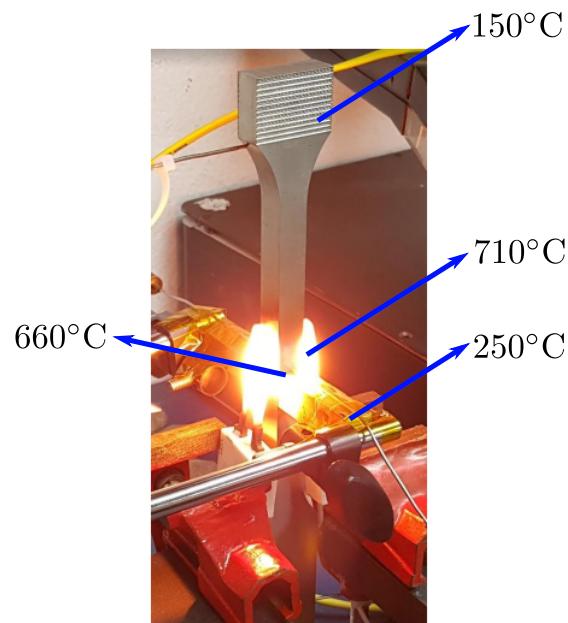


Figure 3.13: Photo with details of the the heating system during an exploratory test.

The control of the heating system is done by a dedicated temperature controller designed by Lynx Technology (Fig. 3.15). In the temperature tests, the maximum temperature reached was 780°C. The stability of the system was also evaluated. For that, a target temperature of 700°C was set. It was monitored by a thermocouple placed

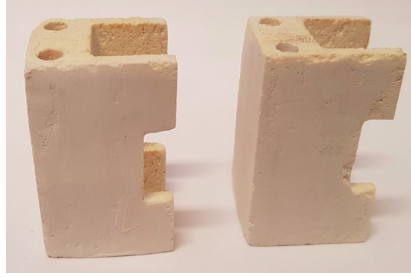


Figure 3.14: Ceramic enclosure parts.

near to the contact zone. The target temperature was reached in a couple minutes. After that, the system was observed for a couple of hours to check its stability. The maximum temperature error observed was about  $\pm 1^{\circ}\text{C}$  (at the controller). Also, the temperature was monitored at the lower and upper grips of the machine to check they were under the limits specified by the manufacturers ( $180^{\circ}\text{C}$ ).



Figure 3.15: Lynx Technology Temperature Controller in operation.

### 3.3.3 . Cooling system

To keep the integrity of all parts of the experimental rig, the fretting apparatus is also equipped with a water cooling system and special high temperature MTS wedges, as seen in Figure 3.16. The pad holders were designed with internal ducts where cool water removes the conducted heat from the contacting parts, keeping the structural integrity and avoiding thermal expansion of the remaining parts of the fretting apparatus and hydraulic actuators.



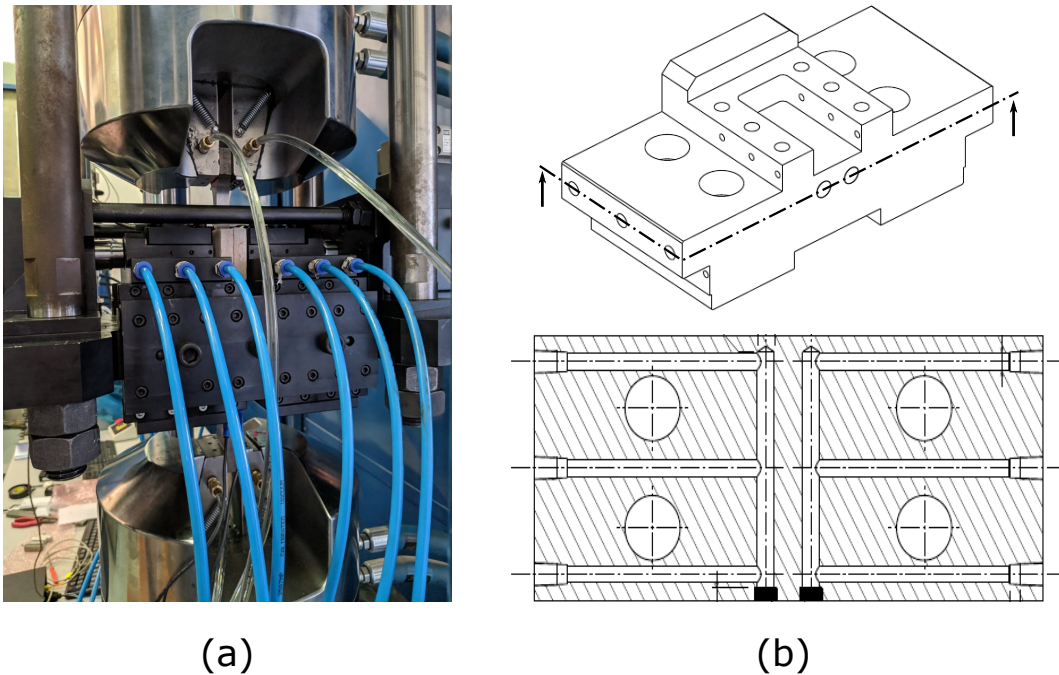


Figure 3.16: Cooling system of the fretting rig: (a) Photo and (b) Isometric and cut view of the pad holder.

### 3.3.4 . Alignment procedure between the contacting parts

The alignment between the contacting parts is a crucial step for conducting fretting fatigue tests. A uniform pressure field is desired along the contact, so the pad and the specimen must be geometrically perpendicular to each other. In addition, the geometry and surface finishing of the contacting parts also play an essential role. Therefore, they have to be precisely machined and polished to obtain a correct alignment between those parts. In this work, one performed the alignment between the cylindrical pad and the flat fretting specimen by employing a pressure-sensitive paper technique. Other authors have already used such a technique, proving itself to be efficient ([Martins et al., 2008](#); [Bellecave, 2015](#); [Ferry, 2017](#); [Gaillieue, 2018](#); [Almeida et al., 2020](#)).

The first step of this process consists of a visual and tactile positioning of the pad into the pad holder. Then, a small value of pressure was imposed between the contact parts. After, the lateral alignment screws were tightened until they reached the pad surface. The top screws were slightly fastened, the contact pressure was released, and a first alignment test was performed with the pressure-sensitive film (Fuji Prescale Film

- Medium Pressure - Mono Sheet Type). If the printed mark indicated misalignment in the pressure field (Fig. 3.17(b)), the upper screws were loosed, the pad alignment was corrected by adjusting the lateral screws, and a new pressure mark was made. This process was repeated until a homogeneous mark was obtained on the pressure film, as shown in Fig. 3.17(a). At this time, the upper screws were tightened gradually and alternately (to avoid misalignment) until they were all fully tightened, and then another pressure mark was made. If the set remains aligned, the alignment process is over, otherwise all screws was loosened, and the procedure was restarted. Moreover, before starting the alignment, the pads and specimen were chemically degreased with alcohol. Figure 3.17 depicts the parts used in the alignment process. Figure 3.17 depicts the fundamental parts and their nomenclature used in the alignment process.

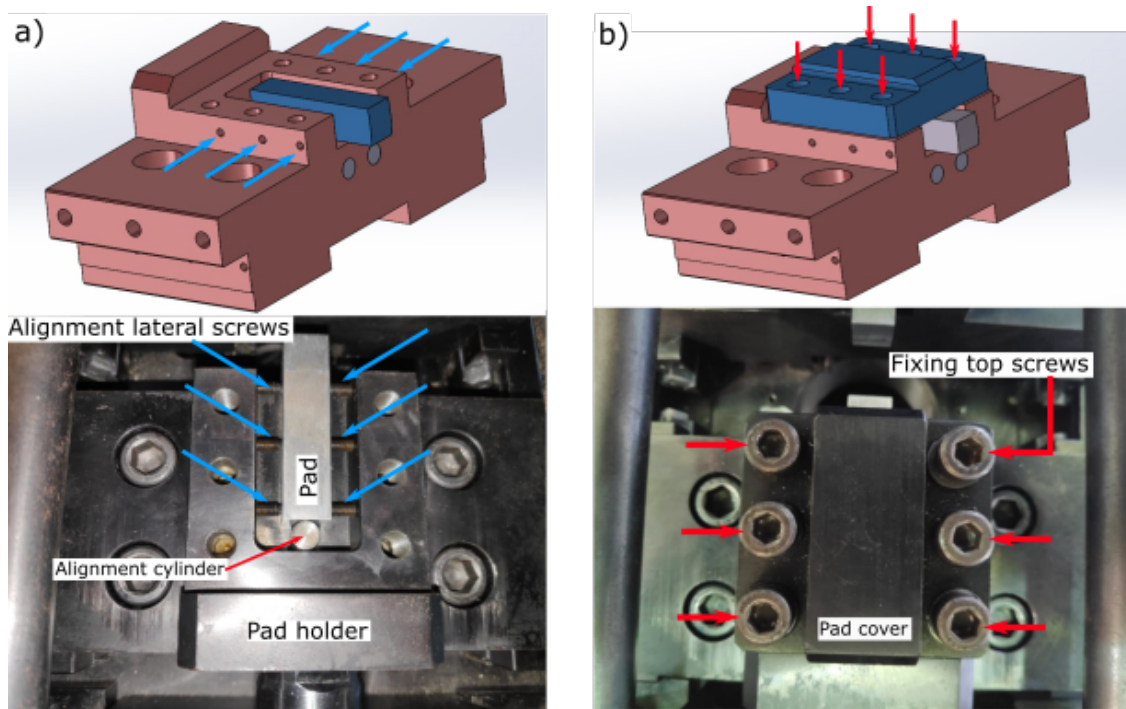


Figure 3.17: CAD drawing and photos of the pad holder and the cylindrical pad. a) Blue arrows indicate the lateral screws used to align the fretting pads, and b) red arrows indicate the top screws used for blocking any pad slip within the slot.

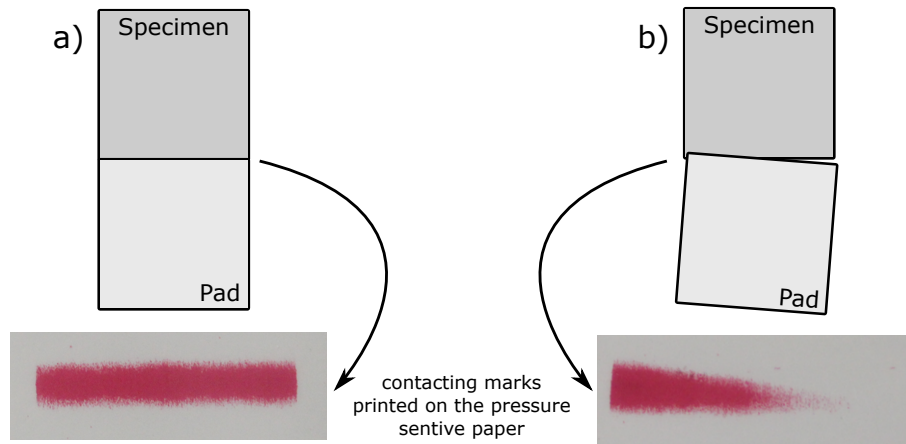


Figure 3.18: Schematic of the alignment between the cylindrical pad and the fretting specimen and photo of the contacting marks on the sensitive pressure paper for the a) aligned and b) misaligned cases.

### 3.3.5 . Temperature calibration

It is not a trivial task to measure the temperature at the contacting surface during a real fretting test. The main reason for this is because the contacting parts obviously block the way (contact zone). Also, welding or attaching any equipment, e.g., a thermocouple, could turn itself into a stress intensity factor and change the stress state of the evaluated fretting case. There are also further complexities in evaluating the temperature at the contact surfaces, for instance, the heat generated by the energy dissipation of the friction force. [Chassaing \(2015\)](#) conducted a study in order to develop a semi-analytical model capable of assessing the thermomechanical problem of the dry friction on Ti-6Al-4V parts.

To carry out the proposed high temperature fretting fatigue tests, an indirect technique of temperature measurement was adopted in this work. Preliminary tests were conducted to develop an equation that correlates the temperatures of the contact region and at a control point. For that, six shallow holes were drilled in an Inconel 718 dummy specimen in order to measure the temperature in a region where the contact would take place and at its vicinity, and another hole was drilled on the pad top surface to place the control thermocouple,  $T_c$ , as depicted in Figure 3.19. In such figure, the faded blue

area illustrates the local where the contact between the specimen and the pad would occur in a fretting test. Figure 3.20 shows the K-type thermocouple used to measure the temperature at the control point and the experimental mounting of the system.

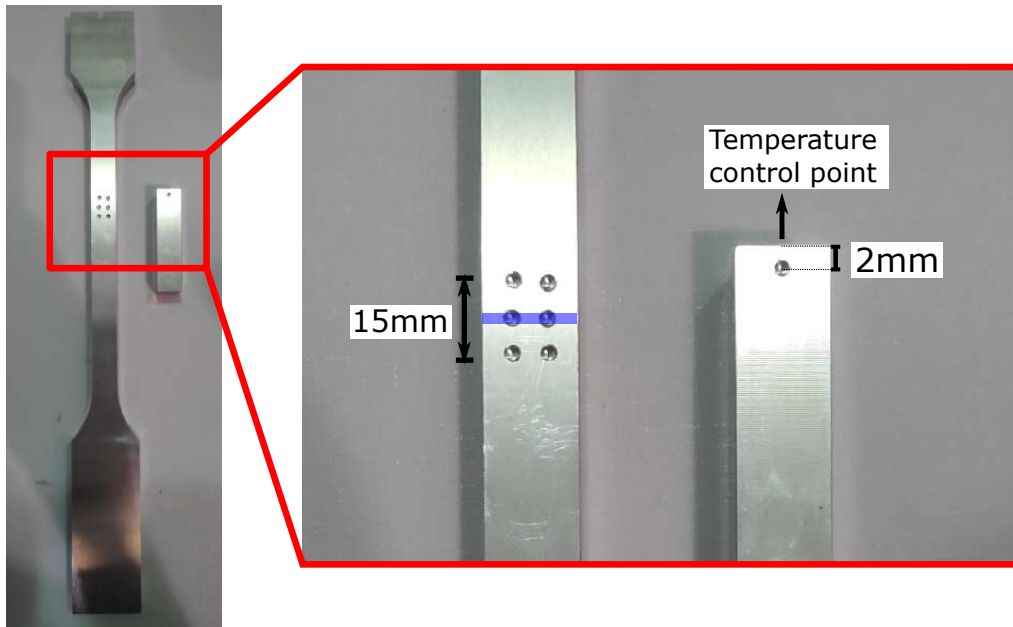


Figure 3.19: Fretting dummy specimen and contact pad with drilled holes where temperatures were measured. The faded blue rectangle illustrates the local where the contact would occur in a fretting test.

The methodology adopted to obtain the equation which correlates the temperature at the contact with the temperature at the control point is as follows: First, the contact parts were aligned, and the ceramic igniters were assembled on the fretting apparatus. Then, the thermocouples were placed at the control point and the dummy specimen. The control thermocouple is controlled and monitored directly by the Lynx temperature controller (Fig. 3.21). The specimen thermocouples (Fig. 3.22b) were connected to an external data acquisition system and monitored during the whole temperature calibration test. When the temperatures measured on the dummy specimen (within the 15mm long region) remained constant, the commanded temperature was increased. Then, the former step was repeated until the heating system reached its maximum capability. In Figures 3.23 and 3.24 one can see a photo of an temperature calibration test, and a graph of temperatures measured on the dummy specimen over time, respectively.

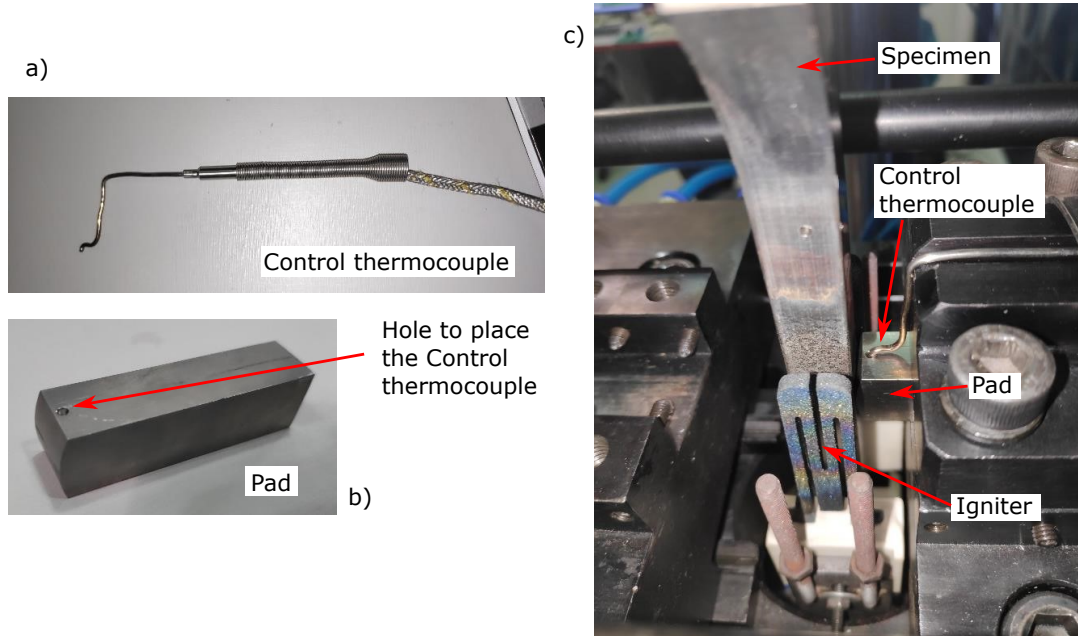


Figure 3.20: a) K-type thermocouple, b) contact pad with hole to place the control thermocouple, and c) experimental setup of the temperature tests.

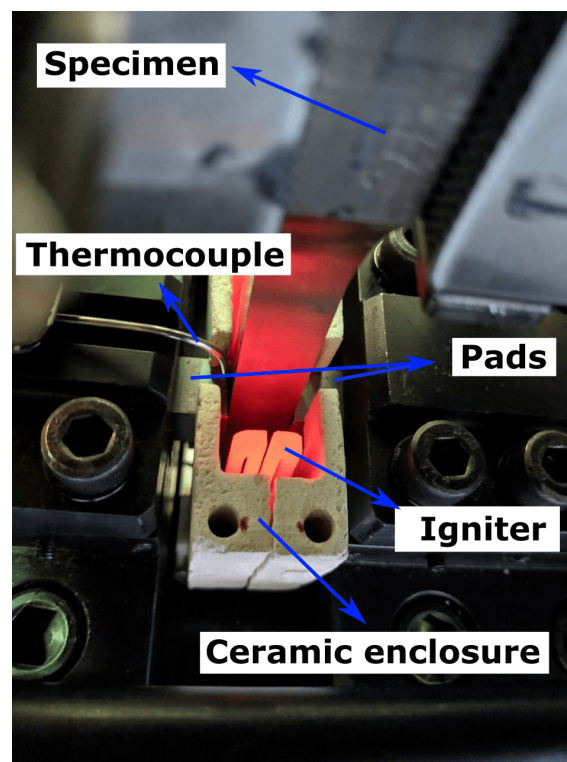


Figure 3.21: Heating system tested in a real fretting testing conditions.

It is essential to note that the measured temperature can vary significantly if the igniters and the control thermocouple are not being mounted in the exact location in all

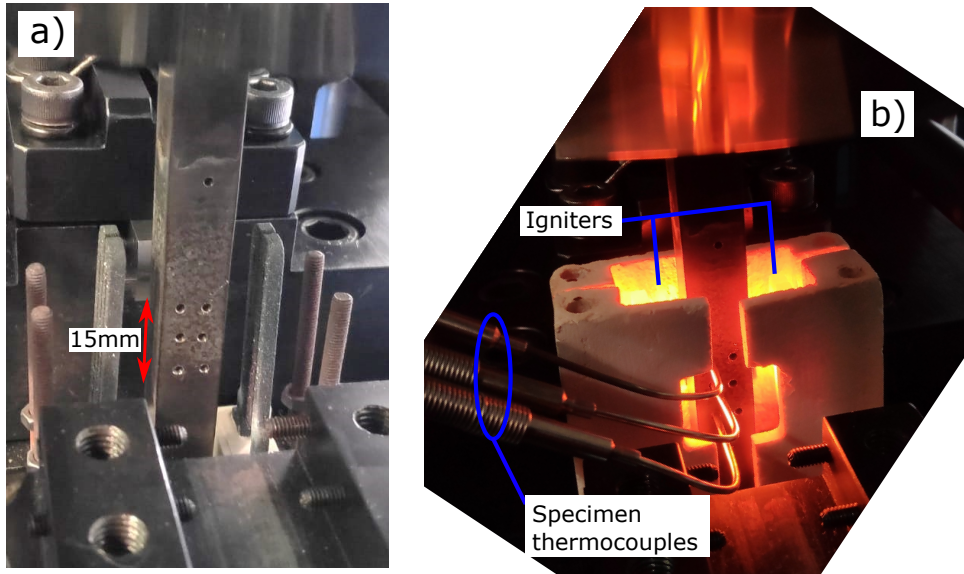


Figure 3.22: a) experimental setup of the temperature test, and b) running temperature test.

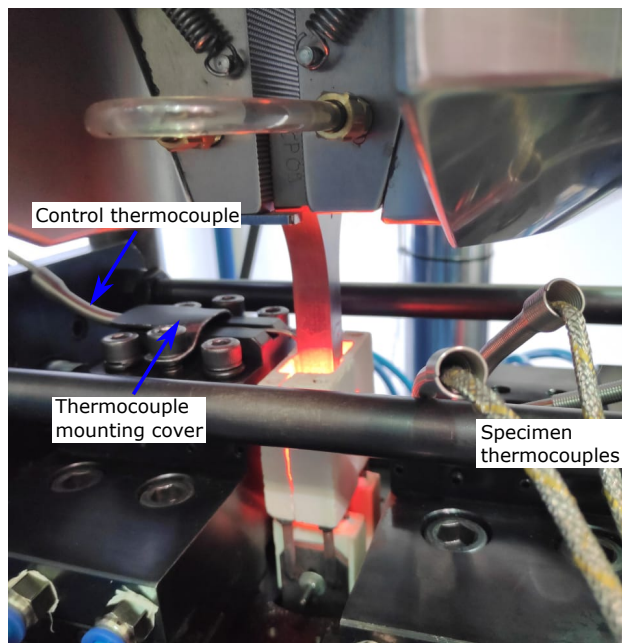


Figure 3.23: Complete view of the temperature test.

tests. To ensure that the holes in the pads have been drilled at the same position and with the same depth (2mm), the Vertical Machine Center model XH 7132 (Fig. 3.25) was used to perform this task. Besides that, the horizontal and vertical positions of each igniter in relation of the specimen were carefully measured by using a digital caliper before all tests. To drill the Inconel 718 pads, it was used the special tool Sandvik

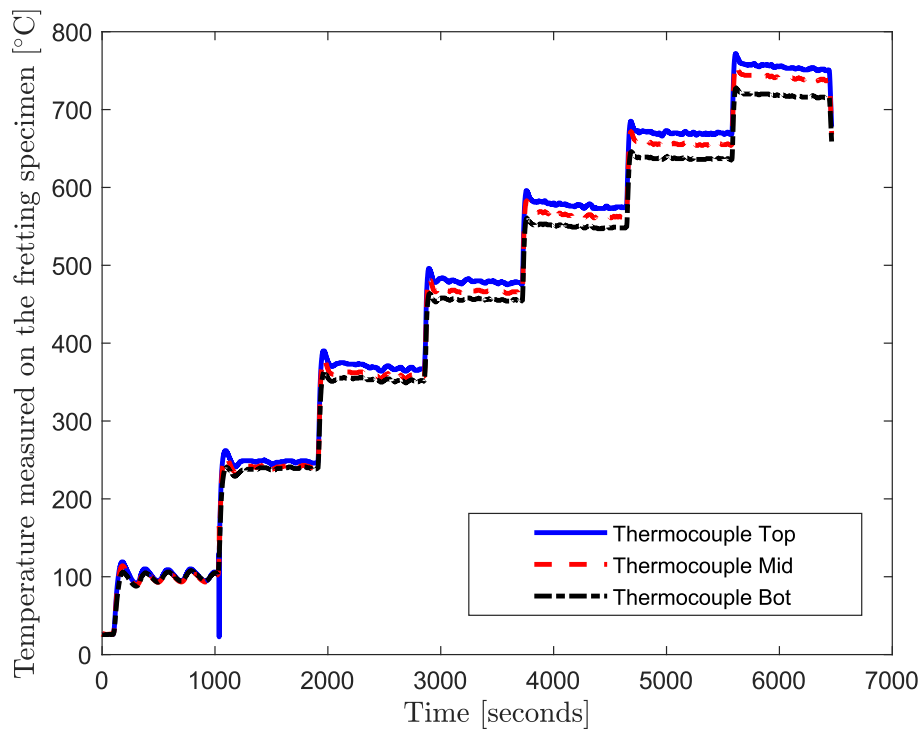


Figure 3.24: Temperature over time measured at different positions on the dummy specimen (along of the 15mm region).

CoroDrill 862-GM with 2mm diameter.



Figure 3.25: Photo of the XH7132 Vertical Machine Center.

Following the test methodology just described, three tests were conducted. In each

of them, all temperatures were recorded, and their results were averaged into the ones reported in Table 3.1. Finally, using a quadratic regression, a function that correlates the commanded temperature ( $T_c$ ) and the average temperatures measured on the dummy fretting specimen for the Inconel 718 was defined as:

$$g(T_c) = -0.002T_c^2 + 1.55T_c - 9.1407 \quad (3.1)$$

where  $g(T_c)$  estimates the average temperature at the contact as a function of the temperature measured on the control point,  $T_c$ , as illustrated in Figure 3.26. By Equation 3.1, the contact will experience the the 540°C target temperature when the commanded one at the Lynx controller was equal to 373°C. A temperature error of  $\pm 10^\circ\text{C}$  is expected in the contact temperature estimation.

Table 3.1: Average temperatures measured from three temperature calibration tests.

Command Temp. [ $^\circ\text{C}$ ]	$T_{top}$ [ $^\circ\text{C}$ ]	$T_{mid}$ [ $^\circ\text{C}$ ]	$T_{bot}$ [ $^\circ\text{C}$ ]	Avg. Temp. on the dummy specimen [ $^\circ\text{C}$ ]
50	66	70	69	68 $\pm$ 2
100	138	142	146	142 $\pm$ 4
150	219	225	220	221 $\pm$ 3
200	287	300	302	296 $\pm$ 8
250	352	377	358	362 $\pm$ 13
300	431	452	441	441 $\pm$ 11
350	505	524	514	514 $\pm$ 10
375	537	558	540	545 $\pm$ 11
400	571	591	583	582 $\pm$ 10
425	608	631	616	618 $\pm$ 12



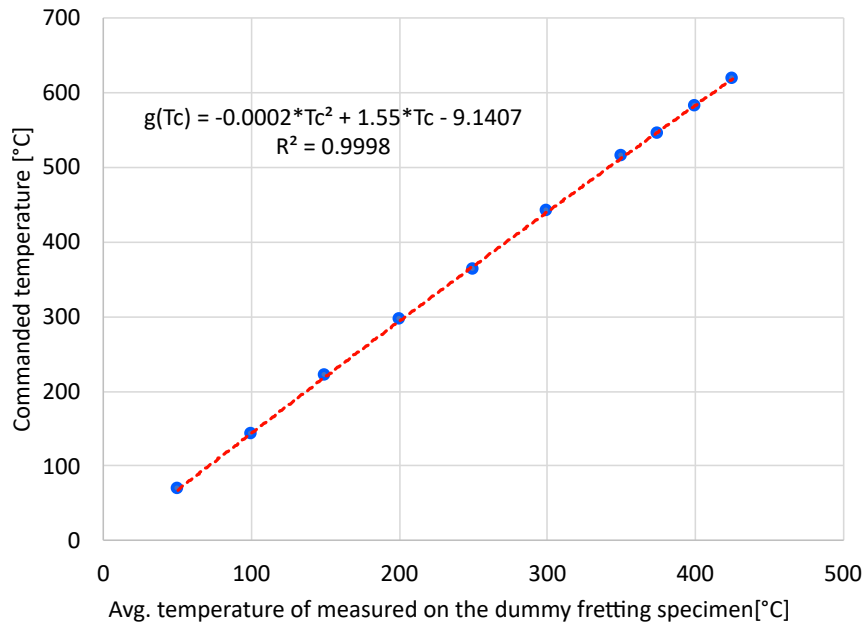


Figure 3.26: Correlation between the temperature measured at the control point by the control thermocouple ( $T_c$ ) and the average temperature measured on the dummy fretting specimen.

### 3.4 . Summary

One of the main objectives of this thesis was to upgrade the previous version of the UnB's fretting fatigue rig (section 3.2) to work with cyclic normal load and high temperatures. The previous configuration of such a rig was already composed of two vertical actuators capable of independently applying fatigue bulk and tangential load. However, the normal contact load was applied only statically. Besides that, it would not be possible to attach and heating and a cooling system to it.

In this way, to reach the goals of this thesis, a new fretting apparatus was specially developed to overcome all limitations of the previous one. The new normal load application system, the heating, and cooling systems were designed and successfully tested. These systems were detailed in the subsections 3.3.1 to 3.3.3, respectively. Moreover, a methodology to align and measure the temperature was proposed and validated in this thesis scope (subsection 3.3.4 and 3.3.5, respectively). At the present moment, it can

be considered one of the most versatile fretting fatigue machines globally. It is capable of applying the contact normal loads up to 15kN, tangential loads up to 100kN, and fatigue bulk loadings up to 250kN, dynamically. Furthermore, all four MTS hydraulic actuators are uncoupled and controlled by a new MTS FlexTest 60 controller. Also, all these loads can be applied in-phase or out-of-phase, and tests can be carried out at temperatures up to 750°C. The Fretting Fatigue machine can be seen in Fig. 3.27 and its schematic view in Fig. 3.28. The forces, displacements, and temperature ranges of this experimental rig are reported in Table 3.2.

Table 3.2: Forces, displacements, and temperature ranges of the New UnB's four actuators high temperature fretting fatigue rig.

	Force range [kN]	Displacement range [mm]
Fatigue actuator	$\pm 250$	$\pm 80$
Fretting actuator	$\pm 100$	$\pm 75$
Contact normal load actuators	$\pm 15$	$\pm 25$
Testing temperature	up to 750 °C	

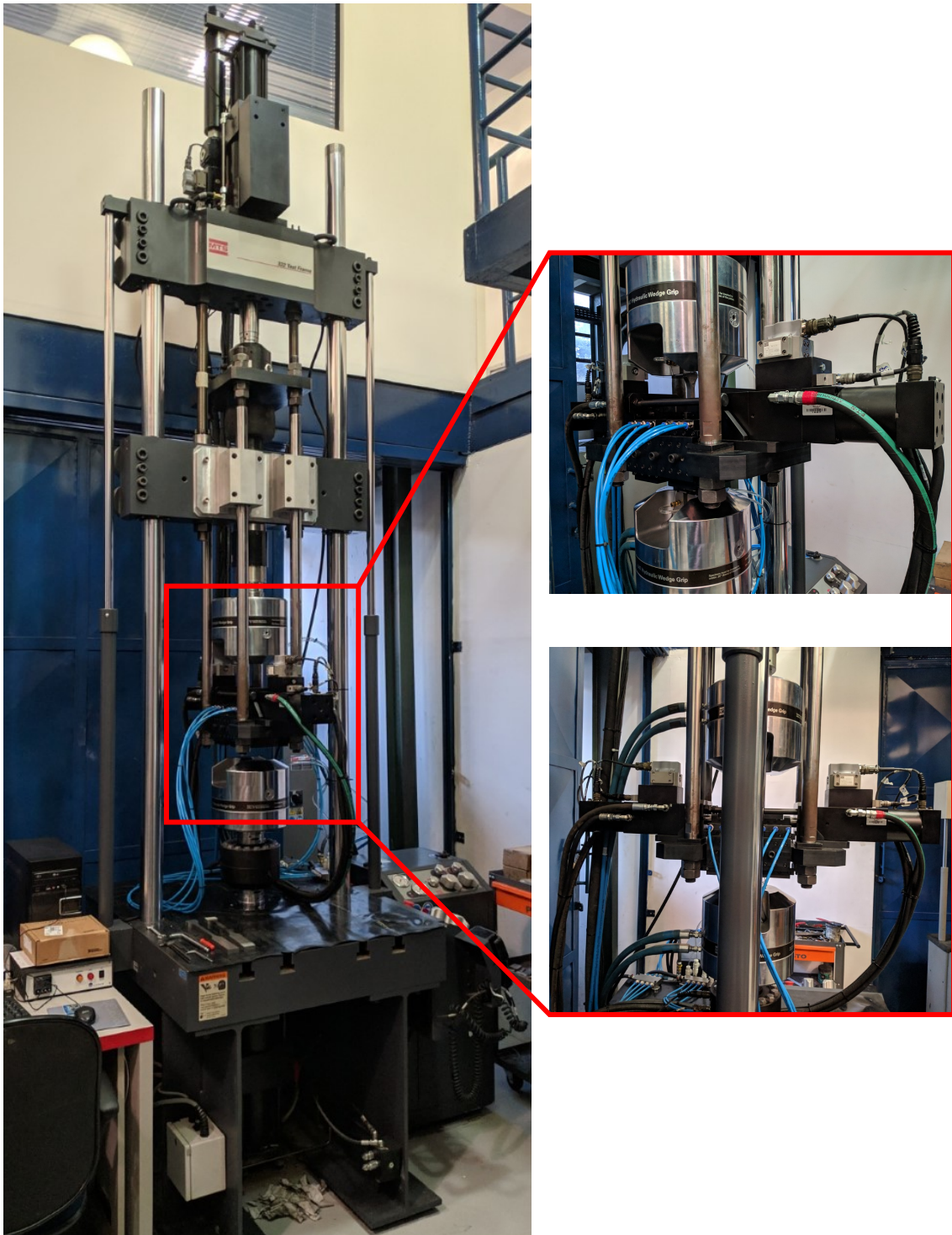


Figure 3.27: New Fretting Fatigue Machine of the University of Brasilia (UnB).

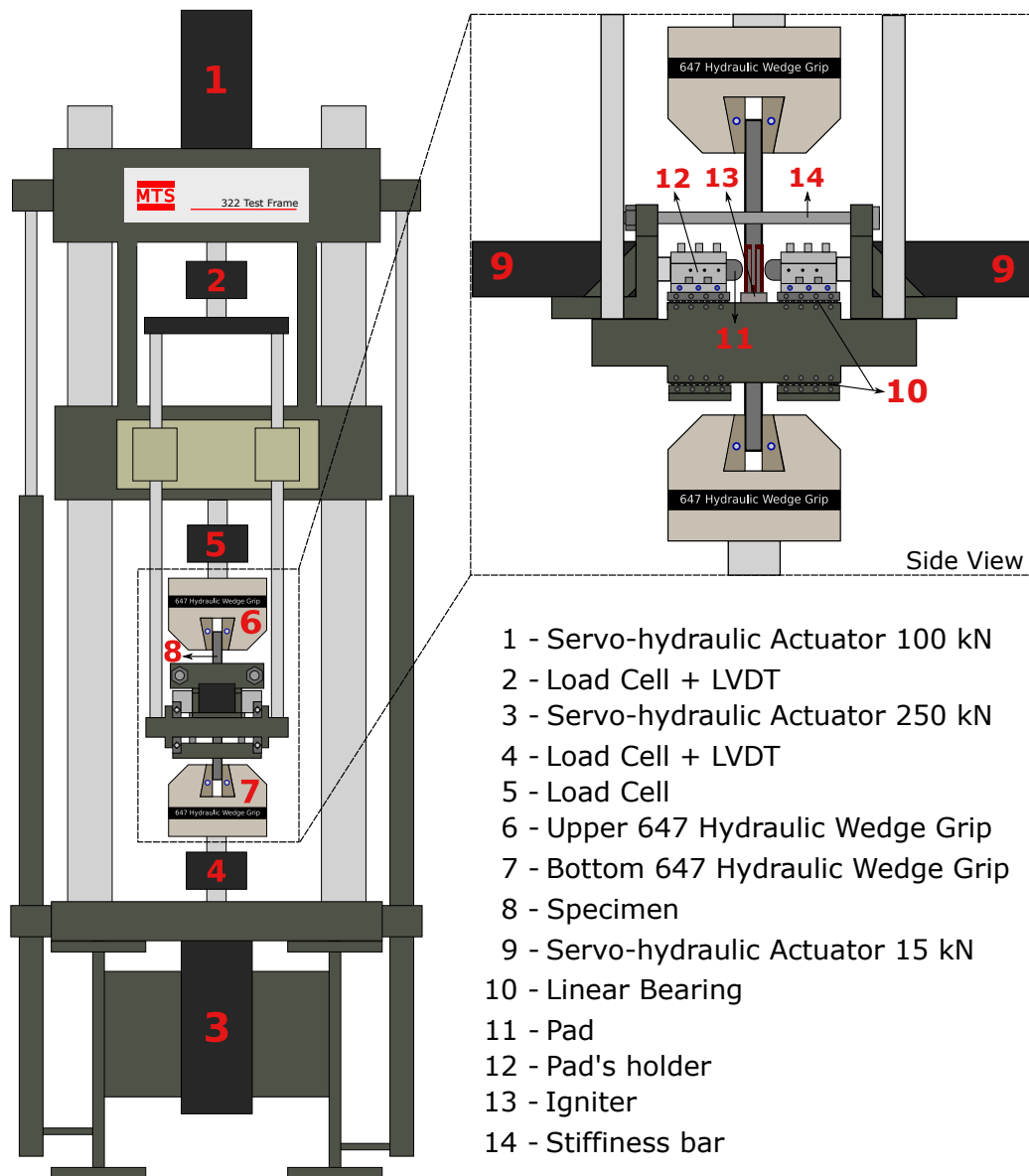


Figure 3.28: Schematic view and component list of the new Fretting Fatigue Machine of the University of Brasilia (UnB).

# Chapter 4

## Experimental methodology and results

*This chapter begins with a brief description of the materials under study, the titanium alloy Ti-6Al-4V, and the nickel alloy Inconel 718. The design of the specimens and pads used here is also described. However, the core of this chapter consists of the description of the experimental methods used to evaluate the influence of the cyclic contact normal load on the friction coefficient and on the fretting fatigue resistance. Moreover, specifically for the Inconel 718, further tests were carried out to evaluate the temperature effect.*

### 4.1 . Materials and specimens

#### 4.1.1 . Ti-6Al-4V

According to the Standard Specification ASTM [B861-19 \(2019\)](#), titanium and titanium alloys are classified into 34 grades. The Ti-6Al-4V alloy, also known as Ti6-4, TA6V, and titanium Grade 5, is the most used titanium alloy, corresponding with almost 50% of the titanium used commercially ([Meriaux, 2010](#)). The aeronautical sector has a significant interest in this specific alloy due to its attractive combination of high mechanical properties, lower mass density, and high corrosion resistance. Compared with a general steel alloy ( $7.84\text{g/cm}^3$ ), this titanium alloy is almost 44% lighter ( $4.42\text{g/cm}^3$ ).

In this alloy, the elements aluminum and vanadium are the most present ones, in addition to titanium itself. The aluminum, which generally represents 6% to 7% of the mass, is an  $\alpha$ -stabilizer. Such an element improves the mechanical strength and creep resistance, while the vanadium, a  $\beta$ -stabilizer that corresponds to around 4% of the mass, increases the ductility but decreases the oxidation resistance ([Combres, 1999](#)).

The properties of the Ti-6Al-4V are determined by the amount of alpha and beta phases present on the microstructure. The chemical composition of the Ti-6Al-4V alloy has been reported in Table 4.1.

Table 4.1: Main elements and chemical composition of the Ti-6Al-4V alloy (ASTM B861-19, 2019).

Element	Minimum [%]	Maximum [%]
Al	5.50	6.75
V	3.50	4.50
Fe	-	0.40
O	-	0.20
C	-	0.08
N	-	0.05
H	-	0.015

The thermo-mechanical treatment applied to the titanium alloy evaluated in this work results in a bimodal  $\alpha + \beta$  microstructure. This process will now be briefly described. In the beginning, the raw alloy ( $\beta$  domain) is forged specifically at 940°C. This specific forging temperature favors the size reduction of the  $\beta$  grains. After that, a hot isostatic pressing is applied, followed by quenching. Next, another treatment is applied to form  $\alpha_p$  grains and quenching to transform the beta phase into a metastable  $\alpha$ -phase. By the end, an annealing (around 700°C) is performed in order to induce the transformation of  $\alpha$ -phase into  $\alpha + \beta$  lamellar grains (secondary  $\alpha_s$  platelets in a  $\beta$ -matrix). The referred thermo-mechanical treatment is illustrated in Figure 4.1, as well as the photos of a typical bimodal microstructure of the Ti-6Al-4V alloy. Moreover, some basic material properties provided by Safran has been reported in Table 4.2.

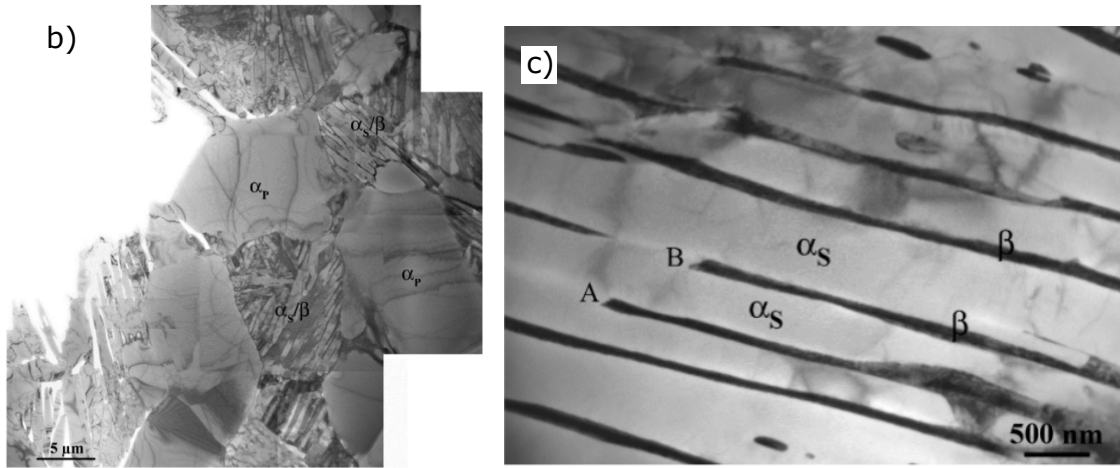
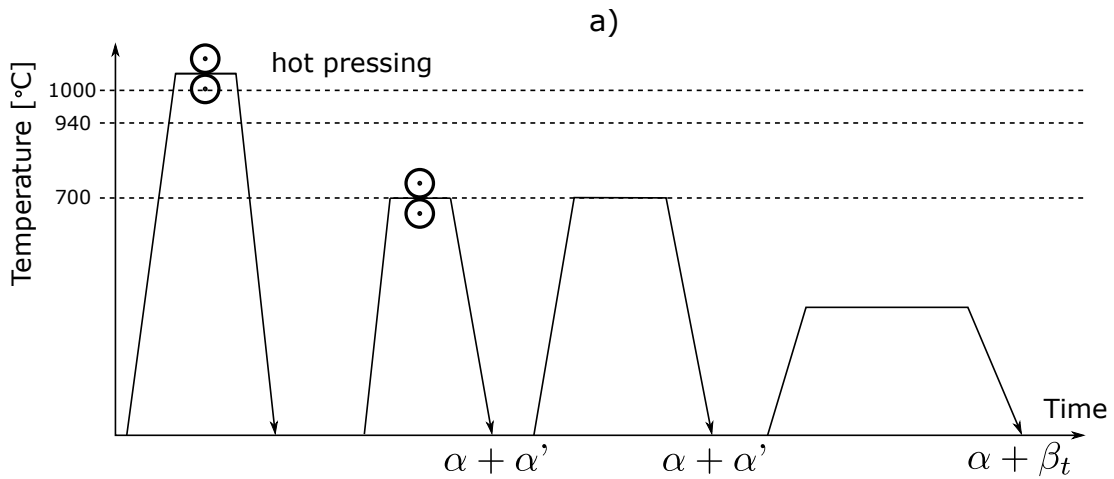


Figure 4.1: a) Thermo-mechanical treatment applied to the Ti-6Al-4V (Modified from (Bellecave, 2015)). b) Nodules  $\alpha_P$  and  $\alpha_S/\beta$  lamellar colonies c) Lamellar colony in detail (Castany, 2007).

Table 4.2: Basic mechanical and material properties of the Ti-6Al-4V alloy at room temperature (20°C).

Material	E [GPa]	$\mu$ [-]	$\sigma_{y=0.2}$ [MPa]	$\sigma_{ult}$ [MPa]
Ti-6Al-4V	120	0.29	940	1005

#### 4.1.2 . Inconel 718

Another material widely used by the aeronautic industry is the Inconel 718. This nickel-based superalloy presents interesting mechanical and material properties such as high strength, fatigue and corrosion resistance even under elevated temperatures. For this particular reason, this alloy is used to manufacture the components of aeroengines operating at medium and high temperatures, e.g. blades and disks of compressors. The Standard Specification ASTM B637-16 (2016) defines the composition limits of this alloy, whose values have been reported in Table 4.3.

A typical microstructure of the Inconel 718 is depicted in Figure 4.2 (Nascimento, 2022). In this figure, one can see carbide inclusions and fine particles of  $\delta$ -phase ( $\text{Ni}_3\text{Nb}$ ) distributed in the matrix. The average grain size for this alloy is  $10\ \mu\text{m}$  as stated by Belan (2015). The thermo-mechanical treatment used in this alloy was as follows: aged at  $720^\circ\text{C}$  for 8 h, aged at  $620^\circ\text{C}$  for another 8 h, and at the end, air-cooled. Moreover, some basic material properties provided by Safran have been reported in Table 4.4 at  $20^\circ\text{C}$  end at  $540^\circ\text{C}$ .

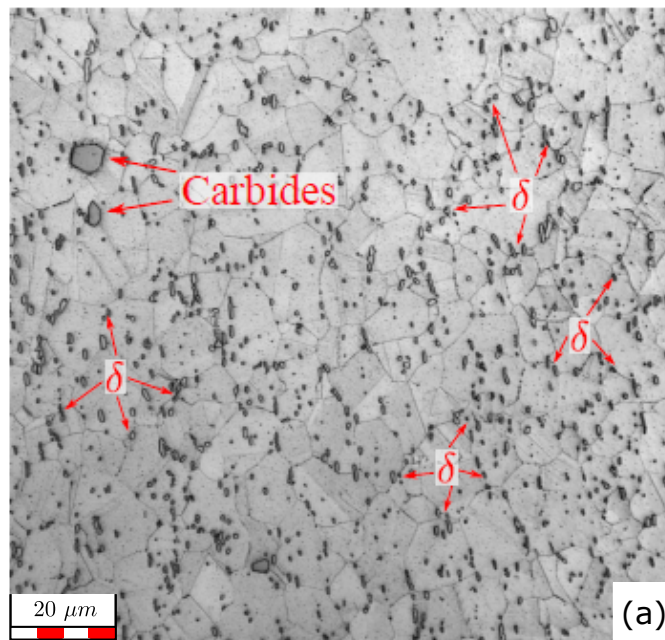


Figure 4.2: Microstructure of the Inconel 718 alloy (Nascimento, 2022).



Table 4.3: Main elements and chemical composition of the Inconel 718 alloy (ASTM B637-16, 2016).

Element	Minimum	Maximum
Ni	50.0	55.0
Cr	17.0	21.0
Nb + Ta	4.75	5.50
Mo	2.80	3.30
Ti	0.65	1.15
Al	0.20	0.80
Co	-	1.0
Mn	-	0.35
Si	-	0.35
Cu	-	0.30
C	-	0.08
P	-	0.015
S	-	0.015
Fe	Remainder	

Table 4.4: Basic mechanical and material properties of the Inconel 718 alloy at room temperature (20°C) and elevated temperature (540°C).

Temp. [°C]	E [GPa]	$\mu$ [-]	$\sigma_{y=0.2}$ [MPa]	$\sigma_{ult}$ [MPa]
25	202	0.3	1231	1434
540	171	0.3	1078	1258

#### 4.1.3 . Fretting specimen and pad design

In this work, flat dog-bone fretting specimens and cylindrical pads were used. The actual shape and dimensions of both specimen and pads are shown in Figures 4.3 and 4.4, respectively. For both materials investigated here, the pads are 55mm long, have a

radius equal to 50mm, and have a rectangular cross-section of 13×15mm. The proper testing region of the Ti-6Al-4V specimens is 13mm in width and 12.90mm in thickness, and for the Inconel 718 ones are 13mm in width and 12.91mm in thickness. Before starting the tests, all specimens and pads had their dimensions and roughness measured to ensure that they were machined and polished as designed. With the exception of the radii, all dimensions were measured using a digital caliper and micrometer. Roughnesses and radii were measured using the Olympus LEXT OLS4100 confocal laser microscope, shown in Figure 4.5. Table 4.5 reports the minimum, maximum, and average superficial roughness values of all specimens and pads measured. For the specimens, the superficial roughness was determined as the average value of three measurements in the central zone of each sample side. The cylindrical surfaces of the pads were mapped using the confocal laser microscope, as shown in Figure 4.6. Then, utilizing a profile feature available in the microscope software, the radius was determined as the average of three individual measurements.

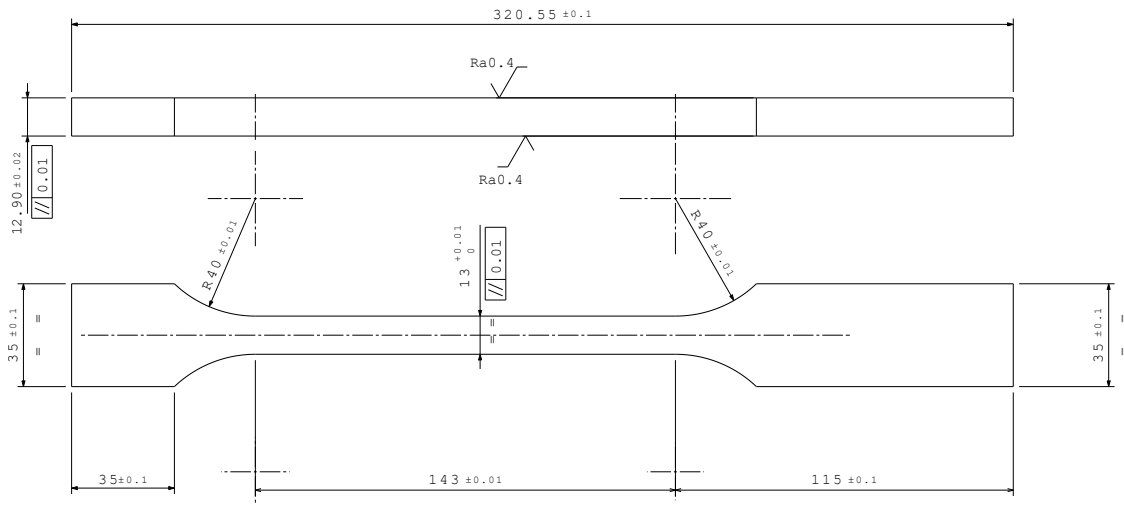


Figure 4.3: Photo and dimensions of the fretting specimen.

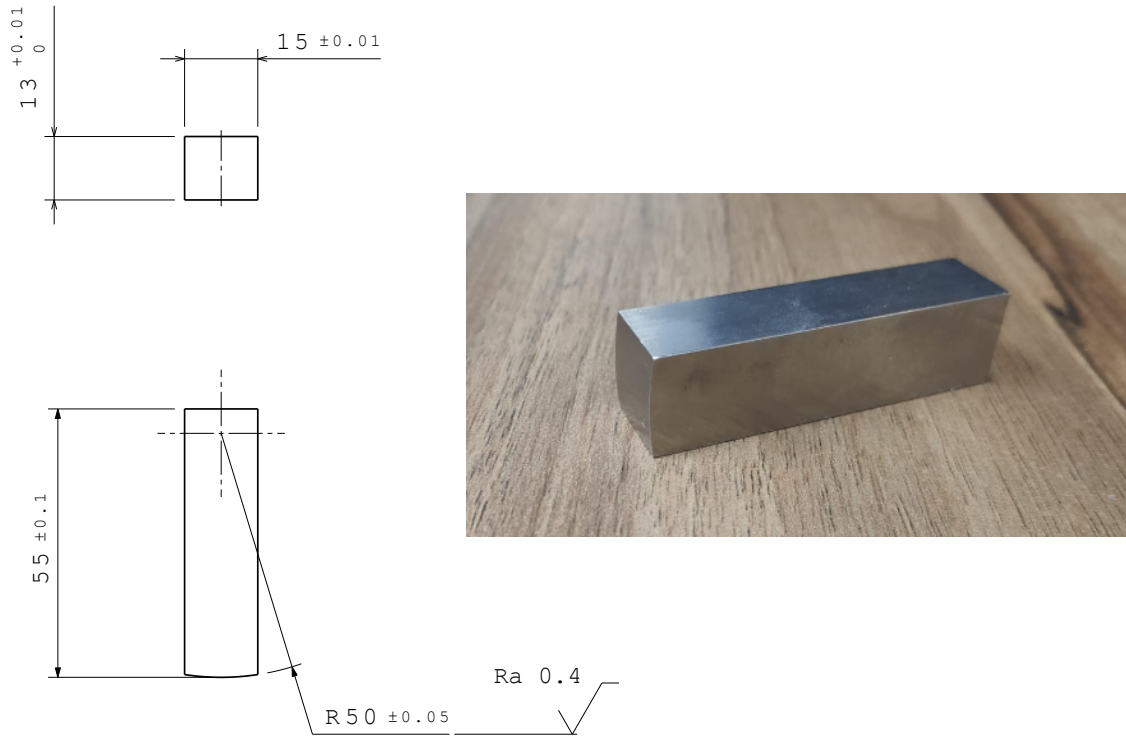


Figure 4.4: Photo and dimensions of the contacting pad.



Figure 4.5: Photo of the Olympus LEXT OLS4100 confocal laser microscope.

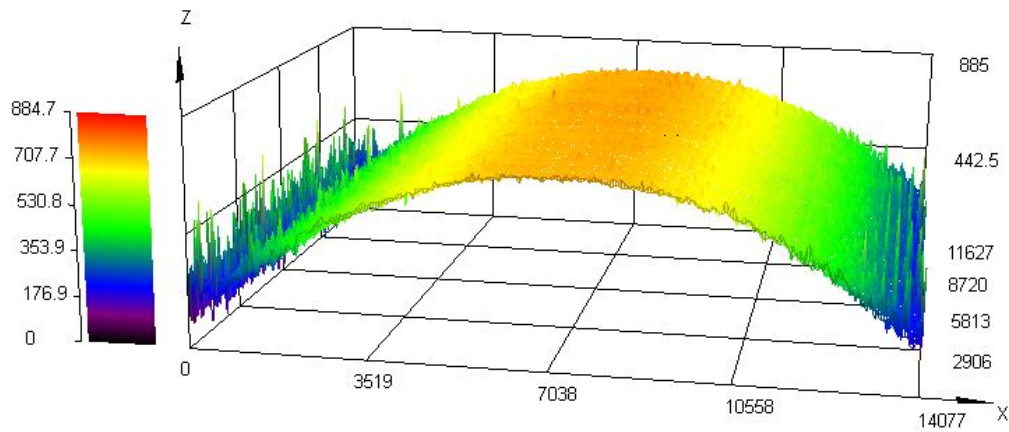


Figure 4.6: Mapped surface of an inconel pad.

Table 4.5: Roughness measurements of the Ti-6Al-4V and Inconel 718 specimens and pads.

	Superficial Roughness, Ra ( $\mu\text{m}$ )					
	Ti-6Al-4V			Inconel 718		
	min.	max.	average	min.	max.	average
Fretting Specimen	0.292	0.887	0.65	0.388	0.874	0.59
Pad	0.341	0.720	0.51	0.391	0.887	0.61

## 4.2 . Tests nomenclature

In this work an extensive experimental campaign was conducted. In order to the reader be able to rapidly associate the test name with its own test type, material, loading condition and test temperature the following nomenclature will be used in this work.

The tests were named as: *test type - material - contact normal load condition - test temperature - test number*. However, for sake of clarity, the following abbreviations were used in order to summarize the testing names:

- Test type:

- $cf$  - coefficient of friction.
- $ff$  - fretting fatigue.
- Material:
  - $ti$  - Titanium Ti-6Al-4V.
  - $in$  - Inconel 718.
- Contact normal load condition:
  - $pc$  - constant contact normal load or pressure constant.
  - $pv$  - cyclic contact normal load or pressure variable.
- Test temperature:
  - $rt$  - room temperature (20°C).
  - $ht$  - high temperature (540°C).

In this way, for instance, the test named as  $cf-in-pv-ht-02$  refers to the second coefficient of friction test conducted with Inconel 718 parts under cyclic contact normal load condition at high temperature.

### 4.3 . Determination of coefficient of friction in partial slip condition

One of the first concepts of the coefficient of friction is derived from the works of [da Vinci \(1400\)](#), [Amontons \(1699\)](#), and [Coulomb \(1821\)](#). [Blau \(2001\)](#) defined this material property as *"the ratio of two forces acting, respectively, perpendicular and parallel to an interface between two bodies under relative motion or impending relative motion, this dimensionless quantity turns out to be convenient for depicting the relative ease with which materials slide over one another under particular circumstances."* The coefficient of friction plays a crucial role in the fretting case. [Dobromirski \(1992\)](#) identify up to 50 variables that influence the fretting case and elected the friction coefficient as

the most important one. For this reason, the coefficients of friction for the Ti-6Al-4V and Inconel 718 alloys under fretting in partial slip conditions will be evaluated in this subsection.

#### 4.3.1 . Methodology

As this work aims to perform fretting fatigue tests with constant and cyclic contact normal load at room and elevated temperature, the coefficient of friction will be evaluated in each of these testing conditions. Tests were carried out to define the coefficient of friction under fretting conditions with constant and cyclic contact normal load for the Ti-6Al-4V only at room temperature (20°C). For the Inconel 718 alloy, the friction coefficients were measured under constant and cyclic contact normal load at room (20°C) and elevated temperature (540°C).

Figure 4.7 (a) and (b) illustrates the so-called Friction Methodology 1. The first part of this test methodology consists in performing a pure fretting test. The tangential displacement amplitude ( $\delta_a$ ) prescribed during the test was increased gradually (steps of 2.5 $\mu\text{m}$  at every 250 cycles) until the tangential force read on its respective load-cell was equal to the one reported in those tables. At this moment, the test was allowed to run for more 10k fretting cycles to develop the fretting scar properly and stabilize the friction coefficient.

The second part of this test, here called Monotonic Friction test, consists in increasing monotonically the tangential displacement until the contact becomes unable to hold the tangential force resulting in a full sliding, as shown in Figure 4.8. In all of these tests, the tangential displacement rate was equal to 0.035 mm/min. The maximum ratio of tangential and normal forces ( $Q/P$ ) recorded on each monotonic friction test is defined as the mean coefficient of friction,  $\mu_m$ , which consists of a composition of the friction coefficients in the slip and the stick zones.

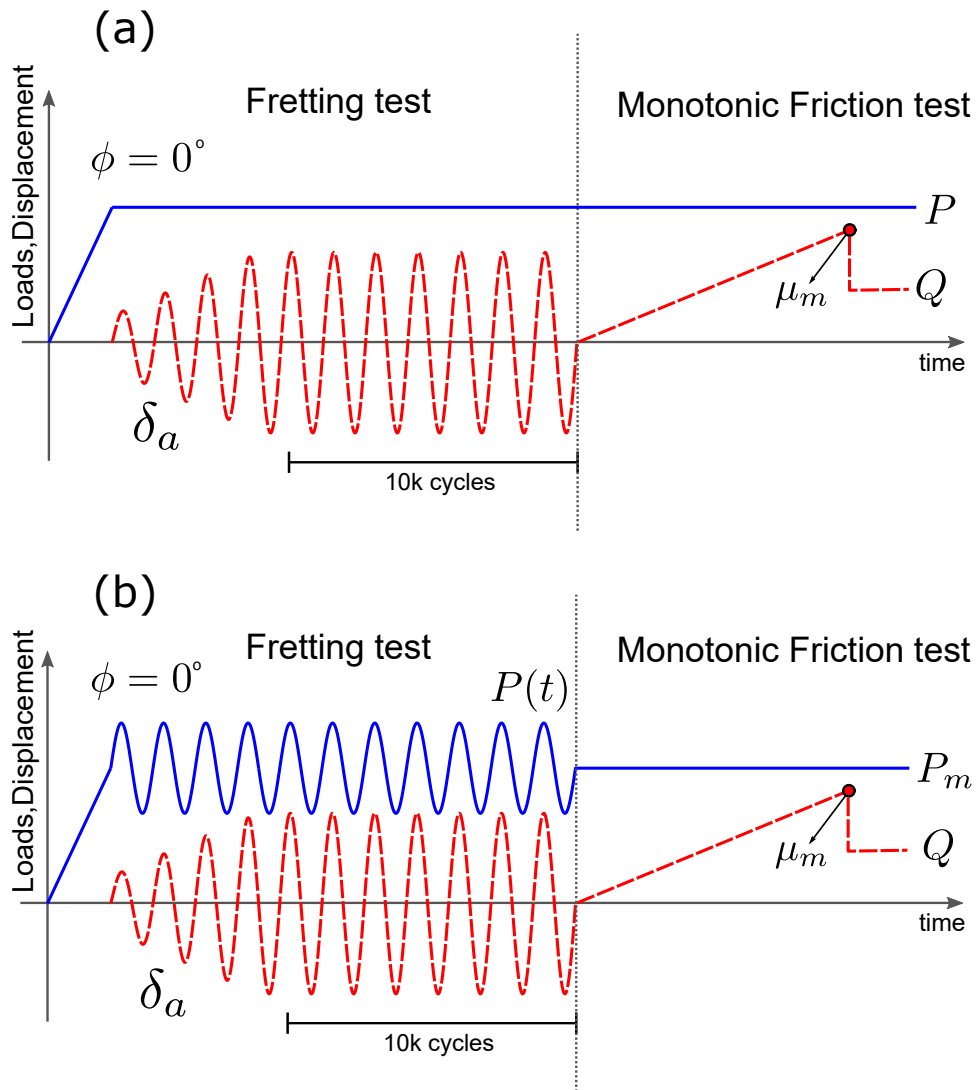


Figure 4.7: Friction Methodology 1: determination of the mean coefficient of friction ( $\mu_m$ ) with (a) constant contact normal load, and (b) cyclic contact normal load.

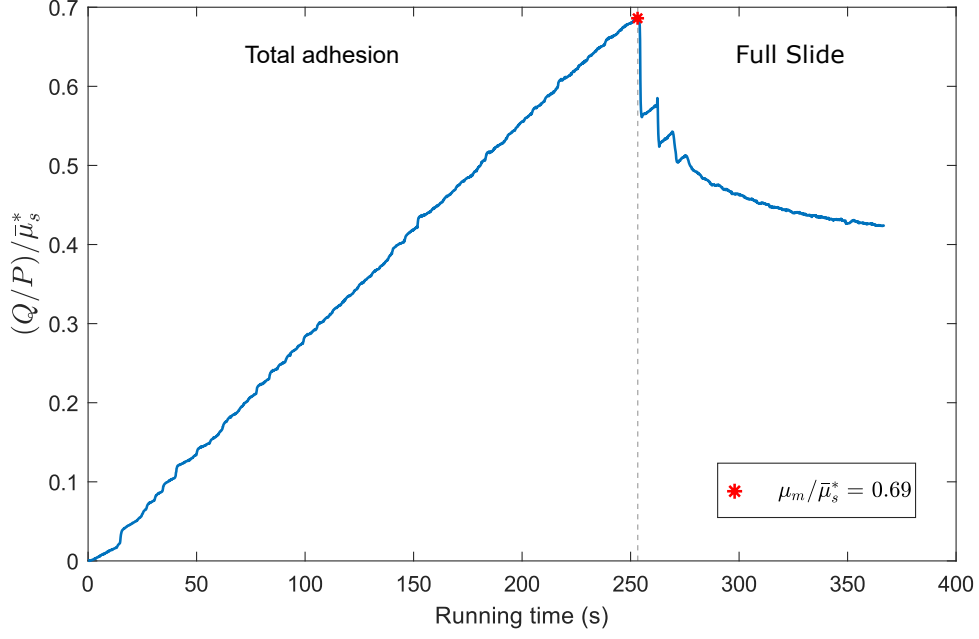


Figure 4.8: Plot of the normal and tangential force ratio against time and determination of the mean friction coefficient ( $\mu_m$ ) for the cf-in-rt-pc-01 test conducted according to the Friction Methodology 1. Normalized with respect to  $\bar{\mu}_s^*$ .

Notice that, in the partial slip regime, the stick and slip zones have different coefficients of friction mainly due to differences in their surface morphology. In other words, the  $\mu_m$  measured from the experimental tests is composed of two distinct coefficients of friction: one from the stick zone and another from the slip zones. To evaluate the tractions and subsurface stress field, one needs to estimate the friction coefficient for the slip zones,  $\mu_s$ . It can be calculated as (Hills and Nowell, 1994; Araujo and Nowell, 2002) :

$$\mu_m = \mu_s + \left[ \frac{4Q}{\pi P} \left( \frac{\pi}{2} - \cot \theta_s - \theta_s \right) - \frac{2}{\pi} \left( \mu_s \phi_s - \frac{Q}{P} \tan \phi_s \right) \right] \quad (4.1)$$

where

$$\theta_s = \sin^{-1} \sqrt{\frac{Q}{\mu_s P}} \quad (4.2)$$

and



$$\phi_s = \cos^{-1} \sqrt{\frac{Q}{\mu_s P}} \quad (4.3)$$

Also, in this work, a second testing methodology was used to determine the coefficient of friction specifically for the Inconel 718 alloy. The so-called Friction Methodology 2 is illustrated in Figure 4.9. This methodology was previously used to determine friction coefficient under fretting wear and fretting fatigue conditions (Kubiak, 2006). In the Friction Methodology 2, a pure fretting test is conducted under displacement control. The tangential displacement amplitude of the sinusoidal waveform is increased by  $2.5\mu\text{m}$  at every 200 fretting cycles while the normal and tangential forces are constantly monitored and recorded.

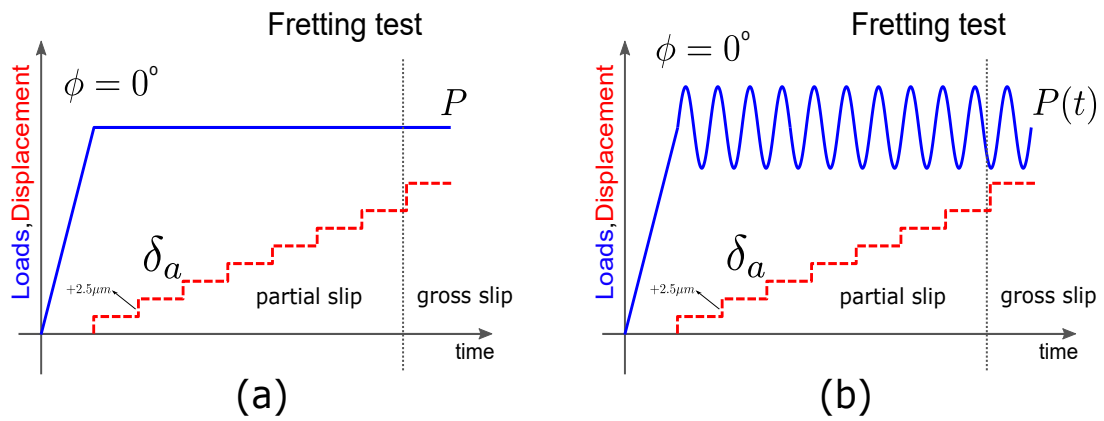


Figure 4.9: Friction Methodology 2: determination of the maximum coefficient of friction ( $\mu_{\text{max}}$ ) with (a) constant contact normal load, and (b) cyclic contact normal load.

This procedure continues until a full sliding is observed on the fretting hysteresis loop. Figure 4.11 shows the fretting hysteresis loop for the (a) partial slip regime and (b) at the first time instant when full sliding was observed in the test. After this moment, the test was stopped. The maximum value of the force ratio  $Q/P$  recorded while the test was respecting the partial slip condition was defined as the maximum coefficient of friction ( $\mu_{\text{max}}$ ), as indicated in Figure 4.10. The results of friction coefficient for this

methodology are reported in Table 4.8. One of the goals for using a different testing methodology was to verify if the friction coefficient measured would vary from one methodology to another. As the results did not show a significant difference between each other, the Friction Methodology 2 was not applied to Inconel 718 at elevated temperature case either for the titanium alloy under study due to the limited number of experimental parts and time limitation.

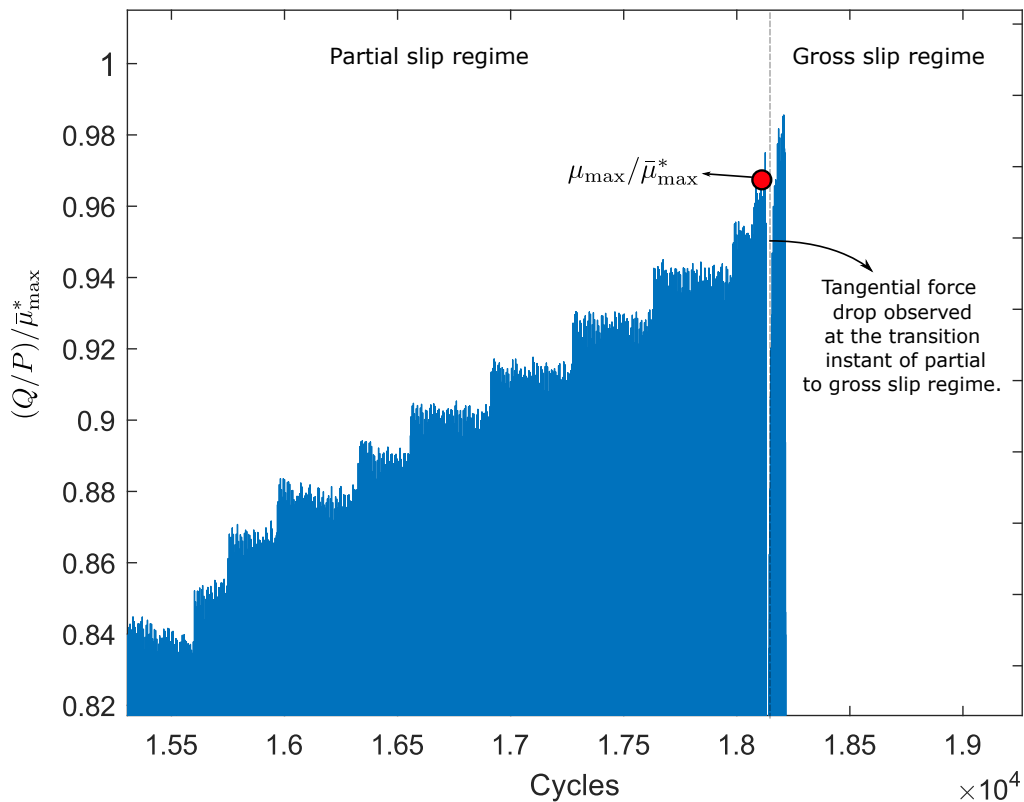


Figure 4.10: Plot of the normal and tangential force ratio against number of cycles, and determination of the maximum friction coefficient ( $\mu_{\max}$ ) for the cf-in-rt-pc-04 test conducted according to the Friction Methodology 2. Normalized with respect to  $\bar{\mu}_{\max}^*$ .

#### 4.3.2 . Results

Following the experimental methodologies detailed in the last subsection (4.3.1), the tests were repeated two or three times for each test condition in order to measure the average coefficient of friction. The following results were normalized due to the industrial requirements. The normalized friction results for the Ti-6Al-4V titanium alloy

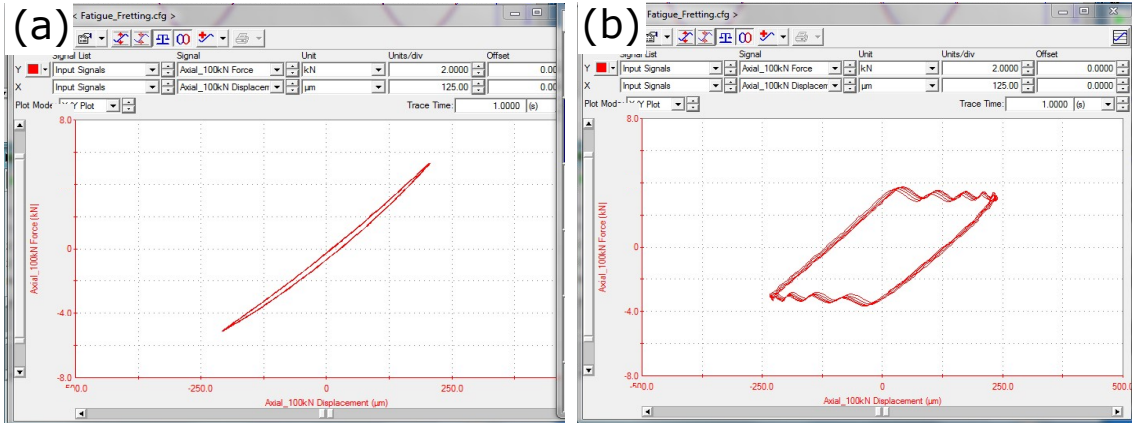


Figure 4.11: Photos of the fretting hysteresis loops recorded by the rig controller/software for the (a) partial slip regime and (b) gross slip regime observed during a friction test conducted according to the Friction Methodology 2.

are reported in Table 4.6 as well as the loading parameters used on those tests. From these results, it is possible to notice that the mean coefficient of friction ( $\mu_m$ ) for the fretting tests performed with cyclic contact normal load is slightly higher than those for the tests with a constant contact normal load. However, when the friction coefficients of the slip zones were estimated by means of the Eq. 4.1, the same values of average coefficients of friction of the slip zone ( $\bar{\mu}_s$ ) were obtained for both contact normal loading conditions. In this thesis,  $\mu_s$  refers to the estimated coefficient of friction in the slip zones for each friction test, while  $\bar{\mu}_s$  stands for the average of them for each test condition (cyclic or constant contact normal loading). Due to the industrial interests, the coefficients of frictions were normalized with respect to the average friction coefficient of the slip zone for the constant contact normal load case,  $\bar{\mu}_s^*$ .

Tables 4.7 and 4.8 report the normalized friction results at room temperature for the Inconel 718 obtained with the Friction Methodology 1 and 2, respectively, and Table 4.9 for the ones conducted at the high temperature condition. From the results reported in Table 4.7, one can notice that the mean coefficient of friction ( $\mu_m$ ) for the fretting tests performed with cyclic contact normal load is essentially the same as that for the tests with a constant contact normal load. Similarly, the friction coefficients of the slip zones estimated by means of the Eq. 4.1, were nearly the same, either for the

constant or for the cyclic contact normal loading conditions. The same trend can be observed on the friction results reported in Table 4.8, i.e., no significant difference on the average values of the friction coefficients under constant and cyclic contact normal load was observed. However, when the coefficient of friction are compared measured from the tests conducted at 20°C to 540°C, a significant reduction of approximately 30% is observed on these coefficients.

Table 4.6: Loading parameters and results for the coefficient of friction tests performed with constant and cyclic contact normal load for the Ti-6Al-4V at room temperature (20°C). Results are normalized with respect to the average friction coefficient of the slip zone for the constant contact normal load condition,  $\bar{\mu}_s^*$ .

Test ID	$Q_a/P_{\max}$	$Q_a/P_{\min}$	$\mu_m/\bar{\mu}_s^*$	$\mu_s/\bar{\mu}_s^*$	$\bar{\mu}_m/\bar{\mu}_s^*$	$\bar{\mu}_s/\bar{\mu}_s^*$
cf-ti-rt-pc-01			0.45	0.97		
cf-ti-rt-pc-02	0.18	0.18	0.47	1.00	0.45	1.00
cf-ti-rt-pc-03			0.45	1.03		
cf-ti-rt-pv-01			0.55	1.05		
cf-ti-rt-pv-02	0.18	0.30	0.53	0.95	0.55	1.00
cf-ti-rt-pv-03			0.57	1.00		

Table 4.7: Loading parameters and normalized results for the coefficient of friction tests performed with constant and cyclic contact normal load for the Inconel 718 at room temperature (20°C). Tests conducted according to the Friction Methodology 1. Results are normalized with respect to the average friction coefficient of the slip zone for the constant contact normal load condition,  $\bar{\mu}_s^*$ .

Test ID	$Q_a/P_{\max}$	$Q_a/P_{\min}$	$\mu_m/\bar{\mu}_s^*$	$\mu_s/\bar{\mu}_s^*$	$\bar{\mu}_m/\bar{\mu}_s^*$	$\bar{\mu}_s/\bar{\mu}_s^*$
cf-in-rt-pc-01			0.69	0.93		
cf-in-rt-pc-02	0.45	0.45	0.75	1.14	0.74	1.00
cf-in-rt-pc-03			0.77	0.94		
cf-in-rt-pv-01			0.75	0.93		
cf-in-rt-pv-02	0.45	0.75	0.77	1.05	0.76	0.99

As two distinct methodologies were used to determine the friction coefficient at room temperature of the Inconel 718, an average of the  $\bar{\mu}_s$  and  $\bar{\mu}_{\max}$  for each contact normal loading condition was used to determine it, as indicated by the following equation:

$$\mu_{M1,M2} = \frac{\bar{\mu}_s + \bar{\mu}_{\max}}{2} \quad (4.4)$$

By the use of Eq. 4.4 and the results reported in Tables 4.7 and 4.8, the friction

Table 4.8: Loading parameters and normalized results for the coefficient of friction tests performed with constant and cyclic contact normal load for the Inconel 718 at room temperature (20°C). Tests conducted according to the Friction Methodology 2. Results normalized with respect to the average friction coefficient for the constant contact normal load condition,  $\bar{\mu}_{\max}^*$ .

Test ID	$\mu_{\max}/\bar{\mu}_{\max}^*$	$\bar{\mu}_{\max}/\bar{\mu}_{\max}^*$
cf-in-rt-pc-04	0.97	1.00
cf-in-rt-pc-05	1.03	
cf-in-rt-pv-03	1.00	0.99
cf-in-rt-pv-04	0.98	

coefficients under constant and cyclic contact normal load conditions were determined. Following the same behaviour, no significant difference was noticed between the average friction coefficients under constant and cyclic contact normal load for the Inconel 718 at room temperature.

Table 4.9: Loading parameters and results for the coefficient of friction tests performed with constant and cyclic contact normal load for the Inconel 718 alloy at elevated temperature (540°C). Tests conducted according to the Friction Methodology 1. Results are normalized with respect to the average friction coefficient of the slip zone for the static contact normal load condition at room temperature,  $\bar{\mu}_s^*$  of Table 4.7.

Test ID	$Q_a/P_{\max}$	$Q_a/P_{\min}$	$\mu_m/\bar{\mu}_s^*$	$\mu_s/\bar{\mu}_s^*$	$\bar{\mu}_m/\bar{\mu}_s^*$	$\bar{\mu}_s/\bar{\mu}_s^*$
cf-in-ht-pc-01	0.45	0.45	0.61	0.70	0.61	0.71
cf-in-ht-pc-02			0.62	0.73		
cf-in-ht-pv-01	0.45	0.50	0.59	0.74	0.58	0.69
cf-in-ht-pv-02			0.57	0.64		

#### 4.3.3 . Summary and final remarks on the friction tests

In the Section 4.3, the influence of the cyclic contact normal load on the coefficient of friction was evaluated. Following the friction methodologies here presented, tests under partial-slip condition with constant and cyclic contact normal load were conducted at room temperature for the Ti-6Al-4V and at room and high temperatures for the Inconel 718.

In summary, the results of these tests showed that the variation of the contact normal load within the ranges here examined did not significantly affect the measured and estimated values of the coefficient of friction independently of the material used and the temperature of the tests. However, in this work, only two materials were tested. In

this way, it is still necessary to conduct more tests with different materials and loading conditions to enhance this conclusion.

As far as the effect of the temperature on the coefficient of friction is concerned, tests with the Inconel 718 at 540°C presented a reduction of approximately 30% with respect to the tests at room temperature either for constant or for varying contact normal loading conditions.

[Hamdy and Waterhouse \(1981\)](#) reported the formation of a *glaze layer* on the surface of Inconel 718 at 540°C, considering for different values of slip amplitude. This *glaze* has a wear-reducing effect due to the formation of Ni-oxide, which acts as a lubricant. Consequently, the coefficient of friction also is reduced. [Bai et al. \(2021\)](#) also affirm that the Inconel 718 alloy has a temperature-dependent tribological behavior which is associated with the formation of a lubricating surface layer mainly composed of Fe, Cr, Ni, and O. Some microscopy and spectroscopy analysis (that will be appropriately presented in subsection 4.4.6) reveals a high mass percentage of these elements at the slip-zone of the fretting tests here conducted at 540°C.

Further, both experimental methodologies for determining the coefficient of friction used in this work provided similar results, which also were consistent with values reported in the literature, at least for fretting tests under constant contact normal loading. For instance, the friction coefficient of the slip-zone for the Ti-6Al-4V under a partial slip regime was found to vary in a range from 83% to 133% ([Araújo, 2000](#); [Proudhon et al., 2005](#); [Bellecave, 2015](#)) of the value we measured in this thesis. For the Inconel 718, these values varied in a range from from 67% to 111% at room temperature ([Hamdy and Waterhouse, 1981](#); [Fellows et al., 1997](#); [Amargier et al., 2010](#); [Amanov, 2020](#)) and 63% at 540°C ([Hamdy and Waterhouse, 1981](#)).

#### **4.4 . Fretting fatigue tests at room and elevated temperature**

##### **4.4.1 . Methodology**

In this work, an experimental campaign was specially designed to evaluate the influence of a varying contact normal load on the fretting fatigue strength for the Ti-6Al-4V and Inconel 718 alloys. In this way, two sets of tests were performed. The first one (Testing Set 1), with constant contact normal load ( $P = const.$ ) and the second one (Testing Set 2) with cyclic contact normal load ( $P(t) = P_m + P_a \sin(t + \phi)$ ), where  $P$  is the normal contact load,  $P_m$  and  $P_a$  are its mean and alternated components, respectively, and  $\phi$  the phase angle with respect to the bulk fatigue waveform.

The tests with cyclic contact normal loading were designed so that the maximum peak pressure,  $p_{0,max}$ , the tangential load amplitude,  $Q_a$ , and the mean and the amplitude values of the fatigue bulk stresses,  $\sigma_{B,m}$  and  $\sigma_{B,a}$ , respectively, were identical to the ones for the tests with a constant contact normal load. All time-varying loads were synchronous and in-phase ( $\phi = 0$ ).

Also, it is important to notice that all fretting tests were performed in the partial slip regime. Thus, for the tests with cyclic contact normal load, although the tangential over contact normal load ratio ( $|Q(t)|/P(t)$ ) could vary, the levels of the shear load were designed so that this ratio was always less than the average friction coefficient of the slip zone,  $\bar{\mu}_s$ .

Figures 4.12 (a) and (b) depict a schematic diagram of the loading histories considered in both set of tests, while Fig. 4.12 (c) shows an scheme of the contact configuration. In addition, to further investigate the influence of the effect of varying contact normal load on fretting fatigue, after the end of the tests (complete failure of the specimen), measurements of crack initiation angle were carried out using the LEXT OLS Olympus 4100 confocal laser microscope.

#### 4.4.2 . Results - Ti-6Al-4V at room temperature

As previously mentioned, the experimental campaign of the fretting fatigue tests was divided into two testing sets. In the first one, the fretting fatigue tests were conducted with a constant contact normal load, and in the second one, a cyclic contact normal load was used. All the tests were interrupted either after the failure of the specimen

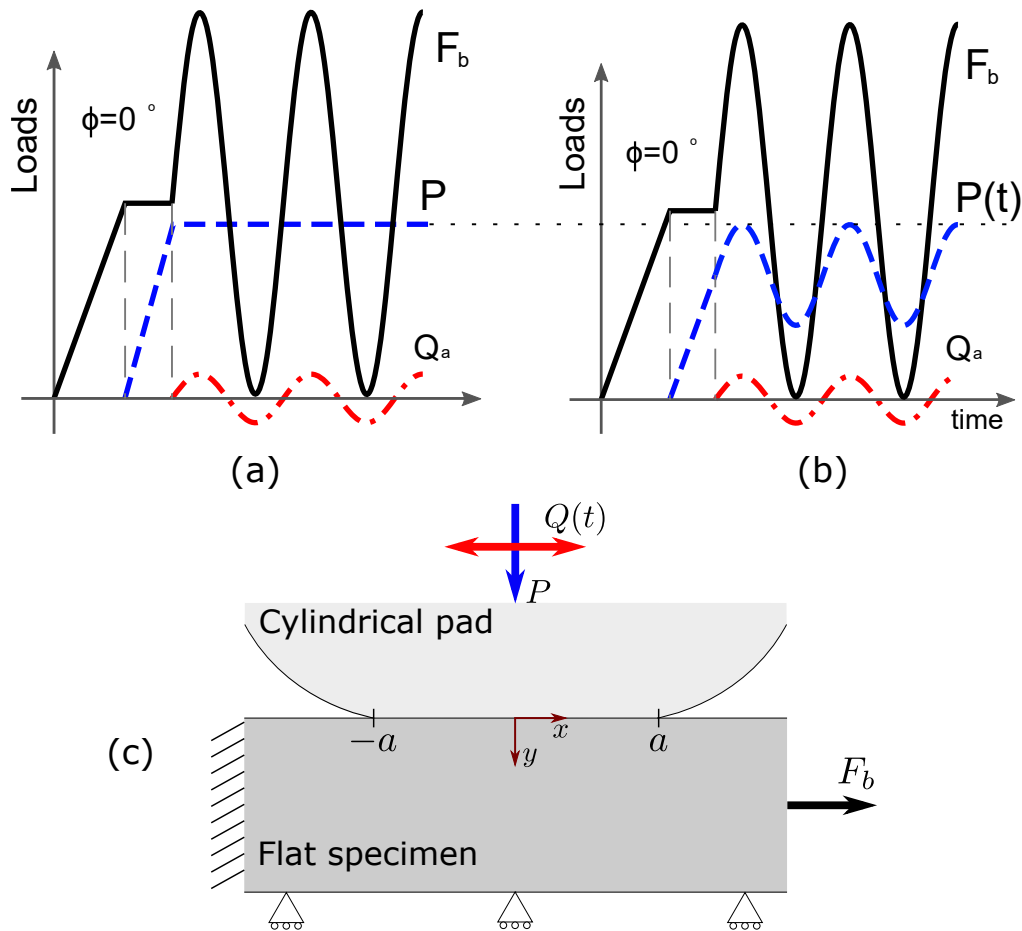


Figure 4.12: Schematic of loading history for (a) Testing Set 1 (constant contact normal load), (b) Testing Set 2 (cyclic contact normal load), and (c) experimental fretting fatigue configuration.

or at run-out conditions ( $2 \times 10^6$  cycles). The load ratios adopted for the bulk ( $R_B$ ), tangential ( $R_Q$ ) and contact normal loads ( $R_P$ ) were 0,  $-1$ , and 0.6, respectively. The experimental lives obtained and the main loadings parameters have been reported in Table 4.10. Four tests (ff-ti-rt-pc-01 to ff-ti-rt-pc-04) were performed within Testing Set 1 (tests with constant contact normal load). The average fretting life for these tests was 840k cycles. Similarly, other four tests (ff-ti-rt-pv-01 to ff-ti-rt-pv-04) were conducted for Testing Set 2 (tests with cyclic contact normal load), and the average life for these tests was 1259k cycles. Comparing these two average lives, it is possible to observe that Testing Set 2 (cyclic contact normal load) presented a life approximately 50% bigger than that for Testing Set 1.



Table 4.10: Loadings parameters and life results of the fretting fatigue tests with constant and cyclic contact normal load at room temperature for the Ti-6Al-4V. Contact normal load ratio  $R_p = 0.6$ .

Test ID	$Q_a/P_{\max}$	$Q_a/P_{\min}$	$\sigma_{B,\max}/p_{0,\max}$	$\sigma_{B,\max}/p_{0,\min}$	Life [cycles]	Avg. Life [cycles]
ff-ti-rt-pc-01					847k	
ff-ti-rt-pc-02	0.18	0.18	0.39	0.39	1016k	840k $\pm$ 158k
ff-ti-rt-pc-03					631k	
ff-ti-rt-pc-04					866k	
ff-ti-rt-pv-01					1253k	
ff-ti-rt-pv-02	0.18	0.30	0.39	0.51	921k	1259k $\pm$ 306k
ff-ti-rt-pv-03					1200k	
ff-ti-rt-pv-04					1663k	

After the specimen total failure, the fracture surfaces of parts were observed under the confocal laser microscope, and the fretting crack initiation angle was measured. Figure 4.13(a) shows the fractography of a test with constant contact normal load and its correspondent surface profile, 4.13(b). Such a profile was obtained following the dashed red line depicted on the fracture surface.

As crack initiation direction can vary along the fractured surface, ten individual fretting crack initiation directions were measured along the fractured surface ( $\theta_1$  to  $\theta_{10}$ ), and the fretting crack initiation angle ( $\theta$ ) for each test is defined as the average of them. Then, the mean crack angle ( $\bar{\theta}$ ) was calculated for Testing Set 1 and 2. The fretting crack initiation directions have been reported in Table 4.11. The mean fretting crack initiation angle  $\bar{\theta}$  for the Testing Set 1 (constant contact normal load) was  $-2.7^\circ$ , whereas for the Testing Set 2 (cyclic contact normal load) it was  $-2.0^\circ$ . In this setting, from an average point of view, one can see that cracks initiated and propagated nearly perpendicular to the contact surface (mode I dominated cracks). Negative angles indicate that the crack propagates outwards the contact zone. Figure 4.14 depicts the fretting contact scar and the fracture surface of selected test conducted with Ti-6Al-4V parts at room temperature under constant contact normal load condition. In this figure, the solid, dotted, and dashed lines symbolize the pad contact, the bearing contact, and the boundary of propagation and fast fracture regions.

This seems to be consistent with other experimental work available where fretting cracks have also been observed to nucleate nearly perpendicular to the contact interface.

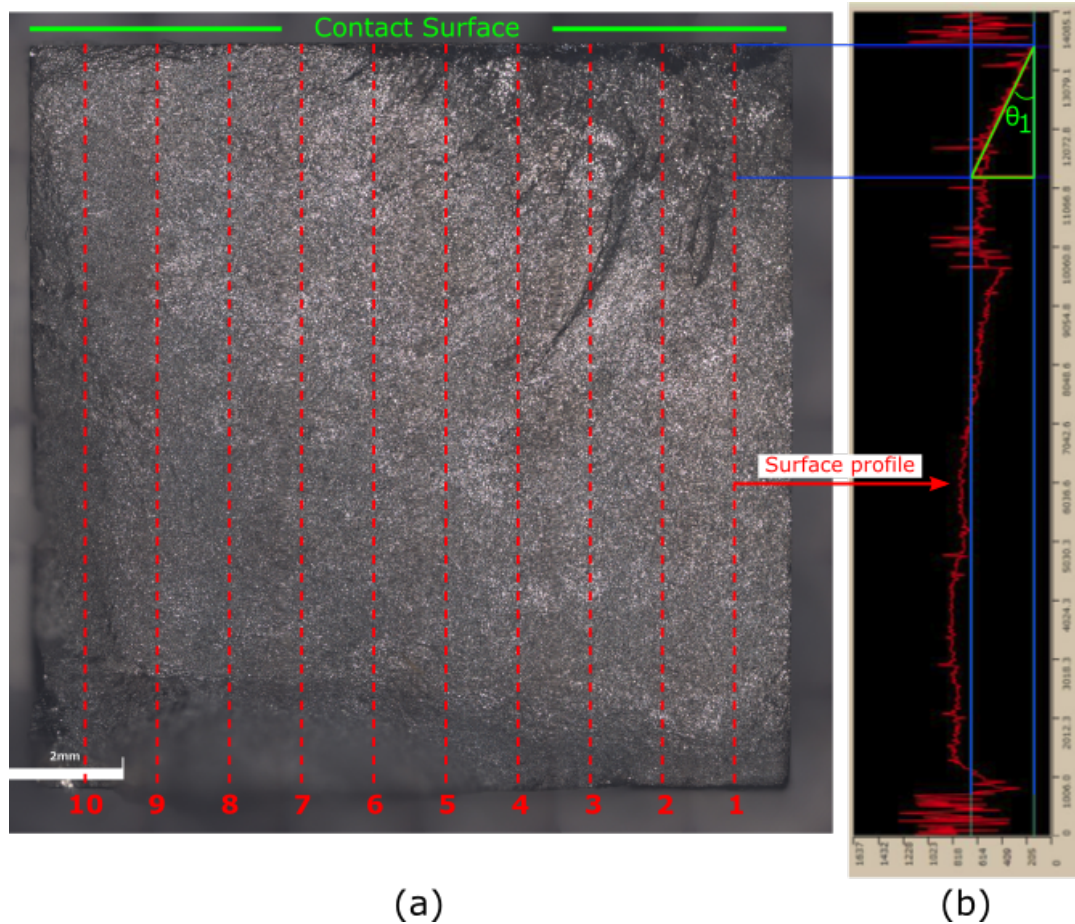


Figure 4.13: (a) Fracture surface of ff-ti-rt-pc-01 specimen, and (b) measurement of the crack initiation angle.

Indeed, the crack initiation path under fretting conditions is somehow complex to estimate due to the severe stress gradient under the contact, which varies quite rapidly. For instance, fretting fatigue for Ti-6Al-4V available in the literature (Lykins et al., 2001), which reported a crack initiation path outwards the contact region for a small distance followed by an abrupt change where additional crack extension was inwards the contact.

#### 4.4.3 . Results - Inconel 718 at room temperature

Here are presented the results of the fretting fatigue experimental campaign of the Inconel 718 alloy at room temperature. The tests were interrupted either after the total failure of the specimen or at run-out conditions ( $2.0 \times 10^6$  cycles). The load ratios adopted for the bulk ( $R_B$ ) and tangential loads ( $R_Q$ ) were equal to 0 and  $-1$ , respectively. For the Testing Set 2, the load ratio of the contact normal load ( $R_b$ ) was



Figure 4.14: Fretting fatigue contact scar and fracture surface of a test with Ti-6Al-4V at RT and constant contact normal load (ff-ti-rt-pc-04).

Table 4.11: Measurements of fretting crack initiation angles for the fretting fatigue tests with Ti-6Al-4V parts at room temperature.

Test ID	Crack angle, $\theta$ [°]	Mean crack angle, $\bar{\theta}$ [°]
ff-ti-rt-pc-01	-1.6	
ff-ti-rt-pc-02	-4.1	$-2.7 \pm 2.0$
ff-ti-rt-pc-03	-0.4	
ff-ti-rt-pc-04	-4.5	
ff-ti-rt-pv-01	-2.4	
ff-ti-rt-pc-02	-0.5	$-2.0 \pm 1.1$
ff-ti-rt-pc-03	-1.9	
ff-ti-rt-pc-04	-3.2	

equal to 0.6. Four tests (ff-in-rt-pc-01 to ff-in-rt-pc-04) were performed with constant contact normal load (Testing Set 1) and further four tests (ff-in-rt-pv-01 to ff-in-rt-pv-04) were conducted under cyclic contact normal load condition (Testing Set 2). The

experimental lives obtained and the main test loads parameters have been reported in Table 4.12. As reported in the refereed table, the average fretting life for the Testing Sets 1 and 2 were 299k and 566k cycles, respectively. Comparing these life results, the one can observe that average fretting life of the Testing Set 2 (cyclic contact normal load) is approximately 89% bigger than that for Testing Set 1 (constant contact normal load).

Table 4.12: Loading parameters and life results of the fretting fatigue tests with constant and cyclic contact normal load at room temperature for the Inconel 718 alloy. Contact normal load ratio  $R_p = 0.6$ .

Test ID	$Q_a/P_{\max}$	$Q_a/P_{\min}$	$\sigma_{B,\max}/p_{0,\max}$	$\sigma_{B,\max}/p_{0,\min}$	Life [cycles]	Avg. Life [cycles]
ff-in-rt-pc-01					286k	
ff-in-rt-pc-02	0.45	0.45	0.61	0.61	275k	299k $\pm$ 28k
ff-in-rt-pc-03					325k	
ff-in-rt-pc-04					310k	
ff-in-rt-pv-01					669k	
ff-in-rt-pv-02	0.45	0.75	0.61	0.78	513k	566k $\pm$ 70k
ff-in-rt-pv-03					548k	
ff-in-rt-pv-04					534k	

Also for such tests one examined the fracture surfaces of the fretting specimens and measured the crack initiation angles at different sites by means of the confocal laser microscope. Figures 4.15 and 4.16 depict the fretting contact scar and the fracture surface of a test conducted with Inconel 718 at room temperature under constant and cyclic contact normal load condition, respectively. In these figures, the solid, dotted, and dashed lines symbolize the pad contact, the bearing support contact, and the boundary of propagation and fast fracture regions.

To measure the crack initiation angle, the same procedure and technique described in the section 4.4.2 and illustrated in Figure 4.13 was applied. In this way, ten individual fretting crack initiation directions were measured along the fractured surface ( $\theta_1$  to  $\theta_{10}$ ). The fretting crack initiation angle ( $\theta$ ) for each Testing Set is defined as the average

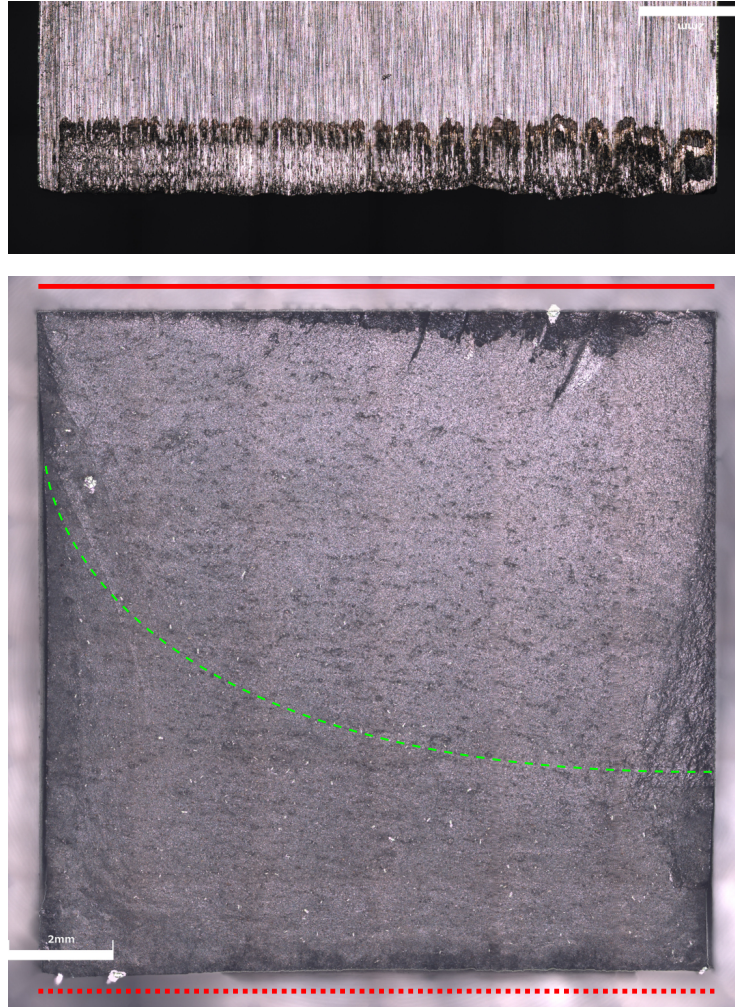


Figure 4.15: Fretting fatigue contact scar and fracture surface of a test for Inconel 718 at RT with constant contact normal load ff-in-rt-pc-01).

of them, as reported in Table 4.13. The mean fretting crack initiation angle  $\bar{\theta}$  for the Testing Set 1 (constant contact normal load) was  $-5.0^\circ$ , whereas for the Testing Set 2 (cyclic contact normal load) it was  $-1.9^\circ$ . Considering the mean fretting crack initiation angle for the studied contact normal load conditions, cracks initiated and propagated nearly perpendicular to the contact surface (mode I dominated cracks). Furthermore, no significant change in the fretting crack initiation direction was measured when cyclic contact normal load was considered. Negative angles indicate that the crack propagates outwards the contact zone.

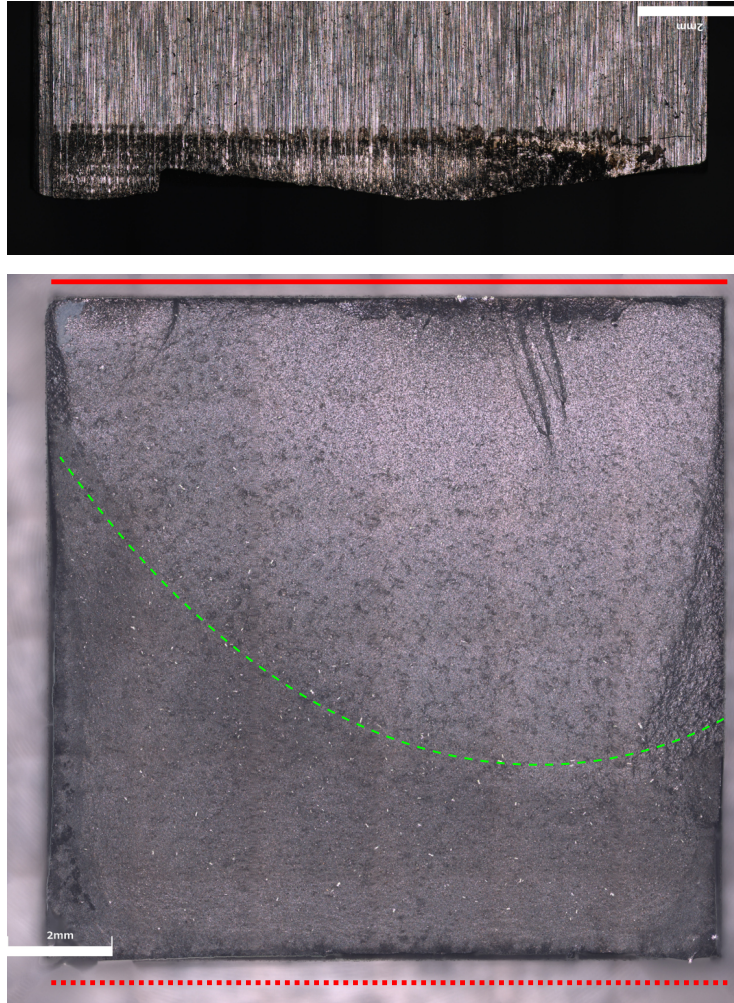


Figure 4.16: Fretting fatigue contact scar and fracture surface of a test for Inconel 718 at RT with cyclic contact normal load test (ff-in-rt-pv-04).

Table 4.13: Measurements of fretting crack initiation angles for the fretting fatigue tests with Inconel 718 parts at room temperature.

Test ID	Crack angle, $\theta$ [°]	Mean crack angle, $\bar{\theta}$ [°]
ff-in-rt-pc-01	-6.5	
ff-in-rt-pc-02	-7.5	$-5.0 \pm 3.8$
ff-in-rt-pc-03	-6.5	
ff-in-rt-pc-04	0.7	
ff-in-rt-pv-01	-6.8	
ff-in-rt-pv-02	-1.4	$-1.9 \pm 4.1$
ff-in-rt-pv-03	3.1	
ff-in-rt-pv-04	-2.3	

#### 4.4.4 . Results - Inconel 718 at elevated temperature

In this subsection the results of the fretting fatigue tests for the Inconel 718 alloy at elevated temperature (540°C) are presented. The tests were interrupted either after the total failure of the specimen or at run-out conditions ( $2 \times 10^6$  cycles). In this experimental investigation, the load ratios adopted for the bulk ( $R_B$ ) and tangential loads ( $R_Q$ ) were 0 and  $-1$ , respectively. For the Testing Set 2, the load ratio of the contact normal load ( $R_b$ ) was 0.8. Three tests (ff-in-ht-pc-01 to ff-in-ht-pc-03) were carried out with a constant contact normal load (Testing Set 1) and further three ones (ff-in-ht-pv-01 to ff-in-ht-pv-03) were conducted under cyclic contact normal load condition (Testing Set 2). All the Inconel 718 tests at elevated temperature were carried out using the two pads configuration, instead of using a bearing as contact support in one of the sides. The experimental lives obtained and the main loading parameters have been reported in Table 4.14. The average fretting lives for the Testing Sets 1 and 2 were 183k and 239k cycles, respectively. Comparing these life results, it is possible to observe that the average fretting life of the Testing Set 2 (cyclic contact normal load) is approximately 31% longer than that for Testing Set 1 (constant contact normal load).

Table 4.14: Loading parameters and life results of the fretting fatigue tests with constant and cyclic contact normal load at elevated temperature (540°C) for the Inconel 718 alloy. Contact normal load ratio  $R_p = 0.8$ .

Test ID	$Q_a/P_{\max}$	$Q_a/P_{\min}$	$\sigma_{B,\max}/p_{0,\max}$	$\sigma_{B,\max}/p_{0,\min}$	Life [cycles]	Avg. Life [cycles]
ff-in-rt-pc-01					160k	
ff-in-rt-pc-02	0.45	0.45	0.61	0.61	195k	183k $\pm$ 20k
ff-in-rt-pc-03					195k	
ff-in-rt-pv-01					211k	
ff-in-rt-pv-02	0.45	0.56	0.61	0.78	279k	239k $\pm$ 35k
ff-in-rt-pv-03					228k	

In the same way, for the post-fracture analysis, the fracture surfaces of fretting specimens were observed under the confocal laser microscope, and the fretting crack initiation angle was measured according to the methodology described in the section 4.4.2. These results are reported in Table 4.15. Figures 4.17 and 4.18 depict the fretting contact scar and the fracture surface of Inconel 718 specimens tested at elevated temperature (540°C) under constant and cyclic contact normal load condition, respectively. In these figures, the solid, and dashed lines symbolize the pad contact, and the boundary of

propagation and fast fracture regions.

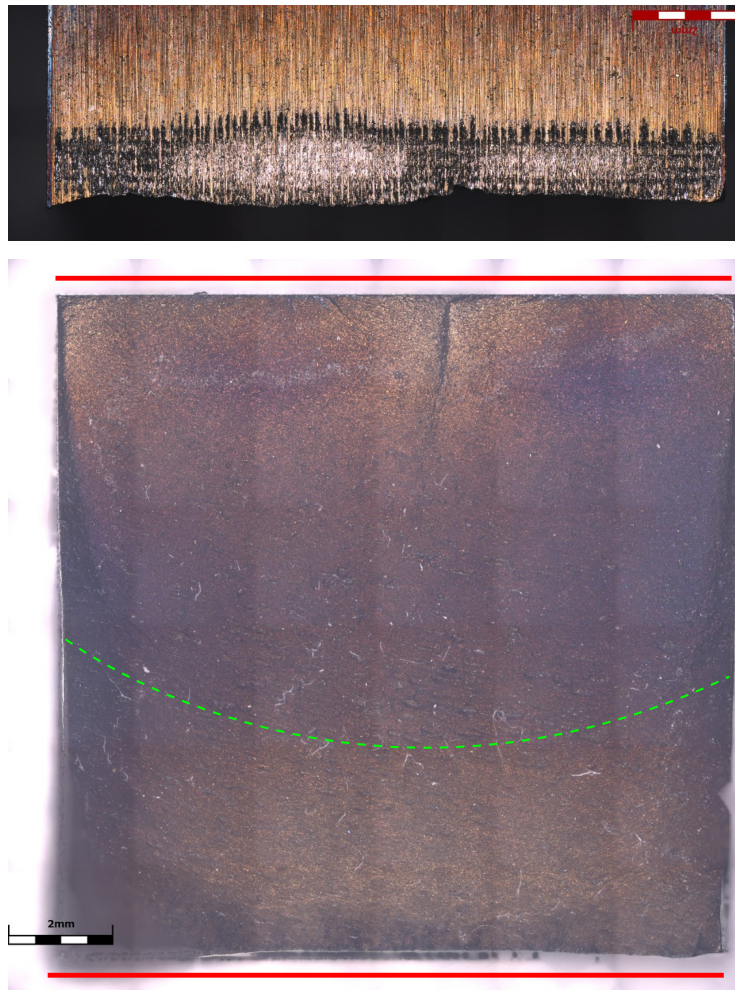


Figure 4.17: Fretting fatigue contact scar and fracture surface of a test for Inconel 718 at 540°C with constant contact normal load (ff-in-ht-pc-03).

The mean fretting crack initiation angle ( $\bar{\theta}$ ) for the Testing Set 1 (constant contact normal load) was  $-3.0^\circ$ , whereas for the Testing Set 2 (cyclic contact normal load) it was  $-3.6^\circ$ . Again, the reader can notice that cracks initiated and propagated nearly perpendicular to the contact surface (mode I dominated cracks) and no significant difference in the fretting crack initiation direction was observed when cyclic contact normal load was considered. Negative angles indicate that the crack propagates outwards the contact zone.



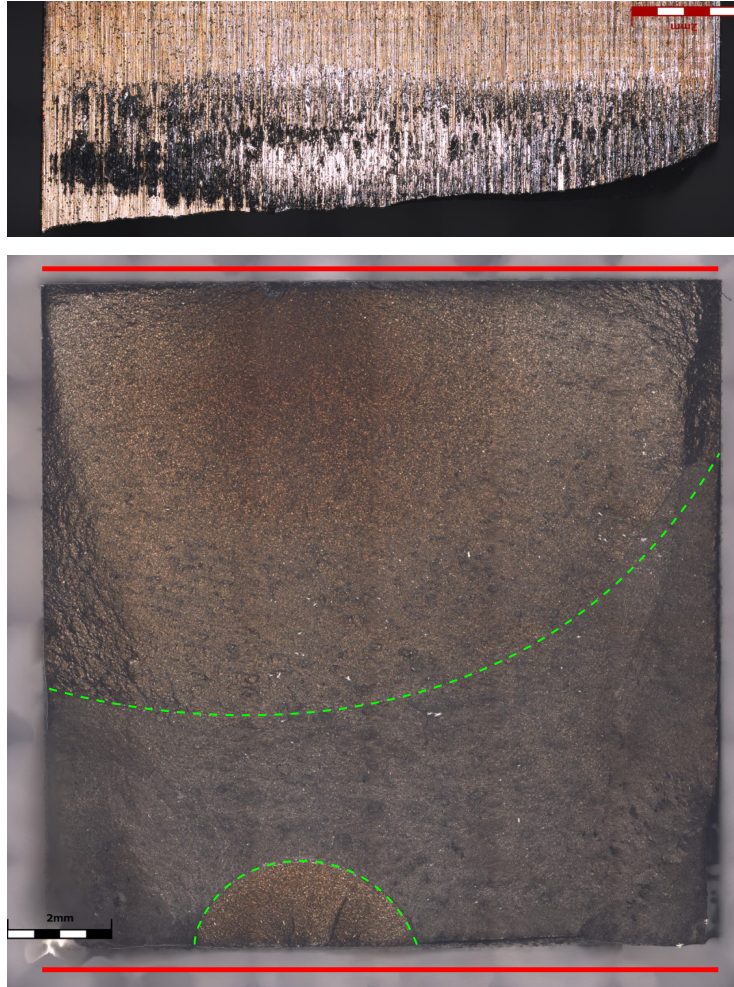


Figure 4.18: Fretting fatigue contact scar and fracture surface of a test for Inconel 718 at 540°C with cyclic contact normal load (ff-in-ht-pv-02).

Table 4.15: Measurements of fretting crack initiation angles for the fretting fatigue tests with Inconel 718 parts at elevated temperature (540°C).

Test ID	Crack angle, $\theta$ [°]	Mean crack angle, $\bar{\theta}$ [°]
ff-in-ht-pc-01	-3.1	
ff-in-ht-pc-02	-0.4	$-3.0 \pm 2.6$
ff-in-ht-pc-03	-5.6	
ff-in-ht-pv-01	-3.6	
ff-in-ht-pv-02	-3.3	$-3.6 \pm 0.7$
ff-in-ht-pv-03	-4.6	

#### 4.4.5 . Scanning Electron Microscope analysis on Inconel 718

In order to provide additional information about the effect of cyclic contact normal load and temperature on the fretting phenomenon, a post-failure investigation of the fractured surfaces and fretted regions of some Inconel 718 specimens was carried out under a JEOL JSM-7100F scanning electron microscope (SEM). A photo of such an equipment is shown in Fig. 4.19. Figures 4.20 and 4.24 show different views of the fretting specimen used in a test with constant contact normal load and at room temperature. Figure 4.20 shows the fretted area and the slip and stick zones in details while Fig. 4.21 shows the specimen fracture surface and a carbide inclusion near to the contact surface.



Figure 4.19: Photo of the JEOL JSM-7100F scanning electron microscope.

Figures 4.22 and 4.23 show some views of a fretting specimen used in a test with cyclic contact normal load and at room temperature (ff-in-rt-pv-04). In these figures, one can observe similarities in the the surfaces of the slip and stick zones when compared with the

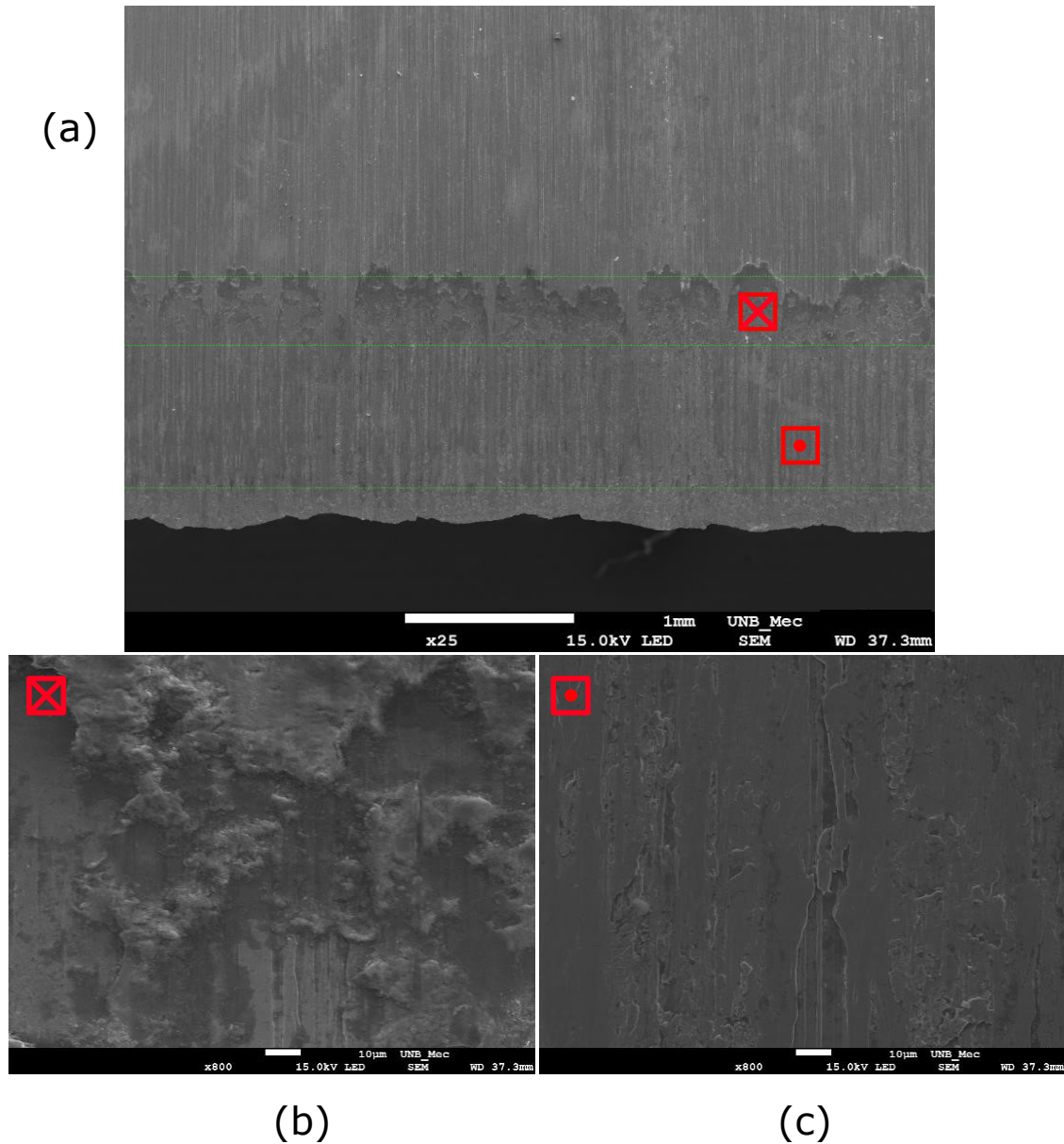


Figure 4.20: SEM observations of the test specimen ff-in-rt-pc-03: (a) Fretting contact mark, (b) Zoom view of the slipping zone, and (c) zoom view of the stick zone.

ones obtained in the test with static contact normal load (Figs. 4.20). Moreover, Figure 4.24 depicts: (a) the fracture surface observed under the confocal laser microscope, (b) the fretted area, (c) the main crack initiation, and (d) and (e) arrested fretting cracks.

A further investigation was also conducted to evaluate some aspects of the temperature effect on the Inconel 718 specimens. In order to do so, a Scanning Electron Microscopy combined with Energy dispersive X-ray spectroscopy (EDX) were used to

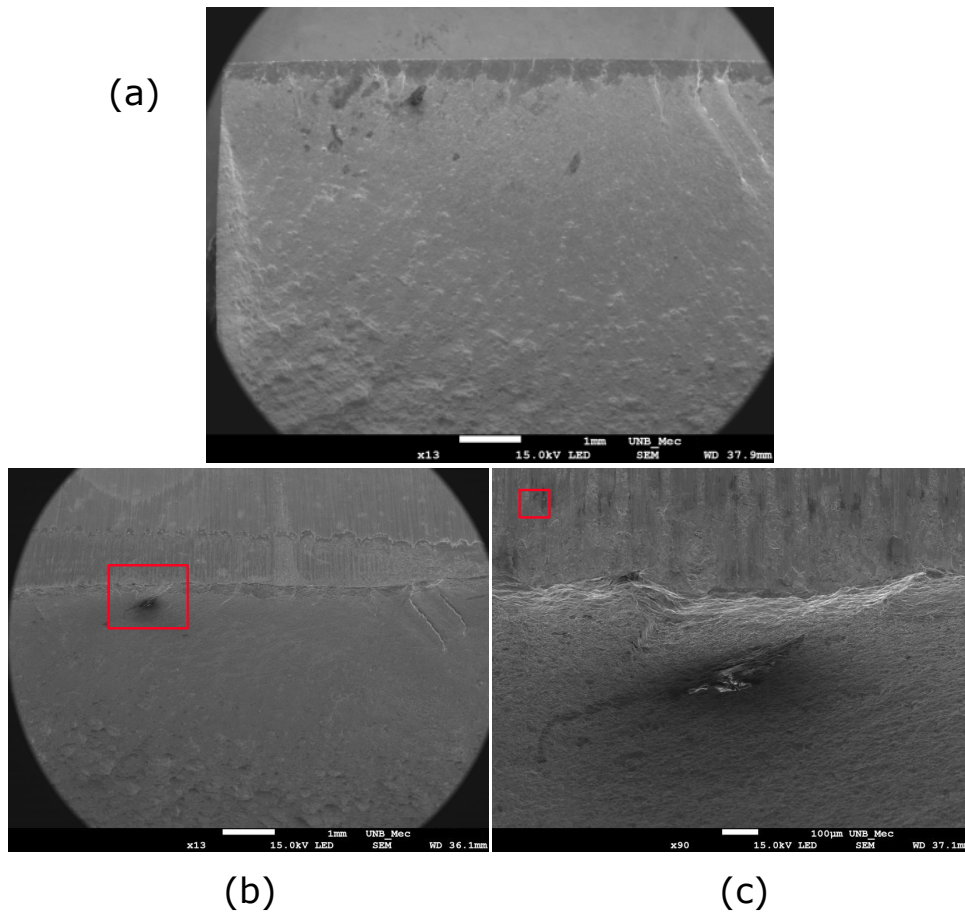


Figure 4.21: SEM observations of the test specimen ff-in-rt-pc-03: (a) Fracture surface, (b) Inclined view, and (c) zoom view of a carbide inclusion.

investigate the oxidation levels on selected surfaces. Figure 4.25 illustrates the locals where the SEM/EDX analyses were conducted on two selected Inconel specimens tested at room temperature (ff-in-rt-pc-03) and at 540°C (ff-in-ht-pc-03). Thus, a surface evaluation was carried out in six distinct regions: without contact, slip zone, stick zone, crack initiation, stable propagation, and fast fracture one. The reader can find all SEM/EDX analyses in the Appendix of this work. Appendix A1 refers to the analyses of the Inconel sample at room temperature, and Appendix A2 to the one conducted at elevated temperature. The Oxygen mass percentages were estimated by the ZAF Method Standarless Quantitative Analysis of each evaluated region and are reported in Table 4.16. Comparing the mass percentage of Oxygen at these surfaces, one can notice that at 540°C, higher oxidation levels are observed in the regions without contact, crack

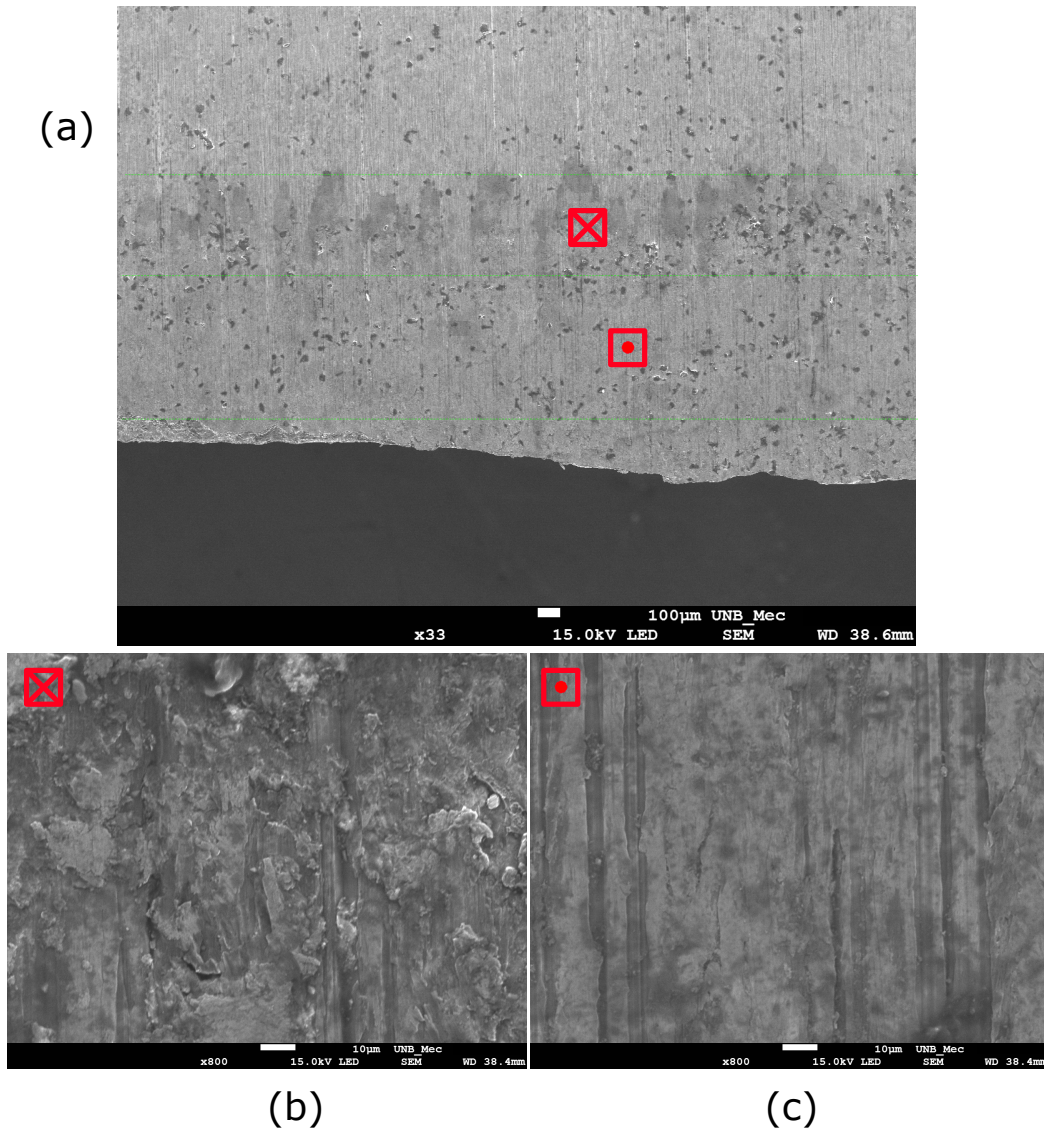


Figure 4.22: SEM observations of the test specimen in-rt-pv-04: (a) Fretting contact mark, (b) zoom view of the slipping zone, and (c) zoom view of the stick zone.

propagation, and fast fracture regions. This fact can be explained by the formation of a protective oxide layer at high temperatures on this nickel-based alloy. On the other hand, higher percentages of Oxygen mass were found in the slip zone and in the crack initiation regions of the Inconel sample tested at 20°C. This could be attributed to the fact that, at room temperature, the wear coefficient is higher, leading to a more severe wear damage, and a more preminent debris formation than at 540°C.

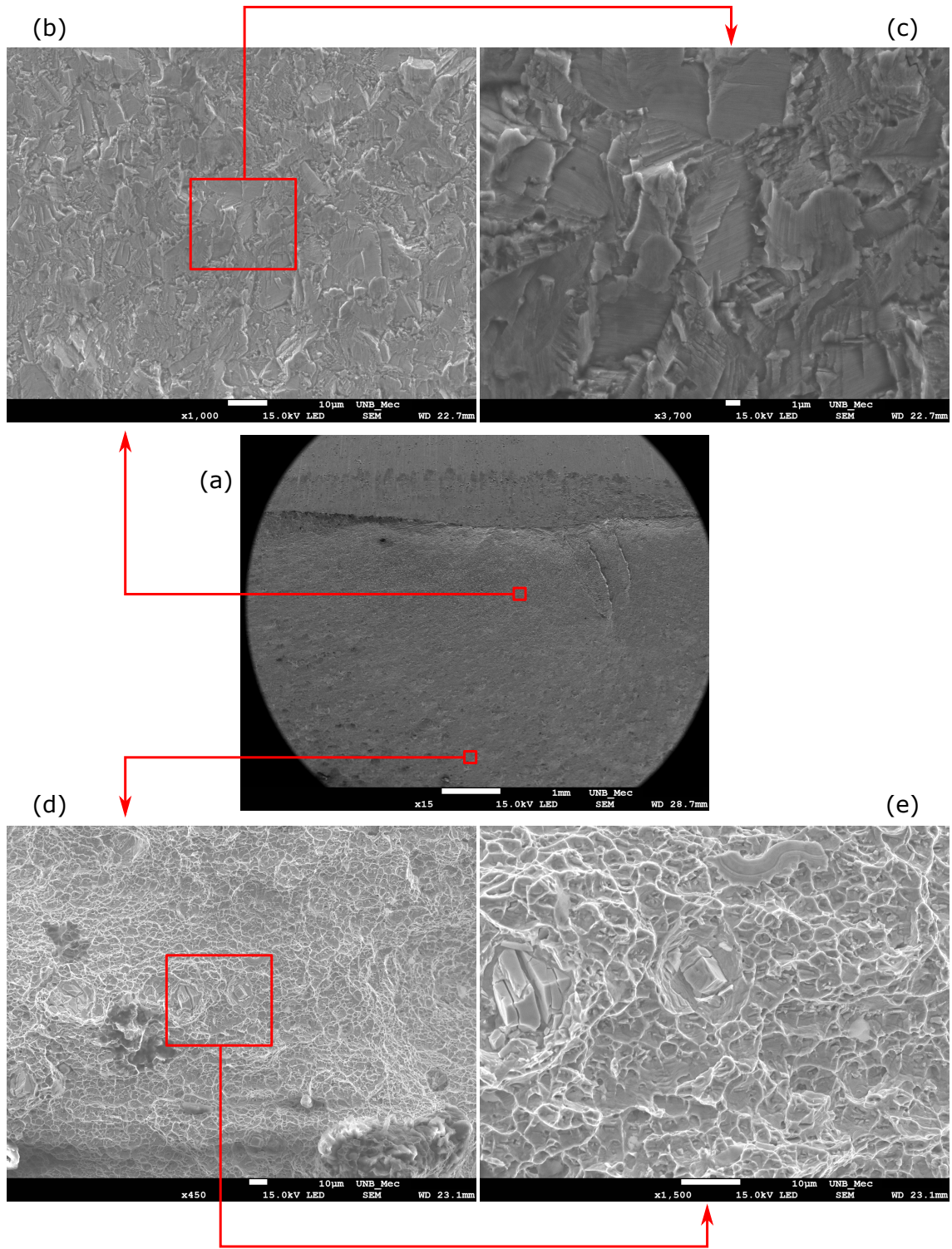


Figure 4.23: SEM observations of the test specimen ff-in-rt-pv-04: (a) Fretting scar and fracture surface, (b) crack propagation region, (c) zoom view of the crack propagation region, (d) fast fracture region, and (e) further amplification of the final fracture region showing the dimples.

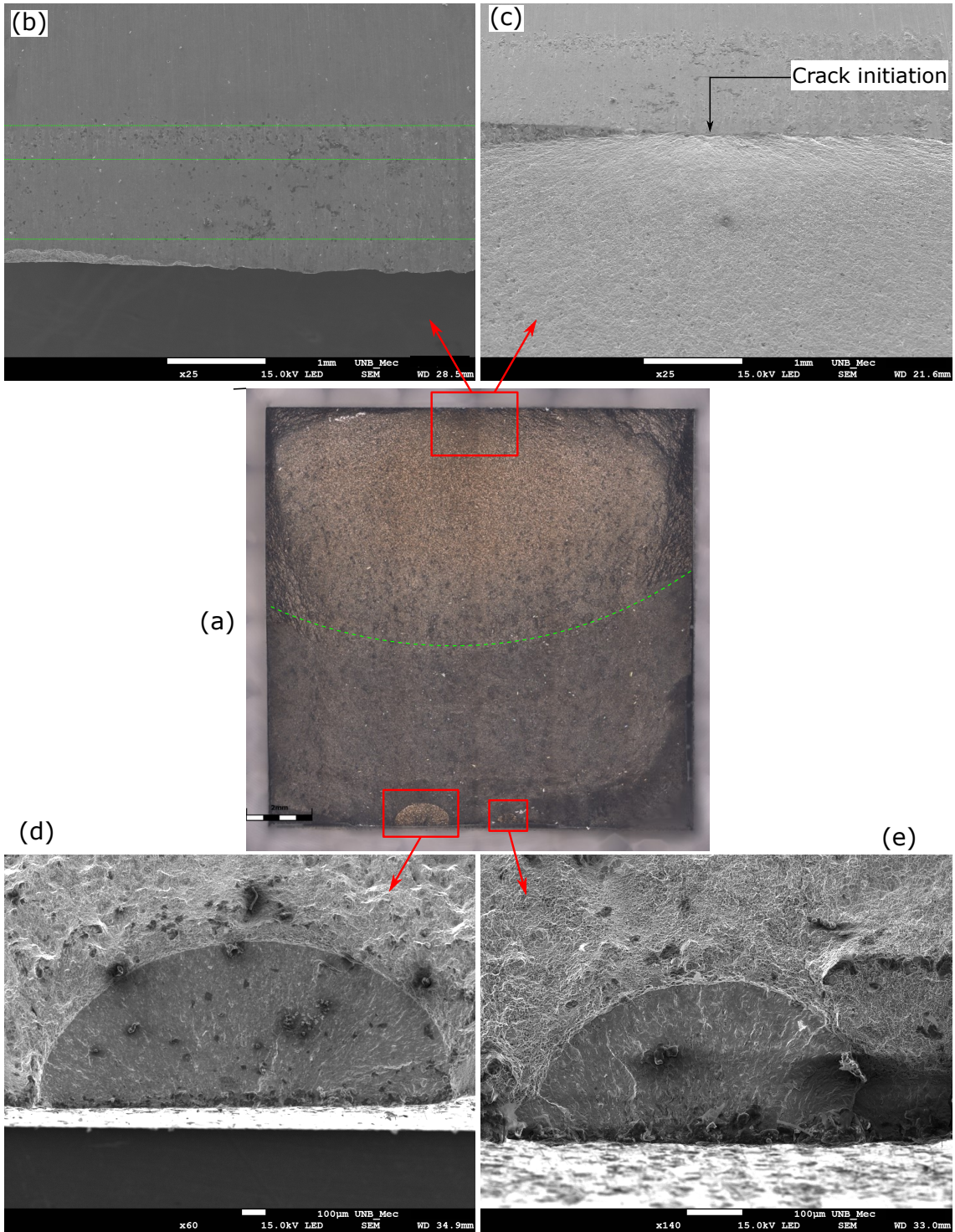


Figure 4.24: SEM and confocal laser observations of the test specimen ff-in-ht-pv-03: (a) Specimen fracture surface, (b) detail of the contact surface, (c) inclined photo with view of the crack initiation site and (d) and (e) arrested cracks at the opposite contact region.

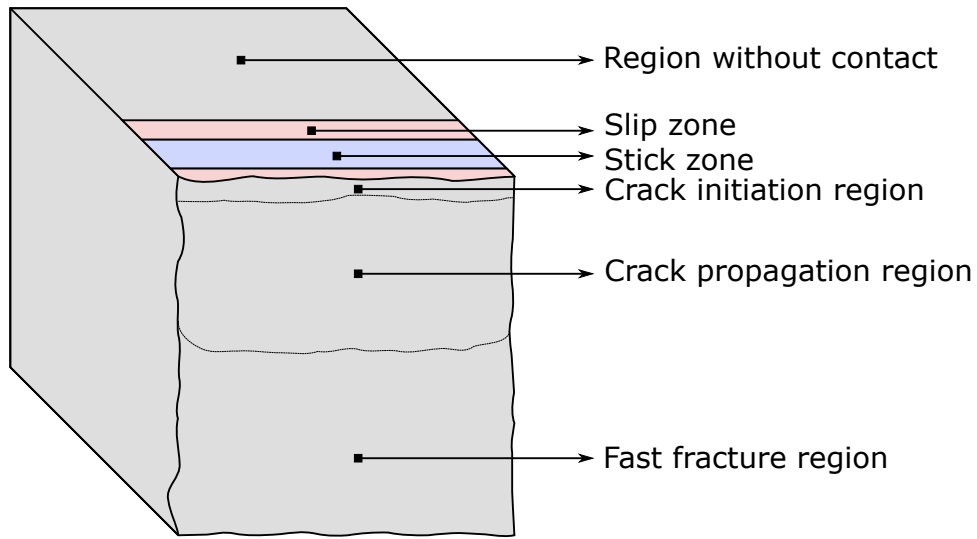


Figure 4.25: Illustration of the locals where the SEM/EDX analyses were carried out.

Table 4.16: Mass percentage of Oxygen estimated by SEM/EDX analyses on different locals of two selected Inconel 718 specimens.

	Mass % of Oxygen element	
	ff-in-rt-pc-03	ff-in-ht-pc-03
Region without contact	1.7%	5.7%
Slip zone	24.5%	14.7%
Stick zone	5.5%	5.2%
Crack initiation region	28.7%	9.6%
Crack propagation region	3.0%	9.5%
Fast fracture region	2.6%	7.9%

#### 4.4.6 . Summary and final remarks on on the fretting fatigue tests

In this Chapter, the results of the fretting fatigue tests were presented. Such experiments aimed to investigate the influence of a variable contact normal loading and also of an elevated temperature on the lives and crack initiation direction. For a sake of clarity, the main results were summarized in Tables 4.17 and 4.18, respectively. According to the results reported in Table 4.17, one can notice that this specific cyclic contact



normal load had a beneficial effect on fretting life. This behaviour was observed for the Ti-6Al-4V and Inconel 718 alloys and at both tested temperatures (20°C and 540°C).

Table 4.17: Average life results of the Fretting Fatigue experimental campaign and life comparison.

Material and Temp.	Testing Set 1	Testing Set 2	Life ratio (Set 2/Set 1)
	Avg. Life [cycles]	Avg. Life [cycles]	
Ti-6Al-4V at RT	840k ± 158k	1259 ± 306k	1.50
Inconel 718 at RT	299k ± 28k	566k ± 70k	1.89
Inconel 718 at HT	183k ± 20k	239k ± 35k	1.31

Table 4.18: Average fretting crack initiation directions of the Fretting Fatigue experimental campaign.

Material and Temp.	Testing Set 1	Testing Set 2
	Mean Crack angle, $\theta$ [°]	Mean Crack angle, $\theta$ [°]
Ti-6Al-4V at RT	-2.7 ± 2.0	-2.0 ± 1.1
Inconel 718 at RT	-5.0 ± 3.8	-1.9 ± 4.1
Inconel 718 at HT	-3.0 ± 2.6	-3.6 ± 0.7

It is vital to notice how the experimental loads were designed to not generalize or misinterpret these results. The so-called Testing Set 1 fixes the maximum peak pressure,  $p_{0,\max}$ , the  $Q_a/P_{\max}$  load ratio, and the maximum fatigue bulk stress,  $\sigma_{B,\max}$ . Then, in Testing Set 2, only the contact normal load was varied in order to isolate the effect of cyclic contact normal load on fretting strength. However, some other parameters will inevitably vary due to the change of the contact normal load, such as the  $Q_a/P_{\min}$  load ratio and the  $\sigma_{B,\max}/p_{0,\min}$  stress ratio. Also, there are other intricacies of comparing fretting fatigue tests with constant and cyclic contact normal load, such as the contact size variation. At this point, one can notice the complexity of evaluating the cyclic contact normal load influence on the fretting case and should keep in mind that the presented results should not be generalized and are specific for the materials, temperature and loading conditions considered in this work.

Moreover, based on the conducted experimental campaign and the results reported in Table 4.18, the presence of a cyclic contact normal loads does not seem to influence significantly the fretting crack initiation direction for all combinations of material and

temperature here tested (Ti-6Al-4V at RT, and Inconel 718 at RT and HT). Further, the titanium and nickel alloys here tested indicate that the measured fretting cracks are mode I dominated.

As far as the influence of the temperature on the lives of the Inco 718 specimens is concerned, from Table 4.17, one can see that, under constant contact normal load (Set 1), the rise of the temperature from 20 to 540°C provoked a reduction of 39% on the fretting life. Here it should be highlighted that, as the temperature had an impact on Young's modulus ( $E = 202$  GPa, 20°C and  $E = 171$  MPa, 540°C), the Set 1 tests were designed to keep the same  $p_{0,max}$ ,  $Q/P$  ratio and  $\sigma_b/p_0$ , but their normal, shear and bulk loads will not be the same. For Testing Set 2, where the contact normal load varies with time, it is not possible to establish a more direct comparison of the influence of the temperature on the lives, as, at high temperature, the contact normal load ratio was different from the one at room temperature. This occurred because once we moved such a test campaign to the high-temperature condition, the fretting pads experienced full sliding. Therefore, it was necessary to raise the contact normal load ratio from  $R_p = 0.6$  at room to  $R_p = 0.8$  at 540°C. Here one could imagine why the author did not run new tests with varying contact normal load at room temperature at  $R_p = 0.8$  to allow such comparison. However, we did not have enough specimens to conduct such new tests.

# Chapter 5

## Life estimation and numeric modelling

*This chapter presents the numerical modelling and results of life estimation provided by non-local mutiaxial models coupled with wear analyses for the tests described in the previous Chapter.*

### 5.1 . Multiaxial fatigue life evaluation

It is well known that fretting fatigue is a multiaxial problem. Besides that, stress gradients are also observed in this problem. Figures 5.1 and 5.1 are plots concerning the loading conditions (with constant and cyclic contact normal load) of the Ti-6Al-4V alloy at room temperature considered in this work. In Figure 5.1, the stress  $\sigma_{xy}$  is plotted against the normal stress  $\sigma_{xx}$  (both normalized in respect to the  $p_0$ ) at the point where the multiaxial criterion is evaluated ( $x/a = -1$ ,  $y = L/2$ ) for both loading cases at the time when the normal load  $P$  reaches its maximum, where  $a$  is the semi-width of the contact and  $L$  is the critical distance. In such a figure, one can observe that the problem assessed is non-proportional and presents a significant level of multiaxiality. Furthermore, Figure 5.1 shows the normalized stresses inwards of the contact. Observing the normal stress  $\sigma_{xx}$ , it is possible to observe a fast stress gradient in such a stress. For these reasons, the author have chosed to estimate fretting fatigue live by means of a combination of a non-local averaging stress method and a multiaxial parameter (TCD by means of the point method and the SWT criterion).

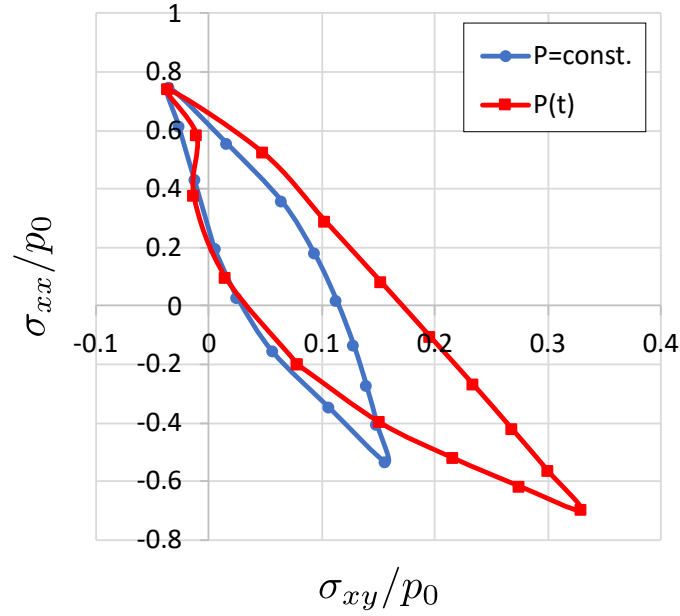


Figure 5.1: Stresses non-proportionality of the loading conditions of the Testing Sets 1 ( $P = const.$ ) and 2 ( $P(t)$ ) for the Ti-6Al-4V at the point where the multiaxial criterion is evaluated ( $x/a = -1, y = L/2$ ) over a complete fretting fatigue cycle.

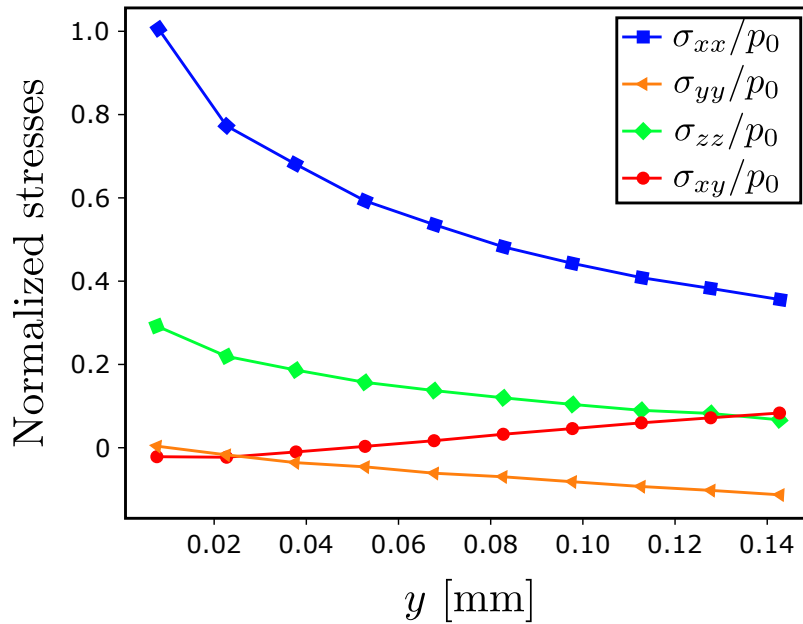


Figure 5.2: Normalized stresses inward the contact for loading conditions with cyclic contact normal load for the Ti-6Al-4V at the point where the multiaxial criterion is evaluated ( $x/a = -1, y = L/2$ ) when  $P(t) = P_{max}$ .

The present chapter aims to evaluate the accuracy of some models available in the literature to estimate the fretting fatigue lives under the more challenging experimental conditions proposed in this work, which considers not only two different aeronautical alloys (Ti-6Al-4V and Inconel 718), but also some tests under varying normal contact loading and under high temperature (only for the Inconel 718). To do so, one of the steps of the analysis is to invoke the  $SWT$  multiaxial fatigue parameter (described in more details in subsection 2.2.3), which requires  $S \times N$  data of the materials under investigation to be calibrated.

For the Ti-6Al-4V alloy, [Cardoso et al. \(2019\)](#) has already calibrated the  $SWT$  parameter as a function of life using  $S \times N$  data generated by [Kallmeyer et al. \(2002\)](#):

$$SWT_{Ti6-4,RT} = 4.35N_f^{-0.093} + 2.45 \times 10^4 N_f^{-0.94} \quad (5.1)$$

where  $N_f$  is the number of cycles to total failure. In Figure 5.3, one can see the plain fatigue data expressed by means of the  $SWT$  parameter and the curve fitting expressed as a two parameters power law.

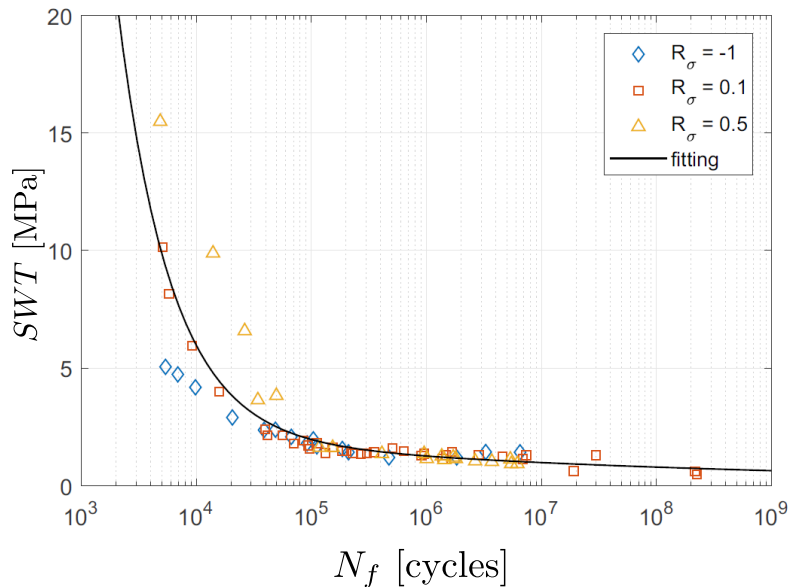


Figure 5.3: Uniaxial fatigue data for the Ti-6Al-4V expressed in terms of the  $SWT$  parameter and curve fitting ([Cardoso, 2019](#)).

Similarly, for the Inconel 718, the  $SWT$  life parameter was calibrated using uniaxial

fatigue data provided by Kawagoishi et al. (2000) and Ma et al. (2010) for the room temperature condition, and in the works by Brinkman and Korth (1973); Chen et al. (1999); Kawagoishi et al. (2000); Yan et al. (2003), for the high temperature one. In Figures 5.4 and 5.5, one can see the plain fatigue data expressed by means of the  $SWT$  parameter and its respective curve fitting expressed by the Equations 5.2 and 5.3, for both temperature conditions.

$$SWT_{In718,RT} = 3.218 \times 10^4 \times N_f^{-0.8506} + 1.085 \quad (5.2)$$

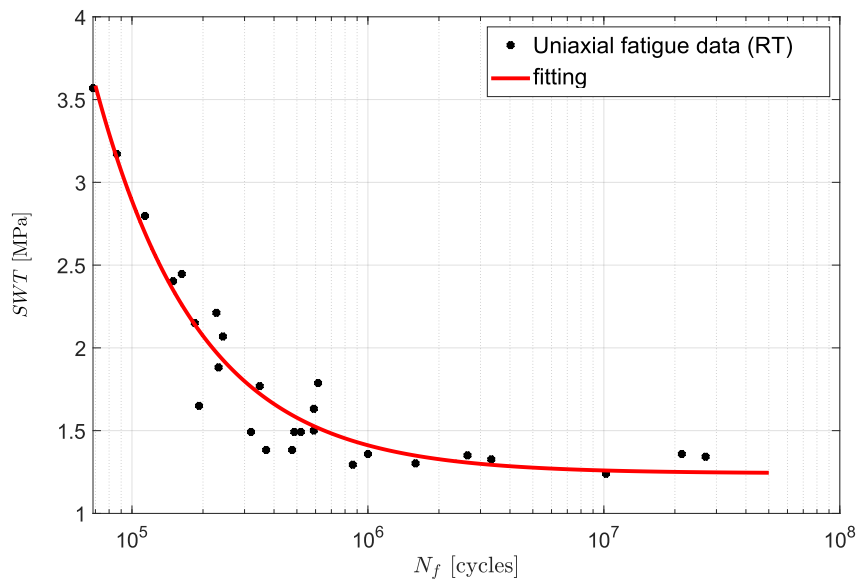


Figure 5.4: Uniaxial fatigue data for the Inconel 718 expressed in terms of the  $SWT$  parameter and curve fitting (room temperature).

$$SWT_{In718,HT} = 4176 \times N_f^{-0.8091} + 2.725 \quad (5.3)$$

## 5.2 . Damage accumulation methodology and surface geometry update

Another step required in the life estimation methodology is to consider the presence of fretting wear, which will provoke changes in the profile of the contact surfaces as the test/analysis evolves and, consequently, will also interfere in the cyclic stress field

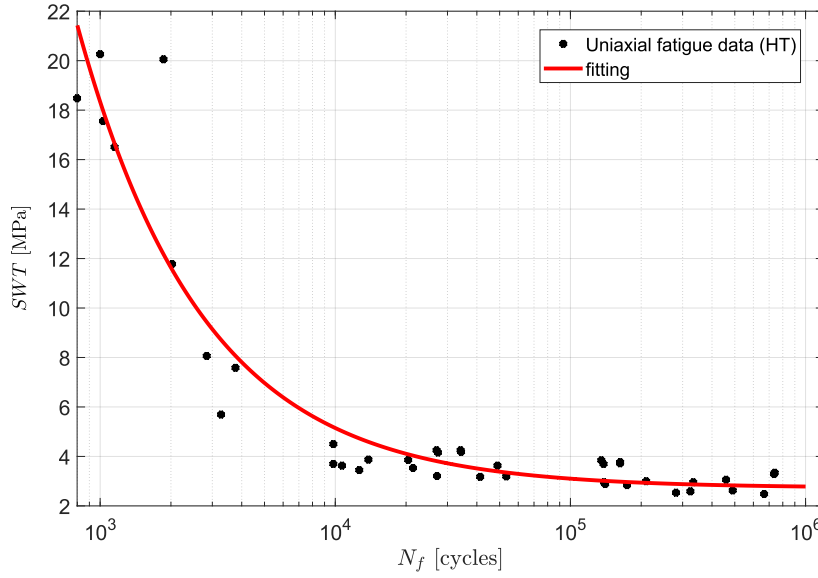


Figure 5.5: Uniaxial fatigue data for the Inconel 718 expressed in terms of the  $SWT$  parameter and curve fitting (elevated temperature).

under the contact. By means of Equations 2.51 and 2.53, wear effects can be easily incorporated on a nodal basis in finite element (FE) analyses. However, it is worth noticing that the wear damage evolves very slowly over a given fretting cycle. In this setting, computing wear and updating contacting surfaces cycle by cycle can be very costly and time-demanding. A common technique used to overcome this problem and speed up the computation of wear depth is to adopt a jumping factor,  $\Delta N$ . Psychically speaking, it consists in assuming that the wear rate is nearly the same for  $\Delta N$  cycles.

By accounting the jumping factor and the FE nodal discretization in Eq. 2.51, the Archad's can be written as:

$$\Delta h_{i,j} = \sum_{k=1}^{n_{inc}} \kappa p(x_j, t_k) \Delta S(x_j, t_k) \Delta N \quad (5.4)$$

where  $\Delta h_{i,j}$  is the increment of wear depth of a node  $j$  located at the contact surface position  $x_j$  for the fretting cycle  $i$ , and  $p(x_j, t_k)$  and  $\Delta S(x_j, t_j)$  are distribution of pressure and the relative slip increment of the node  $j$  at the time increment  $t_k$ .

Similarly, now considering the FE nodal discretization in Eq. 2.53, the friction energy

wear approach  $\Delta h_{i,j}$  can be calculated as:

$$\Delta h_{i,j} = \sum_{k=1}^{n_{inc}} \alpha q(x_j, t_k) \Delta S(x_j, t_k) \Delta N \quad (5.5)$$

where  $q(x_j, t_k)$  is the shear traction for the node  $j$  at the time instant  $t_k$ .

By the end of each simulated fretting cycle, the geometry of the contact interface is updated. Thus, the subsurface stress field is modified at every  $\Delta N$  cycles. This essentially means that it is necessary to introduce a damage rule, such as the Miner's rule (Miner, 1945), to sum up the fatigue damage:

$$D_{f,n}(\mathbf{x}) = \sum_{i=1}^n \frac{\Delta N}{N_{f,i}(\mathbf{x})} \quad (5.6)$$

where  $N_{f,i}$  is the total life estimated (Eqs. 5.1, 5.2, and 5.3) for a given subsurface point with position  $\mathbf{x}$ . The simulation ends when  $D_{f,n} \geq 1$  or at a run-out condition ( $2 \times 10^6$  cycles).

In order to update the surface geometry, it was considered the remeshing technique (McColl et al., 2004; Ding et al., 2004; Garcin et al., 2015). Such a technique consists in vertically moving (according to Eqs. 5.4 and 5.5) the coordinates of the contacting nodes after the fretting simulated cycle and generate a new mesh to avoid element distortion. A flowchart illustrating the FE-based wear model combined with the remeshing technique is shown in Fig.5.8. A Python script manages all simulation phases which consists in the simulation of each fretting cycle  $i$  followed by the update of the contacting surfaces, where the contact nodes are vertically moved depending on the selected wear approach (Achard's or Friction energy wear).

To allow comparisons, the non-local multiaxial fatigue approach will also be assessed in the absence of fretting wear. In such cases, the stresses components required in the *SWT* criterion will simply be directly extracted at a vertical critical distance ( $L/2$ ) from the trailing edge of the contact ( $x/a = -1$ ), as depicted in Fig. 5.7(a). On the other hand, when wear effects were considered, the so called hot-spot point at the contact



surface is not fixed at the same local. For this specific case, the damage parameter is defined by Eq. 5.6 as usual, however failure is only considered for those points located at least  $L/2$  deeper than the contact surface, as illustrated in Figure 5.7b). [Cardoso \(2019\)](#) has produced an excellent work containing many details of the numerical methodology required to implement a similar coupled fretting wear-life analysis.

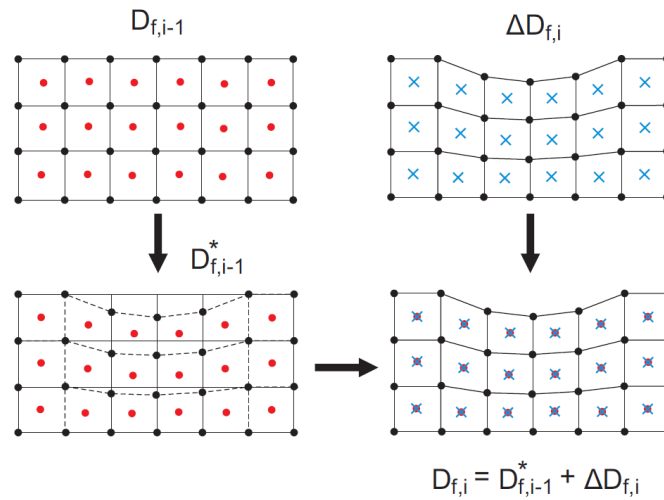


Figure 5.6: Illustration of the methodology used in order to transfer the cumulative damage from a previous fretting cycle simulation to the next (adapted from [Cardoso \(2019\)](#)).

### 5.3 . Numerical model

The numerical analysis carried out in this work was conducted using the commercial FE software ABAQUS 6.14. The 2D FE model is illustrated in Fig. 5.9. To be consistent with the experimental campaign, the same loading sequence was adopted into the simulations, as depicted in Figs. 4.12(a) and (b) for the cases with constant and cyclic contact normal load, respectively. Notice in Fig. 5.9 that surrounding the contact between the cylindrical pad and the plain specimen, a highly refined rectangular region composed of four-node plane strain elements (CPE4R) was used, and outside this area, the mesh consisted of coarse triangular elements. For the Ti-6Al-4V and Inconel 718 simulations the element sizes adopted in the refined rectangular regions were  $15\mu\text{m}$  and  $10\mu\text{m}$ , respectively. Frictional contact constraints were enforced through the Penalty

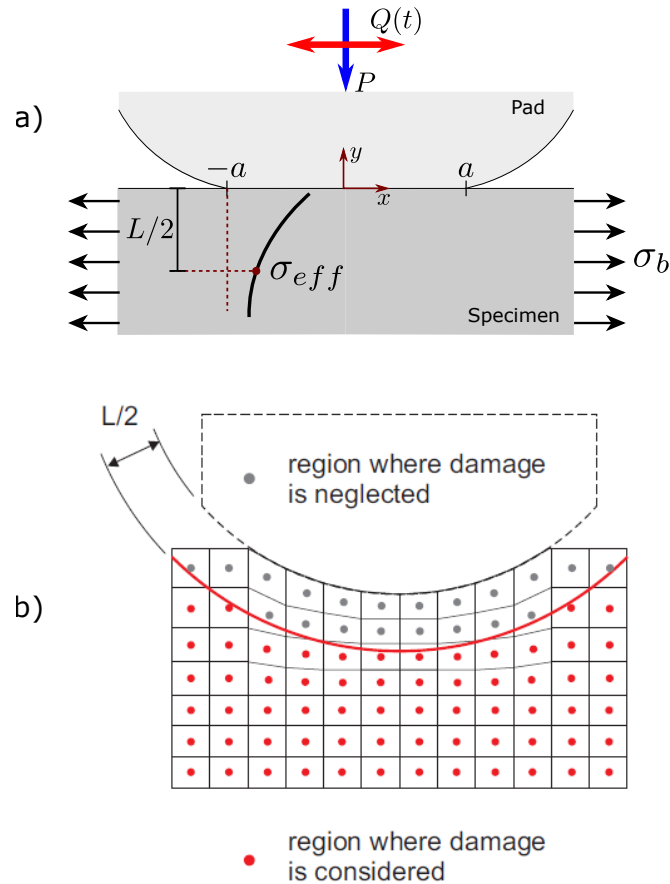


Figure 5.7: TCD applied to fretting problems when wear effects are a) neglected and b) included (adapted from Cardoso (2019)).

method.

Simulations for the fretting tests involving the presence of constant and of cyclic contact normal loading were carried out initially without considering wear effects and later including the energy friction law to update the worn contact profile. In order to evaluate the accuracy of the finite element model, a comparison between the analytical and numerical solutions for the normal and shear tractions (test with constant contact normal load) was conducted, as seen in Fig. 5.10.

## 5.4 . Results

In the present numerical analysis, the wear was computed by using both wear approaches presented in Section 2.4, the Archard and friction energy approaches. For the

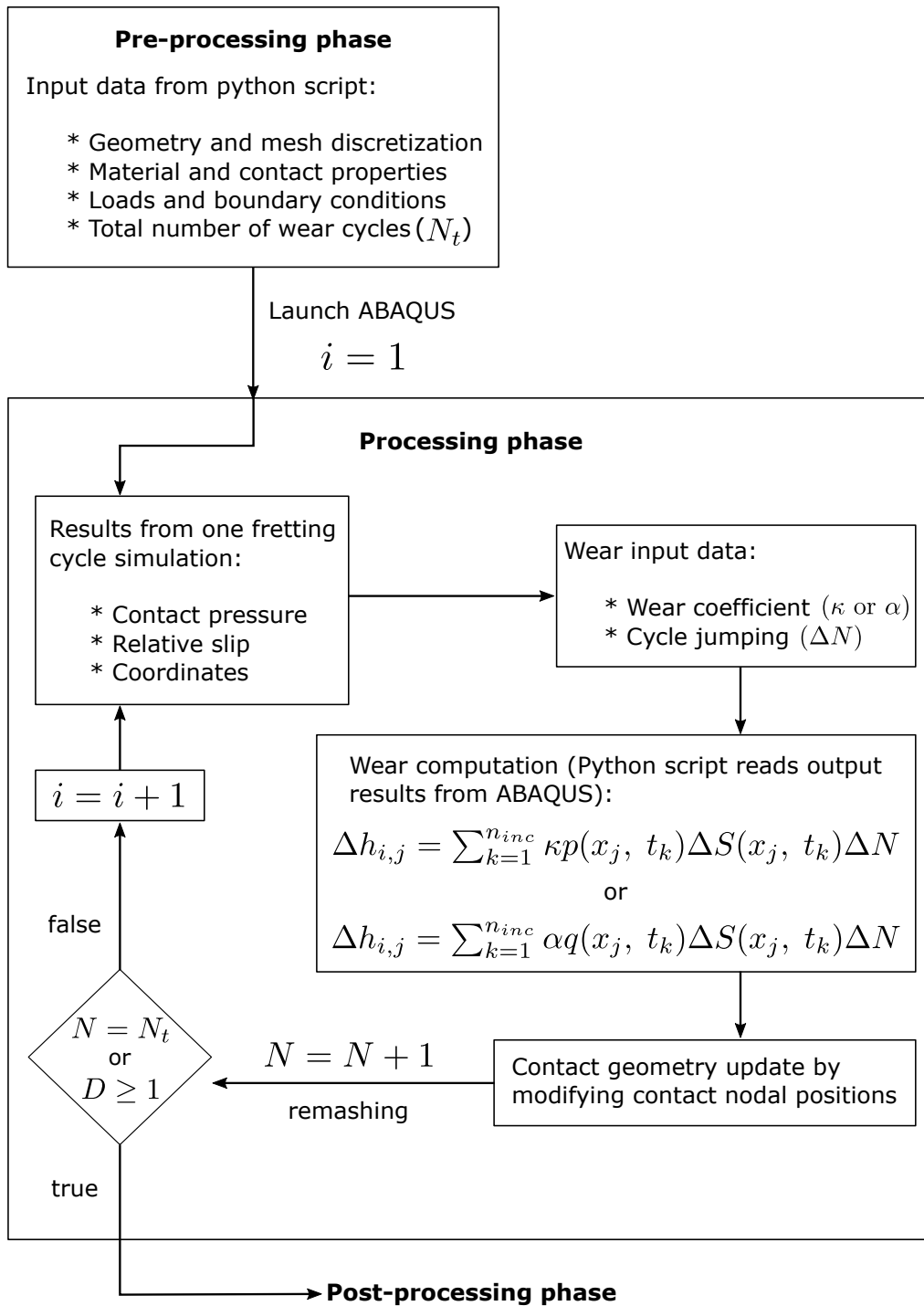


Figure 5.8: FE-based model for wear analysis using the remeshing technique.

Ti-6Al-4V, the former one was used and the friction energy wear coefficient ( $\alpha$ ) adopted was  $1.43 \times 10^{-8} \text{ MPa}^{-1}$  (Garcin et al., 2015). On the other hand, for the Inconel 718 alloy, the wear damage was calculated by the Archard's approach and the wear coefficients were estimated at room ( $\kappa = 2.82 \times 10^{-9} \text{ MPa}^{-1}$ ) and at  $540^\circ\text{C}$  ( $\kappa = 1.09 \times 10^{-9}$

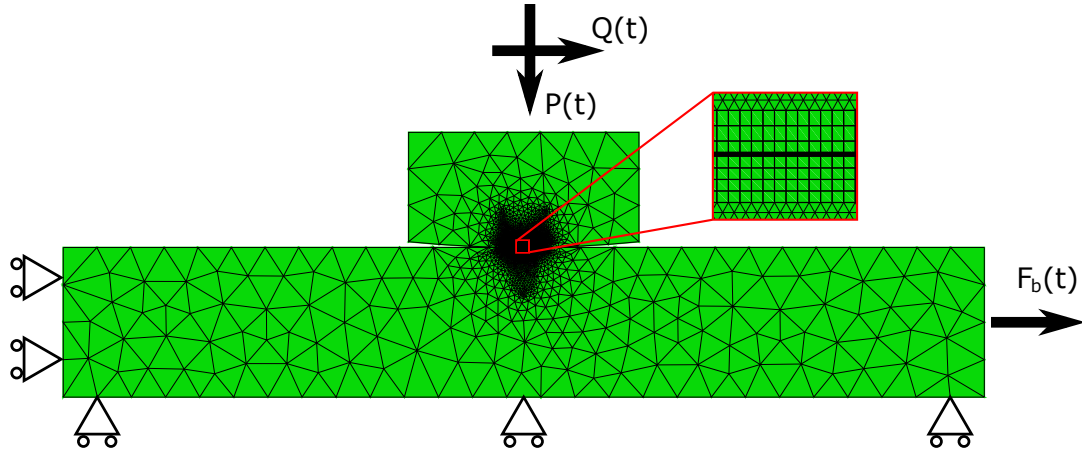


Figure 5.9: Finite element model used to simulate fretting fatigue.

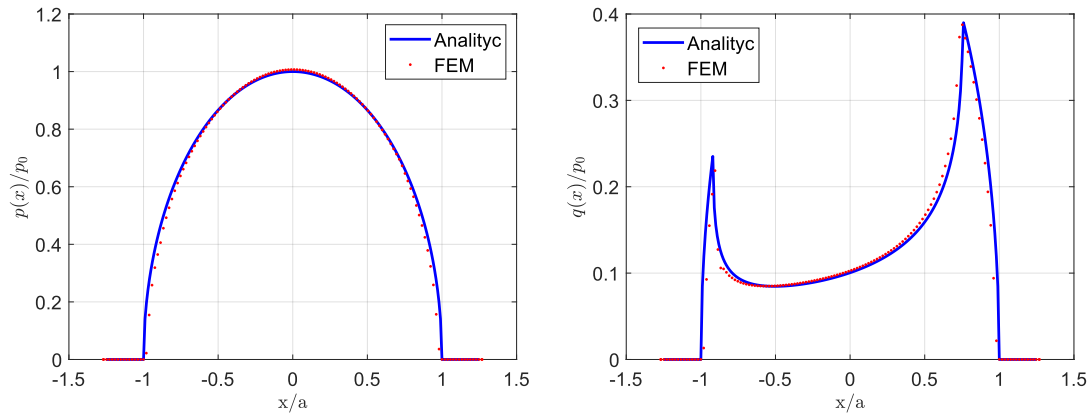


Figure 5.10: Comparison between the analytical and numerical solutions for the normal and shear tractions (test with constant contact normal load).

$\text{MPa}^{-1}$ ) from the work by [Hamdy and Waterhouse \(1981\)](#). A jump factor ( $\Delta N$ ) of 2000 cycles has been considered in the analysis for all cases. Moreover, the critical distance adopted in this work for the Ti-6Al-4V at room temperature is  $L = 30 \mu\text{m}$  ([Bellecave et al., 2014](#)). The critical distances for the Inconel 718 alloy were calculated using fatigue material properties provided by Safran and the threshold stress intensity factor from [Jeong et al. \(2014\)](#). In such a manner, the critical distances at room and  $540^\circ\text{C}$  are  $L = 101 \mu\text{m}$ , and  $L = 39 \mu\text{m}$ , respectively.

The final worn surface profiles for the case with constant contact normal load and cyclic one can be observed in Figure 5.11. Considering the Ti-6Al-4V material and the room temperature (Fig. 5.11a)), it is possible to observe that wear was more severe for the cyclic contact contact normal load configuration where, in this case, material loss

was 31% higher than that verified at the constant contact normal load case. For the Inconel 718, one also can observe an increase of wear volume of the case with cyclic normal contact load when compared with the constant one. Such increases corresponded to 36% and 128% at room and elevate temperature, respectively. Table 5.1 reports all these results besides the estimated worn volume of each case.

Table 5.1: Wear volume comparison between the constant and cyclic contact normal load cases. All volumes expressed in  $10^{-4}\text{mm}^3$

Material and Temperature	Contact normal loading		Wear volume ratio
	Constant	Cyclic	
Ti-6Al-4V at RT	3.06	4.03	1.31
Inconel 718 at RT	1.13	1.55	1.36
Inconel 718 at HT	1.14	2.60	2.28

One reason for explaining this effect is due to the fact that under cyclic normal contact load, the size of the contact zone changes, as illustrated in Fig. 5.12. Note that when one compares the constant and normal contact loading cases investigated in this work, all the other loads involved in the test are the same but the normal contact load, which varies sinusoidally in phase with the fretting loads. In this case, for the cyclic contact normal load case, when the tangential load achieves its minimum value, the contact normal load is lower than the one observed in the constant contact normal load configuration. Therefore, not only the contact zone, but also the stick zone size for the time instant in which  $P(t)$  reaches its valley (and also  $Q(t) = Q_{\min}$ ), will be smaller than the one for the case where  $P$  is constant and  $Q(t) = Q_{\min}$ . In the reverse of the normal contact load, the contact size and the stick zone will both increase reaching a maximum at the peak of the contact normal load,  $P(t) = P_{\max}$  (which coincides with  $Q(t) = Q_{\max}$ ). At end, the resulting fretting scar for the time varying normal contact load test will be larger than that for the constant contact normal load test (see scheme of the resulting fretting scars in both cases in Figure 5.12).

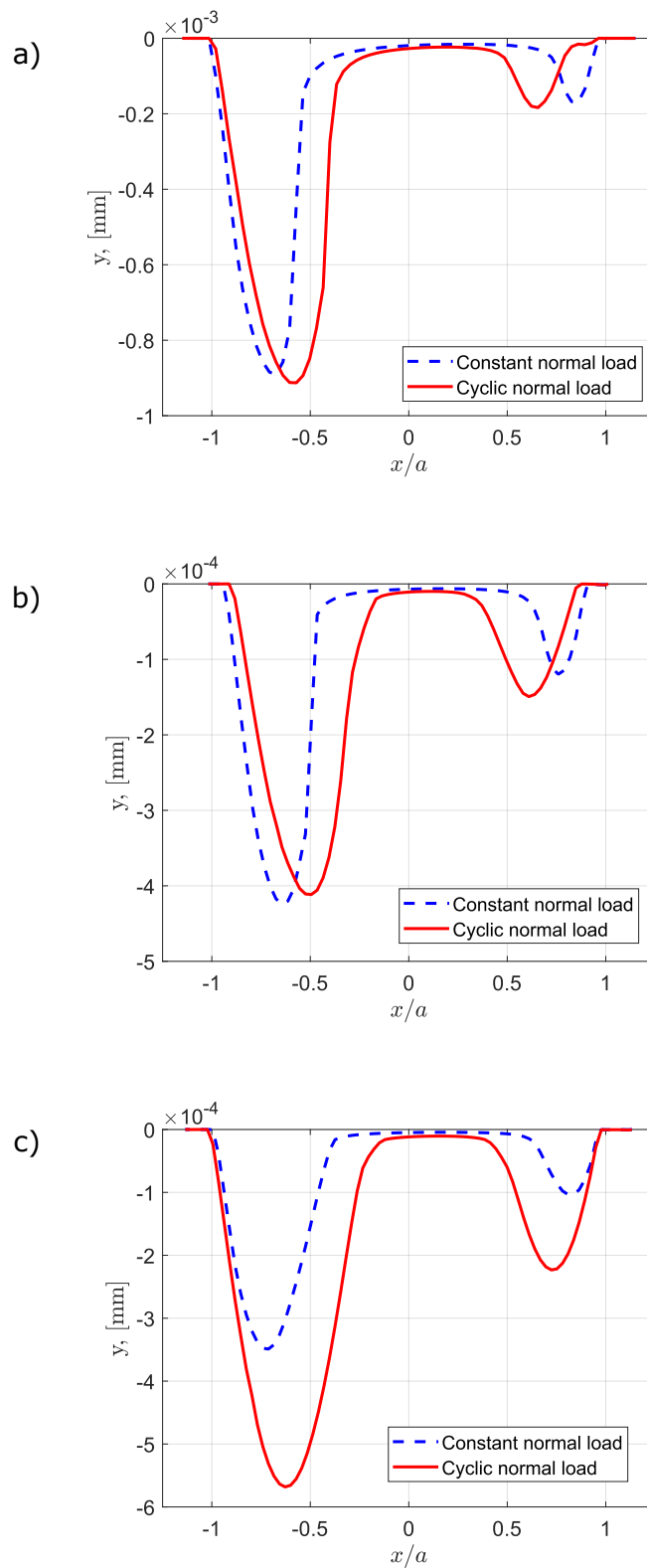


Figure 5.11: Specimen final worn superficial profiles predicted by the FE simulations for the loading case with constant contact normal load (dashed line), and cyclic contact normal load (solid line). a) Ti-6Al-4V at RT; b) Inconel 718 at RT; c) Inconel 718 at HT.

Additionally, Figure 5.13 shows contacts tractions observed in the Ti-6Al-4V simulations for the following cases: (a) with constant contact normal load and neglecting wear, (b) with constant contact normal load and considering wear, (c) with cyclic contact normal load and neglecting wear, and (d) with cyclic contact normal load and considering wear. In the same way, Figures 5.14 and 5.15 depict the tractions for the Inconel 718 at room temperature and at 540°C, respectively.

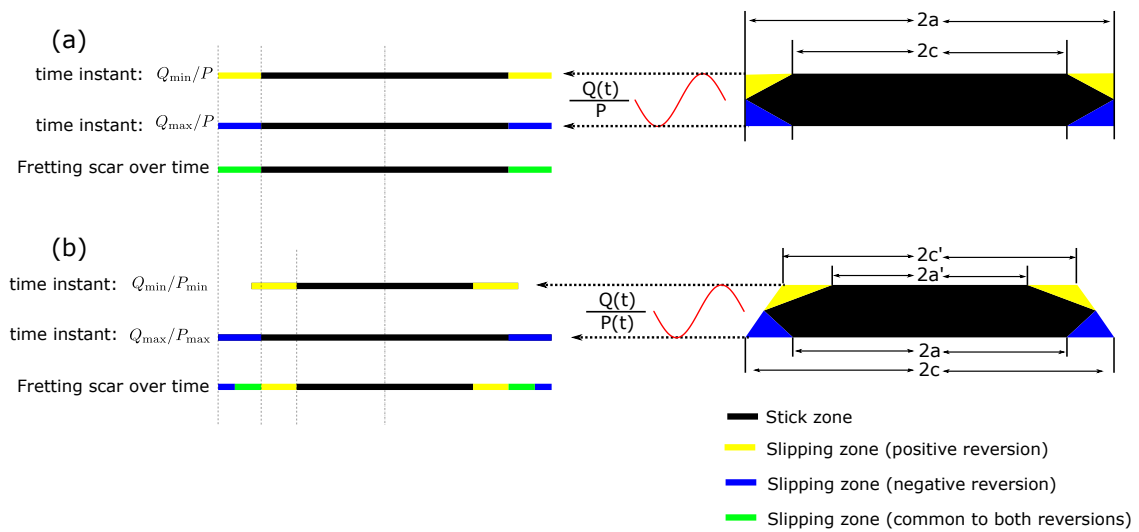


Figure 5.12: Illustration of changes in the contact, stick and slip zones showing the resulting fretting scar for (a) constant contact normal load and (b) cyclic contact normal load.

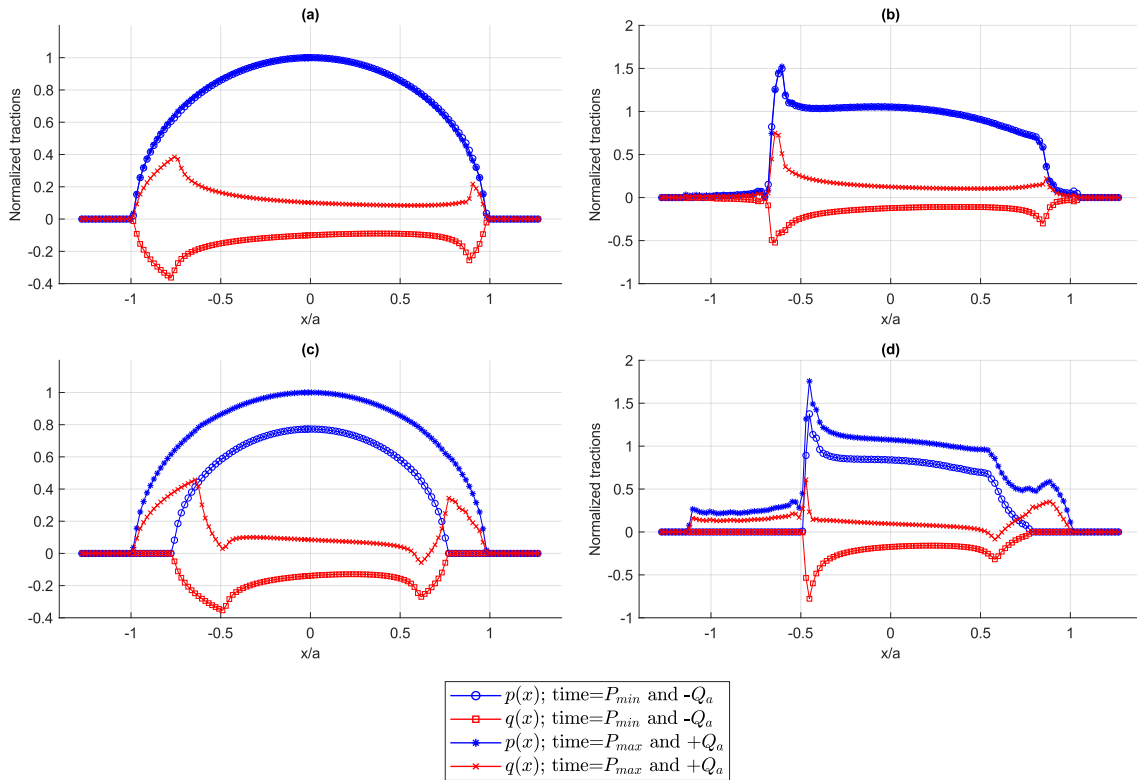


Figure 5.13: Tractions for Ti-6Al-4V tests at room temperature: (a) with constant contact normal load and neglecting wear, (b) with constant contact normal load and considering wear, (c) with cyclic contact normal load and neglecting wear, and (d) with cyclic contact normal load and considering wear. All tractions were normalized considering the peak pressure,  $p_0$ , for the case with constant contact normal load and neglecting wear.



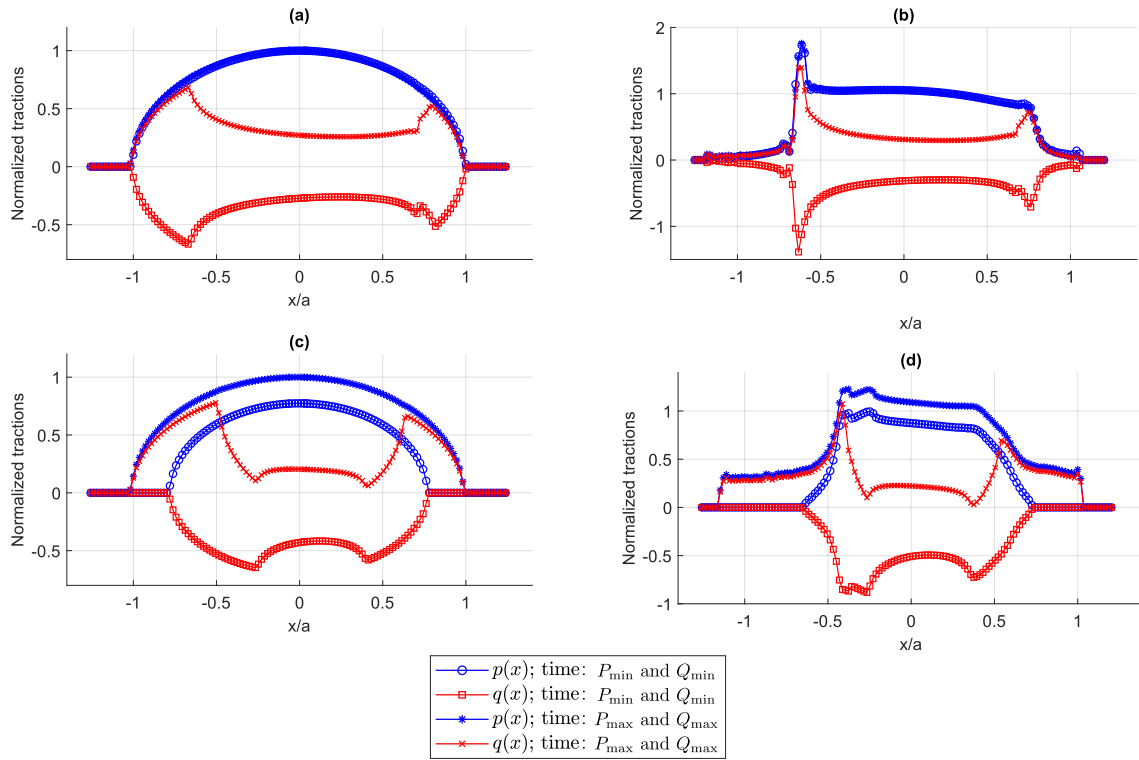


Figure 5.14: Tractions for Inconel 718 tests at room temperature: (a) with constant contact normal load and neglecting wear, (b) with constant contact normal load and considering wear, (c) with cyclic contact normal load and neglecting wear, and (d) with cyclic contact normal load and considering wear. All tractions were normalized considering the peak pressure,  $p_0$ , for the case with constant contact normal load and neglecting wear.

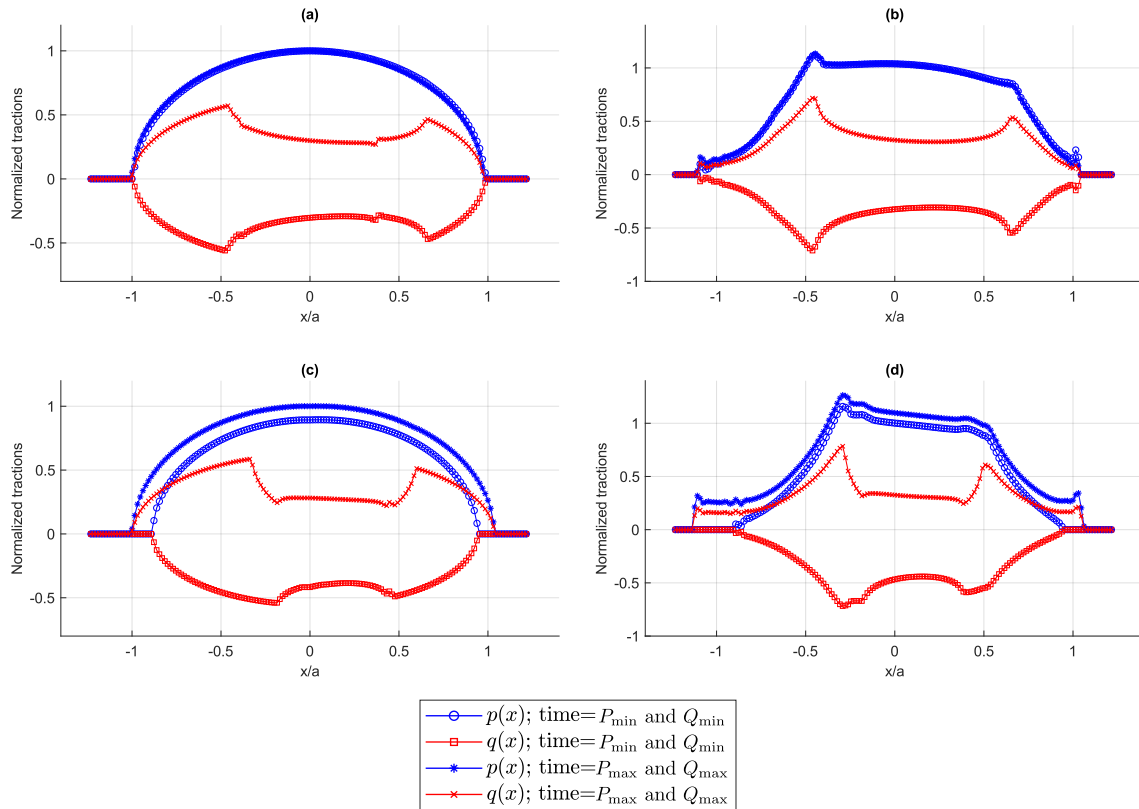


Figure 5.15: Tractions for Inconel 718 tests at elevated temperature: (a) with constant contact normal load and neglecting wear, (b) with constant contact normal load and considering wear, (c) with cyclic contact normal load and neglecting wear, and (d) with cyclic contact normal load and considering wear. All tractions were normalized considering the peak pressure,  $p_0$ , for the case with constant contact normal load and neglecting wear.

Besides wear damage profiles were predicted by the FE model, compare these results with the experimental observations was not possible for several reasons. Both materials under study in this thesis present high hardness and low wear coefficients. The fretting fatigue tests were conducted under the partial-slip regime and moderated levels of contact pressure to avoid plasticity in the contact. The tests run out up to the total failure of the fretting specimen, sectioning the fretting scar. Moreover, the superficial quality of the experimental parts were not the ideal one to evaluate wear damage in such a low levels. For instance, considering the Ti-6Al-4V alloy, the average superficial roughness

of the specimens was  $0.65\mu\text{m}$  and the wear depth predicted by the simulations for the constant constant normal load case was equal to  $0.9\mu\text{m}$ , in other words, the specimen surface has defects with almost the same depth of the predicted wear. In Figure 5.16 one can observe a fretting contact scar of a fretting fatigue test under constant contact normal load in a Ti-6Al-4V specimen under three different microscope magnifications: (a) 108x, (b) 432x, and (c) 1080x. Figures 5.16(b) and (c) show also the superficial profiles measured using a confocal laser microscope. It can be noted that these profiles practically do not show any variation along the contact mark and also in the region that has not suffered damage by fretting. For these reasons the reader can imagine why in this thesis a comparison between the simulated and experimental wear damage profiles was not presented. The combination of a hard and wear resistant material, moderate contact load, low tangential amplitude reflected in an unmeasurable wear depth by the means available for the author.

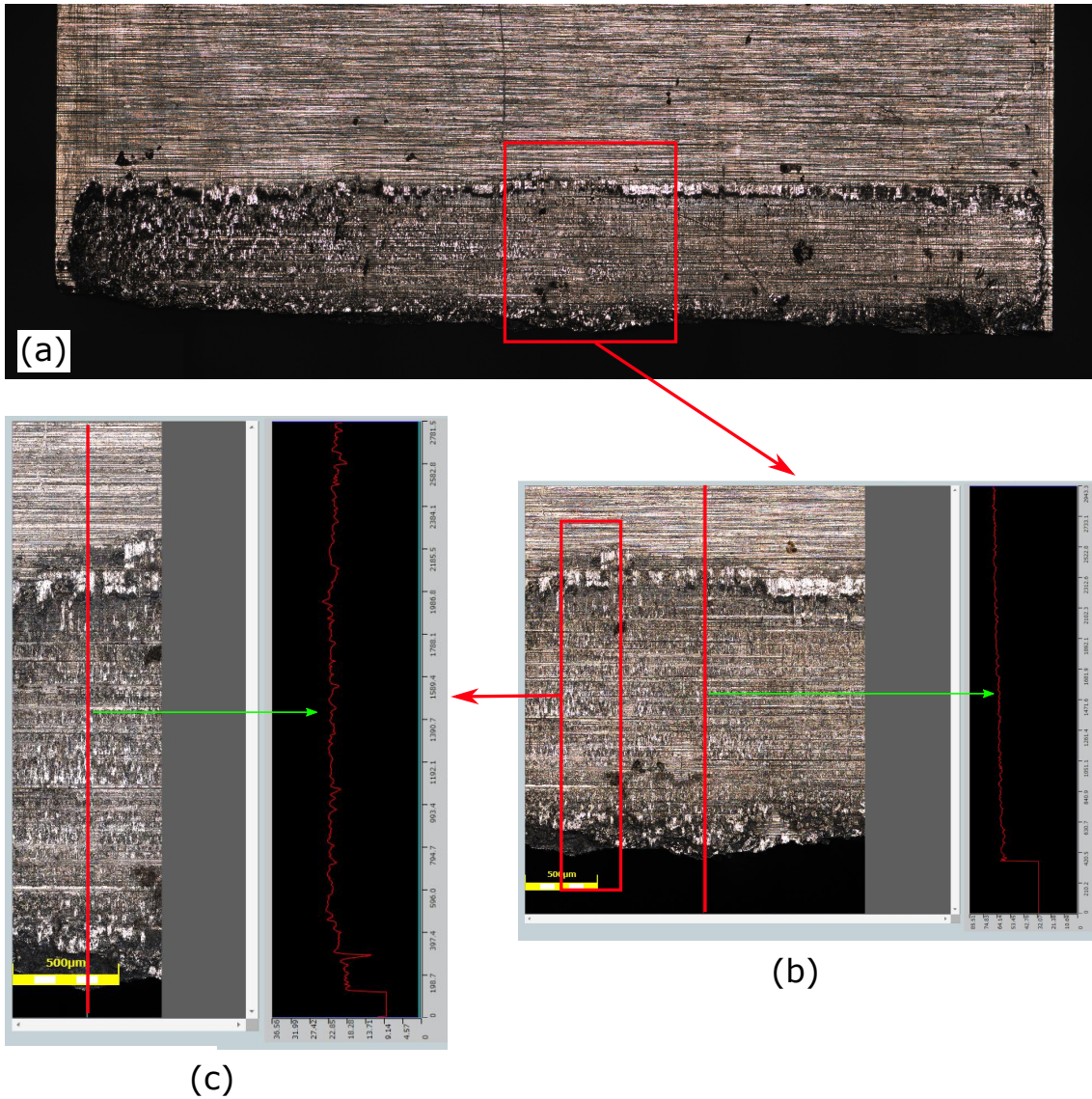


Figure 5.16: Attempts to determine wear depth of the specimen ff-ti-pc-04 under different magnifications: (a) 108x, (b) 432x, and (c) 1080x.

Table 5.2 reports the estimated lives provided by the simulations considering the impact of the inclusion of wear in the computations for these new experimental data involving all the materials, temperature and loading conditions used in the experimental campaign. For the Ti-6Al-4V, the experimental results show an increase in fretting life under cyclic load conditions compared with those with a constant contact normal load. The numerical results for the model neglecting the presence of fretting wear in the analysis were able to capture this effect predicting fretting lives of 764k and 1440k

cycles for the conditions with constant and cyclic contact normal load, respectively, while tests provided 840k and 1259k cycles. However, when wear was included in the analysis, a reduction in estimated lives from 800k cycles (constant  $P$  condition) to 688k cycles (varying  $P(t)$ ) was noticed.

Considering the Inconel 718 at room temperature, the experimental fretting life under cyclic load condition (591k cycles) was also higher than the one associated with a constant contact normal load (299k cycles). However, the numerical predictions for the models (neglecting and considering wear) fail to capture this effect. Disregarding wear, the model estimated fretting lives of 357k and 282k cycles for the conditions with constant and cyclic contact normal load, respectively. Including wear, the model estimated fretting lives of 420k and 316k cycles for the conditions with constant and cyclic contact normal load, respectively.

At last, but not least the experimental lives for the Inconel 718 at elevated temperature (540°C) show the same trend presenting a higher fretting life for the tests conducted under static contact normal load condition than the cyclic ones. For this material and temperature condition, the simulation including wear was able to capture this life effect. However, no significant difference was observed between the predicted lives for the cases with constant and cyclic contact normal load.

Table 5.3 presents errors between the experimental and estimated lives calculated by Eq. 5.7. As presented in this table, for the Ti-6Al-4V and constant contact normal load condition, the FE model, which includes wear effects was slightly more accurate (-5%) than the one which neglects wear (-9%). However, the opposite trend was observed for the case with cyclic contact normal load, and the models without wear provide a small error (14%) than when considering wear (-45%). Concerning the Inconel 718 alloy and constant contact normal load condition, huge values of errors were observed, 19% and 40% for the models neglecting and including wear effects, respectively, while for the cyclic contact normal load lower errors were presented (-52% and -47%) for the model with and without wear, respectively. For the Inconel 718 at high temperature, the lives

estimations were more accurate when the model disregards wear, 13% and less than 1% against 180% and 244% (model regarding wear) for the static and cyclic contact normal load condition, respectively.

Table 5.2: Experimental and estimated lives for the Inconel 718 alloy and Ti-6Al-4V alloys. RT = 20°C and HT = 540°C. All lives are expressed in cycles.

Material and Temperature	Contact normal load	Exp. life	Estimated life (without wear)	Estimated life (with wear)
Ti-6Al-4V at RT	Constant	840k	764k	800k
	Cyclic	1259k	1440k	688k
Inconel 718 at RT	Constant	299k	357k	420k
	Cyclic	591k	282k	316k
Inconel 718 at HT	Constant	178k	202k	498k
	Cyclic	201k	201k	692k

$$Error[\%] = \left( \frac{\text{estimated life}}{\text{experimental life}} - 1 \right) \times 100 \quad (5.7)$$

Table 5.3: Percentile error of experimental and estimated fretting lives.

Material and Temperature	Normal loading	Error [%] (without wear)	Error [%] (with wear)
Ti-6Al-4V at RT	Constant	-9	-5
	Cyclic	14	-45
Inconel 718 at RT	Constant	19	40
	Cyclic	-52	-47
Inconel 718 at HT	Constant	13	180
	Cyclic	0	244

## 5.5 . Summary

In general, considering the partial slip condition and both alloys studied, the life estimates provided by the non-local multiaxial fatigue (SWT criterion) analysis without considering the presence of wear in the modelling provided more accurate results for both cases studied, i.e., with a constant and with a cyclic normal contact load in the fretting configuration, as reported in Table 5.2. In four out of six tested conditions, the estimated life was better when the fretting wear was not computed, excluding only the life predictions for the Ti-6Al-4V tests at room temperature with normal contact load and for the one with Inconel 718 at room temperature but under cyclic normal contact load. The titanium case have presented only a slight difference between the life estimates with the models neglecting (764k cycles) and considering wear damage in the analysis (800k cycles). Similarly, for the Inconel, a negligible difference in life estimation was noticed when the model includes wear (316k cycles) or disregards wear effects (282k cycles). Despite the slight improvements in life estimations for these two specific test conditions, this analysis, which took wear effects into account, proved to be excessively more expensive than the other without wear.

Here one should keep in mind that the coefficient of wear energy  $\alpha$  or the wear coefficient  $k$  used in our analysis was obtained from literature, and this may have a strong influence on the computations. The majority of wear data found by the author available on literature concerns of reciprocating or rotating ball-on-disk tests under a constant contact normal load. Such tests are usually conducted under gross-slip regime. For the Inconel 718 alloy there is another difficulty in finding the a proper value for wear properties once it can be determined at the same temperature of the fretting fatigue tests here conducted.

Ideally, the wear coefficient should have been estimated for the specific material and loading conditions considered in this work. However, as the fretting fatigue tests were performed under partial slip regime, the wear depth is very small, which poses some

difficulties in properly determining the worn profile and estimating the wear coefficient.

For the case with the cyclic contact normal load, as the contact size varies, the simulated wear damage was higher compared with the one with constant contact normal load, as shown in Fig.5.11, which depicts the specimen worn superficial profiles predicted by the FE simulations. Further, Figure 5.17 shows the evolution of the accumulated fatigue damage against the  $x$  position at a depth of  $L/2$ . Besides, even though experiments conducted in this work have shown that the cyclic contact normal load condition has little effect on the measured friction coefficient, the same cannot be asserted concerning the wear coefficient.

It is worthy of notice that, among many multiaxial fatigue available in the literature, only the *SWT* criterion was chosen for the life estimates here conducted. There are several reasons for this choice: (i) [Cardoso et al. \(2019\)](#) evaluated the use of different multiaxial fatigue criteria to compute the fretting lives for tests with Ti-6Al-4V where size and gradient effects were present. They concluded that the application of the non-local *SWT* criterion provided the most accurate results; (ii) the fractography (under the Confocal Laser microscope) of the fractured surfaces for all fretting fatigue tests in this work indicating that the crack initiation was mode I dominated, thus in line with mechanical principle of the *SWT* parameter, which is appropriate for material and loading conditions where cracks initiate in material planes dominated by maximum amplitude of normal stress; (iii) the *SWT* criterion is simpler to implement and calculate than shear stress based critical plane models.

For the life estimates of tests under high temperature, one should notice that, the methodology adopted in this thesis incorporated the effects of elevated temperature only in the material mechanical properties used in the analysis. For instance, the coefficient of friction, the Young's modulus, the fatigue limit and threshold stress intensity factor were altered in the simulation for these tests. Such analysis seems to be perfectly justifiable by the fact that, not only the tests were within the medium-high cycle fatigue regime (negligible levels of macroscopic plasticity), but also they were conducted at 540°C, a



temperature at which no significant effects of creep have been observed by others in the literature for such a material under these loading conditions (Ni and Dong, 2017). Thus, an elastic stress analysis is adequate for tackle the problem.

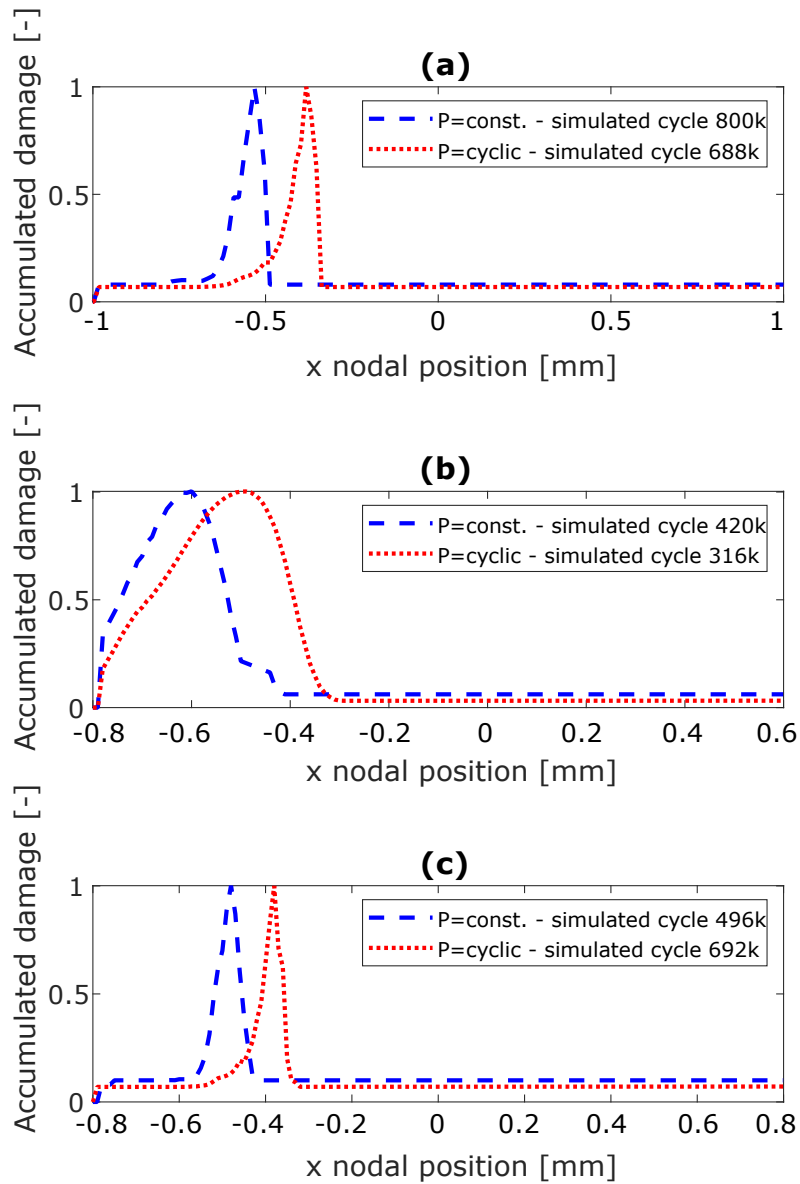


Figure 5.17: Comparison of accumulated fatigue damage along contact at  $L/2$  depth for the cases with constant and cyclic contact normal loads. a) Ti-6Al-4V at RT; b) Inconel 718 at RT; c) Inconel 718 at HT.



# Chapter 6

## Conclusions and perspectives

### 6.1 . Overview

This thesis studied the effect of a time varying normal contact load on the fretting fatigue life at ambient and elevated temperatures for two aeronautical alloys: Ti-6Al-4V and Inconel 718. For this, a new four-actuator fretting fatigue machine was designed to perform such complex tests (Chapter 3). A substantial experimental campaign was carried out in this work (Chapter 4). Tests were carried out to determine the friction coefficient under fretting conditions (with constant and cyclic contact normal loads) for Ti-6Al-4V and Inconel 718 materials. Fretting fatigue tests were also conducted to assess the effect of time-varying contact normal load on the fretting resistance. Furthermore, the effect of temperature was evaluated exclusively for Inconel 718 alloy. In this way, tests to determine the friction coefficient and the fretting resistance were carried out also at 540 degrees Celsius. In addition, life estimation was performed using the *SWT* parameter associated with two numerical approaches: one that included wear damage in the simulation and another that did not (Chapter 5).

### 6.2 . Concluding remarks

The main conclusions of this work can be summarized as follows:

- A new fretting fatigue apparatus was designed and successfully performed fretting fatigue tests with static and cyclic contact normal load at room and elevated temperatures. The new normal contact load application system with two opposite servo-hydraulic actuators resulted in accurate test control of this load. The

heating system using a pair of ceramic igniters proved to be effective, reaching temperatures of up to 750° and to keep the test temperature stable during the tests at 540° within a small range of 10 degrees. Moreover, a methodology was developed and validated to estimate and control the temperature at the fretting contact indirectly.

- Based on the experimental results, the presence of the cyclic contact normal load in the fretting tests provoked an advantageous effect on the specimens durability for both materials under study and at room and high temperatures. However, it is important to notice that such conclusion is valid for specific loading conditions, temperatures and materials evaluated in this PhD work. Further more, as previously mentioned, comparisons between fretting tests with constant and time varying contact normal loads must be exercised with care, as the  $Q(t)/P(t)$  ratio is not constant during the cycle. Additional tests with different loading conditions, materials and temperature should be performed in order to better understand such an effect of the cyclic contact normal load on fretting fatigue and to enforce this statement.
- The increase of temperature from 20°C to 540°C lead to a 39% reduction in fretting life of the Inconel 718 specimens under constant contact normal load (Testing Set 1).
- The presence of a time varying (cyclic) contact normal load did not affected the values measured (mean friction between the one in the stick and the slip zones) or estimated (for the slip zones) of the coefficient of friction for the Ti-6Al-4V and Inconel 718. No significant changes were observed between the coefficients of friction measured for the fretting tests with constant and cyclic contact normal load conditions, for both Ti-6Al-4V and Inconel 718 materials. However, the increase of temperature proved to cause a significant reduction (30%) in the friction coefficient for the Inconel 718 either under  $P = const.$  or for  $P = P(t)$ .

- The available life methodologies considered in this work (non-local multiaxial fatigue) to estimate the fretting fatigue lives under the more challenging test conditions used in this work proved to provide life estimates within a factor of three. Therefore, they are capable to capture the effects of varying contact normal loading and temperature in fretting fatigue. Surely, to generalize such a conclusion, more tests are required.
- For the fretting tests under constant contact normal load, life estimates based on the methodology which includes fretting wear in the analysis were slightly more accurate than the one without wear only for the Ti-6Al-4V and Inconel 718 alloys at room temperature. However, the high computational cost introduced in the wear analysis does not justify its use, at least for the partial slip regime conditions considered in our test campaign. Moreover, for the tests with Inconel 718 at high temperature, the non-local stress based methodology which does not introduce wear in the simulation proved to provide more accurate results.
- For the fretting tests under cyclic contact normal load, the life methodology without inclusion of wear effects provided more accurate results for the Ti-6Al-4V and for the Inconel 718 at elevated temperature. Moreover, the inclusion of the wear into the simulations resulted in life estimates, which did not represent the actual effect of such load variation. While the experiments registered an increase in life with variation of the normal contact load, the life methodology which included the update of the contact surface profile by the introduction of wear, estimated a reduction in the life.
- No significant difference was observed between the mean fretting crack initiation angle,  $\bar{\theta}$ , for the constant and cyclic contact normal load tests. In both cases and for the two materials under study, cracks initiated and propagated nearly perpendicular to the contact surface (mode I dominated cracks).

### 6.3 . Suggestions for future work

This work and the current four actuators fretting fatigue rig open several perspectives for future research. Studies As we saw in the review of the state of the art, studies on the effects of a cyclic varying contact normal load on fretting fatigue are scarce and some have been reported to be questionable. Thus are much more questions to be investigated.

For instance, the effect of varying the load ratio of the contact normal load on the fretting life could also be considered. In this work, the contact normal load ratios ( $R_p$ ) of 0.6 and 0.8 were used for the fretting fatigue tests at room and elevated temperatures, respectively. However, what would happen should different values of contact normal load ratio be used? Increasing or decreasing it would be more beneficial or detrimental in terms of fretting life? Is the influence of  $R_p$  on fretting life linear or non-linear? Furthermore, new tests under different high temperatures and considering phase differences among the normal, axial, and tangential loads would surely produce crucial results for the scientific and industrial communities.

Significant upgrades were done in the UnB's fretting fatigue rig on the scope of this work. However, there is still space for improvements to make such an experimental rig even more robust, sophisticated, and versatile. One of them that would bring remarkable advantages to the fretting rig is the implementation of a crack detection and monitoring system (eddy current, ultrasonic, digital image correlation, and others). Since the physical space is very restricted in the current fretting apparatus due to the contact parts, pad holders, heating system, hydraulic actuators, and numerous other components, implementing such a solution would be very challenging, undoubtedly.

# Bibliography

- Abbasi, F. and Majzoobi, G. (2017). Effect of contact pressure on fretting fatigue behavior under cyclic contact loading. *Surface Review and Letters*, 24(Supp02):1850032.
- Abbasi, F. and Majzoobi, G. (2018a). Effect of out-of-phase loading on fretting fatigue response of al7075-t6 under cyclic normal loading using a new testing apparatus. *Engineering Fracture Mechanics*, 188:93–111.
- Abbasi, F. and Majzoobi, G. (2018b). Effect of out-of-phase loading on fretting fatigue response of al7075-t6 under cyclic normal loading using a new testing apparatus. *Engineering Fracture Mechanics*, 188:93–111.
- Abbasi, F. and Majzoobi, G. (2018c). An investigation into the effect of elevated temperatures on fretting fatigue response under cyclic normal contact loading. *Theoretical and Applied Fracture Mechanics*, 93:144–154.
- Abbasi, F. and Majzoobi, G. H. (2018d). An investigation into the effect of elevated temperatures on fretting fatigue response under cyclic normal contact loading. *Theoretical and Applied Fracture Mechanics*, 93:144–154.
- Al-Noaimi, A. A. (2008). Investigation into fretting fatigue under cyclic contact load and in conjunction with fatigue of titanium alloy. Master's thesis, Air Force Institute of Technology.
- Almajali, M. (2006). Effects of phase difference between axial and contact loads on fretting fatigue behavior of titanium alloy. Master's thesis, Air Force Institute of Technology.
- Almeida, G. M. J. (2017). Ensaios e avaliação da direção de iniciação de trinca sob condições de fretting. Master's thesis, Universidade de Brasília.

- Almeida, G. M. J., Cardoso, R. A., Garcia, M. A., Chassaing, G., Pommier, S., and Araújo, J. A. (2022). Four actuators fretting fatigue rig and tests with cyclic normal load for ti-6al-4v. *Theoretical and Applied Fracture Mechanics*, 119:103292.
- Almeida, G. M. J., Pessoa, G. C. V., Cardoso, R. A., Castro, F. C., and Araújo, J. A. (2020). Investigation of crack initiation path in aa7050-t7451 under fretting conditions. *Tribology International*, 144:106103.
- Amanov, A. (2020). Improvement in mechanical properties and fretting wear of inconel 718 superalloy by ultrasonic nanocrystal surface modification. *Wear*, 446:203208.
- Amargier, R., Fouvry, S., Poupon, C., and Chambon, L. (2010). A non local multiaxial fatigue approach to account for stress gradient effect applied to crack initiation in fretting. *Journal of ASTM International*, 7(3):1–19.
- Amontons, G. (1699). De la resistance cause'e dans les machines (1). *Memoires de L'Academie Royale*.
- Araújo, J., Dantas, A., Castro, F., Mamiya, E., and Ferreira, J. (2011). On the characterization of the critical plane with a simple and fast alternative measure of the shear stress amplitude in multiaxial fatigue. *International Journal of Fatigue*, 33(8):1092–1100.
- Araújo, J. and Nowell, D. (2009). Mixed high low fretting fatigue of ti6al4v: Tests and modelling. *Tribology international*, 42(9):1276–1285.
- Araújo, J. A. and Nowell, D. (1999). Analysis of pad size effects in fretting fatigue using short crack arrest methodologies. *International Journal of Fatigue*, 21(9):947–956.
- Araujo, J. A. and Nowell, D. (2002). The effect of rapidly varying contact stress fields on fretting fatigue. *International Journal of Fatigue*, 24(7):763–775.
- Araújo, J. A. (2000). *On the initiation and arrest fretting fatigue cracks*. PhD thesis, University of Oxford.



- Araújo, J. A., Nowell, D., and de Castro, F. C. (2022). Fretting fatigue. In *Reference Module in Materials Science and Materials Engineering*. Elsevier.
- ATSB (2002). Examination of a failed rolls-royce rb211-524 turbofan engine. Technical report, Boeing Commercial Aircraft Group.
- Attia, M. H. (2000). Fretting Fatigue of Some Nickel-Based Alloys in Steam Environment at 265C. *ASTM International*, 231:231–246.
- B637-16, A. S. (2016). Standard specification for precipitation-hardening and cold worked nickel alloy bars, forgings, and forging stock for moderate or high temperature service.
- B861-19, A. (2019). Standard specification for titanium and titanium alloy seamless pipe.
- Bai, L., Wan, S., Yi, G., Shan, Y., Tieu, A. K., Li, Y., Wang, R., et al. (2021). Temperature-mediated tribological characteristics of 40crnimoa steel and inconel 718 alloy during sliding against si3n4 counterparts. *Friction*, 9(5):1175–1197.
- Belan, J. (2015). High frequency fatigue test of in 718 alloy–microstructure and fractography evaluation. *Metalurgija*, 54(1):59–62.
- Bellecave, J. (2015). *Stress Gradients In Fretting Fatigue*. PhD thesis, École normale supérieure de Cachan-ENS Cachan.
- Bellecave, J., Pommier, S., Nadot, Y., Meriaux, J., and Araújo, J. A. (2014). T-stress based short crack growth model for fretting fatigue. *Tribology International*, 76:23–34.
- Bill, R. C. (1974). Fretting of Nickel-Chromium-Aluminum Alloys at Temperatures to 816°C. *Nasa Technical Note*.
- Bill, R. C. (1982). Review of Factors That Influence Fretting Wear. *ASTM Special Technical Publication*, pages 165–182.

- Bill, R. C. (1985). Selected Fretting-Wear-Resistant Coatings for Ti-6%Al-4%V alloy. *Wear*, 106:283–301.
- Blau, P. J. (2001). The significance and use of the friction coefficient. *Tribology International*, 34(9):585–591.
- Bramhall, R. (1973). *Studies in fretting fatigue*. PhD thesis, University of Oxford.
- Brinkman, C. R. and Korth, G. E. (1973). Strain fatigue and tensile behavior of inconel 718 from room temperature to 650<sup>sup</sup>0 c. Technical report, Aerojet Nuclear Co., Idaho Falls, Idaho (USA).
- Brown, M. W. and Miller, K. J. (1973). A theory for fatigue failure under multiaxial stress-strain conditions. *Proceedings of the Institution of Mechanical engineers*, 187(1):745–755.
- Cardoso, R. A. (2019). *Numerical studies on fretting fatigue modelling*. PhD thesis, University of Brasilia and Université Paris-Saclay.
- Cardoso, R. A., Doca, T., Neron, D., Pommier, S., and Araujo, J. A. (2019). Wear numerical assessment for partial slip fretting fatigue conditions. *Tribology International*, 136:508–523.
- Castany, P. (2007). *Etude des micromécanismes de déformation d'un alliage Ti-6Al-4V par déformation MET in situ: influence d'un traitement de surface*. PhD thesis, Institut National des Sciences Appliquées de Toulouse.
- Castro, F., Araújo, J., and Zouain, N. (2009). On the application of multiaxial high-cycle fatigue criteria using the theory of critical distances. *Engineering fracture mechanics*, 76(4):512–524.
- Cattaneo, C. (1938). Sul contatto di due corpi elastici: distribuzione locale degli sforzi. *rend. accad. naz. lincei* 27.

- Chassaing, G. (2015). *Frottement sec à grande vitesse du couple Ti6Al4V-Ti6Al4V: étude expérimentale et modélisation du comportement thermomécanique*. PhD thesis, Université de Lorraine.
- Chen, Q., Kawagoishi, N., and Nisitani, H. (1999). Evaluation of notched fatigue strength at elevated temperature by linear notch mechanics. *International journal of fatigue*, 21(9):925–931.
- Ciavarella, M. (2018). Discussion on “effect of out-of-phase loading on fretting fatigue response of al7075-t6 under cyclic normal loading using a new testing apparatus” by f. abbasi and gh majzooobi. *Engineering Fracture Mechanics*, 192:205–209.
- Combres, Y. (1999). Properties of titanium and titanium alloys; propriétés du titane et de ses alliages.
- Coulomb, C. A. (1821). *Théorie des machines simples en ayant égard au frottement de leurs parties et à la roideur des cordages*. Bachelier.
- Cowles, B. A. (1996). High Cycle Fatigue in Aircraft Gas Turbines - An Industry Perspective. *International Journal of Fracture*, 80(2-3):147–163.
- Crossland, B. (1956). Procedia international conference on fatigue of metals. *Proc. Inst. Mech., London*, pages 138–149.
- da Vinci, L. (1400). Notebooks and manuscripts, prepared in the late 1400s.
- Deperrois, A. R. C. (1991). *Sur le calcul de limites d'endurance des aciers*. PhD thesis, Palaiseau, Ecole polytechnique.
- Ding, J., Leen, S. B., and McColl, I. R. (2004). The effect of slip regime on fretting wear-induced stress evolution. *International Journal of Fatigue*, 26(5):521–531.
- Dobromirski, J. M. (1992). Variables of fretting process: are there 50 of them? *ASTM Special Technical Publication*, 1159:60–60.

- Doca, T. and Pires, F. A. (2017). Finite element modeling of wear using the dissipated energy method coupled with a dual mortar contact formulation. *Computers & Structures*, 191:62–79.
- Done, V., Kesavan, D., Chaise, T., Nelias, D., et al. (2017). Semi analytical fretting wear simulation including wear debris. *Tribology International*, 109:1–9.
- Eden, E. M., Rose, W. N., and Cunningham, P. L. (1911). The endurance of metals: experiments on rotating beams at university college, london. *Proceedings of the Institution of Mechanical Engineers*, 81(1):839–974.
- Fajdiga, G. and Sraml, M. (2009). Fatigue crack initiation and propagation under cyclic contact loading. *Engineering Fracture Mechanics*, 76(9):1320–1335.
- Fatemi, A. and Socie, D. F. (1988). A critical plane approach to multiaxial fatigue damage including out-of-phase loading. *Fatigue & Fracture of Engineering Materials & Structures*, 11(3):149–165.
- Fellows, L. J., Nowell, D., and Hills, D. A. (1997). Analysis of crack initiation and propagation in fretting fatigue: The effective initial flaw size methodology. *Fatigue & Fracture of Engineering Materials & Structures*, 20(1):61–70.
- Ferry, B. C. M. (2017). *Study of the stress gradient and the size effect in fretting fatigue*. PhD thesis, University of Brasilia.
- Fleury, R. M. N. (2015). *Investigation of fretting fatigue in turbine fir tree blade to disc joints at high temperature*. PhD thesis, University of Oxford.
- Fouvry, S., Liskiewicz, T., Kapsa, P., Hannel, S., and Sauger, E. (2003). An energy description of wear mechanisms and its applications to oscillating sliding contacts. *Wear*, 255(1-6):287–298.
- Gailliegue, T. (2018). *Effects of Phase Angle between the Fretting Load and the Bulk*

*Load on the Life of the Al7050 T7451 and ASTM 734 CA6NM*. PhD thesis, University of Brasilia.

Gallego, L. and Nelias, D. (2007). Modeling of fretting wear under gross slip and partial slip conditions.

Gallego, L., Nelias, D., and Deyber, S. (2010). A fast and efficient contact algorithm for fretting problems applied to fretting modes i, ii and iii. *Wear*, 268(1-2):208–222.

Garcin, S., Fouvry, S., and Heredia, S. (2015). A fem fretting map modeling: Effect of surface wear on crack nucleation. *Wear*, 330:145–159.

Garrison, B. (2000). High cycle fatigue (hcf) science and technology program 2000 annual report. Technical report, UNIVERSAL TECHNOLOGY CORP DAYTON OH.

Gean, M. and Farris, T. (2006). Fretting Fatigue Testing of Ti-17 at Elevated Temperatures. *Structures, Structural Dynamics, and Materials Conference*, 47(May):1–11.

Giannakopoulos, A., Lindley, T., Suresh, S., and Chenut, C. (2000). Similarities of stress concentrations in contact at round punches and fatigue at notches: implications to fretting fatigue crack initiation. *Fatigue and Fracture of Engineering Materials and Structures*, 23(7):561–572.

Gladwell, G. M. L. (1980). *Contact problems in the classical theory of elasticity*. Springer Science & Business Media.

Gough, H. J. and Pollard, H. V. (1935). The strength of metals under combined alternating stresses. *Proceedings of the institution of mechanical engineers*, 131(1):3–103.

Gowda, B. M. A., Yeshovanth, H. R., and Siddaraju, C. (2014). Investigation and efficient modeling of an dovetail attachment in aero-engine. *Procedia Materials Science*, 5:1873–1879.

- Grubisic, V. and Simbürger, A. (1976). Fatigue under combined out-of-phase multi-axial stresses. In *Fatigue Testing and Design 2, Proceedings of SEE International Conference*, volume 5, pages 27–1.
- Hager, C. H., Sanders, J., Sharma, S., Voevodin, A., and Segall, A. (2009). The effect of temperature on gross slip fretting wear of cold-sprayed nickel coatings on Ti6Al4V interfaces. *Tribology International*, 42(3):491–502.
- Hager, C. H., Sanders, J. H., and Sharma, S. (2006). Effect of high temperature on the characterization of fretting wear regimes at Ti6Al4V interfaces. *Wear*, 260(4-5):493–508.
- Hamdy, M. M., Overs, M. P., and Waterhouse, R. B. (1981). A new high-temperature fretting wear test rig. *Journal of Physics & Scientific Instruments*, 14(7):889–894.
- Hamdy, M. M. and Waterhouse, R. B. (1979a). The fretting fatigue behaviour of a nickel-based alloy (Inconel 718) at elevated temperatures. *Wear of Materials*, ASME:351–355.
- Hamdy, M. M. and Waterhouse, R. B. (1979b). The fretting fatigue behaviour of Ti-6Al-4V at temperatures up to 600 °C. *Wear*, 56(1):1–8.
- Hamdy, M. M. and Waterhouse, R. B. (1981). The fretting wear of Ti-6Al-4v and aged inconel 718 at elevated temperatures. *Wear*, 71(2):237–248.
- Hamdy, M. M. and Waterhouse, R. B. (1982). The Fretting fatigue Behaviour of the Titanium Alloy IMI 829 at Temperatures up to 600°C. 5(4):267–274.
- Hannel, S., Fouvry, S., Kapsa, P., and Vincent, L. (2001). The fretting sliding transition as a criterion for electrical contact performance. *Wear*, 249(9):761–770.
- Hansson, T., Kamaraj, M., Mutoh, Y., and Petterssin, B. (2000). High Temperature Fretting Fatigue Behavior in an XD  $\gamma$ -base TiAl. *ASTM International*, pages 65–79.

- Hertz, H. (1882). Über die berührung fester elastischer körper. *Journal für die reine und angewandte Mathematik*, 92(156-171):22.
- Hills, D. A. and Nowell, D. (1994). *Mechanics of Fretting Fatigue*. Springer Netherlands.
- Hills, D. A., Nowell, D., and Sackfield, A. (1993). Mechanics of elastic contacts. *Butterworth-Heinemann, Oxford*.
- Hojjati-Talemi, R., Wahab, M. A., and De Baets, P. (2014). Finite element simulation of phase difference effects on fretting fatigue crack nucleation behaviour. *Proceedings of the Institution of Mechanical Engineers, Part J: Journal of Engineering Tribology*, 228(4):470–479.
- Huq, M. Z., Butaye, C., and Celis, J.-P. (2000). An innovative system for fretting wear testing under oscillating normal force. *Journal of Materials Research*, 15(7):1591–1599.
- Huq, M. Z. and Celis, J.-P. (2002). Fretting fatigue in alumina tested under oscillating normal load. *Journal of the American Ceramic Society*, 85(4):986–988.
- Hurricks, P. L. (1972). The fretting to 200°C wear of mild steel from room temperature. *Wear*, 19(2):207–229.
- Hurricks, P. L. (1974). The fretting wear of mild steel from 200° to 500°C. *Wear*, 30(2):189–212.
- Jeong, D.-H., Choi, M.-J., Goto, M., Lee, H.-C., and Kim, S. (2014). Effect of service exposure on fatigue crack propagation of inconel 718 turbine disc material at elevated temperatures. *Materials characterization*, 95:232–244.
- Jin, O., Mall, S., and Sahan, O. (2005). Fretting fatigue behavior of Ti-6Al-4V at elevated temperature. *International Journal of Fatigue*, 27(4):395–401.

- Juoksukangas, J., Lehtovaara, A., and Mäntylä, A. (2016). Experimental and numerical investigation of fretting fatigue behavior in bolted joints. *Tribology International*, 103:440–448.
- Jutte, A. J. (2004). Effect of a variable contact load on fretting fatigue behavior of ti-6al-4v. Master's thesis, Air Force Institute of Technology.
- Kallmeyer, A. R., Krgo, A., and Kurath, P. (2002). Evaluation of multiaxial fatigue life prediction methodologies for ti-6al-4v. *J. Eng. Mater. Technol.*, 124(2):229–237.
- Kawagoishi, N., Chen, Q., and Nisitani, H. (2000). Fatigue strength of Inconel 718 at elevated temperatures. *Fatigue & Fracture of Engineering Materials & Structures*, (23):209–216.
- Kayaba, T. and Iwabuchi, A. (1981). The fretting wear of 0.45% C steel and austenitic stainless steel from 20 to 650 °C in air. *Wear*, 74(2):229–245.
- Korashy, A., Attia, H., Thomson, V., and Oskooei, S. (2015). Characterization of fretting wear of cobalt-based superalloys at high temperature for aero-engine combustor components. *Wear*, 330-331:327–337.
- Kubiak, K. (2006). *Quantification de la fissuration d'un contact soumis a des sollicitations complexes en Fretting wear et fretting fatigue*. PhD thesis, ECOLE CENTRALE DE LYON.
- Kwon, J.-D., Jeung, H.-K., Chung, I., Yoon, D.-H., and Park, D.-K. (2011). A study on fretting fatigue characteristics of Inconel 690 at high temperature. *Tribology International*, 44(11):1483–1487.
- Kwon, J.-D., Park, D.-K., Woo, S.-W., Yoon, D.-H., and Chung, I. (2010). A study on fretting fatigue life for the Inconel alloy 600 at high temperature. *Nuclear Engineering and Design*, 240(10):2521–2527.



- Lavella, M., Botto, D., and Gola, M. M. (2013). Design of a high-precision, flat-on-flat fretting test apparatus with high temperature capability. *Wear*, 302(1-2):1073–1081.
- Lee, C.-h. (2004). Effects of variable contact load on fretting fatigue behavior of shot-peened and un-peened titanium alloy. Master's thesis, Air Force Institute of Technology.
- Lee, H., Jin, O., and Mall, S. (2003). Fretting fatigue behaviour of shot-peened Ti-6Al-4V at room and elevated temperatures. *Fatigue and Fracture of Engineering Materials and Structures*, 26(9):767–778.
- Lee, H. and Mall, S. (2004). Stress relaxation behavior of shot-peened Ti-6Al-4V under fretting fatigue at elevated temperature. *Materials Science and Engineering A*, 366(2):412–420.
- Li, B., Santos, J. L. T., and Freitas, M. d. (2000). A unified numerical approach for multiaxial fatigue limit evaluation.
- Limmer, L., Nowell, D., and Hills, D. (2001). A combined testing and modelling approach to the prediction of the fretting fatigue performance of splined shafts. *Proceedings of the Institution of Mechanical Engineers, Part G: Journal of Aerospace Engineering*, 215(2):105–112.
- Liskiewicz, T. and Dini, D. (2022). *Fretting Wear and Fretting Fatigue - Fundamental Principles and Applications*. Elsevier Series on Tribology and Surface Engineering.
- Lykins, C. D., Mall, S., and Jain, V. K. (2001). Combined experimental–numerical investigation of fretting fatigue crack initiation. *International journal of fatigue*, 23(8):703–711.
- Ma, X.-f., Duan, Z., Shi, H.-j., Murai, R., and Yanagisawa, E. (2010). Fatigue and fracture behavior of nickel-based superalloy inconel 718 up to the very high cycle regime. *Journal of Zhejiang University-Science A*, 11(10):727–737.

- Madge, J. J., Leen, S. B., McColl, I. R., and Shipway, P. H. (2007a). Contact-evolution based prediction of fretting fatigue life: effect of slip amplitude. *Wear*, 262(9-10):1159–1170.
- Madge, J. J., Leen, S. B., and Shipway, P. H. (2007b). The critical role of fretting wear in the analysis of fretting fatigue. *Wear*, 263(1-6):542–551.
- Majzoubi, G. and Abbasi, F. (2017). On the effect of shot-peening on fretting fatigue of al7075-t6 under cyclic normal contact loading. *Surface and Coatings Technology*, 328:292–303.
- Majzoubi, G. H. and Abbasi, F. (2018). An investigation into the effect of normal load frequency on fretting fatigue behavior of al7075-t6. *Tribology Transactions*, 61(3):547–559.
- Mall, S., Jin, O., Yuskel, H., and Calcaterra, J. R. (2002). Investigation into fretting fatigue behavior of shot-peened ti-6al-4v. In *Proceedings of the Seventh National Turbine Engine High Cycle Fatigue Conference, West Palm Beach*.
- Mall, S., Jutte, A. J., Fuchs, S. P., and Copeland, D. P. (2004). Investigation into variable contact load effects on fretting fatigue behavior of ti-6al-4v. In *Int. Congress of Theoretical and Applied Mechanics*, pages 15–21.
- Mamiya, E. N. and Araújo, J. A. (2002). Fatigue limit under multiaxial loadings: on the definition of the equivalent shear stress. *Mechanics Research Communications*, 29(2-3):141–151.
- Martins, L. H. L., Rossino, L. S., Filho, W. B., and Araújo, J. A. (2008). Detailed design of fretting fatigue apparatus and tests on 7050-t7451 al alloy. *Tribology-Materials, Surfaces & Interfaces*, 2(1):39–49.
- Mary, C. (2009). *Simulation expérimentale de l'usure du contact aube-disque de compresseur sous sollicitations de fretting*. PhD thesis, Ecole Centrale de Lyon.

- Mary, C., Fouvry, S., Martin, J. M., and Bonnet, B. (2008). High temperature fretting wear of a Ti alloy/CuNiIn contact. *Surface and Coatings Technology*, 203(5-7):691–698.
- Matlik, J. F. and Farris, T. N. (2003). High-frequency fretting fatigue experiments. In *Fretting fatigue: Advances in basic understanding and applications*. ASTM International.
- Matlik, J. F., Farris, T. N., Haake, F. K., Swanson, G. R., and Duke, G. C. (2006). High-frequency, high-temperature fretting-fatigue experiments. *Wear*, 261(11-12):1367–1382.
- McColl, I. R., Ding, J., and Leen, S. B. (2004). Finite element simulation and experimental validation of fretting wear. *Wear*, 256(11-12):1114–1127.
- McDiarmid, D. (1974). A new analysis of fatigue under combined bending and twisting. *The Aeronautical Journal*, 78(763):325–329.
- McDowell, J. (1952). Fretting corrosion tendencies of several combinations of materials. In *Symposium on fretting corrosion*, pages 24–39. ASTM International.
- Meggiolaro, M. A. and de Castro, J. T. P. (2015). The moment of inertia method to calculate equivalent ranges in non-proportional tension–torsion histories. *Journal of Materials Research and Technology*, 4(3):229–234.
- Meriaux, J. (2010). *Etude expérimentale et modélisation de l'endommagement du contact aube-disque de soufflante soumis à des chargements de fretting fatigue*. Theses, Ecole Centrale de Lyon.
- Mi, X., Wang, W. X., Xiong, X. M., Qian, H., Tang, L. C., Xie, Y. C., Peng, J. F., Cai, Z. B., and Zhu, M. H. (2015). Investigation of fretting wear behavior of Inconel 690 alloy in tube/plate contact configuration. *Wear*, 328-329:582–590.
- Mindlin, R. D. (1949). Compliance of elastic bodies in contact.

- Miner, M. A. (1945). Cumulative damage in fatigue.
- Mohrbacher, H., Celis, J.-P., and Roos, J. (1995). Laboratory testing of displacement and load induced fretting. *Tribology international*, 28(5):269–278.
- Montebello, C. (2015). *Analysis of the stress gradient effect in Fretting-Fatigue through a description based on nonlocal intensity factors*. PhD thesis, Université Paris-Saclay.
- Mugadu, A., Hills, D. A., and Limmer, L. (2002). An asymptotic approach to crack initiation in fretting fatigue of complete contacts. *Journal of the Mechanics and Physics of Solids*, 50(3):531–547.
- Murthy, H. and Farris, T. N. (2003). Elevated temperature fretting of turbine materials subjected to engine type-loading. In *44th AIAA/ASME/ASCE/AHS/ASC Structures, Structural Dynamics, and Materials Conference*, page 1525.
- Murthy, H., Gao, G., and Farris, T. N. (2006). Fretting fatigue of single crystal nickel at 600 °C. *Tribology International*, 39(10):1227–1240.
- Murthy, H., Rajeev, P. T., Okane, M., and Farris, T. N. (2003). Development of Test Methods for High Temperature Fretting of Turbine Materials Subjected to Engine-Type Loading. *ASTM International*, pages 273–288.
- Muskhelishvili, N. I. (1953). Some basic problems of the mathematical theory of elasticity. *Noordhoff, Groningen*.
- Mutoh, Y., Satoh, T., Tanaka, K., and Tsunoda, E. (1989). Fretting fatigue at elevated temperatures in two steam turbine steels. *Fatigue & Fracture of Engineering Materials & Structures*, 12(5):409–421.
- Mutoh, Y., Satoh, T., and Tsunoda, E. (1992). Improving Fretting Fatigue Strength at Elevated Temperatures by Shot Peening in Steam Turbine Steel. *ASTM*, pages 199–209.

- Nascimento, V. C. F. (2022). Fatigue behavior of forged inconel 718 including the effects of axial/torsional loading and high temperature. Master's thesis, Universidade de Brasília.
- Ni, T. and Dong, J. (2017). Creep behaviors and mechanisms of inconel718 and allvac718plus. *Materials Science and Engineering: A*, 700:406–415.
- Nishihara, T., Kawamoto, M., et al. (1945). The strength of metals under combined alternating bending and torsion with phase difference. *Memories of the College of Engineering, Kyoto Imperial University*, 11(85):112.
- Nowell, D. (1988). *An analysis of fretting fatigue*. PhD thesis, University of Oxford.
- Ownby, J. F. (2008). *The Effect of Elevated Temperature on the Fretting Fatigue Behavior of Nickel Alloy IN-100*. PhD thesis, Air Force Institute of Technology.
- Pinto, A. L., Cardoso, R. A., Talemi, R., and Araújo, J. A. (2020). Fretting fatigue under variable amplitude loading considering partial and gross slip regimes: numerical analysis. *Tribology International*, 146:106199.
- Proudhon, H., Fouvry, S., and Buffière, J.-Y. (2005). A fretting crack initiation prediction taking into account the surface roughness and the crack nucleation process volume. *International Journal of Fatigue*, 27(5):569–579.
- Rajasekaran, R. and Nowell, D. (2006). Fretting fatigue in dovetail blade roots: Experiment and analysis. *Tribology International*, 39(10):1277–1285.
- Ramalho, A. and Celis, J. P. (2002). High temperature fretting behaviour of plasma vapour deposition TiN coatings. *Surface and Coatings Technology*, 155(2-3):169–175.
- Ruiz, C. and Nowell, D. (2000). Designing against fretting fatigue in aeroengines. *European Structural Integrity Society*, 26:73–95.

- Rybiak, R., Fouvry, S., and Bonnet, B. (2010). Fretting wear of stainless steels under variable temperature conditions: Introduction of a 'composite' wear law. *Wear*, 268(2-3):413–423.
- Sahan, O. (2002). Fretting fatigue behavior of a titanium alloy ti-6al-4v at elevated temperature. Master's thesis, Air Force Institute of Technology, Wright-Patterson Air Force Base, Ohio.
- Sines, G. (1955). Failure of materials under combined repeated stresses with superimposed static stresses. Technical report, California. Univ., Los Angeles.
- Smith, R. N., Watson, P., and Topper, T. H. (1970). A stress strain parameter for the fatigue of metal. *Journal of Materials*, 5(4).
- Socie, D. F. (1987). Multiaxial fatigue damage models.
- Stott, F. H., Lin, D. S., and Wood, G. C. (1973). The structure and mechanism of formation of the 'glaze' oxide layers produced on nickel-based alloys during wear at high temperatures. *Corrosion Science*, 13(6).
- Susmel, L. and Lazzarin, P. (2002). A bi-parametric wöhler curve for high cycle multi-axial fatigue assessment. *Fatigue & Fracture of Engineering Materials & Structures*, 25(1):63–78.
- Swikert, M. A. and Johnson, R. L. (1968). Friction and wear under fretting conditions of materials for use as wire friction dampers of compressor blade vibration. Technical report, NATIONAL AERONAUTICS AND SPACE ADMINISTRATION.
- Taylor, D. (1999). Geometrical effects in fatigue: a unifying theoretical model. *International Journal of Fatigue*, 21(5):413–420.
- Tomlinson, G. (1927). The rusting of steel surfaces in contact. *Proceedings of the Royal Society of London. Series A, Containing Papers of a Mathematical and Physical Character*, 115(771):472–483.

- Uhlig, H. H., Feng, I. M., Tierney, W. D., and McClellan, A. (1953). A fundamental investigation of fretting corrosion. *National Advisory Committee for Aeronautics*, 3029.
- VAN, K. and Griveau, B. (1989). On a new multiaxial fatigue limit criterion- theory and application. *Biaxial and multiaxial fatigue(A 90-16739 05-39)*. London, *Mechanical Engineering Publications, Ltd.*, 1989,, pages 479–496.
- Warlow-Davies, E. (1941). Fretting corrosion and fatigue strength: brief results of preliminary experiments. *Proceedings of the Institution of Mechanical Engineers*, 146(1):32–38.
- Waterhouse, R. B. (1984). Fretting wear. *Wear*, 100(1-3):107–118.
- Waterhouse, R. B. and Iwabuchi, A. (1985). High Temperature Fretting Wear of Four Titanium Alloys. *Wear*, 74(10):618.
- Yan, N., Kawagoishi, N., Chen, Q., Wang, Q. Y., Nisitani, H., and Kondo, E. (2003). Fatigue properties of inconel 718 in long life region at elevated temperature. In *Key Engineering Materials*, volume 243, pages 321–326. Trans Tech Publ.
- Zhai, Y., Huang, Z. Y., Zhu, S.-P., and Wang, Q. Y. (2020). Very high cycle fretting fatigue damage and crack path investigation of nimonic 80a at elevated temperature. *International Journal of Fatigue*, 132:105345.
- Zhang, X. and Liu, D. (2009). Effect of shot peening on fretting fatigue of Ti811 alloy at elevated temperature. *International Journal of Fatigue*, 31(5):889–893.
- Zhou, Z., Cardou, A., Goudreau, S., and Fiset, M. (1996). Fundamental investigations of electrical conductor fretting fatigue. *Tribology International*, 29(3):221–232.
- Zouain, N., Mamiya, E. N., and Comes, F. (2006). Using enclosing ellipsoids in multiaxial fatigue strength criteria. *European Journal of Mechanics-A/Solids*, 25(1):51–71.

# Appendix

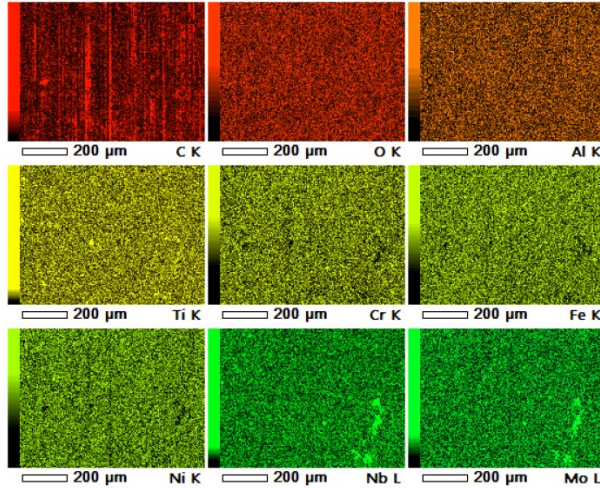


# A1 - SEM/EDX analyses of the sample FF-IN-RT-PC-03

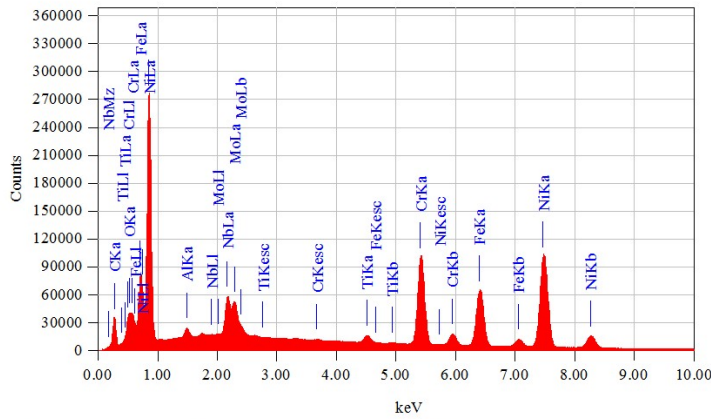
## Region without contact

ff-in-rt-pc-03 - region without contact

Lab 1/1



Date : 25/06/2  
 Resolution : 256 x 1  
 -----  
 Instrument : 7100F  
 Acc. Volt. : 15 kV  
 Magnification : x 150  
 Dwell Time : 0.2 mse  
 Sweep Count : 50



Acquisition Parameter  
 Instrument : 7100F  
 Acc. Voltage : 15.0 kV  
 Probe Current: 1.00000 nA  
 PHA mode : T2  
 Real Time : 594.93 sec  
 Live Time : 491.52 sec  
 Dead Time : 17 %  
 Counting Rate: 34866 cps  
 Energy Range : 0 - 20 keV

ZAF Method Standardless Quantitative Analysis

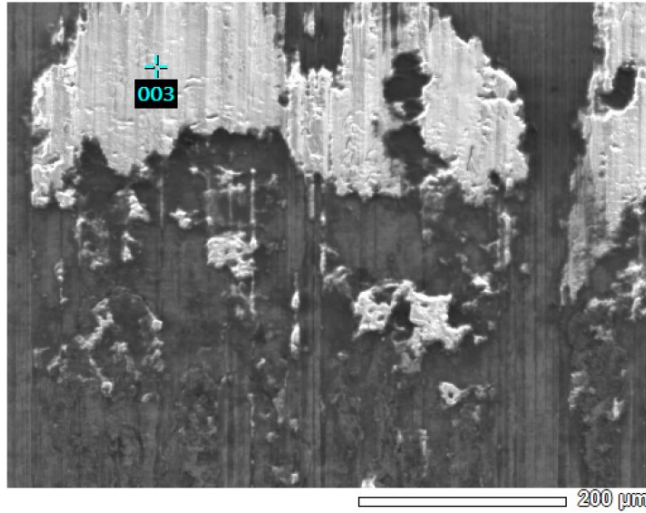
Fitting Coefficient : 0.0530

Element	(keV)	Mass%	Sigma	Atom%	Compound	Mass%	Cation	K
C	0.277	8.62	0.01	30.34				2.3122
O	0.525	1.67	0.01	4.41				1.8657
Al	1.486	0.43	0.00	0.68				0.2903
Ti	4.508	0.94	0.01	0.83				1.0349
Cr	5.411	16.49	0.02	13.40				18.5307
Fe	6.398	16.56	0.03	12.53				18.6413
Ni	7.471	47.93	0.06	34.50				51.3484
Nb	2.166	4.74	0.01	2.15				3.8165
Mo	2.293	2.61	0.01	1.15				2.1600
Total		100.00		100.00				

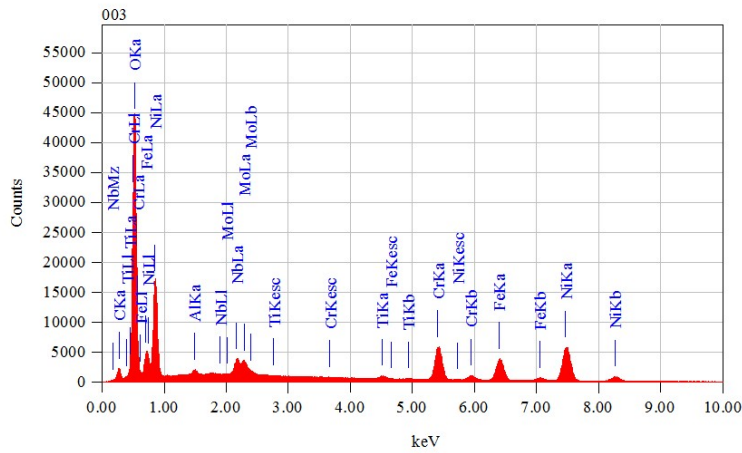
# Slip zone

ff-in-rt-pc-03 - slip zone

Lab 1/1



Title : IMG1  
 Instrument : 7100F  
 Volt : 15,00 kV  
 Mag. : x 190  
 Date : 2022/06/25  
 Pixel : 1024 x 768



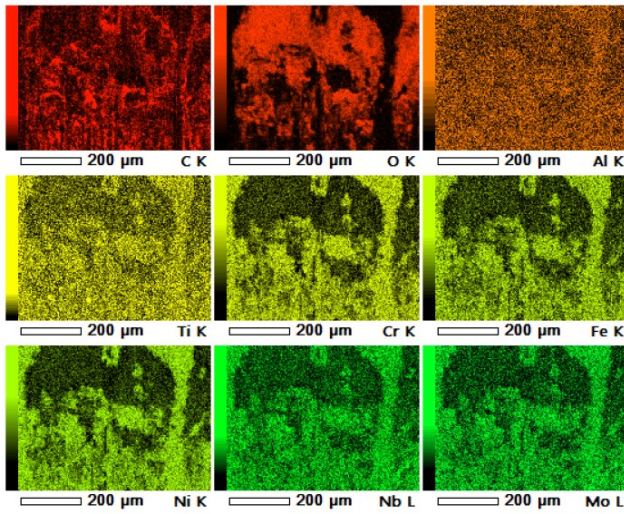
Acquisition Parameter  
 Instrument : 7100F  
 Acc. Voltage : 15.0 kV  
 Probe Current: 1.00000 nA  
 PHA mode : T2  
 Real Time : 58.17 sec  
 Live Time : 50.00 sec  
 Dead Time : 14 %  
 Counting Rate: 28832 cps  
 Energy Range : 0 - 20 keV

ZAF Method Standardless Quantitative Analysis  
 Fitting Coefficient : 0.0361

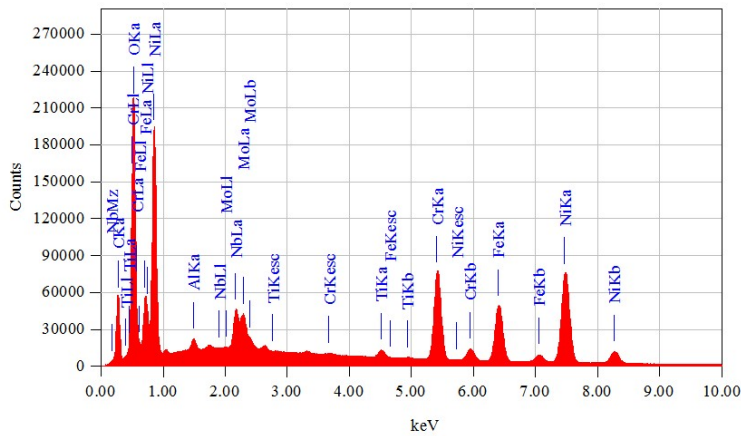
Element	(keV)	Mass%	Sigma	Atom%	Compound	Mass%	Cation	K
C	0.277	4.02	0.03	8.34				1.0810
O	0.525	44.70	0.11	69.64				54.2414
Al	1.486	0.29	0.01	0.27				0.1763
Ti	4.508	0.51	0.01	0.26				0.4575
Cr	5.411	9.64	0.06	4.62				8.7930
Fe	6.398	9.58	0.07	4.27				8.7288
Ni	7.471	26.98	0.15	11.45				23.4734
Nb	2.166	2.71	0.03	0.73				1.9139
Mo	2.293	1.58	0.03	0.41				1.1346
Total		100.00		100.00				

ff-in-rt-pc-03 - slip zone

Lab 1/1



Date : 25/06/2  
 Resolution : 256 x 1  
 -----  
 Instrument : 7100F  
 Acc. Volt. : 15 kV  
 Magnification : x 190  
 Dwell Time : 0.2 mse  
 Sweep Count : 50



Acquisition Parameter  
 Instrument : 7100F  
 Acc. Voltage : 15.0 kV  
 Probe Current: 1.00000 nA  
 PHA mode : T2  
 Real Time : 579.19 sec  
 Live Time : 491.53 sec  
 Dead Time : 15 %  
 Counting Rate: 31076 cps  
 Energy Range : 0 - 20 keV

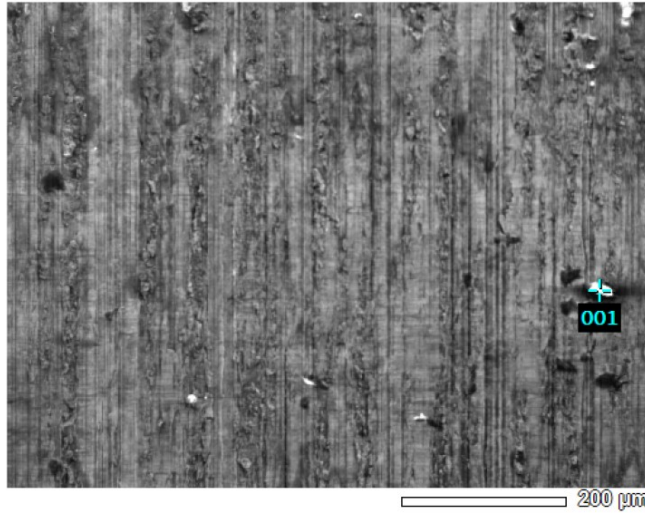
ZAF Method Standardless Quantitative Analysis  
 Fitting Coefficient : 0.0445

Element	(keV)	Mass%	Sigma	Atom%	Compound	Mass%	Cation	K
C K	0.277	12.20	0.01	27.90				3.7402
O K	0.525	24.55	0.03	42.15				28.9673
Al K	1.486	0.36	0.00	0.37				0.2594
Ti K	4.508	0.66	0.00	0.38				0.7281
Cr K	5.411	11.81	0.02	6.24				13.1817
Fe K	6.398	11.83	0.02	5.82				13.1962
Ni K	7.471	33.45	0.05	15.65				35.5578
Nb L	2.166	3.24	0.01	0.96				2.7380
Mo L	2.293	1.89	0.01	0.54				1.6313
Total		100.00		100.00				

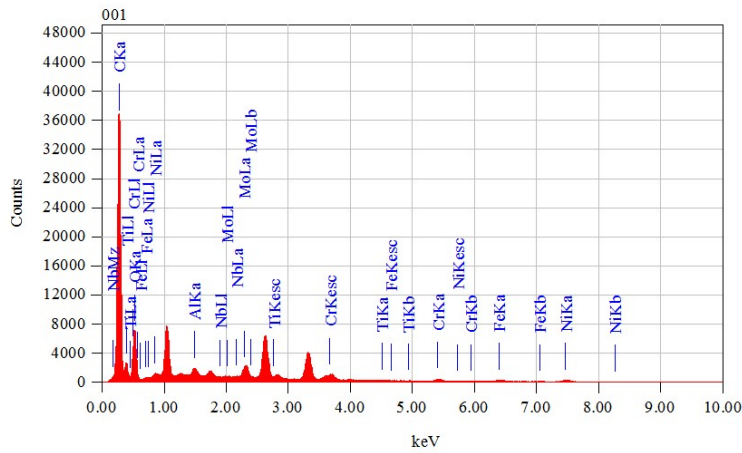
Stick zone

ff-in-rt-pc-03 - stick zone

Lab 1/1



Title : IMG1  
 Instrument : 7100F  
 Volt : 15,00 kV  
 Mag. : x 150  
 Date : 2022/06/25  
 Pixel : 1024 x 768



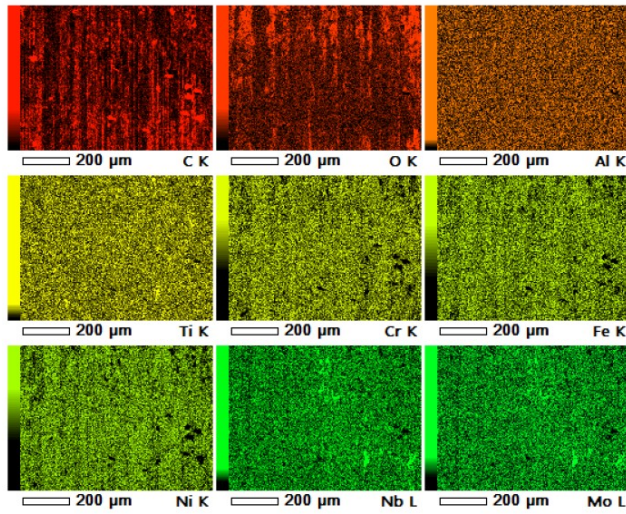
Acquisition Parameter  
 Instrument : 7100F  
 Acc. Voltage : 15.0 kV  
 Probe Current: 1.00000 nA  
 PHA mode : T2  
 Real Time : 54.27 sec  
 Live Time : 50.00 sec  
 Dead Time : 8 %  
 Counting Rate: 17100 cps  
 Energy Range : 0 - 20 keV

ZAF Method Standardless Quantitative Analysis  
 Fitting Coefficient : 0.2595

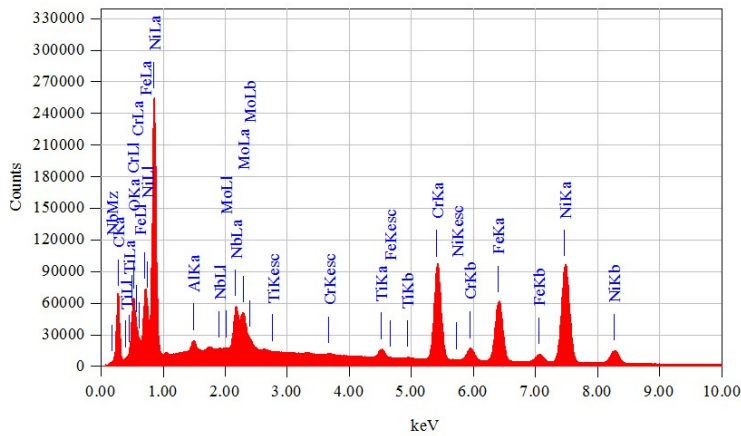
Element	(keV)	Mass%	Sigma	Atom%	Compound	Mass%	Cation
C	0.277	61.75	0.09	71.86			K
O	0.525	30.21	0.17	26.39			
Al	1.486	0.50	0.01	0.26			
Ti	4.508	0.17	0.01	0.05			
Cr	5.411	0.73	0.02	0.20			
Fe	6.398	0.97	0.03	0.24			
Ni	7.471	1.82	0.05	0.43			
Nb	2.166	0.61	0.02	0.09			
Mo	2.293	3.25	0.04	0.47			
Total		100.00		100.00			

ff-in-rt-pc-03 - stick zone

Lab 1/1



Date : 25/06/2  
 Resolution : 256 x 1  
 -----  
 Instrument : 7100F  
 Acc. Volt. : 15 kV  
 Magnification : x 150  
 Dwell Time : 0.2 mse  
 Sweep Count : 50



Acquisition Parameter  
 Instrument : 7100F  
 Acc. Voltage : 15.0 kV  
 Probe Current: 1.00000 nA  
 PHA mode : T2  
 Real Time : 591.99 sec  
 Live Time : 491.54 sec  
 Dead Time : 16 %  
 Counting Rate: 34202 cps  
 Energy Range : 0 - 20 keV

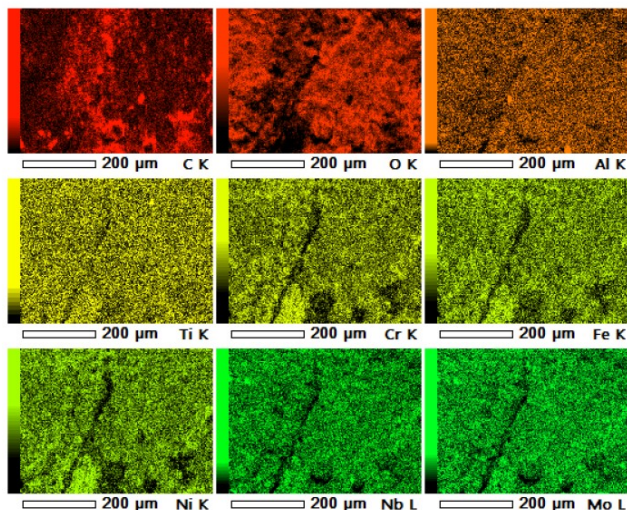
ZAF Method Standardless Quantitative Analysis  
 Fitting Coefficient : 0.0502

Element	(keV)	Mass%	Sigma	Atom%	Compound	Mass%	Cation	K
C K	0.277	15.77	0.02	43.56				4.7222
O K	0.525	5.51	0.01	11.44				6.0761
Al K	1.486	0.41	0.00	0.51				0.3051
Ti K	4.508	0.85	0.01	0.59				0.9960
Cr K	5.411	14.57	0.02	9.30				17.3566
Fe K	6.398	14.57	0.03	8.66				17.3667
Ni K	7.471	41.87	0.06	23.67				47.4957
Nb L	2.166	4.16	0.01	1.48				3.6374
Mo L	2.293	2.28	0.01	0.79				2.0441
Total		100.00		100.00				

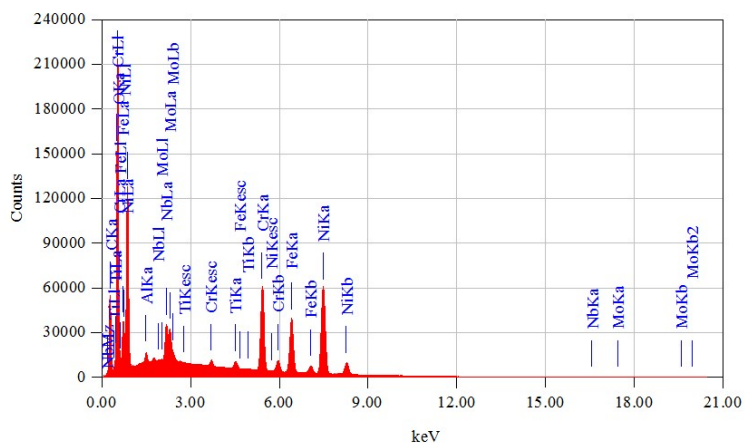
### Crack initiation region

ff-in-rt-pc-03 - crack initiation region

Lab 1/1



Date : 25/06/2  
Resolution : 256 x 1  
-----  
Instrument : 7100F  
Acc. Volt. : 15 kV  
Magnification : x 230  
Dwell Time : 0.2 mse  
Sweep Count : 50



Acquisition Parameter  
Instrument : 7100F  
Acc. Voltage : 15.0 kV  
Probe Current: 1.00000 nA  
PHA mode : T2  
Real Time : 559.19 sec  
Live Time : 491.53 sec  
Dead Time : 12 %  
Counting Rate: 24153 cps  
Energy Range : 0 - 20 keV

ZAF Method Standardless Quantitative Analysis

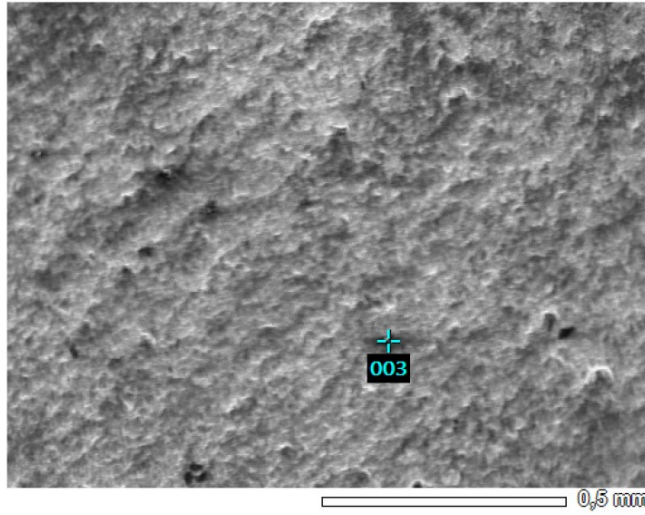
Fitting Coefficient : 0.0415

Element	(keV)	Mass%	Sigma	Atom%	Compound	Mass%	Cation	K
C K*	0.277	13.13	0.02	28.10				4.1666
O K	0.525	28.67	0.03	46.07				34.1305
Al K	1.486	0.32	0.00	0.30				0.2306
Ti K	4.508	0.63	0.00	0.34				0.6929
Cr K	5.411	10.82	0.02	5.35				12.0192
Fe K	6.398	10.94	0.02	5.04				12.1400
Ni K	7.471	30.99	0.05	13.57				32.7574
Nb L	2.166	2.88	0.01	0.80				2.4503
Mo L	2.293	1.63	0.01	0.44				1.4124
Total		100.00		100.00				

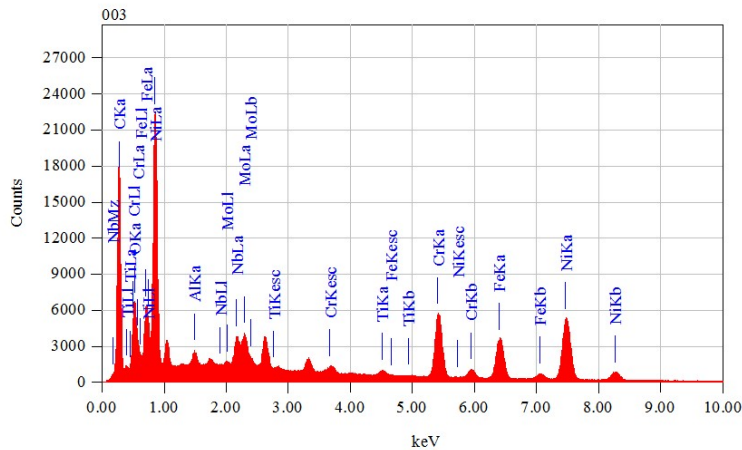
### Crack propagation region

ff-in-rt-pc-03 - propagation region

Lab 1/1



Title : IMG1  
 Instrument : 7100F  
 Volt : 15,00 kV  
 Mag. : x 90  
 Date : 2022/06/25  
 Pixel : 1024 x 768



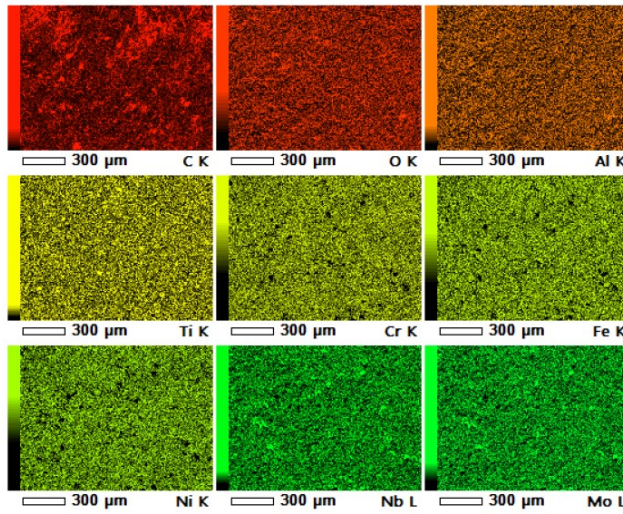
Acquisition Parameter  
 Instrument : 7100F  
 Acc. Voltage : 15.0 kV  
 Probe Current: 1.00000 nA  
 PHA mode : T2  
 Real Time : 57.93 sec  
 Live Time : 50.00 sec  
 Dead Time : 13 %  
 Counting Rate: 28036 cps  
 Energy Range : 0 - 20 keV

ZAF Method Standardless Quantitative Analysis  
 Fitting Coefficient : 0.0817

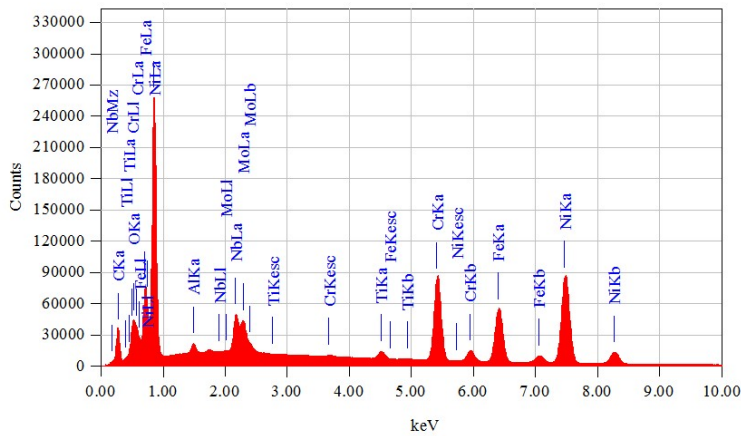
Element	(keV)	Mass%	Sigma	Atom%	Compound	Mass%	Cation	K
C	0.277	37.75	0.08	67.45				17.3588
O	0.525	9.88	0.08	13.26				10.2619
Al	1.486	0.47	0.01	0.37				0.4803
Ti	4.508	0.54	0.01	0.24				0.7838
Cr	5.411	9.83	0.06	4.06				14.2747
Fe	6.398	9.79	0.07	3.76				14.1687
Ni	7.471	26.33	0.15	9.63				36.3838
Nb	2.166	2.85	0.03	0.66				3.2856
Mo	2.293	2.56	0.03	0.57				3.0025
Total		100.00		100.00				

ff-in-rt-pc-03 - propagation region

Lab 1/1



Date : 25/06/2  
 Resolution : 256 x 1  
 Instrument : 7100F  
 Acc. Volt. : 15 kV  
 Magnification : x 90  
 Dwell Time : 0.2 mse  
 Sweep Count : 50



Acquisition Parameter  
 Instrument : 7100F  
 Acc. Voltage : 15.0 kV  
 Probe Current: 1.00000 nA  
 PHA mode : T2  
 Real Time : 579.86 sec  
 Live Time : 491.52 sec  
 Dead Time : 15 %  
 Counting Rate: 30214 cps  
 Energy Range : 0 - 20 keV

ZAF Method Standardless Quantitative Analysis

Fitting Coefficient : 0.0532

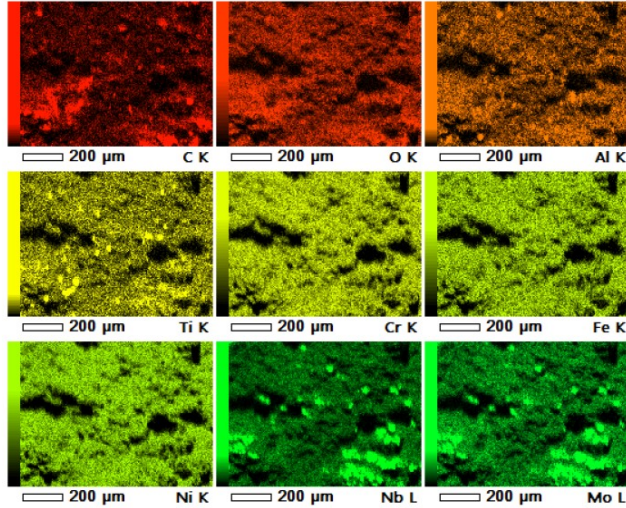
Element	(keV)	Mass%	Sigma	Atom%	Compound	Mass%	Cation	K
C K	0.277	10.08	0.01	33.29				2.7623
O K	0.525	2.93	0.01	7.26				3.2597
Al K	1.486	0.46	0.00	0.68				0.3146
Ti K	4.508	0.99	0.01	0.82				1.1018
Cr K	5.411	16.03	0.03	12.23				18.2163
Fe K	6.398	16.15	0.03	11.47				18.3645
Ni K	7.471	46.25	0.06	31.25				50.0935
Nb L	2.166	4.65	0.01	1.99				3.8116
Mo L	2.293	2.47	0.01	1.02				2.0756
Total		100.00		100.00				



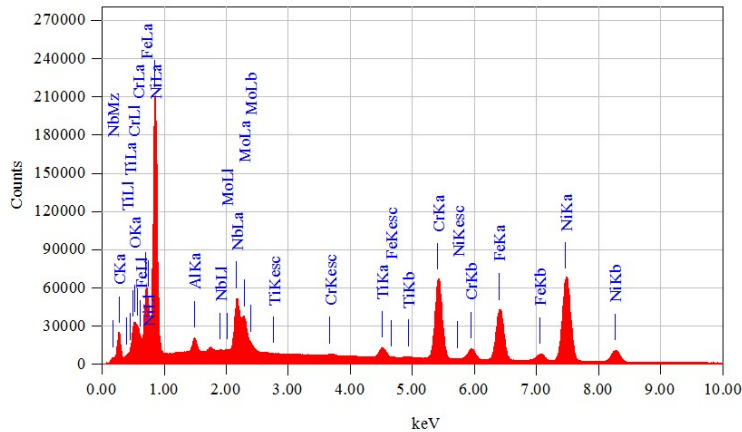
# Fast fracture region

ff-in-rt-pc-03 - fast fracture region

Lab 1/1



Date : 25/06/2  
 Resolution : 256 x 1  
 Instrument : 7100F  
 Acc. Volt. : 15 kV  
 Magnification : x 130  
 Dwell Time : 0.2 mse  
 Sweep Count : 50



Acquisition Parameter  
 Instrument : 7100F  
 Acc. Voltage : 15.0 kV  
 Probe Current: 1.00000 nA  
 PHA mode : T2  
 Real Time : 561.42 sec  
 Live Time : 491.50 sec  
 Dead Time : 12 %  
 Counting Rate: 24986 cps  
 Energy Range : 0 - 20 keV

ZAF Method Standardless Quantitative Analysis  
 Fitting Coefficient : 0.0522

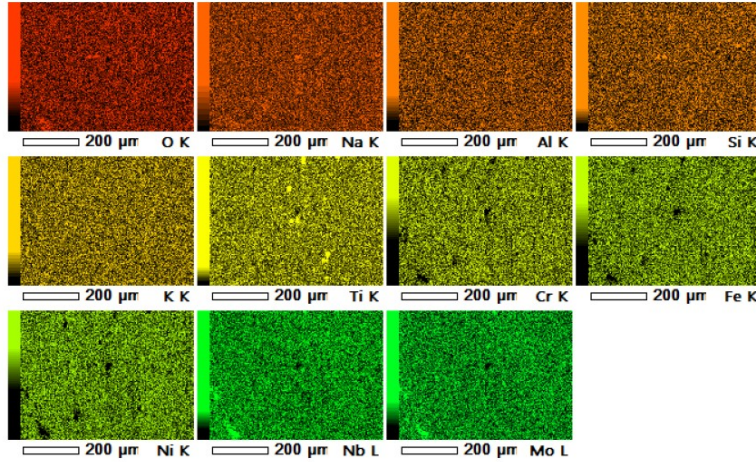
Element	(keV)	Mass%	Sigma	Atom%	Compound	Mass%	Cation
C K	0.277	8.36	0.02	29.18			2.2140
O K	0.525	2.56	0.01	6.70			2.7828
Al K	1.486	0.70	0.01	1.09			0.4777
Ti K	4.508	1.32	0.01	1.16			1.4589
Cr K	5.411	15.87	0.03	12.80			17.8633
Fe K	6.398	15.96	0.03	11.99			18.0155
Ni K	7.471	46.35	0.07	33.11			49.9174
Nb L	2.166	6.79	0.02	3.06			5.5248
Mo L	2.293	2.09	0.01	0.91			1.7454
Total		100.00		100.00			

# A2 - SEM/EDX analyses of the sample FF-IN-HT-PC-03

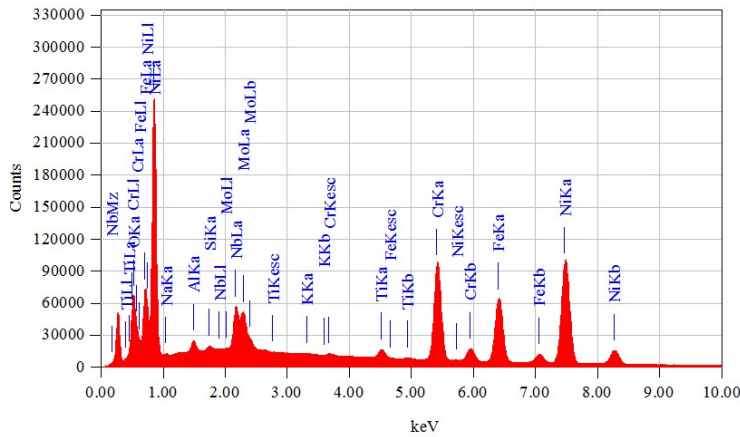
Region without contact

ff-in-ht-pc-03

Lab 1/1



Date : 24/06/2  
 Resolution : 256 x 1  
 Instrument : 7100F  
 Acc. Volt. : 15 kV  
 Magnification : x 200  
 Dwell Time : 0.2 mse  
 Sweep Count : 50



Acquisition Parameter  
 Instrument : 7100F  
 Acc. Voltage : 15.0 kV  
 Probe Current: 1.00000 nA  
 PHA mode : T2  
 Real Time : 594.16 sec  
 Live Time : 491.52 sec  
 Dead Time : 17 %  
 Counting Rate: 34536 cps  
 Energy Range : 0 - 20 keV

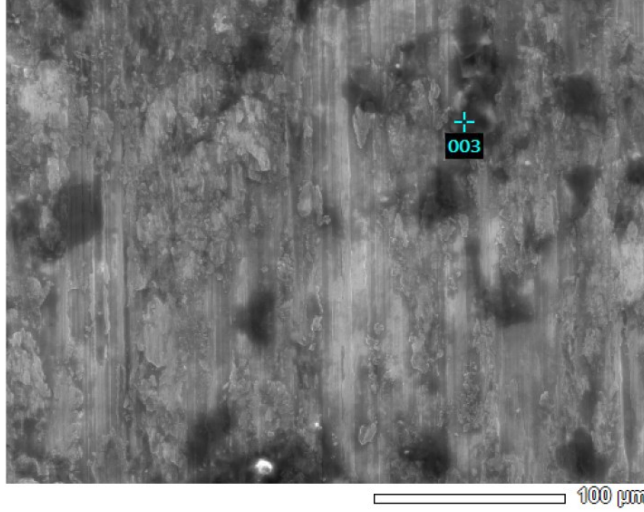
ZAF Method Standardless Quantitative Analysis  
 Fitting Coefficient : 0.0976

Element	(keV)	Mass%	Sigma	Atom%	Compound	Mass%	Cation
O	0.525	5.69	0.01	17.85		6.6424	K
Na	1.041	0.34	0.00	0.74		0.1379	
Al	1.486	0.51	0.00	0.95		0.3126	
Si	1.739	0.16	0.00	0.29		0.1140	
K	3.312	0.07	0.00	0.09		0.0732	
Ti	4.508	1.03	0.01	1.08		1.0556	
Cr	5.411	17.03	0.03	16.44		17.7877	
Fe	6.398	17.51	0.03	15.74		18.3253	
Ni	7.471	49.93	0.07	42.69		49.7722	
Nb	2.166	4.97	0.01	2.68		3.6780	
Mo	2.293	2.76	0.01	1.45		2.1011	
Total		100.00		100.00			

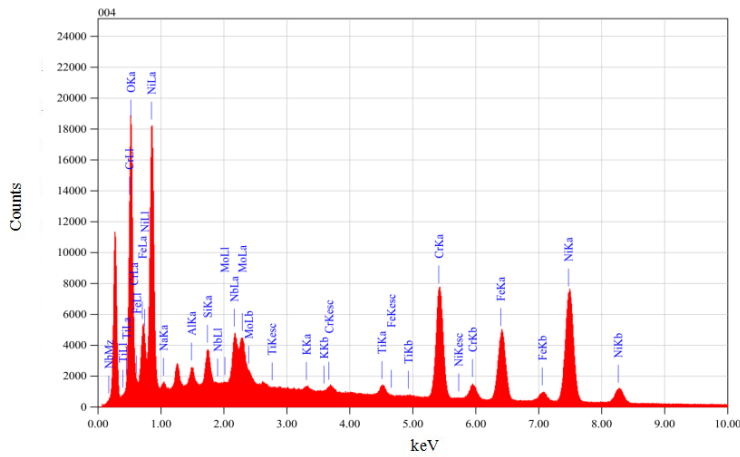
# Slip zone

ff-in-ht-pc-03 - slip zone

Lab 1/1



Title : IMG1  
 Instrument : 7100F  
 Volt : 15.00 kV  
 Mag. : x 350  
 Date : 2022/06/24  
 Pixel : 1024 x 768



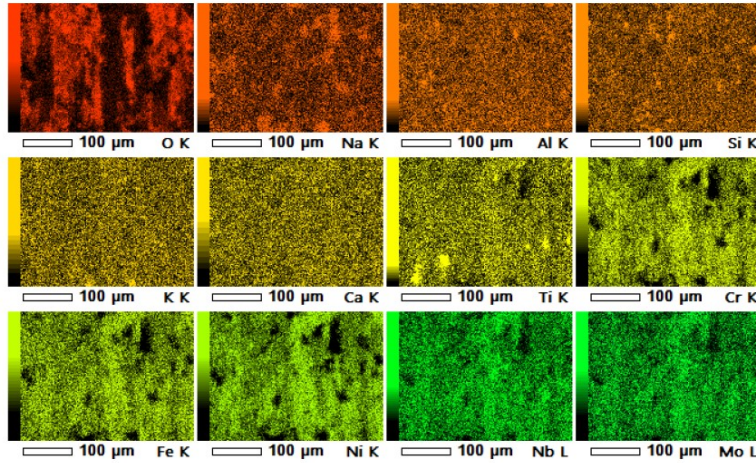
Acquisition Parameter  
 Instrument : 7100F  
 Acc. Voltage : 15.0 kV  
 Probe Current: 1.00000 nA  
 PHA mode : T2  
 Real Time : 59.36 sec  
 Live Time : 50.00 sec  
 Dead Time : 15 %  
 Counting Rate: 31727 cps  
 Energy Range : 0 - 20 keV

ZAF Method Standardless Quantitative Analysis  
 Fitting Coefficient : 0.1699

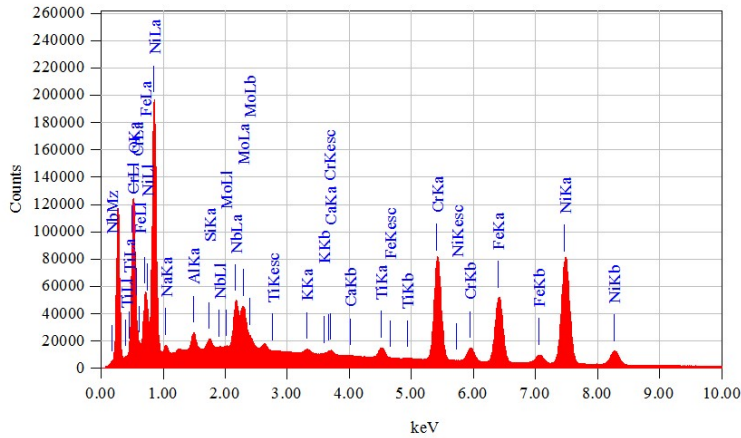
Element	(keV)	Mass%	Sigma	Atom%	Compound	Mass%	Cation	K
O	0.525	22.64	0.09	50.83				27.0143
Na	1.041	0.60	0.02	0.94				0.2485
Al	1.486	0.59	0.01	0.78				0.3624
Si	1.739	1.02	0.02	1.31				0.7273
K	3.312	0.20	0.01	0.19				0.2133
Ti	4.508	0.87	0.02	0.65				0.8532
Cr	5.411	14.11	0.07	9.75				14.1099
Fe	6.398	13.98	0.09	8.99				13.9877
Ni	7.471	39.16	0.19	23.96				37.4352
Nb	2.166	4.14	0.04	1.60				3.0268
Mo	2.293	2.70	0.04	1.01				2.0213
Total		100.00		100.00				

ff-in-ht-pc-03 - slip zone

Lab 1/1



Date : 24/06/2  
 Resolution : 256 x 1  
 Instrument : 7100F  
 Acc. Volt. : 15 kV  
 Magnification : x 350  
 Dwell Time : 0.2 mse  
 Sweep Count : 50



Acquisition Parameter  
 Instrument : 7100F  
 Acc. Voltage : 15.0 kV  
 Probe Current: 1.00000 nA  
 PHA mode : T2  
 Real Time : 583.03 sec  
 Live Time : 491.53 sec  
 Dead Time : 15 %  
 Counting Rate: 31605 cps  
 Energy Range : 0 - 20 keV

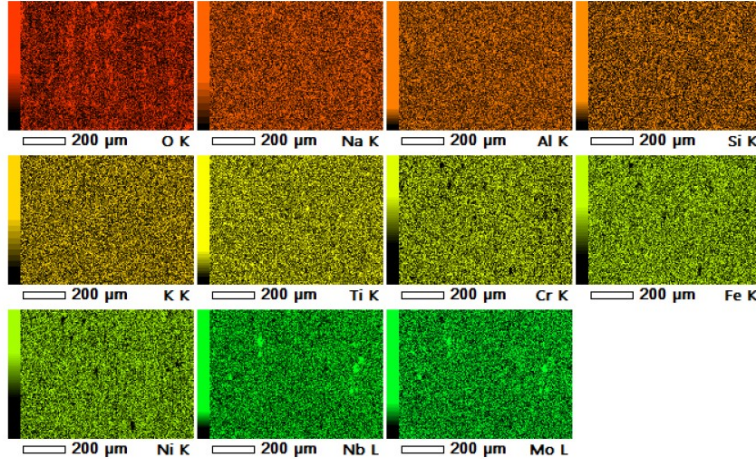
ZAF Method Standardless Quantitative Analysis  
 Fitting Coefficient : 0.1751

Element	(keV)	Mass%	Sigma	Atom%	Compound	Mass%	Cation	K
O	0.525	14.73	0.02	38.04				17.3779
Na	1.041	0.82	0.01	1.48				0.3404
Al	1.486	0.66	0.00	1.02				0.4104
Si	1.739	0.33	0.00	0.49				0.2363
K	3.312	0.24	0.00	0.25				0.2523
Ti	4.508	1.03	0.01	0.88				1.0329
Cr	5.411	15.41	0.03	12.25				15.8210
Fe	6.398	15.39	0.03	11.39				15.8282
Ni	7.471	44.02	0.06	30.97				43.1955
Nb	2.166	4.64	0.01	2.06				3.4408
Mo	2.293	2.72	0.01	1.17				2.0643
Total		100.00		100.00				

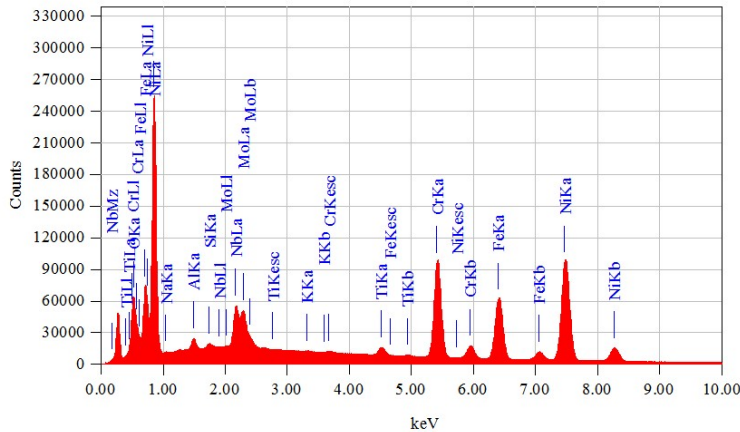
# Stick zone

ff-in-ht-pc-03 - stick zone

Lab 1/1



Date : 24/06/2  
 Resolution : 256 x 1  
 Instrument : 7100F  
 Acc. Volt. : 15 kV  
 Magnification : x 150  
 Dwell Time : 0.2 mse  
 Sweep Count : 50



Acquisition Parameter  
 Instrument : 7100F  
 Acc. Voltage : 15.0 kV  
 Probe Current: 1.00000 nA  
 PHA mode : T2  
 Real Time : 593.00 sec  
 Live Time : 491.52 sec  
 Dead Time : 17 %  
 Counting Rate: 34147 cps  
 Energy Range : 0 - 20 keV

### ZAF Method Standardless Quantitative Analysis

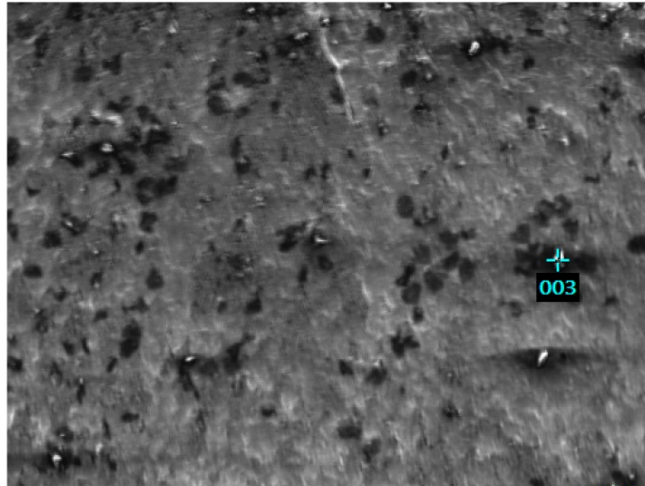
Fitting Coefficient : 0.0958

Element	(keV)	Mass%	Sigma	Atom%	Compound	Mass%	Cation	K
O K	0.525	5.24	0.01	16.63				6.1306
Na K	1.041	0.30	0.00	0.66				0.1218
Al K	1.486	0.51	0.00	0.97				0.3143
Si K	1.739	0.17	0.00	0.31				0.1228
K K	3.312	0.05	0.00	0.06				0.0501
Ti K	4.508	0.99	0.01	1.05				1.0096
Cr K	5.411	17.41	0.03	16.98				18.1892
Fe K	6.398	17.46	0.03	15.86				18.2741
Ni K	7.471	50.13	0.07	43.31				50.0018
Nb L	2.166	4.96	0.01	2.71				3.6715
Mo L	2.293	2.78	0.01	1.47				2.1141
Total		100.00		100.00				

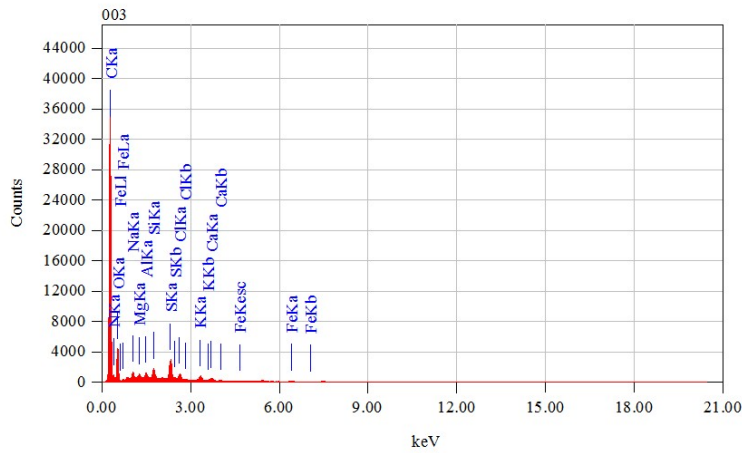
# Crack initiation region

ff-in-ht-pc-03 - near to crack initiation

Lab 1/1



Title : IMG1  
 Instrument : 7100F  
 Volt : 15,00 kV  
 Mag. : x 100  
 Date : 2022/06/24  
 Pixel : 1024 x 768



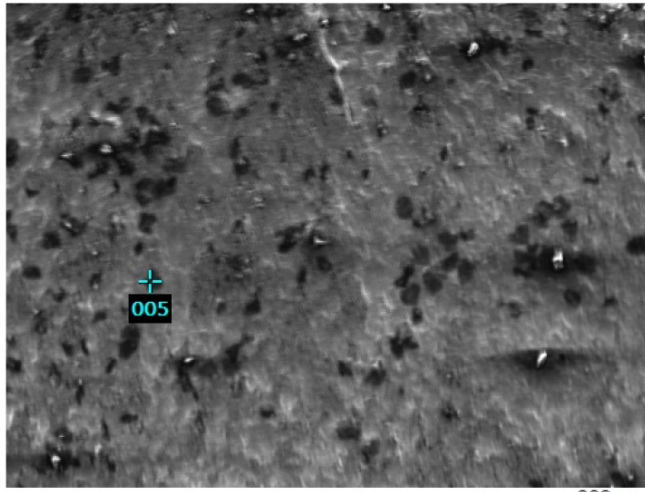
Acquisition Parameter  
 Instrument : 7100F  
 Acc. Voltage : 15.0 kV  
 Probe Current: 1.00000 nA  
 PHA mode : T2  
 Real Time : 52.66 sec  
 Live Time : 50.00 sec  
 Dead Time : 5 %  
 Counting Rate: 11190 cps  
 Energy Range : 0 - 20 keV

ZAF Method Standardless Quantitative Analysis  
 Fitting Coefficient : 0.0254

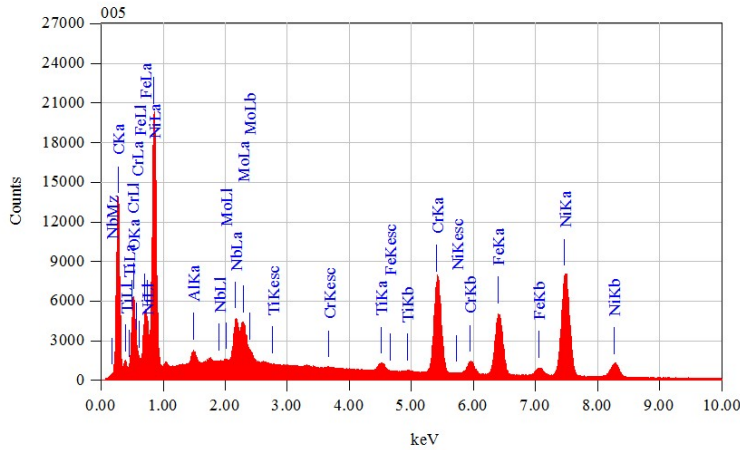
Element	(keV)	Mass%	Sigma	Atom%	Compound	Mass%	Cation
C	0.277	55.52	0.08	62.37			K
N	0.392	18.50	0.23	17.82			59.5639
O	0.525	21.05	0.16	17.75			15.7900
Na	1.041	0.51	0.01	0.30			15.6985
Mg	1.253	0.24	0.01	0.13			0.7203
Al	1.486	0.28	0.01	0.14			0.3253
Si	1.739	0.52	0.01	0.25			0.4684
S	2.307	1.54	0.02	0.65			0.9059
Cl	2.621	0.50	0.01	0.19			3.0534
K	3.312	0.50	0.01	0.17			0.9902
Ca	3.690	0.37	0.01	0.13			0.9806
Fe	6.398	0.47	0.02	0.11			0.7487
Total		100.00		100.00			0.7549

ff-in-ht-pc-03 - near to crack initiation

Lab 1/1



Title : IMG1  
 Instrument : 7100F  
 Volt : 15,00 kV  
 Mag. : x 100  
 Date : 2022/06/24  
 Pixel : 1024 x 768



Acquisition Parameter  
 Instrument : 7100F  
 Acc. Voltage : 15.0 kV  
 Probe Current: 1.00000 nA  
 PHA mode : T2  
 Real Time : 58.48 sec  
 Live Time : 50.00 sec  
 Dead Time : 14 %  
 Counting Rate: 29146 cps  
 Energy Range : 0 - 20 keV

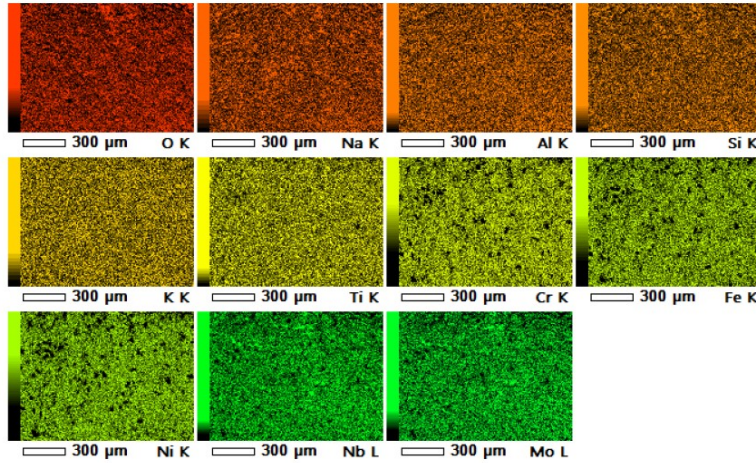
ZAF Method Standardless Quantitative Analysis

Fitting Coefficient : 0.0509

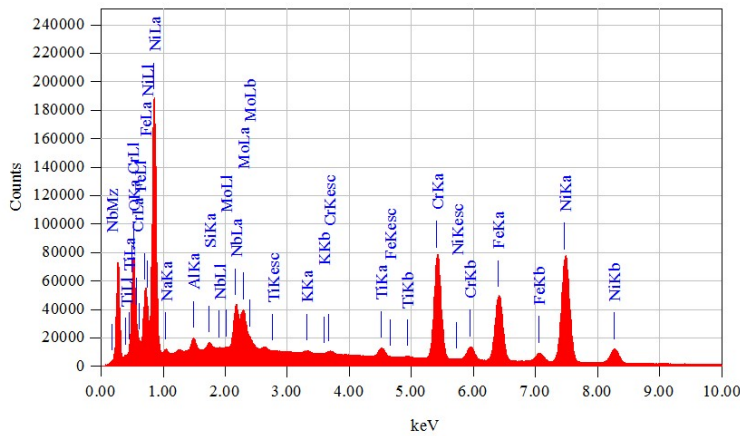
Element	(keV)	Mass%	Sigma	Atom%	Compound	Mass%	Cation	K
C K	0.277	28.52	0.07	59.85				10.7443
O K	0.525	7.99	0.06	12.60				8.5486
Al K	1.486	0.38	0.01	0.36				0.3387
Ti K	4.508	0.64	0.01	0.34				0.8410
Cr K	5.411	11.54	0.06	5.59				15.4029
Fe K	6.398	11.62	0.07	5.24				15.5082
Ni K	7.471	34.00	0.16	14.60				43.1552
Nb L	2.166	3.26	0.03	0.88				3.3276
Mo L	2.293	2.05	0.03	0.54				2.1335
Total		100.00		100.00				

ff-in-ht-pc-03 - near to crack initiation

Lab 1/1



Date : 24/06/2  
 Resolution : 256 x 1  
 Instrument : 7100F  
 Acc. Volt. : 15 kV  
 Magnification : x 100  
 Dwell Time : 0.2 mse  
 Sweep Count : 50



Acquisition Parameter  
 Instrument : 7100F  
 Acc. Voltage : 15.0 kV  
 Probe Current: 1.00000 nA  
 PHA mode : T2  
 Real Time : 571.08 sec  
 Live Time : 491.52 sec  
 Dead Time : 13 %  
 Counting Rate: 27680 cps  
 Energy Range : 0 - 20 keV

ZAF Method Standardless Quantitative Analysis

Fitting Coefficient : 0.1343

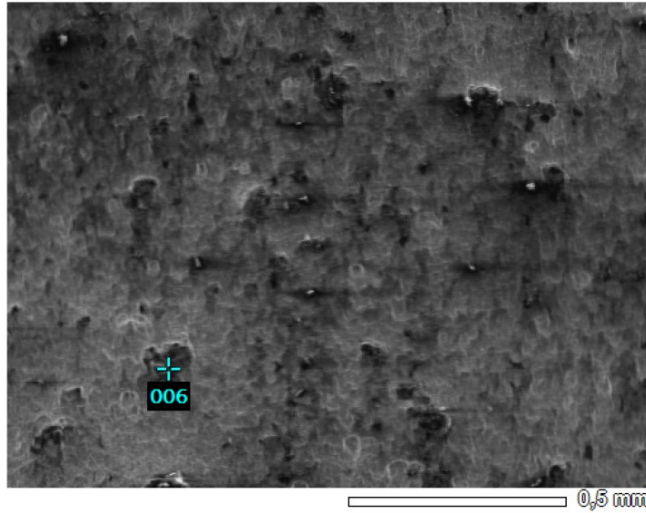
Element	(keV)	Mass%	Sigma	Atom%	Compound	Mass%	Cation	K
O K	0.525	9.60	0.02	27.55				11.3148
Na K	1.041	0.53	0.01	1.05				0.2155
Al K	1.486	0.53	0.00	0.90				0.3258
Si K	1.739	0.24	0.00	0.40				0.1714
K K	3.312	0.13	0.00	0.15				0.1405
Ti K	4.508	0.97	0.01	0.93				0.9881
Cr K	5.411	16.74	0.03	14.79				17.3504
Fe K	6.398	16.61	0.03	13.66				17.2313
Ni K	7.471	47.27	0.07	36.97				46.7564
Nb L	2.166	4.66	0.01	2.30				3.4455
Mo L	2.293	2.71	0.01	1.30				2.0603
Total		100.00		100.00				



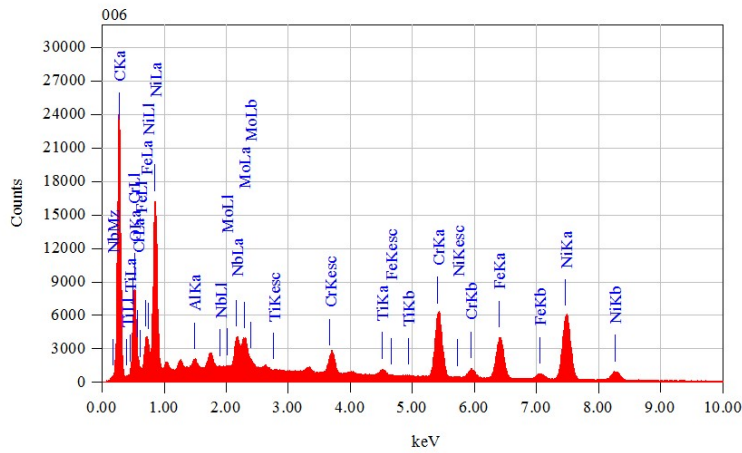
# Crack propagation region

ff-in-ht-pc-03 - propagation region

Lab 1/1



Title : IMG1  
 Instrument : 7100F  
 Volt : 15.00 kV  
 Mag. : x 80  
 Date : 2022/06/24  
 Pixel : 1024 x 768



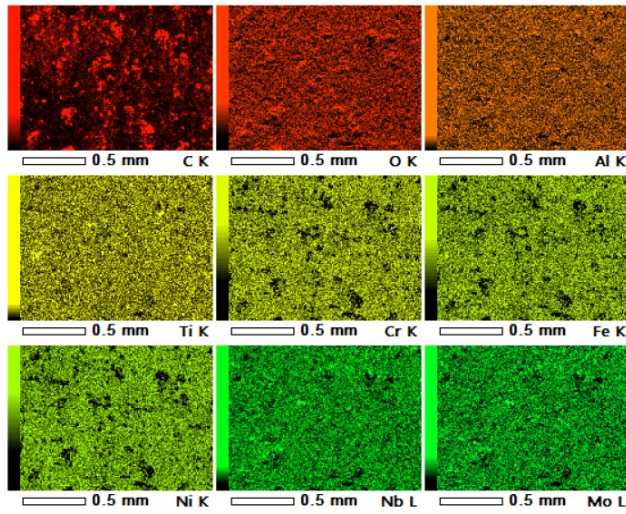
Acquisition Parameter  
 Instrument : 7100F  
 Acc. Voltage : 15.0 kV  
 Probe Current: 1.00000 nA  
 PHA mode : T2  
 Real Time : 57.93 sec  
 Live Time : 50.00 sec  
 Dead Time : 13 %  
 Counting Rate: 27760 cps  
 Energy Range : 0 - 20 keV

ZAF Method Standardless Quantitative Analysis  
 Fitting Coefficient : 0.0582

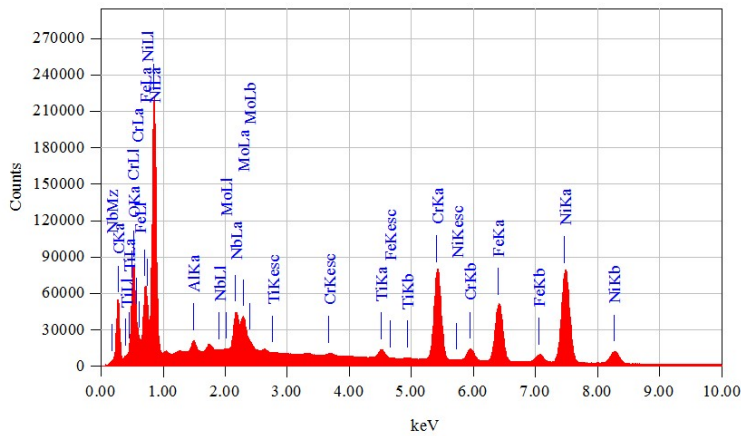
Element	(keV)	Mass%	Sigma	Atom%	Compound	Mass%	Cation	K
C	0.277	40.21	0.07	67.88				20.0730
O	0.525	12.30	0.07	15.59				12.8780
Al	1.486	0.26	0.01	0.20				0.2801
Ti	4.508	0.55	0.01	0.23				0.8046
Cr	5.411	8.94	0.05	3.48				13.2179
Fe	6.398	8.81	0.06	3.20				12.9962
Ni	7.471	24.53	0.13	8.47				34.4867
Nb	2.166	2.60	0.03	0.57				3.0926
Mo	2.293	1.80	0.03	0.38				2.1710
Total		100.00		100.00				

ff-in-ht-pc-03 - propagation region

Lab 1/1



Date : 24/06/2  
 Resolution : 256 x 1  
 -----  
 Instrument : 7100F  
 Acc. Volt. : 15 kV  
 Magnification : x 80  
 Dwell Time : 0.2 mse  
 Sweep Count : 50



Acquisition Parameter  
 Instrument : 7100F  
 Acc. Voltage : 15.0 kV  
 Probe Current: 1.00000 nA  
 PHA mode : T2  
 Real Time : 575.37 sec  
 Live Time : 491.51 sec  
 Dead Time : 14 %  
 Counting Rate: 29111 cps  
 Energy Range : 0 - 20 keV

ZAF Method Standardless Quantitative Analysis

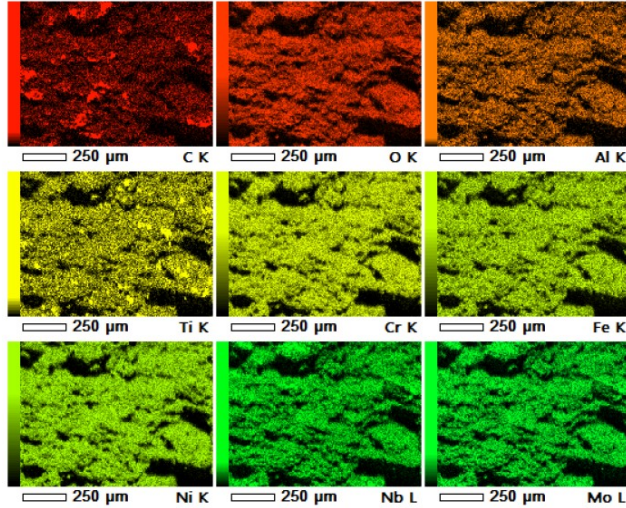
Fitting Coefficient : 0.0545

Element	(keV)	Mass%	Sigma	Atom%	Compound	Mass%	Cation	K
C K	0.277	14.19	0.02	38.19				4.2390
O K	0.525	9.54	0.02	19.27				10.7212
Al K	1.486	0.44	0.00	0.53				0.3191
Ti K	4.508	0.91	0.01	0.61				1.0443
Cr K	5.411	14.24	0.02	8.85				16.6915
Fe K	6.398	14.31	0.03	8.28				16.7523
Ni K	7.471	40.28	0.06	22.17				44.9224
Nb L	2.166	3.89	0.01	1.35				3.3581
Mo L	2.293	2.21	0.01	0.74				1.9521
Total		100.00		100.00				

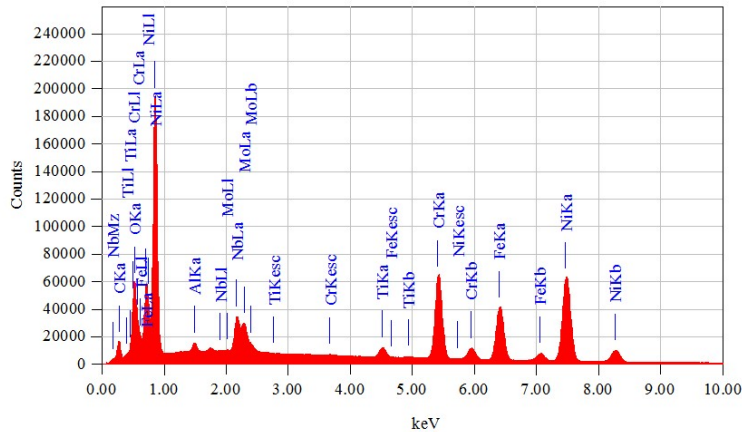
# Fast fracture region

ff-in-ht-pc-03 - fast fracture region

Lab 1/1



Date : 24/06/2  
 Resolution : 256 x 1  
 Instrument : 7100F  
 Acc. Volt. : 15 kV  
 Magnification : x 110  
 Dwell Time : 0.2 mse  
 Sweep Count : 50



Acquisition Parameter  
 Instrument : 7100F  
 Acc. Voltage : 15.0 kV  
 Probe Current: 1.00000 nA  
 PHA mode : T2  
 Real Time : 556.87 sec  
 Live Time : 491.52 sec  
 Dead Time : 11 %  
 Counting Rate: 22736 cps  
 Energy Range : 0 - 20 keV

ZAF Method Standardless Quantitative Analysis  
 Fitting Coefficient : 0.0558

Element	(keV)	Mass%	Sigma	Atom%	Compound	Mass%	Cation
C K	0.277	5.31	0.01	18.17			K
O K	0.525	7.86	0.02	20.18			1.3963
Al K	1.486	0.46	0.00	0.70			9.0432
Ti K	4.508	1.27	0.01	1.09			0.2968
Cr K	5.411	16.32	0.03	12.89			1.3517
Fe K	6.398	16.38	0.04	12.05			17.6878
Ni K	7.471	45.79	0.08	32.04			17.7436
Nb L	2.166	4.48	0.02	1.98			47.2869
Mo L	2.293	2.13	0.01	0.91			3.4930
Total		100.00		100.00			1.7007